EXCITED STATE PROCESSES IN RUTHENIUM(II) POLYPYRIDYL COMPLEXES AND CERIUM OXIDE NANOPARTICLES

by

Charles William Stark

A dissertation submitted in partial fulfillment
of the requirements for the degree

of

Doctor of Philosophy

in

Chemistry

MONTANA STATE UNIVERSITY
Bozeman, Montana

November 2016

DEDICATION

To Dolly, who taught me knowing what's important is the most important thing to know.

ACKNOWLEDGEMENTS

I would first like to thank my advisor Professor Bern Kohler for his patience and persistent support throughout my Ph.D studies. His guidance helped in many ways make my research more respectable, and his vast knowledge illuminated deeper meanings to my findings that I would have not noticed on my own. I simply could not have gotten where I am now without his help.

Besides my advisor, I would also like to thank the rest of my committee: Professor Aleks Rebane, Professor Pat Callis, Professor Erik Grumstrup, as well as Professor Rob Walker. The meetings that we had helped me develop the ability to set clear research goals and meet them in a (somewhat) timely manner. Moreover, I am extremely grateful to have had such people available as resources when I was confronted with a bewildering problem.

I would also like to express my gratitude towards my research collaborators: Professor Trevor Douglas, Dr. Wolfgang Schreier, Dr. Janice Lucon, Dr. Ethan Edwards, Natasha Pettinger and Arianna Celis, without whom I would have been unable to perform the majority of my research. In particular, I would like to thank Dr. Wolfgang Schreier, who taught me much of the artistry that is data collection, and that electronic manipulation can be just as important as the optics in spectroscopy.

Finally, I thank my fellow lab mates: Tom Zhang, Jinquan Chen, Jacob Remington, Ashley Beckstead, David Skowron, Jordan Dood, Rebecca Danforth and Ben Smith. Although science can sometimes be painfully unforgiving, it helps to know that I am not alone.

TABLE OF CONTENTS

TABLE OF CONTENTS – CONTINUED

TABLE OF CONTENTS – CONTINUED

LIST OF TABLES

LIST OF FIGURES

TABLE OF FIGURES – CONTINUED

TABLE OF FIGURES – CONTINUED

TABLE OF FIGURES – CONTINUED

LIST OF ABBREVIATIONS

CA: Citric Acid
EOM: Electro-optic Modulator
ESA: Excited State Absorption
HPLC: High-Performance Liquid Chromatography
TA: Transient Absorption
TRIR: Time Resolved Infrared
TCSPC: Time-Correlated Single Photon Counting
TEM: Transmission Electron Microscope

ABSTRACT

Solar driven hydrogen production from water is a sustainable alternative to fossil fuels, but suffers greatly from the large energy cost associated with splitting water. This report uses ultrafast transient absorption and other spectroscopic techniques to analyze several components that show potential for this photocatalysis, in particular observing the excited state dynamics of electron separation and recombination. In ruthenium(II) polypyridyl systems, the rate of interligand electron transfer (ILET) was found to change with time, initially behaving as an ultrafast barrierless process, but transforming into a much slower activated process as excess energy is vibrationally released over 100 ps following excitation. The change in ILET rates lead to changes in the population of localized ^{3}MLCT states distributed among each ligand, which are initially randomized, but favor the lower energy bipyridine ligands at longer times. Three analogous ruthenium complexes were then linked via a triazole bridge to a cobalt(II) polypyridyl center known to catalyze the formation of H_2, observing the electron transfer from ruthenium to cobalt using emission decay signals of the ruthenium complex. The electron transfer decay pathway was slower and relatively minor compared to similar ruthenium(II)-cobalt(II) systems; however, this reduced efficiency can potentially be explained by localizations on peripheral ligands, as well as a possible energy barrier on the 5-position of phenanthroline.

Finally, citrate coated CeO_2 nanoparticles displayed ultrafast trapping of holes upon excitation with UV light, forming significantly deeper traps than has been observed in other metal oxides. Transient absorption signals of the excited holes decayed over hundreds of picoseconds, with lifetimes dependent on the pH of the solution, indicating that the trapping sites are influenced by the surface of the nanoparticle. The corresponding electrons appear to form long lived Ce^{3+} sites, observable on timescales of minutes. The fate of these Ce^{3+} sites is also pH dependent, indicating that CeO_2 may be an effective water-splitting photocatalyst under basic conditions.

CHAPTER 1

INTRODUCTION

Ever since the industrial revolution, there has been a steady increase in the demand for energy in the form of chemical fuels, the vast majority of which have been based on hydrocarbon materials extracted from underground reserves. In recent years, worldwide rates of oil production have begun to slow, indicating that globally, we are near the peak of oil production.[1] While recent advances in extraction techniques (i.e. fracking) have opened access to reserves previously assumed to be inaccessible, these methods are somewhat environmentally contentious, and suffer from the same long term issue of being a finite resource. Numerous alternative renewable energy sources have been developed, with solar and wind technologies having the most potential for growth.[2,3] However, in many cases these renewable sources provide less reliable energy production, with one of the major issues being that they are ill-equipped to store energy they produce for later use. If the energy economy is to transition away from a finite supply of fossil fuels, these renewable sources of energy need to be able to create a replacement chemical fuel.

Water-splitting photocatalysts offer a direct means of using solar energy to produce hydrogen and oxygen gas, which can be later combusted or electrochemically reacted as fuel.[4–8] Hydrogen gas has been commended as a zero-emission fuel, meaning that its combustion does not produce pollutants such as CO_2; however, the energy required to split water is large at 1.23 eV/e, making the photocatalytic step difficult to achieve efficiently. While this energy is equivalent to the energy of a single 1008 nm

photon, making it theoretically possible to use most of the solar energy spectrum for catalysis (Figure 1.1), there are often significant barriers associated with the chemical reactions of the H and O atoms, requiring much higher energies to overcome.[9,10] These barriers typically limit the functional wavelengths of light to the UV. In many cases, it has become more feasible to partition the water-splitting reaction into the two photocatalytic half-reactions:

$$2H_2O \rightarrow O_2 + 4e^- + 4H^+ \quad (1.1)$$

$$4H^+ + 4e^- \rightarrow 2H_2 \quad (1.2)$$

Where one photocatalyst oxidizes water to form O_2 and H^+, while a second photocatalyst reduces H^+ to H_2, as shown in Figure 1.2. These two reactions can be linked by an intermediate redox shuttle, which transfers electrons from one photoactive center to the other. This two-step system theoretically takes twice as many photons to produce O_2 and H_2 gas. However, it offers the advantage of having two separate photocatalysts, which can make use of lower photon energies and can be optimized separately to improve the overall efficiency.[10,11]

To understand what factors are important for the photocatalytic efficiency of water-splitting, it is useful to observe the excited state processes that occur in a photocatalyst after the absorption of light. As both half-reactions involved in water-splitting are redox reactions (equations 1.1 & 1.2), it is important that excited state processes lead to the localization of charges at the reactive center, while extraneous processes are minimized. Monitoring the evolution of an excited state can be performed

using transient absorption and emission spectroscopic techniques, which are discussed in Chapter 2.

The two photocatalysts in this report are cerium oxide nanoparticles and a multimetal complex comprised of linked ruthenium and cobalt polypyridyl centers, shown in Figure 1.3. Cerium oxide nanoparticles have been observed to catalyze the production of O_2 gas from water under UV irradiation in aqueous solution[12,13], while cobalt polypyridyl complexes have been shown to catalyze the production of H_2 gas[14–21]. The cobalt center is connected to ruthenium polypyridyl complexes, which are well known for the formation of long-lived charge-separated excited states, and have been used many times as an electron donor in photocatalysis or dye sensitized solar cells.[5,6,18,22–36] The primary focus of this report is to understand the excited state processes in these two photocatalytic systems after photon absorption.

The photophysics of the ruthenium polypyridine center is first analyzed in order to understand the initial charge separation and localization processes that occur among the chelated polypyridine rings. This initial charge separated state is metal-to-ligand charge-transfer (MLCT) in nature, localizing the excited electron on one of the attached pyridyl ligands. While it has been known that this localized state was able to "hop" from one ligand to another via interligand electron-transfer (ILET), there were previous disagreements as to the rate of this hopping process.[37–39] Chapter 3 analyzes the kinetics of ILET using the two ligands 2,2'-bipyridine and 1,10-phenanthroline, which have different transient absorption signatures, but very similar MLCT excited state energies. It was found that the rate of hopping between ligands dynamically changes; initially

hopping is very rapid, but slows as the complex reaches vibrational equilibrium with the surroundings. As this hopping rate slows, there is a preference of localization on lower energy ligands, which could be useful for transferring this excited electron across a bridging ligand.

In Chapter 4, three modified ruthenium polypyridyl complexes are covalently linked with a cobalt tris-phenanthroline complex via 1,2,3-triazole bridges (Figure 1.3). While intra-[34,40–52] and intermolecular[14,15,31,53–59] electron transfer has been observed between polypyridyl complexes of ruthenium and cobalt previously, the triazole bridge offers a novel synthetic approach. The synthesis of triazole follows the mechanism of Huisgen cycloaddition, which is a member of "click chemistry" reactions.[60] The term "click" is used due to the simple and efficient means of joining individual units in a macromolecular structure; in this case allowing the individual metal centers to be fully coordinated before the creation of extended structures. Electron transfer has been observed to occur across other triazole bridged systems, which have displayed long-lived charge separated states.[32,33,61–63] In the case of the ruthenium-cobalt system, the rate of electron transfer could be modeled from the biphasic kinetics observed for the time-resolved emission of the ruthenium center. This electron transfer rate was unremarkable in comparison with other studies, and appeared to suffer from a significant back electron transfer. This slow kinetics was rather surprising, as intermolecular studies have indicated that electron transfer between ruthenium and cobalt polypyridyl complexes is diffusion limited in many cases.[16] While the back electron transfer could be explained by the charge separated state having slightly higher energy than the initial MLCT state of the

ruthenium center, the exact reasons for overall slow transfer kinetics were not able to be determined without further investigations in the attachment positions of the triazole bridge.

Chapter 5 addresses the photophysical processes associated with UV excitation of cerium oxide (CeO_2) nanoparticles, which first had to be stabilized using citrate as a surface coating to prevent agglomeration. It was observed that upon the absorption of light, both the excited electron and corresponding hole are rapidly trapped. This trapping processes has been observed previously for TiO_2;[64–66] however, the trapping sites for both holes and excited electrons in CeO_2 are significantly deeper than in TiO_2, which is thought to alter the observed recombination dynamics. The excited state lifetime of these citrate coated nanoparticles was observed to be pH dependent, becoming longer-lived in lower pH solutions. This increase in lifetime corresponded to increases in photochemical degradation of the nanoparticle at low pH. However, nanoparticle solutions at pH 9.5 showed dynamics that were assigned to changes in the redox state of cerium within the nanoparticle without ultimate degradation, indicating that this basic region would be ideal for redox reactions photocatalyzed by CeO_2.

These studies illustrate the photophysical processes of charge separation and recombination in several components for use in water-splitting photocatalysis. The results obtained herein allow for future studies to improve the efficiency of analogous components using a mechanistic approach to optimization, ultimately for the synthesis of solar fuels.

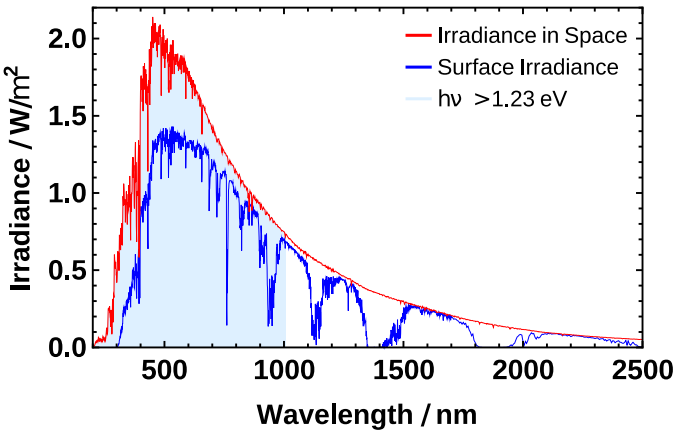

Figure 1.1 The spectrum of solar irradiance at 0 (red) and 1.5 (blue) air masses, obtained from the American Society for Testing and Materials. [67] The light blue shading indicates photon energies above the water splitting threshold.

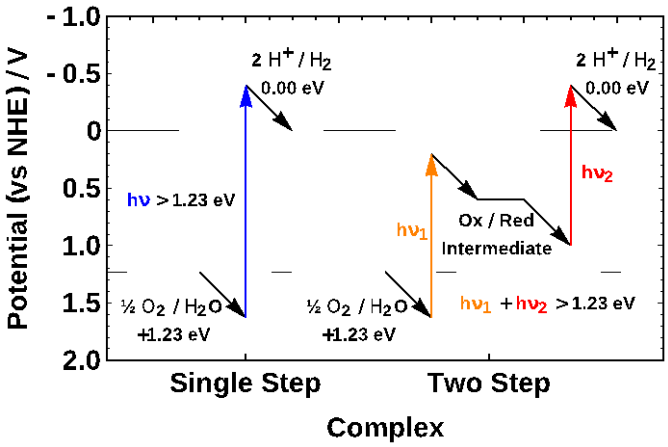

Figure 1.2 Single-step and two-step mechanisms for photocatalysis. Colored arrows indicate light-absorption, while black arrows show redox processes. The dotted and dashed lines indicate the minimum voltages required to oxidize water and reduce hydrogen, respectively.

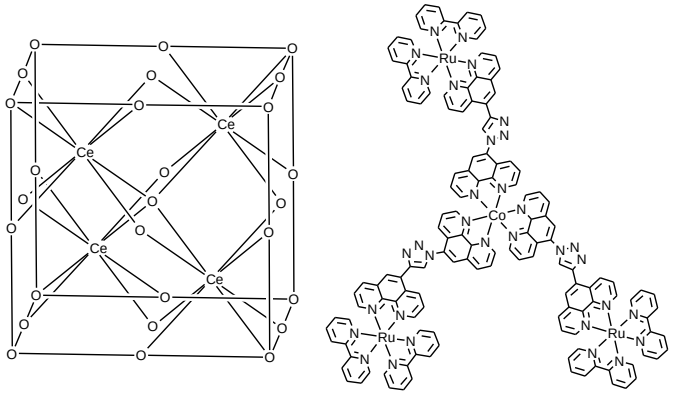

Figure 1.3 Chemical structures of (A) CeO_2 and (B) $[Ru\text{-}Co]^{8+}$.

■ REFERENCES

(1) Madureira, N. L. *Key Concepts in Energy*; Springer International Publishing: Cham, **2014**.

(2) Perez, M.; Perez, R. UPDATE 2015–A FUNDAMENTAL LOOK AT SUPPLY SIDE ENERGY RESERVES FOR THE PLANET. *Int. Energy Agency SHC Programme Sol. Update* **2015**, *62*, 4–6.

(3) Statistical Review of World Energy | Energy economics | BP Global http://www.bp.com/en/global/corporate/energy-economics/statistical-review-of-world-energy.html.

(4) Artero, V.; Fontecave, M. Solar Fuels Generation and Molecular Systems: Is It Homogeneous or Heterogeneous Catalysis? *Chem Soc Rev* **2013**, *42*, 2338–2356.

(5) Stoll, T.; Castillo, C. E.; Kayanuma, M.; Sandroni, M.; Daniel, C.; Odobel, F.; Fortage, J.; Collomb, M.-N. Photo-Induced Redox Catalysis for Proton Reduction to Hydrogen with Homogeneous Molecular Systems Using Rhodium-Based Catalysts. *Coord. Chem. Rev.* **2015**, *304–305*, 20–37.

(6) Kärkäs, M. D.; Johnston, E. V.; Verho, O.; Åkermark, B. Artificial Photosynthesis: From Nanosecond Electron Transfer to Catalytic Water Oxidation. *Acc. Chem. Res.* **2014**, *47*, 100–111.

(7) Concepcion, J. J.; Jurss, J. W.; Brennaman, M. K.; Hoertz, P. G.; Patrocinio, A. O. T.; Murakami Iha, N. Y.; Templeton, J. L.; Meyer, T. J. Making Oxygen with Ruthenium Complexes. *Acc. Chem. Res.* **2009**, *42*, 1954–1965.

(8) Artero, V.; Chavarot-Kerlidou, M.; Fontecave, M. Splitting Water with Cobalt. *Angew. Chem. Int. Ed.* **2011**, *50*, 7238–7266.

(9) Osterloh, F. E. Inorganic Materials as Catalysts for Photochemical Splitting of Water. *Chem. Mater.* **2008**, *20*, 35–54.

(10) Kudo, A.; Miseki, Y. Heterogeneous Photocatalyst Materials for Water Splitting. *Chem Soc Rev* **2009**, *38*, 253–278.

(11) Kalisman, P.; Nakibli, Y.; Amirav, L. Perfect Photon-to-Hydrogen Conversion Efficiency. *Nano Lett.* **2016**, *16*, 1776–1781.

(12) Bamwenda, G. R.; Arakawa, H. Cerium Dioxide as a Photocatalyst for Water Decomposition to O_2 in the Presence of Ce^{4+} and Fe^{3+} Species. *J. Mol. Catal. Chem.* **2000**, *161*, 105–113.

(13) Bamwenda, G. R.; Uesigi, T.; Abe, Y.; Sayama, K.; Arakawa, H. The Photocatalytic Oxidation of Water to O_2 over Pure CeO_2, WO_3, and TiO_2 Using Fe^{3+} and Ce^{4+} as Electron Acceptors. *Appl. Catal. Gen.* **2001**, *205*, 117–128.

(14) Brown, G. M.; Brunschwig, B. S.; Creutz, C.; Endicott, J. F.; Sutin, N. Homogeneous Catalysis of the Photoreduction of Water by Visible Light. Mediation by a tris(2,2'-bipyridine)ruthenium(II)-cobalt(II) Macrocycle System. *J. Am. Chem. Soc.* **1979**, *101*, 1298–1300.

(15) Krishnan, C. V.; Creutz, C.; Mahajan, D.; Schwarz, H. A.; Sutin, N. Homogeneous Catalysis of the Photoreduction of Water by Visible Light. 3. Mediation by Polypyridine Complexes of Ruthenium(II) and Cobalt(II). *Isr. J. Chem.* **1982**, *22*, 98–106.

(16) Creutz, C.; Sutin, N. Photogeneration and Reactions of Cobalt(I) Complexes. *Coord. Chem. Rev.* **1985**, *64*, 321–341.

(17) Bigi, J. P.; Hanna, T. E.; Harman, W. H.; Chang, A.; Chang, C. J. Electrocatalytic Reduction of Protons to Hydrogen by a Water-Compatible Cobalt Polypyridyl Platform. *Chem Commun* **2010**, *46*, 958–960.

(18) Cropek, D. M.; Metz, A.; Müller, A. M.; Gray, H. B.; Horne, T.; Horton, D. C.; Poluektov, O.; Tiede, D. M.; Weber, R. T.; Jarrett, W. L.; *et al.* A Novel Ruthenium(II)–cobaloxime Supramolecular Complex for Photocatalytic H_2 Evolution: Synthesis, Characterisation and Mechanistic Studies. *Dalton Trans.* **2012**, *41*, 13060.

(19) Staehle, R.; Losse, S.; Filipovic, M. R.; Ivanović-Burmazović, I.; Vos, J. G.; Rau, S. Photocatalytic Generation of Hydrogen from Water under Aerobic Conditions. *ChemPlusChem* **2014**, *79*, 1614–1621.

(20) Willkomm, J.; Muresan, N. M.; Reisner, E. Enhancing H_2 Evolution Performance of an Immobilised Cobalt Catalyst by Rational Ligand Design. *Chem Sci* **2015**, *6*, 2727–2736.

(21) Deponti, E.; Luisa, A.; Natali, M.; Iengo, E.; Scandola, F. Photoinduced Hydrogen Evolution by a Pentapyridine Cobalt Complex: Elucidating Some Mechanistic Aspects. *Dalton Trans* **2014**, *43*, 16345–16353.

(22) Asbury, J. B.; Wang, Y.-Q.; Hao, E.; Ghosh, H. N.; Lian, T. Evidences of Hot Excited State Electron Injection from Sensitizer Molecules to TiO_2 Nanocrystalline Thin Films. *Res. Chem. Intermed.* **2001**, *27*, 393–406.

(23) Kallioinen, J.; Benkö, G.; Sundström, V.; Korppi-Tommola, J. E. I.; Yartsev, A. P. Electron Transfer from the Singlet and Triplet Excited States of $Ru(dcbpy)_2(NCS)_2$ into Nanocrystalline TiO_2 Thin Films. *J. Phys. Chem. B* **2002**, *106*, 4396–4404.

(24) Benkö, G.; Kallioinen, J.; Myllyperkiö, P.; Trif, F.; Korppi-Tommola, J. E. I.; Yartsev, A. P.; Sundström, V. Interligand Electron Transfer Determines Triplet Excited State Electron Injection in RuN3−Sensitized TiO_2 Films. *J. Phys. Chem. B* **2004**, *108*, 2862–2867.

(25) Johansson, O.; Borgström, M.; Lomoth, R.; Palmblad, M.; Bergquist, J.; Hammarström, L.; Sun, L.; Åkermark, B. Electron Donor−Acceptor Dyads Based on Ruthenium(II) Bipyridine and Terpyridine Complexes Bound to Naphthalenediimide. *Inorg. Chem.* **2003**, *42*, 2908–2918.

(26) Meylemans, H. A.; Lei, C.-F.; Damrauer, N. H. Ligand Structure, Conformational Dynamics, and Excited-State Electron Delocalization for Control of Photoinduced Electron Transfer Rates in Synthetic Donor-Bridge-Acceptor Systems. *Inorg. Chem.* **2008**, *47*, 4060–4076.

(27) Wenger, O. S. How Donor−Bridge−Acceptor Energetics Influence Electron Tunneling Dynamics and Their Distance Dependences. *Acc. Chem. Res.* **2011**, *44*, 25–35.

(28) Baron, A.; Herrero, C.; Quaranta, A.; Charlot, M.-F.; Leibl, W.; Vauzeilles, B.; Aukauloo, A. Efficient Electron Transfer through a Triazole Link in Ruthenium(II) Polypyridine Type Complexes. *Chem. Commun.* **2011**, *47*, 11011.

(29) Arachchige, S. M.; Shaw, R.; White, T. A.; Shenoy, V.; Tsui, H.-M.; Brewer, K. J. High Turnover in a Photocatalytic System for Water Reduction to Produce Hydrogen Using a Ru, Rh, Ru Photoinitiated Electron Collector. *ChemSusChem* **2011**, *4*, 514–518.

(30) White, T.; Knoll, J.; Arachchige, S.; Brewer, K. A Series of Supramolecular Complexes for Solar Energy Conversion via Water Reduction to Produce Hydrogen: An Excited State Kinetic Analysis of Ru(II), Rh(III), Ru(II) Photoinitiated Electron Collectors. *Materials* **2011**, *5*, 27–46.

(31) McNamara, W. R.; Han, Z.; Yin, C.-J.; Brennessel, W. W.; Holland, P. L.; Eisenberg, R. Cobalt-Dithiolene Complexes for the Photocatalytic and Electrocatalytic Reduction of Protons in Aqueous Solutions. *Proc. Natl. Acad. Sci.* **2012**, *109*, 15594–15599.

(32) Herrero, C.; Batchelor, L.; Baron, A.; El Ghachtouli, S.; Sheth, S.; Guillot, R.; Vauzeilles, B.; Sircoglou, M.; Mallah, T.; Leibl, W.; *et al.* Click Chemistry as a

Convenient Tool for the Incorporation of a Ruthenium Chromophore and a Nickel-Salen Monomer into a Visible-Light-Active Assembly. *Eur. J. Inorg. Chem.* **2013**, 494–499.

(33) Herrero, C.; Quaranta, A.; El Ghachtouli, S.; Vauzeilles, B.; Leibl, W.; Aukauloo, A. Carbon Dioxide Reduction via Light Activation of a ruthenium–Ni(cyclam) Complex. *Phys. Chem. Chem. Phys.* **2014**, *16*, 12067.

(34) López, A. M.; Natali, M.; Pizzolato, E.; Chiorboli, C.; Bonchio, M.; Sartorel, A.; Scandola, F. A Co(II)–Ru(II) Dyad Relevant to Light-Driven Water Oxidation Catalysis. *Phys. Chem. Chem. Phys.* **2014**, *16*, 12000–12007.

(35) Stoll, T.; Gennari, M.; Fortage, J.; Castillo, C. E.; Rebarz, M.; Sliwa, M.; Poizat, O.; Odobel, F.; Deronzier, A.; Collomb, M.-N. An Efficient Ru^{II} -Rh^{III} -Ru^{II} Polypyridyl Photocatalyst for Visible-Light-Driven Hydrogen Production in Aqueous Solution. *Angew. Chem. Int. Ed.* **2014**, *53*, 1654–1658.

(36) Herrero, C.; Quaranta, A.; Sircoglou, M.; Sénéchal-David, K.; Baron, A.; Marín, I. M.; Buron, C.; Baltaze, J.-P.; Leibl, W.; Aukauloo, A.; *et al.* Successive Light-Induced Two Electron Transfers in a Ru–Fe Supramolecular Assembly: From Ru–Fe(II)–OH_2 to Ru–Fe(IV)–oxo. *Chem Sci* **2015**, *6*, 2323–2327.

(37) Wallin, S.; Davidsson, J.; Modin, J.; Hammarström, L. Femtosecond Transient Absorption Anisotropy Study on $[Ru(bpy)_3]^{2+}$ and $[Ru(bpy)(py)_4]^{2+}$. Ultrafast Interligand Randomization of the MLCT State. *J. Phys. Chem. A* **2005**, *109*, 4697–4704.

(38) Malone, R. A.; Kelley, D. F. Interligand Electron Transfer and Transition State Dynamics in Ru(II)-trisbipyridine. *J. Chem. Phys.* **1991**, *95*, 8970–8976.

(39) Yeh, A. T.-W. *Ultrafast Excited State Dynamics of Tris-(2, 2'-bipyridine) Ruthenium (II)*; Ernest Orlando Lawrence Berkeley National Lab., CA (US), 2000.

(40) Horvath, R.; Lombard, J.; Leprêtre, J.-C.; Collomb, M.-N.; Deronzier, A.; Chauvin, J.; Gordon, K. C. Excited-State Spectroscopic Investigations of Multinuclear Complexes Based on $[Ru(bpy)_3]^{2+}$ Moieties Connected to 2,2′-Bipyridine and 2,2′;6′,2″-Terpyridine Ligands. *Dalton Trans.* **2013**, *42*, 16527.

(41) Lombard, J.; Boulaouche, R.; Amilan Jose, D.; Chauvin, J.; Collomb, M.-N.; Deronzier, A. Synthesis and Properties of Trinuclear Polypyridyl Complexes Ru(II)–Co(II)–Ru(II) and Ru(II)–Co(III)–Ru(II): Their Photoinduced Interconversion. *Inorganica Chim. Acta* **2010**, *363*, 234–242.

(42) Kuhar, K.; Fredin, L. A.; Persson, P. Exploring Photoinduced Excited State Evolution in Heterobimetallic Ru(II)–Co(III) Complexes. *J. Phys. Chem. B* **2015**, *119*, 7378–7392.

(43) Holbrook, R. J.; Weinberg, D. J.; Peterson, M. D.; Weiss, E. A.; Meade, T. J. Light-Activated Protein Inhibition through Photoinduced Electron Transfer of a Ruthenium(II)–Cobalt(III) Bimetallic Complex. *J. Am. Chem. Soc.* **2015**, *137*, 3379–3385.

(44) Feskov, S. V.; Kichigina, A. O.; Ivanov, A. I. Kinetics of Nonequilibrium Electron Transfer in Photoexcited Ruthenium(II)−Cobalt(III) Complexes. *J. Phys. Chem. A* **2011**, *115*, 1462–1471.

(45) Torieda, H.; Nozaki, K.; Yoshimura, A.; Ohno, T. Low Quantum Yields of Relaxed Electron Transfer Products of Moderately Coupled Ruthenium(II)−Cobalt(III) Compounds on the Subpicosecond Laser Excitation. *J. Phys. Chem. A* **2004**, *108*, 4819–4829.

(46) Torieda, H.; Yoshimura, A.; Nozaki, K.; Sakai, S.; Ohno, T. Temperature-Independent Rate of Electron-Transfer between a Cobalt(II) and a Ruthenium(III) of Doublet Electronic Configuration. *J. Phys. Chem. A* **2002**, *106*, 11034–11044.

(47) Downward, A. M.; Moore, E. G.; Hartshorn, R. M. Photoinduced Ligand Release in a Ruthenium(II)-Cobalt(III) Heterodinuclear System. *Chem. Commun.* **2011**, *47*, 7692.

(48) Shao, Y.; Lu, X.; Li, K.; Zhao, Z.; Shi, X.; Jin, D.; Zhu, H.; Yang, G.; Guo, W. Theoretical Insight into Photo-Induced Intramolecular Electron Transfer in Heterodinuclear Ru(II)–Co(III) Complexes. *Mater. Chem. Phys.* **2015**, *162*, 6–10.

(49) Yoshimura, A.; Nozaki, K.; Ikeda, N.; Ohno, T. Photoinduced Electron-Transfer and Back Electron-Transfer Within Binuclear Complexes of Ru(II) and Co(III). *J. Am. Chem. Soc.* **1993**, *115*, 7521–7522.

(50) Song, X.; Lei, Y.; Vanwallendal, S.; Perkovic, M.; Jackman, D.; Endicott, J.; Rillema, D. Photoinduced Electron-Transfer Processes Involving Covalently Linked Ruthenium and Cobalt Polypyridyl Complexes - Comparison of Electronic Coupling in Bridged and Nonbridged Ruthenium and Cobalt Complexes. *J. Phys. Chem.* **1993**, *97*, 3225–3236.

(51) Fihri, A.; Artero, V.; Razavet, M.; Baffert, C.; Leibl, W.; Fontecave, M. Cobaloxime-Based Photocatalytic Devices for Hydrogen Production. *Angew. Chem. Int. Ed.* **2008**, *47*, 564–567.

(52) Canton, S. E.; Kjær, K. S.; Vankó, G.; van Driel, T. B.; Adachi, S.; Bordage, A.; Bressler, C.; Chabera, P.; Christensen, M.; Dohn, A. O.; *et al.* Visualizing the Non-Equilibrium Dynamics of Photoinduced Intramolecular Electron Transfer with Femtosecond X-Ray Pulses. *Nat. Commun.* **2015**, *6*, 6359.

(53) Kirch, M.; Lehn, J.-M.; Sauvage, J.-P. Hydrogen Generation by Visible Light Irradiation of Aqueous Solutions of Metal Complexes. An Approach to the Photochemical Conversion and Storage of Solar Energy. *Helv. Chim. Acta* **1979**, *62*, 1345–1384.

(54) Krist, K.; Gafney, H. An Analysis of the Mechanistic Pathways in the Reversible Photoinduced Reactions Between $Ru(bpy)_3^{2+}$ and $Co(phen)_3^{3+}$ by Flash-Photolysis Techniques. *J. Phys. Chem.* **1982**, *86*, 951–958.

(55) Huang, S.-M. Y.; Gafney, H. D. The Effect of Molecular Structure on the Quenching of the Charge-Transfer Luminescence of Ruthenium(II) Complexes. *J. Phys. Chem.* **1977**, *81*, 2602–2604.

(56) Creutz, C.; Sutin, N. Electron-Transfer Reactions of Excited States. Reductive Quenching of the tris(2,2'-bipyridine)ruthenium(II) Luminescence. *Inorg. Chem.* **1976**, *15*, 496–499.

(57) Yoshimura, A.; Uddin, M. J.; Amasaki, N.; Ohno, T. Low Quantum Yields of Electron-Transfer Reaction of Photoexcited $Ru(bpydc)_3^{4-}$ with $Co(tpy)_2^{3+}$ and Methyl viologen^{2+} (Bpydc : 2,2 '-Bipyridine-4,4 '-Dicarboxylate and Tpy : 2,2 ': 6 ',2 -Terpyridine). *J. Phys. Chem. A* **2001**, *105*, 10846–10853.

(58) Berkoff, R.; Krist, K.; Gafney, H. D. Measurement of the Rates of the Electron-Transfer Reactions between $[Ru(bpy)_3]^{3+}$ and $[Co(phen)_3]^{2+}$ or $[Co(bpy)_3]^{2+}$ by Flash Photolysis Techniques. *Inorg. Chem.* **1980**, *19*, 1–7.

(59) Lin, C.-T.; Sutin, N. Quenching of the Luminescence of the tris(2,2'-bipyridine) Complexes of ruthenium(II) and osmium(II). Kinetic Considerations and Photogalvanic Effects. *J. Phys. Chem.* **1976**, *80*, 97–105.

(60) Schulze, B.; Schubert, U. S. Beyond Click Chemistry – Supramolecular Interactions of 1,2,3-Triazoles. *Chem. Soc. Rev.* **2014**, *43*, 2522.

(61) Natali, M.; Ravaglia, M.; Scandola, F.; Boixel, J.; Pellegrin, Y.; Blart, E.; Odobel, F. Long-Range Charge Separation in a Ferrocene–(Zinc Porphyrin)–Naphthalenediimide Triad. Asymmetric Role of 1,2,3-Triazole Linkers. *J. Phys. Chem. C* **2013**, 130912075807001.

(62) Natali, M.; Orlandi, M.; Chiorboli, C.; Iengo, E.; Bertolasi, V.; Scandola, F. Porphyrin–cobaloxime Dyads for Photoinduced Hydrogen Production: Investigation of the Primary Photochemical Process. *Photochem. Photobiol. Sci.* **2013**, *12*, 1749.

(63) Cardiel, A. C.; Benson, M. C.; Bishop, L. M.; Louis, K.; Yeager, J.; Tan, Y.; Hamers, R. J. Chemically Directed Assembly of Photoactive Metal Oxide Nanoparticle Heterojunctions via the Copper-Catalyzed Azide-Alkyne Cycloaddition "click" reaction. *Abstr. Pap. Am. Chem. Soc.* **2012**, *243*.

(64) Schneider, J.; Matsuoka, M.; Takeuchi, M.; Zhang, J.; Horiuchi, Y.; Anpo, M.; Bahnemann, D. W. Understanding TiO_2 Photocatalysis: Mechanisms and Materials. *Chem. Rev.* **2014**, *114*, 9919–9986.

(65) Bahnemann, D.; Henglein, A.; Lilie, J.; Spanhel, L. Flash Photolysis Observation of the Absorption Spectra of Trapped Positive Holes and Electrons in Colloidal TiO2. *J. Phys. Chem.* **1984**, *88*, 709–711.

(66) Zawadzki, P. Absorption Spectra of Trapped Holes in Anatase TiO_2. *J. Phys. Chem. C* **2013**, *117*, 8647–8651.

(67) ASTM G173-03(2012), Standard Tables for Reference Solar Spectral Irradiances: Direct Normal and Hemispherical on 37° Tilted Surface. In; ASTM International: West Conshohocken, PA, 2012.

CHAPTER 2

GENERAL METHODS

Preface

This chapter outlines the procedures used to analyze photophysical processes of ruthenium polypyridyl complexes as well as cerium oxide nanoparticles. The first section is about the transient absorption system, which was used for both samples. Later sections generally proceed by describing techniques used in ruthenium experiments before discussing techniques used to analyze cerium dioxide.

2.1 Transient Absorption

2.1.1 Transient Absorption Spectrometers

Ultrashort pulses for use in the transient absorption experiments were generated by a Ti:Sapphire femtosecond laser amplification system (Libra, Coherent Inc., Santa Clara, CA). This system consists of a mode-locked femtosecond Titanium-Sapphire oscillator (Vitesse, Coherent Inc., Santa Clara, CA) which provides a low-energy seed pulse centered at 800 nm with a repetition rate of 76 MHz. The seed pulses undergo temporal stretching by a stretcher with a grating before entering a regenerative amplifier. This amplifier consists of two Pockels cells and a waveplate to overlap the seed pulse with a high energy nanosecond 532 nm pump pulse (Evolution, Coherent Inc., Santa Clara, CA) in a Titanium-Sapphire crystal. This overlap transfers energy into the seed pulse, which is then sent into a grating compressor to achieve femtosecond pulse

duration. The output pulses have energies of 3.5 mJ and a FWHM duration of 85 fs. The repetition rate is 1 kHz.

2.1.2 Visible Pump/Probe Transient Absorption: General Methods

The experimental setups for UV/visible-pump/Visible-probe measurements are shown in (Figure 2.1). The fundamental pulse is split by an 80/20 beamsplitter, directing 80% of the power to pump three optical parametric amplifiers (OPA) (two OperAsolo and one TOPAS, Coherent Inc., Santa Clara, CA) and the other 20% passed through a second 95/5 beamsplitter. This second beam splitter directed 95% of the power to produce second harmonic generation (SHG) and the remaining 5% was used for white light generation (WL).

White light continuum probe pulses were generated by focusing the 800 nm fundamental with a lens (f = 150 mm) into a 4 mm thick Calcium Fluoride (CaF_2) crystal. This crystal was mounted in a circular translation stage,[1] which moved the crystal in a small circle perpendicular to the incident beam without rotating the crystal. This motion was done to prevent damage to the crystal and minimize polarization changes due to birefringence within the material. This rotation stage moved at a rate of about 1 Hz. In order to achieve stability in the white light signal at wavelengths below 340 nm, the angle of incidence of pulses to the CaF_2 crystal was optimized, monitoring the resulting continuum spectrum with a charge-coupled device (CCD) spectrograph (Model USB2000+, Ocean Optics, Dunedin, FL). After generating a white-light continuum, the probe pulses were collimated, and passed through a polarizer before being focused into

the sample. The probe beam at the sample had a full-width half-maximum (FWHM) cross section of 60 μm. The generation of white light and subsequent polarization created a down-chirp in the probe pulse (Figure 2.2), which was unaccounted for when acquiring broadband transient spectra.

Pump pulses at 400 nm were generated by the SHG of the 800 nm fundamental. This was done by focusing the pulses (f = 200 mm) through a 1-mm type-I β-barium borate (BBO) crystal, resulting in energy efficiencies of about 35%.

Pump pulses at other wavelength and single-wavelength probe pulses were generated via two OPAs (OperA Solo, Coherent Inc., Santa Clara, CA). Using different harmonic packages, the output wavelength can be tuned from 240 nm to 2000 nm. To briefly summarize the internal processes, a white light continuum is first generated from a sapphire plate as the seed beam. This seed pulse is mixed with a small amount of 800 nm fundamental in a BBO crystal to generate pre-amplified signal pulses. The signal pulses are mixed with a high energy 800 nm pulse in a second BBO crystal to generate amplified signal and idler pulses. The amplified signal and idler pulses can be frequency doubled or mixed with a fresh 800 nm pulse in a third BBO crystal to generate photons in the ultraviolet and visible region.

Depending on the setup (Figure 2.1), either the pump or the probe pulses were delayed using a 60 cm computer-controlled IMS600PP optical delay stage (Newport Inc. Irvine, CA) with a maximum time delay of 4 ns, and a minimum step-size of ~8 fs, which was used to set a time delay between pump and probe pulses.

2.1.3 Visible Pump/Probe Transient
Absorption: Single Wavelength Signals

Pump pulses were chopped at 333 Hz by a mechanical chopper (New Focus, Santa Clara, CA), allowing one out of every three pulses to pass, which continued through a neutral density filter and polarizer, such that the pump pulse energy was approximately 1 μJ per pulse. The polarization angle between pump and probe pulses was set to the magic angle (54.7^o) at the sample. After passing through the sample, the pump is blocked, while the probe pulses are passed through a monochromator (f = 300 mm) into a photomultiplier tube (PMT). This PMT signal was amplified with a lock-in-amplifier (Model SR830, Stanford instruments) synchronized with the mechanical chopper. Amplified signals were retrieved through a GPIB interface from the lock-in amplifier and recorded by an in-house LabVIEW based data collection software in a computer.

2.1.4 Visible Pump/Probe Transient
Absorption: Anisotropic Signals

Transient absorption anisotropy measurements were made with the single wavelength setup described above. To collect anisotropy signals at a single wavelength, two back-to-back single wavelength signals were recorded, orienting the pump polarizer such that the pump linear polarization was 90^o ($I_\perp$) or 0^o ($I_\parallel$) with respect to the probe at the sample, which were used to calculate $r(t)$, defined as:

$$r(t) = \frac{I_\parallel - I_\perp}{I_\parallel + 2I_\perp} \tag{2.1}$$

The perpendicular and parallel signals had to be aligned separately, as modifying the polarization affected the overlap of the pump and probe spatially, as well as altered the time delay between the two pulses. To counter the effects that changing conditions may have, the resultant signals were scaled to have the same average amplitude at delay times longer than 300 ps.

2.1.5 Visible Pump/Probe Transient Absorption: Broadband Spectra

Transient spectra at specific delay times could be generated when using the white-light probe pulse, acquired with a CCD spectrograph (Model USB2000+, Ocean Optics, Dunedin, FL). This detector has a slower response than the PMT, so trigger signals from the Libra needed to be delayed by 0.9995 ms using a delay generator (Model DG535, Stanford Research Systems Inc., Sunnyvale, CA), which sent a fifth harmonic (200 Hz) trigger signal for spectral acquisition by the CCD detector. This 200 Hz signal was also sent to the chopper, where it was further divided to produce a 100 Hz signal. The chopper alternately passed or blocked five pulses, to generate pump-on and pump-off cycles. These groups of pulses had to be phase matched to the CCD trigger, which was done by sending the chopped pump-pulses to a fast photodiode detector (201/579-7227, Thorlabs Inc., Ann Arbor, MI) attached to an oscilloscope (TDS 420, Tektronix, Beaverton, OR) This oscilloscope also received the CCD acquisition trigger signal from the delay generator. The phase of the chopper was then adjusted such that groups of five pump pulses were all in the same bin triggered by the delay generator, while the other bin contained no pump pulses.

After the pump-pulses were in phase with the CCD trigger signal, both the probe pulses and stray light from the pump pulses were directed with a fiber optic cable (Ocean Optics, f_{in} = 42 mm, f_{out} = 68 mm) into the CCD. The CCD detector was placed into high-speed acquisition mode with an external trigger using the accompanying software (Spectrasuite, Ocean Optics, Dunedin, FL). This mode would integrate spectra over 3 ms, and had an inherent 2 ms dead time after each acquisition as the detector reset. In this manner, a spectrum of the transmitted probe pulse was collected every 5 ms with pump pulses alternatively on or off. A total of 6000 spectra were acquired at each delay time. Software written in LabWindows/CVI (National Instruments, Austin, TX) used the detected pump pulses to sort individual spectra into pump-on or pump-off, and calculated transient absorption changes. Because the white-light probe pulse was chirped, broadband spectra at times <3 ps were generally disregarded.

2.1.6 Visible Pump/Infrared Probe Transient Absorption Spectra

Time resolved Infrared (TRIR) absorption was acquired using a separate section of the transient absorption laser setup (Figure 2.1). Pump pulses were generated by OPA and delayed using a translation stage as described in section 2.1.2. Pump pulses were chopped at 500 Hz by a mechanical chopper (New Focus, Santa Clara, CA), which blocked every other pulse. The pulses were subsequently polarized, attenuated by a neutral density filter, and focused to a spot size of 500 μm (FWHM) at the sample. After passing through the sample, the pump was directed at a fast diode (DET210, Thorlabs, Ann Arbor, MI).

Mid-IR probe pulses were generated in a two-part optical parametric amplifier system consisting of an OPA (TOPAS-C, Light Conversion, Vilnius, Lithuania) and a non-collinear difference frequency generator (NDFG) (Light Conversion, Vilnius Lithuania), with a potential output wavelength range of 2.6 – 20 μm. The OPA produced signal and idler beams in an identical way as described above in 2.1.2, however there are no options for frequency doubling or sum frequency generation with another 800 nm pulse. Instead, both the signal and idler were steered into the NDFG where they were mixed in a non-collinear manner in a GaSe crystal, which produced difference frequency pulses in the mid-IR. The power and polarization of these mid-IR pulses was adjusted using two CaF_2 polarizers before being split in a 50/50 ZnSe beam splitter to produce a probe pulse and a reference pulse. The reference pulse was used to normalize the signal obtained by the probe pulse in order to reduce the effects of pulse-to-pulse noise. Both the signal and reference pulses were directed at the sample, but were vertically separated by 7.5 mm. Each had a spot size of ~ 300 μm (FWHM) and was attenuated to ~200 μW. The UV/visible-pump pulse was overlaid with the probe at the sample, with its polarization set to magic angle (54.7^o) with respect to the probe.

The probe and reference pulses were recollimated after the sample and focused into a spectrograph (Triax 190, Horiba Scientific, Edison, NJ) with a 0.75 mm slit width (f = 190 mm). Both beams were dispersed by a set of interchangeable gratings (50 lines/mm, 100 lines/mm or 300 lines/mm) and projected onto a liquid nitrogen-cooled dual-row 64-element (pixel) Mercury-Cadmium-Telluride detector (Infrared Systems

Development Corp., Winter Park, FL). The upper row was used to record the reference signals, while the lower row was for probe signals.

2.2 Emission Lifetimes

2.2.1 Emission Lifetime Single Wavelength Signals

Emission lifetimes were measured using the Time-Correlated Single Photon Counting (TCSPC) technique using a commercial spectrometer system (FluoTime200, PicoQuant Photonics North America, West Springfield, MA), which can be viewed in Figure 2.3. Excitation pulses were obtained from a femtosecond Ti:Sapphire laser (Chameleon Ultra II, Coherent Inc.) equipped with a second and third harmonic generator. The laser produces sub-picosecond excitation pulses at a repetition rate of 80 MHz. The repetition rate was decreased using one of two electro-optic modulators (EOM), for either second harmonic (M350-105, Conoptics, Danbury, CT), or third harmonic (M350-80, Conoptics, Danbury, CT) pulses. These selected pulses were focused into a 1 cm cuvette containing the sample under study. Emitted photons were collected at 90^{o} and directed through a monochromator (f = 100 mm) onto a microchannel plate photomultiplier tube (model R3809U-50, Hamamatsu Corp.). The emission polarizer was set to magic angle with respect to the excitation polarizer.

The arrival time of individual pulses was determined by comparing them to an electronic reference signal. This signal originated from a diode located inside the Ti:Sapphire laser chamber, which was relayed through a synchronous countdown system (Model 305, Conoptics, Danbury, CT). This system would select signals above a

threshold, generating a trigger pulse after counting a set number of input signals. This trigger pulse had an inherent bias, which had to be passed through a differentiator (TDL800, PicoQuant, Berlin, Germany) before being sent to the detector's timing system (Picoharp 300, PicoQuant, Berlin, Germany). The synchronous countdown also created a 10 ns electric pulse, which was amplified (Model 25D, Conoptics, Danbury, CT) and sent to one of the two electro-optic modulators in order to allow a laser pulse through. This electric signal showed a slight oscillation after the initial pulse, which persisted for several nanoseconds (Figure 2.4), and could cause abnormal structures in pulse selection if the repetition rate was faster than 5 MHz. Repetition rates actually used were typically 160 kHz.

Each sample analyzed using the TCSPC technique had a corresponding colloidal silica solution (LUDOX HS-40, Sigma Aldrich St. Louis, MO) recorded before and after each scan. The emission monochromator was set to the excitation wavelength, to collect scattered pulses from the colloidal solution until the maximum signal in any single channel matched the corresponding samples signal. The time-resolved scattering signals were used as the instrument response function (IRF) for fitting procedures, as well as to ensure that electro-optic modulation of excitation pulses had not changed over the course of the sample acquisition measurement.

2.2.2 Time Resolved Emission Spectra

Time resolved emission spectra were obtained by scanning the emission monochromator of the TCSPC setup, collecting time resolved signals at select wavelengths for identical amounts of time. These spectra were corrected for the

wavelength dependent response of the PMT using a correction factor described in section 2.5.4.

As the TCSPC had a more sensitive detector than the steady-state fluorometer, it was occasionally advantageous to integrate the time-resolved spectra to obtain a steady-state emission spectrum. This integrated time-resolved technique was necessary when the emission spectrum of a sample was unobservable using the steady-state fluorometer. In the cases where both steady-state and integrated time-resolved data were observable, a comparison of the two techniques showed no differences in emission spectral shape or position.

2.3 Steady-State Measurements

2.3.1 UV/Vis/NIR Absorption Measurements

Steady-State UV/Vis absorption spectra were measured on a Lambda-25 spectrometer (Perkin-Elmer, Wellesley, MA) at room temperature. Samples were held in a 1 cm quartz cuvette (Starna Cells, Atascadero, CA). All spectra were corrected by subtracting a reference spectrum of the solvent used.

2.3.2 Visible/NIR Emission Measurements

Steady-State emission was collected using a Fluorolog-3-11 Emission spectrometer (Horiba Ltd., Kyoto Japan) at room temperature. Emitted photons were collected at 90^{o}, using a photomultiplier tube (1911, Jobin Yvon (Horiba), Edison, NJ). The emission polarizer was set to magic angle with respect to the excitation polarizer. All

emission spectra were corrected for by multiplying by a correction factor, which had been obtained for each wavelength used.

Emission quantum yields for samples were determined using steady-state absorption and emission spectra. The emission spectra (*E*) were integrated over all wavelengths and compared to the absorption (*A*) at the excitation wavelength for the same sample, using the equation:

$$\Phi_s = \Phi_r \left(\frac{\int E_s}{\int E_r} \right) \left(\frac{A_r}{A_s} \right) \left(\frac{\eta_s}{\eta_r} \right)^2 \qquad (2.2)$$

where η is the refractive index of the solvent. To obtain an absolute emission quantum yield, each sample (*s*) was compared to a reference solution (*r*) of $[Ru(bpy)_3]^{2+}$ in acetonitrile, which had a quantum yield of 0.062.[2]

2.3.3 Fourier Transform Infrared Spectroscopy

Infrared absorption spectra were collected using a Fourier transform infrared spectrometer (FTIR 4200, Jasco, Easton, MD). Liquid samples were analyzed in a 0.39 mm diameter flow-cell (DLC-S25, Harrick, Pleasantville, NY), assembled with CaF_2 windows. Solid samples were analyzed using the method of attenuated total reflection (ATR), where powder was placed on a ZnSe prism and gently pressed into a firm film (ATR PRO450-S, Jasco, Easton, MD). After inserting any sample, the spectrometer purged with dry air (6 SCFH) from a generator (Model 75-62, Parker Balston, Haverhill, MA) for ten minutes before measuring absorbance, to remove the additional absorption from water vapor and carbon dioxide.

2.3.4 Transmission Electron Microscopy

Solutions of CeO_2 nanoparticles were pipetted onto a polymer-coated copper grid 3.05 mm in diameter. The water was then wicked away using paper, leaving the dry nanoparticles suspended on the grid. This nanoparticle coated grid was then analyzed using a transmission electron microscope (TEM, Leo 912 AB, Carl Zeiss Inc., Pleasanton, CA), with dark field, strong atomic number (Z) contrast techniques. Electrons with an accelerating voltage of 100 keV and a thermionic emission current of 5 μA were produced from a tungsten filament, focused on the sample, and detected using a CCD. The resulting microscopic images were occasionally modified to enhance contrast and brightness, but were otherwise unaltered.

2.3.5 Acid-Base Titration

Acid base titrations were performed by sequentially pipetting small μL volumes of 1 M HCl into concentrated basic solutions. The pH was monitored using a pH probe (MI-410 Micro Combination pH Electrode, Microelectrodes Inc., Bedford NH) recording pH with a OrionStar A121 pH meter (Thermo Scientific, Waltham, MA). The pH probe was calibrated using three standard buffer solutions (pH: 4.0, 6.86 and 10.0).

2.4 Sample Handling

2.4.1 Materials

In the study of dynamics of interligand electron transfer of ruthenium-bipyridine/phenanthroline complexes ($[Ru(bpy)_{3-n}(phen)_n]^{2+}$), each polypyridyl complex was synthesized and purified by the Douglas research group and was used as received.

In the study of electron transfer in a multimetal ruthenium-cobalt polypyridyl complex, all complexes were synthesized by the Douglas research group. The single metal complexes were used as received, however the multimetal complex had to be isolated from a cobalt contaminant using high-performance liquid chromatography (HPLC) separation methods, described in section 2.4.4.

Polypyridyl complexes were prepared in deuterated (Acetonitrile-D3 (D, 99.8%), Cambridge Isotope Laboratories Inc., Andover MA) or normally protonated acetonitrile (99.98% HPLC Grade, Honeywell, Morris Plains, NJ) or ultrapure water (Millipore, Billerica, MA). Each solution was diluted such that the absorbance of the sample was ~0.1 at whatever wavelength was used for excitation in the TCSPC or UV-vis transient absorption setup. In the case of infrared absorption, liquid samples were prepared to have 0.3 absorbance at the excitation wavelength.

In the cerium oxide nanoparticle study, >25 nm diameter cerium oxide (CeO_2, Sigma Aldrich, St. Louis MO) and >25 nm titanium dioxide (TiO_2, Sigma Aldrich, St. Louis MO) nanoparticles were purchased from Sigma Aldrich. Smaller 8 nm diameter nanoparticles of cerium oxide were purchased from STREM (Strem Chemicals Inc., Newburyport, MA). Each was dissolved in ultrapure water, containing measured amounts of citric acid (99.5%, Sigma Aldrich, St. Louis MO), citrate (>99% Sodium Citrate Dihydrate, Sigma Aldrich, St. Louis MO), perchloric acid (???), nitric acid (???) and potassium hydroxide (87.6%, J.T. Baker Inc., Phillipsburg NJ).

2.4.2 Spectroscopic Cuvettes

All samples were measured in either a 1 cm (1-Q-10-GL14-S, Starna Cells, Atascadero CA) or 1 mm path length quartz cuvette (21-Q-1, Starna Cells, Atascadero CA). The 1 cm cuvette was used for all steady-state spectroscopy and for the TCSPC emission lifetime data, while the 1 mm cuvette was used during UV-visible transient absorption experiments. Transient absorption was also collected with a 1 mm flow cell (DLC-S25, Harrick Scientific Products, Pleasantville, NY), which was assembled from two CaF_2 windows separated by a 1 mm Teflon spacer. The samples were circulated through the flow cell via a Masterflex7524-00 peristaltic pump (Cole-Parmer, Vernon Hills, IL). The flow cell apparatus was used for single wavelength UV/visible transient absorption, as well as for TRIR studies.

2.4.3 Nitrogen Purging

Emission for either the TCSPC or steady state analysis methods was performed on nitrogen purged sealed cuvettes. To remove oxygen from the samples, cuvettes were gently bubbled with nitrogen through a syringe for 10 minutes. At the end of this bubbling process, a Parafilm seal (Parafilm “M”, Bemis Flexible Packaging, Neenah WI) was placed over the top of the cuvette, while the syringe was slowly removed. After removing the syringe, a screw cap was tightened over the Parafilm seal. Samples sealed in this manner showed no aeration over the course of several days, observed by constant quantum yield of $[Ru(bpy)_3]^{2+}$ emission. Every samples steady-state emission intensity was also checked before and after each TCSPC experiment to ensure emission quenching from O_2 had not occurred over the course of the measurement.

2.4.4 High-Performance Liquid Chromatography Purification

The purity of several ruthenium samples was checked using high-performance liquid chromatography (HPLC, 1100 Agilent, Santa Clara, CA). A 10 mL sample was injected into a solvent line of H_2O:ACN in a ratio of 30:70 with 0.1% of trifluoroacetic acid as a slight buffer to prevent pH changes during separation. After degassing the solution (G1322A, Agilent, Santa Clara, CA), the sample was flowed through a C-18 reverse phase column (Sigma Aldrich, St. Louis, MO), the solvent ratio was increased to 60:40 over the course of 10 minutes after which it remained constant for a minute before being returned to initial conditions. Sample exit times from the column were continuously monitored with a visible-light diode array, (G1315B DAD, Agilent, Santa Clara, CA) the monitored wavelengths selected were at 450 and 285 nm, selected for identification of Ruthenium and Ligand/Cobalt signals. The filtered sample was collected and lyophilized after observing separation.

2.4.5 Cerium Oxide Nanoparticle Preparation

Cerium oxide nanoparticles were prepared in numerous ways, to determine conditions in which the nanoparticles are stable and do not agglomerate. A summary of quantitative measurements for acidic solutions can be found in Table 5.1. In general, a mass of cerium oxide was weighed on an analytical balance (AE 240, Mettler, Leicester, United Kingdom) and added to 50-150 μL volumes of either 1 M $HClO_4$ for acidic solutions (pH 1 to 2.6), or 50-800 μL 0.67 M KOH for basic or neutral solutions. Some solutions also contained 200 μL additions of 0.38 M citric acid or 200-800 μL 0.2 M

sodium chloride, added using a micropipette (FinnPipette EHO6712-4500, Thermo Scientific, Waltham, MA). This mixture was diluted to 3 mL with ultrapurified water (Millipore, Billerica, MA) resulting in solutions with pH's of 2.6, 6.5, 7.5, 9.5, 10.5, and 12. These solutions were sonicated (Model 1510 Ultrasonic Cleaner, Branson, Henrico, VA) for a time up to 2 hours, followed by aging in a dark room for 1 to 14 days at room temperature. Basic and neutral solutions were filtered with 0.2 μm pore syringe filters (Hydrophilic PTFE, Millex-LG SLLGH25NS, EMD Millipore, Darmstadt, Germany); although exact masses of nanoparticles were known before filtration, nanoparticle concentrations after filtering are not known.

2.4.6 UV Photoreactor

Solutions of cerium oxide nanoparticles were irradiated with 254 nm light in a photoreactor (Srinivasan-Griffin Rayonet Type, The Southern New England Ultraviolet Co., Middleton, CT), in a sealed 1 cm quartz cuvette positioned in the center of the reaction chamber (Figure 2.5). Typically, irradiation was performed with 13 out of the 16 lamps present, which supplied the cuvette with 27 ± 2 mW of radiant power. This power was determined using the chemical dosimeter 1,3-dimethyluracil (1,3-DMU) (99%, Sigma Aldrich, St. Louis MO) in 0.2 mM concentrations, which undergoes a pseudo-zero order hydration reaction (Φ_{rxn} = 0.0130 at 254 nm) upon UV irradiation.[3–5] The concentration of 1,3-DMU was monitored on the UV/Visible spectrometer at 266 nm (ε_{266} = 8900 $M^{-1}cm^{-1}$) at irradiation intervals of 5 minutes (Figure 2.6). Changing the number of lamps in the photoreactor appeared to linearly change the radiant power penetrating the sample.

2.5 Data Treatment

2.5.1 Modeling Transient Absorption Signals

Transient absorption single wavelength and anisotropy signals were each fit to sums of *i* exponentials with decay rates of k_i and amplitudes C_i, convoluted with a normalized Gaussian instrument response function (IRF), which had a FWHM of $2\sqrt{2\ln 2}\sigma$ resulting in the equation:

$$\Delta A(t) = \int_0^\infty \frac{\exp\left(\frac{-(\tau - t)^2}{2\sigma^2}\right)}{\sigma\sqrt{2\pi}} \sum_i C_i \cdot \exp(-k_i \cdot \tau) d\tau \tag{2.3a}$$

$$\Delta A(t) = \sum_i \frac{C_i}{2} \exp\left(-k_i \cdot t + \frac{k_i{}^2\sigma^2}{2}\right)\left(1 - Erf\left(\frac{k_i\sigma - \frac{t}{\sigma}}{\sqrt{2}}\right)\right) \tag{2.3b}$$

Fitting was performed using the IGOR Pro 6.2 program (Wavemetrics Inc. Portland, OR). Transient spectra and multiple single wavelength signals were each globally fit by linking the k_i parameter for different probe wavelengths.

2.5.2 Modeling Emission Lifetimes

Emission decay lifetimes were obtained by reconvoluting sums of exponentials with a separately collected IRF on the TCSPC instrument software package FluoFit (PicoQuant, Berlin, Germany).

2.5.3 Emission Spectral Corrections

Both steady state and time resolved emission spectra were corrected for the detector responses at different wavelengths by the creation of a correction spectrum (Figure 2.7). For the Fluorolog steady-state spectrometer, the correction factor was produced using a set of five laser dyes as emission standards, using a method outlined by Gardecki & Maroncelli [6]. Briefly, each dye's emission spectrum was obtained and compared to a set of standard spectra. The ratio of the standard to the acquired spectra at any given wavelength produced a correction factor at that wavelength. Near the edges of each dyes emission band, this ratio becomes less defined, so emission from a different dye would be used. However, different dyes had different absolute correction factors for overlapping wavelengths, as the intensity of the lamp used for excitation varied with wavelength. The correction factors obtained for each dye were scaled by an arbitrary constant, such that the overlapping sections of adjacent dyes correction factors had the same magnitude, producing a single continuous correction spectrum. Raw emission spectra for experimental samples would be multiplied by this correction spectrum to produce the corrected spectra.

The correction factor for the TCSPC emission spectra was acquired using two methods. The first method was analogous to the above procedure used for the steady state emission correction factor. Five dyes were prepared and the time resolved emission spectra was obtained for each, acquiring emission signals at many individual wavelengths for the identical periods of time. Each dye was monitored over the time scale at which the dye's signal decayed completely. A steady state emission spectrum was then created by

integrating the decay signal at each wavelength over all collected times. Once the steady state spectra were reproduced, the ratio of the standard spectra from Gardecki and & Maroncelli and these new spectra was created. These ratios were again scaled by arbitrary constants such that they created a smooth single curve.

As some dyes had much longer emission lifetimes than others, it was unclear how accurate this correction factor was, as effects such as effects of blocked excitation pulses and dark current change with different integration times. To remedy the effects that might happen with different integration times at different locations of the correction spectra, a second method was derived.

A 40 W incandescent lightbulb (appliance40, General Electric, Fairfield, CT) was placed into the steady-state emission spectrometer while blocking the spectrometers excitation slits. This allowed for the acquisition of the 40W lightbulb spectrum using the steady state detector, which was subsequently corrected using the steady-state correction factor. The absolute intensity of the lightbulb was reduced by moving it away from the emission slit.

This same 40 W bulb was then placed in front of the TCSPC sample chamber, while blocking the excitation laser. The spectrum of the lightbulb was once again taken, maintaining the maximum photon counts at any wavelength to below 10^4 s^{-1} by adjusting an iris. This time resolved spectrum was constant in time, and so could be averaged to get a collected spectrum of the lightbulb. The ratio of the corrected spectrum from the steady state fluorometer and this acquired spectrum was then taken, which produced a single correction factor for all wavelengths.

Both correction factors for the TCSPC were compared to each other (Figure 2.7b), and show remarkable agreement at most wavelengths. There is a distinct disagreement between the two methods at wavelengths ranging from 400-500 nm, which is a transition region between two dyes, where both dyes are relatively weakly emitting. As the correction factor obtained from the incandescent lightbulb does not suffer this problem, it was used to correct all the time resolved emission spectra for experimental samples. This correction was performed by multiplying time resolved emission signals at each wavelength by the correction factor value at that same wavelength.

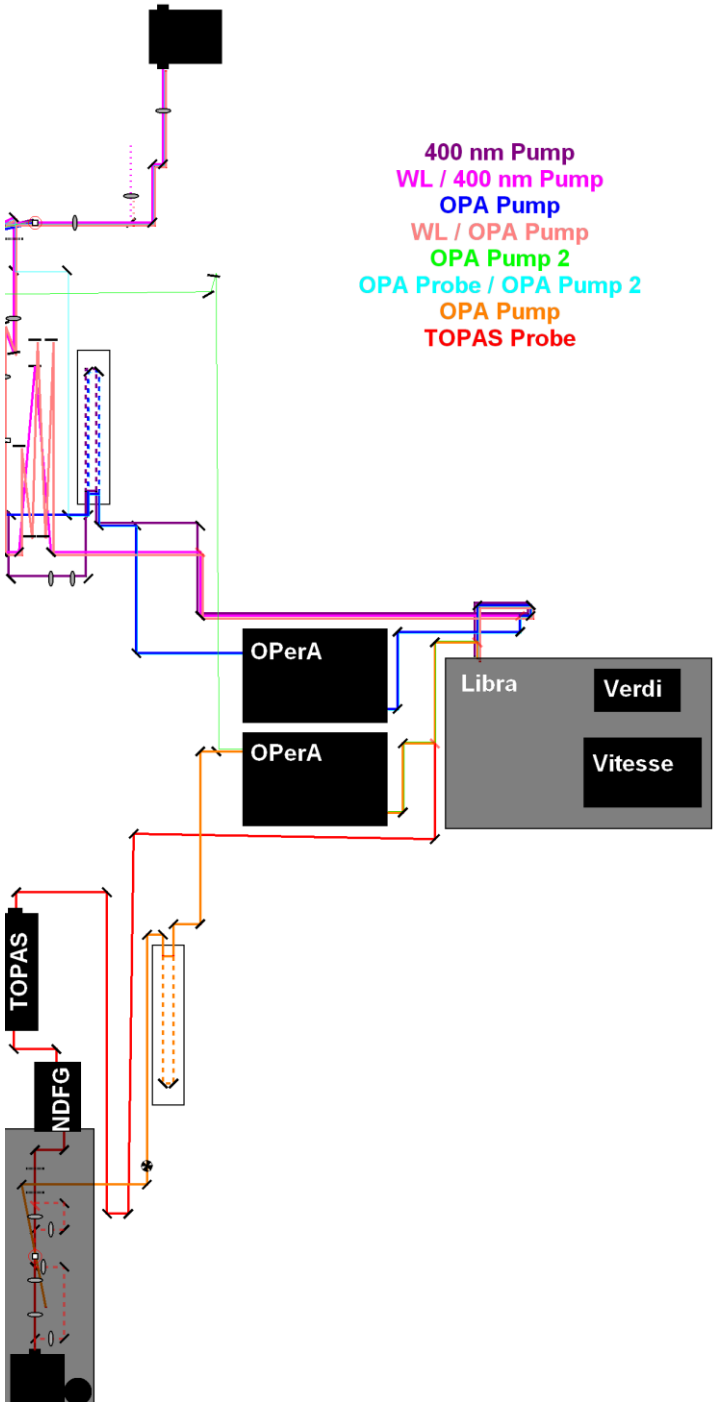

Figure 2.1. Transient absorption setup, displaying the pathways for pump and probe pulses. The top half of the figure is the UV-visible probe setup, while the lower half is for TRIR.

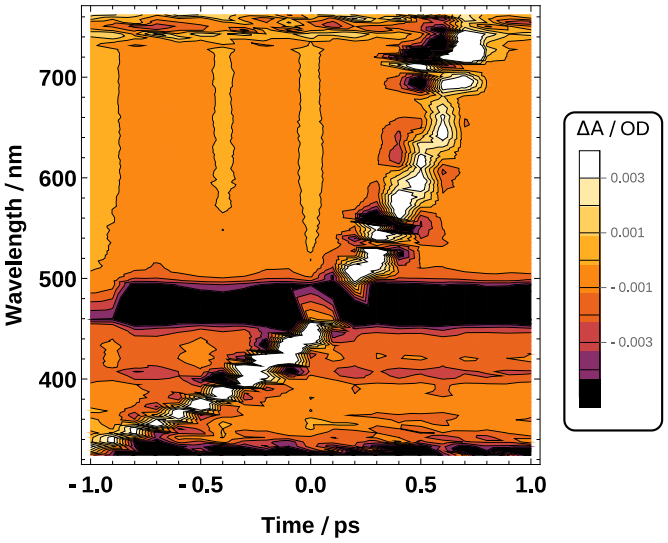

Figure 2.2. Chirp in white light continuum probe signal (white peaks) using a 480 nm pump pulse to excite an acetonitrile solution. Red wavelengths are observed to reach the sample before blue wavelengths, following a linear frequency-time relationship.

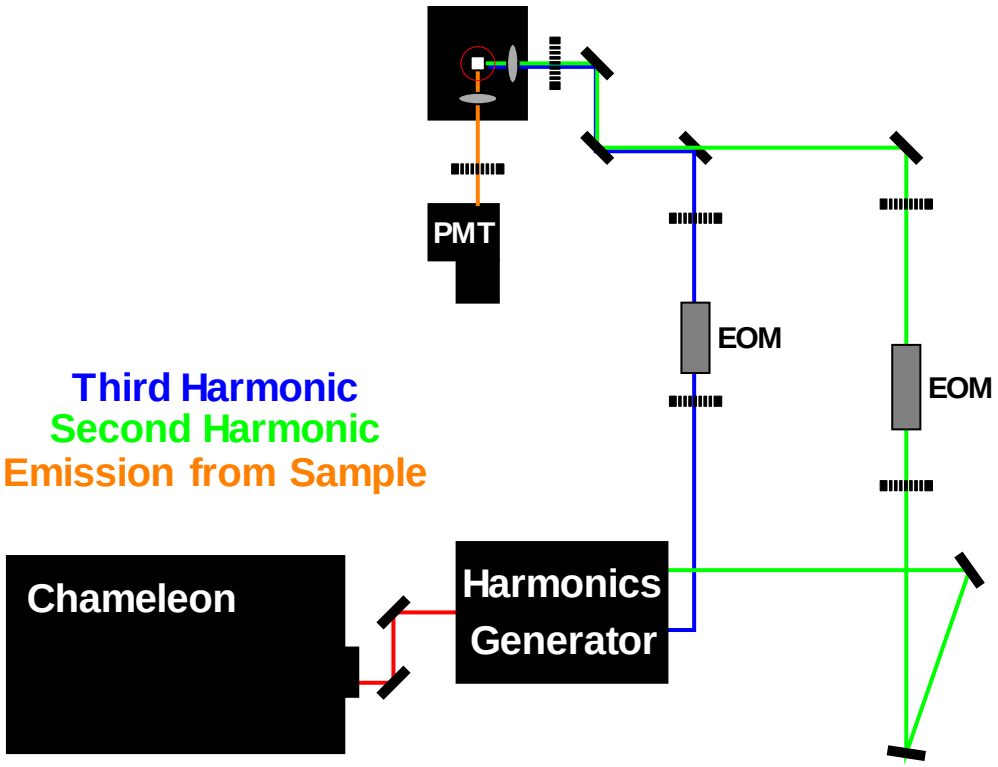

Figure 2.3. TCSPC fluorometer setup, showing both the THG (Blue) and SHG (Green) excitation pathways.

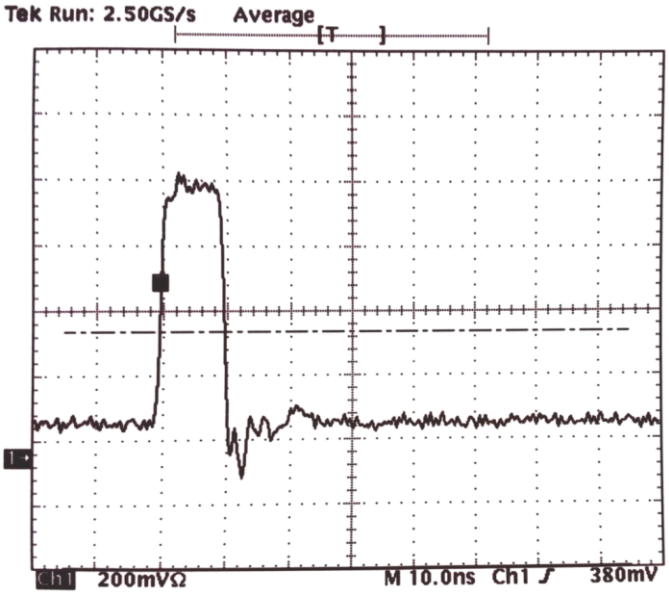

Figure 2.4. The pulse used to trigger the electro-optic modulator had a duration of 10 ns, followed by a minor oscillation. These oscillations became larger at fast repetition rates, so pulses were selected triggering the modulator with repetition rates < 5 MHz.

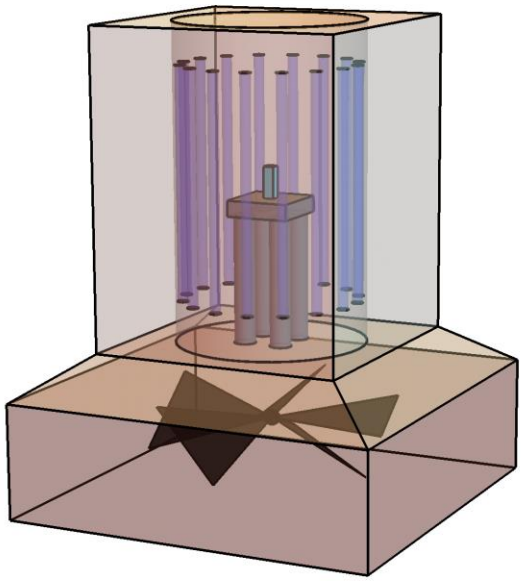

Figure 2.5. The layout of the photoreactor. The cuvette (cyan) is placed in the center of a cylindrical chamber with up to 16 UV lamps (purple) which is cooled from below by a fan (black).

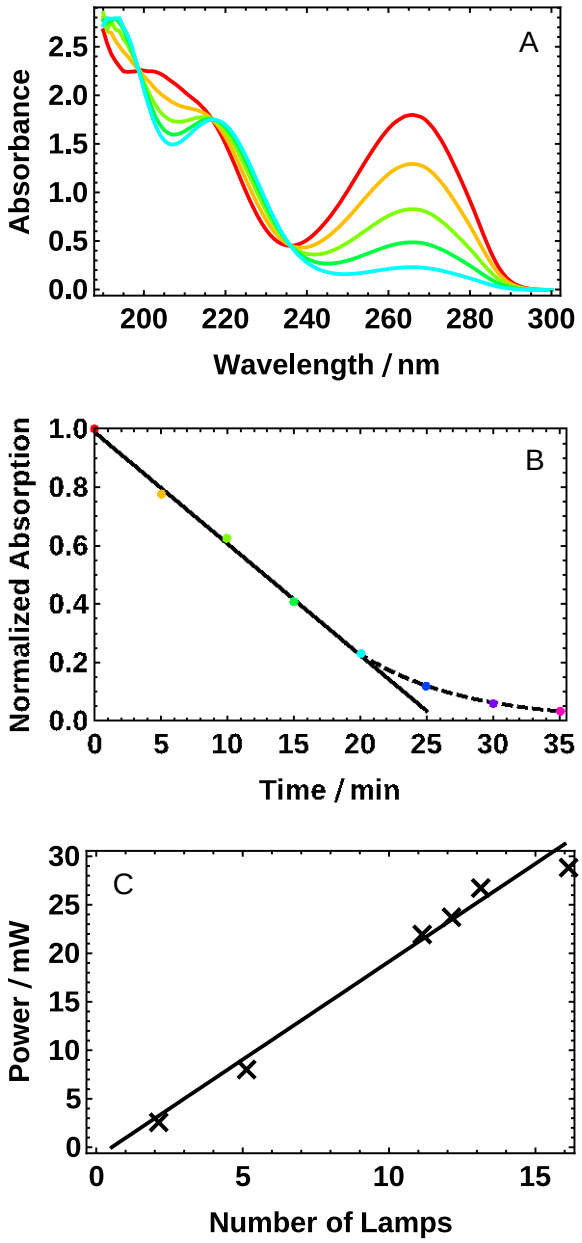

Figure 2.6. The decay of the chemical dosimeter 1,3-DMU used to obtain the radiant power supplied to the cuvette. (A) The initial spectrum (red) and subsequent decay of 1,3-DMU during irradiation. (B) The decay of the absorbance at 260 nm shows a pseudo-zero order kinetics, which can be fit at early times to a line to obtain the radiant power. (C) The radiant power as a function of the number of lamps in the photoreactor.

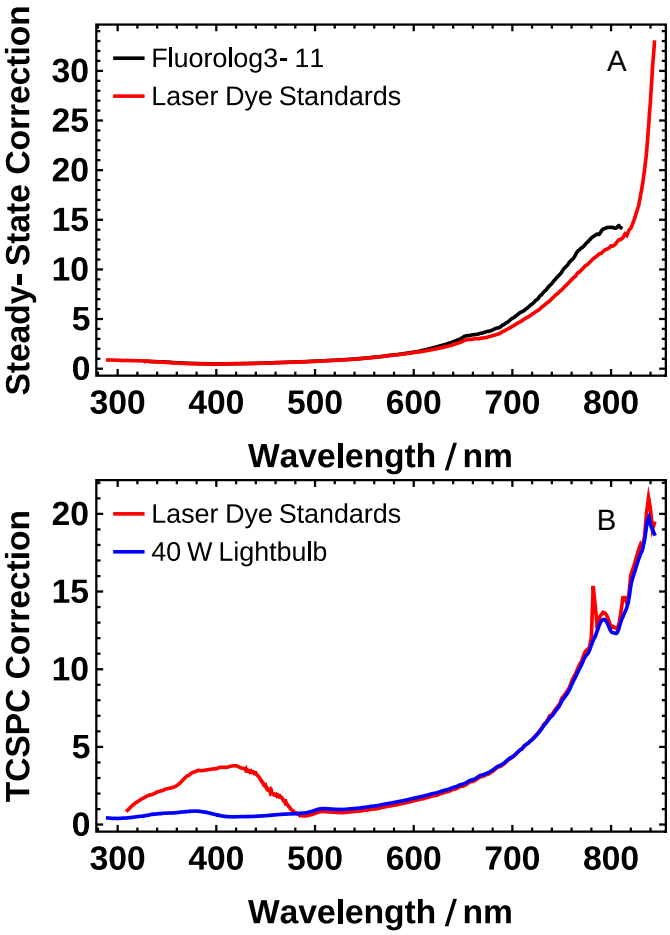

Figure 2.7. Correction factors for emission spectrometers. (A) Shows steady-state emission corrections supplied by the Fluorolog 3-11 (black) and formed using the correction factor using five laser dyes as standards (red). (B) Depicts the correction factors for the TCSPC using five laser dyes (red) or the 40 W lightbulb (blue).

■ REFERENCES

(1) Laimgruber, S.; Schachenmayr, H.; Schmidt, B.; Zinth, W.; Gilch, P. A Femtosecond Stimulated Raman Spectrograph for the near Ultraviolet. *Appl. Phys. B* **2006**, *85*, 557–564.

(2) Juris, A.; Balzani, V.; Barigelletti, F.; Campagna, S.; Belser, P. l; Von Zelewsky, A. Ru(II) Polypyridine Complexes: Photophysics, Photochemistry, Eletrochemistry, and Chemiluminescence. *Coord. Chem. Rev.* **1988**, *84*, 85–277.

(3) Wang, S. Analysis of the Rate of the Ultraviolet Irradiation and Reconstitution Reactions of 1,3-Dimethyluracil and Uridine. *Photochem. Photobiol.* **1962**, *1*, 135–145.

(4) Kuhn, H. J.; Braslavsky, S. E.; Schmidt, R. Chemical Actinometry. *Pure Appl. Chem.* **2004**, *76*, 2105–2146.

(5) Numao, N.; Hamada, T.; Yonemitsu, O. Ph Dependent Quantum Yield in Photocyclizations of N-Chloroacetyldimethylaminophenethylamines - Use of 1,3-Dimethyluracil and Cyclohepta-1,3-Diene as Simple and Convenient Actinometers for 2537 a Radiation. *Tetrahedron Lett.* **1977**, 1661–1664.

(6) Gardecki, J. A.; Maroncelli, M. Set of Secondary Emission Standards for Calibration of the Spectral Responsivity in Emission Spectroscopy. *Appl. Spectrosc.* **1998**, *52*, 1179–1189.

CHAPTER 3

INTERLIGAND ELECTRON TRANSFER IN HETEROLEPTIC RUTHENIUM(II) COMPLEXES OCCURS ON MULTIPLE TIME SCALES

Contribution of Authors and Co-Authors

Manuscript in Chapter 3

Author: Charles W. Stark

Contributions: Performed transient absorption studies on all complexes using broadband, single wavelength, and anisotropy experimental parameters. Performed emission lifetime measurements for each complex. Acquired steady state measurements for all complexes. Formulated and applied a model describing the characteristic behavior of intermediate complexes as a sum of archetypical homoleptic complexes. Generated figures and wrote the manuscript.

Co-Author: Wolfgang J. Schreier

Contributions: Acquired single wavelength transient absorption signals on $[Ru(bpy)_3]^{2+}$ and $[Ru(bpy)_2(phen)]^{2+}$. Aided in the acquisition of broadband transient spectra.

Co-Author: Janice Lucon

Contributions: Synthesized and purified $[Ru(bpy)_3]^{2+}(PF_6)_2$, $[Ru(bpy)_2(phen)]^{2+}(PF_6)_2$, and

$[Ru(bpy)_2(phen)]^{2+}(PF_6)_2$.

Co-Author: Ethan Edwards

Contributions: Synthesized and purified $[Ru(bpy)(phen)_2]^{2+}(PF_6)_2$.

Co-Author: Trevor Douglas

Contributions: Provided insight and guidance for synthetic procedures.

Co-Author: Bern Kohler

Contributions: Provided important insight and overview of physical mechanisms investigated, as well as for transient lab techniques. Wrote and aided in the preparation of the manuscript and figures.

Manuscript Information Page

Charles W. Stark, Wolfgang J. Schreier, Janice Lucon, Ethan Edwards, Trevor Douglas, Bern Kohler
The Journal of Physical Chemistry A
Status of the manuscript:
___ Prepared for submission to a peer-reviewed journal
___ Officially submitted to a peer-reviewed journal
___ Accepted by a peer-reviewed journal
_X_ Published in a peer-reviewed journal

Published by the American Chemical Society
In Volume 119, 4813-4824 (2015)

INTERLIGAND ELECTRON TRANSFER IN HOMOLEPTIC RUTHENIUM(II) COMPLEXES OCCURS ON MULTIPLE TIME SCALES

Charles W. Stark, Wolfgang J. Schreier,† Janice Lucon,‡ Ethan Edwards, Trevor Douglas,§ and Bern Kohler*

Department of Chemistry and Biochemistry, Montana State University, Bozeman, Montana 59717, United States
* Supporting Information

Abstract

The time-dependent localization of the metal-to-ligand charge transfer (MLCT) excited states of ruthenium(II) complexes containing 2,2'-bipyridine (bpy) and 1,10-phenanthroline (phen) ligands was studied by femtosecond transient absorption spectroscopy. Time-resolved anisotropy measurements indicate that the excited state hops randomly among the three ligands of each complex by subpicosecond interligand electron transfer (ILET). Although the bpy- and phen-localized ^{3}MLCT states have similar energies and steady-state emission spectra, pronounced differences in their excited-state absorption spectra make it possible to observe changes in excited state populations using magic angle transient absorption measurements. Analysis of the magic angle signals shows that the excited electron is equally likely to be found on any of the three ligands approximately 1 ps after excitation, but this statistical distribution subsequently evolves to a Boltzmann distribution with a time constant of approximately 10 ps. The apparent contradiction between ultrafast ILET revealed by time-dependent anisotropy measurements and the slower ILET seen in magic angle measurements on the tens of picoseconds time scale is explained by a model in which the underlying rates depend

dynamically on excess vibrational energy. The insight that ILET can occur over multiple time scales reconciles contradictory literature observations and may lead to improved photosensitizer performance.

3.1 Introduction

Ruthenium(II) tris(2,2'-bipyridine), hereafter $[Ru(bpy)_3]^{2+}$, is an archetypal photosensitizer with a long excited-state lifetime of 0.85 μs in deaerated acetonitrile solution at room temperature.[1] $[Ru(bpy)_3]^{2+}$ and other ruthenium(II) polypyridyl complexes are attractive building blocks for capturing solar energy on account of their intense metal-to-ligand charge transfer (MLCT) absorption and the redox activity of their long-lived triplet metal-to-ligand charge transfer (^{3}MLCT) excited states. The initial ^{1}MLCT excited state undergoes intersystem crossing in less than 300 fs to a ^{3}MLCT state,[2,3] which is responsible for the long-lived luminescence.

The MLCT excited states of ruthenium(II) polypyridyl complexes are best described as states in which a d electron from the metal ion is transferred to a π* orbital of a single ligand. The excited electron appears to be localized on one ligand at a time, perhaps already in the initial Franck−Condon or ^{1}MLCT excited state.[4] When two or more kinds of ligands are present (i.e., for heteroleptic complexes), the distribution of ^{3}MLCT excited states depends on the propensity of the different ligands to accept an electron.

In many metal polypyridyl complexes used for solar energy conversion, a single ligand is functionalized to facilitate the transfer of an electron from that ligand to a more

distant electron acceptor. For example, polypyridyl ligands with carboxylate functional groups are often used to adsorb ruthenium(II) dyes to a semiconducting metal oxide nanomaterial. [4,5] In these applications, the ability to direct the excited electron to a particular ligand before excited-state deactivation is of paramount importance. Consequently, any trapping of the excited electron on the ancillary ligands can compromise photosensitization. The problem is inherently a dynamical one: If the barriers separating the ^{3}MLCT states localized on different ligands are sufficiently low, then the excited electron can transfer or hop from one ligand to another in a process known as interligand electron-transfer (ILET). Despite several decades worth of spectroscopic studies of model complexes[2,6−11] the principles that govern excitation hopping in transition metal complexes remain elusive.[12]

In this study, we investigate the evolution of ^{3}MLCT excited states in heteroleptic complexes with the formula $[Ru\text{-}(bpy)_{3-n}(phen)_n]^{2+}$, where n = 0, 1, 2, or 3, bpy stands for 2,2'-bipyridine, and phen is 1,10-phenanthroline (structures are shown in Figure 3.1). These four complexes were studied earlier by time-resolved resonance Raman spectroscopy using 30 ps laser pulses,[13,14] and by luminescence spectroscopy at room temperature in aqueous solution[15] and 77 K in ethanol:methanol (4:1 v/v) glass,[16] but only $[Ru(bpy)_3]^{2+}$ has been studied previously by femtosecond laser spectroscopy.[2,9,17−19] The bpy and phen-localized ^{3}MLCT states are virtually isoenergetic, yet the phen ligand has a larger cross section for absorption than bpy at shorter wavelengths in the MLCT absorption band. This makes it possible to prepare nonequilibrated excited state

populations by judicious selection of the excitation wavelength and to study their subsequent evolution toward Boltzmann distributed populations due to ILET.

Here, we show using femtosecond transient absorption (TA) spectroscopy that ILET occurs on an ultrafast time scale in all four complexes studied, causing the ^{3}MLCT states to be randomly distributed among the various ligands. Differences in the excited-state absorption (ESA) spectra of the different ^{3}MLCT states allow the time-evolving populations of each ligand type to be followed by magic angle TA spectroscopy. These experiments reveal that although a random distribution is established in hundreds of femtoseconds, significant population redistribution from phen- to bpy-localized ^{3}MLCT states takes place over tens of picoseconds. As a result of this slow equilibration, the ensemble of photoexcited complexes does not achieve a Boltzmann distribution for nearly 100 ps. A model in which ILET rates depend sensitively on excess vibrational energy is proposed as an explanation for the experimental observation that ILET takes place on multiple time scales in these complexes.

Note that throughout this article the ILET dynamics of each complex will be interpreted in terms of three ligand-localized ^{3}MLCT states. Such a model fits the experimental observations and captures the essential dynamics. However, it must be kept in mind that these three states represent a simplified view of the actual manifold of states that arise from splitting of triplet sublevels and from higher-energy ^{3}MLCT states in which the hole on the metal center adopts various orientations with respect to the ligand on which the photoexcited electron is localized.[20] We will also refer to hopping of the photoexcited electron from ligand to ligand for the sake of simplicity, even though

electron hopping will be accompanied in general by simultaneous “reorientation” or transfer of the metal-centered hole.[20]

3.2 Experimental Methods

3.2.1. Ruthenium Complex Synthesis

The hexafluorophosphate (PF_6^-) salts of the four ruthenium complexes were synthesized by following previously published work or were obtained directly from commercial sources. $[Ru(bpy)_3](PF_6)_2$ was purchased from Sigma-Aldrich and used as received. The remaining complexes were prepared as follows:

$[Ru(phen)(bpy)_2](PF_6)_2$. $Ru(bpy)_2Cl_2$ was first synthesized using established procedures.[21] In a round-bottom flask 370.4 mg (0.764 mmol) $Ru(bpy)_2Cl_2$ and 166.7 mg (0.840 mmol) of 1,10-phenanthroline were added to 10 mL of methanol and allowed to reflux under argon for 3 h. To this red solution 3 mL of water were added and the solution was gravity filtered before 1.5 mL of a saturated solution of aqueous ammonium hexafluorophosphate (NH_4PF_6) were added to the warm mixture. The precipitate was collected and washed with cold water and ether then further cleaned on a silica gel column (1% sat. aqueous potassium nitrate, 9% water, 90% acetonitrile). The product fractions were evaporated to dryness, dissolved in methanol, and then reprecipitated with aqueous ammonium hexafluorophosphate (NH_4PF_6). The resulting precipitate was collected via vacuum filtration and washed with cold water and ether to obtain 416.7 mg of the desired product (0.472 mmol, 62% yield). MS: M 2+ 297.0406 (found), 297.0550 (calculated).

[Ru(phen)$_2$(bpy)](PF$_6$)$_2$. Ru(phen)$_2$Cl$_2$ was first synthesized using established procedures.[21] Small amounts of a Ru(phen)$_3$Cl$_2$ contaminant, present as red crystals in the starting material, were removed by soaking the material in cold methanol and removing the supernatant before using the remaining solid in further reactions. In a round-bottom flask 200 mg (0.35 mmol) Ru(phen)$_2$Cl$_2$ and 65 mg (0.41 mmol) 2,2'-bipyridine were suspended in 10 mL methanol. This mixture was refluxed under argon for 4 h then filtered and 6 mL water were added and the product was precipitated using aqueous ammonium hexafluorophosphate (NH_4PF_6). The precipitate was washed with water and ether then further cleaned on a silica gel column (1% sat aq potassium nitrate, 9% water, 90% acetonitrile). The product fractions were evaporated to dryness, dissolved in methanol, and then reprecipitated with aqueous ammonium hexafluorophosphate (NH_4PF_6). The resulting microcrystals were collected via vacuum filtration and washed with water and ether to yield 88 mg (0.097 mmol, 28% yield) of the desired product. MS: M 2+ 309.0662 (found), 309.0552 (calculated).

[Ru(phen)$_3$](PF$_6$)$_2$. Ru(DMSO)$_4$Cl$_2$ was first synthesized using established procedures.[22,23] In a round-bottom flask 66 mg (0.14 mmol) Ru(DMSO)$_4$Cl$_2$ and 91 mg (0.45 mmol) 1,10-phenanthroline was added to 3 mL of ethylene glycol. The mixture was heated at 120 °C using a sand bath for 4 h. To the hot mixture about 5 mL water were added followed by addition of 3 mL of a saturated solution of aqueous ammonium hexafluorophosphate (NH_4PF_6). The resulting bright orange precipitate was collected by vacuum filtration and washed with water and ether with a yield of 68.1 mg (0.073 mmol, 53% yield). MS: M 2+ 321.05 (found), 321.06 (calculated).

3.2.2. Spectroscopic Measurements

All samples were studied in acetonitrile (>99.9%, Sigma-Aldrich) solution. UV−vis absorption measurements were recorded over the spectral range of 190−700 nm with a lamp spectrophotometer (Lambda25, PerkinElmer) using 1 nm slit widths. Solutions were held in 1 cm path length fused silica cuvettes. Figure 3.1. Top: Structures for the bidentate ligands 2,2'-bipyridine (bpy), 1,10-phenanthroline (phen) and the ruthenium complexes. Bottom: Molar absorption coefficient (ε) of $[Ru(bpy)_3]^{2+}$ (black), $[Ru(bpy)_2(phen)]^{2+}$ (blue), $[Ru(bpy)(phen)_2]^{2+}$ (green), and $[Ru(phen)_3]^{2+}$ (red) in acetonitrile solution. The spectra have been scaled using the ε values from Table 3.1. The dashed lines denote the pump wavelengths used in the transient absorption experiments.

Emission lifetimes were measured by the time-correlated single photon counting (TCSPC) technique using a commercial spectrometer system (FluoTime200, PicoQuant Photonics North America, West Springfield, MA). Excitation pulses at 450 nm were obtained from a femtosecond Ti:sapphire laser (Chameleon Ultra II, Coherent Inc.) equipped with a second and third harmonic generator. The laser produces sub-picosecond excitation pulses at a repetition rate of 80 MHz. The repetition rate was decreased to 160 kHz using an electro-optic modulator (M350 105, Conoptics) before being focused into a 1 cm cuvette containing the sample under study. Emitted photons were collected at 90° and directed through a monochromator (f = 100 mm) onto a microchannel plate photomultiplier tube (model R3809U-50, Hamamatsu Corp.). The emission polarizer was set to magic angle with respect to the excitation polarizer. Emission signals were

collected over a range of 5 μs using a bin width of 256 ps. Signal acquisition was stopped after approximately 10^4 photons had been detected in any single channel.

The absorbance of each solution was kept below 0.1 at the excitation wavelength for the TCSPC experiments. Each solution was deaerated by bubbling with dry nitrogen gas for 30 min before performing time-resolved measurements. Steady-state emission spectra were recorded before and after TCSPC measurements to confirm that oxygen from air had not diffused into the sealed cuvettes.

Femtosecond TA measurements were performed using a 1 kHz amplified Ti:Sapphire laser system (Libra-HE, Coherent Inc.). Pump pulses at 400 nm were generated by frequency doubling the fundamental in a BBO second harmonic crystal, while 480 nm pump pulses were produced with an optical parametric amplifier (OPerA Solo, Coherent). For the generation of broadband probe pulses a small amount of the fundamental beam was focused in a 4-mm-thickness CaF_2 window to produce a white light continuum. In order to avoid damaging the CaF_2 crystal surface and to minimize polarization changes due to the birefringence of the crystal material, the window was continually moved without rotation using a circularly translating stage.[24] Pump and probe pulses were focused on the sample yielding diameters of 250 and 60 μm at the spatial overlap region in the sample. The pump pulse energy was approximately 1 μJ. A computer-controlled translation stage, with a minimum step size of 2.4 μm and a total travel range of 600 mm, was used to control the time delay between pump and probe pulses.

Signals were recorded either in a broadband mode to obtain transient spectra at specific delay times or in a single wavelength mode to observe kinetics with high accuracy. For broadband transient absorption measurements the probe light was directed with a fiber optic cable (Ocean Optics, f_{in} = 42 mm, f_{out} = 68 mm) into a CCD spectrometer (model 2000+, Ocean Optics). To synchronize the 1 kHz laser pulse train and the CCD spectrometer, the trigger output of the regenerative laser amplifier system was fed into a delay generator and converted to the fifth subharmonic of the trigger signal. The resulting 200 Hz signal triggered spectral acquisition by the CCD. It was further divided by two to produce a 100 Hz signal used to synchronize a mechanical chopper placed in the pump beam. The chopper alternately passed or blocked groups of five consecutive pump pulses to generate the pump on and pump off cycles.

The CCD detector was placed in high-speed data acquisition mode with a 3 ms integration time, allowing 2 ms for the detector to reset. In this manner, a spectrum of the transmitted probe pulse was collected every 5 ms with pump pulses alternately on or off. A total of 6000 spectra were acquired at each position of the delay line. Software written in LabWindows/CVI (National Instruments) was used for data processing and to calculate transient absorption changes. Stray light from the pump pulse provided an easy criterion for sorting pump on and pump off spectra. The arrival time of the probe pulse varied by ~1.5 ps from 320 to 700 nm due to chirp in the continuum probe pulse. As the transient spectra were not chirp corrected, broadband data were analyzed only at times >3 ps.

Single-wavelength transient absorption measurements were performed by passing the white light probe pulse through a monochromator (f = 300 mm) to a photomultiplier tube (PMT). The PMT signal was amplified with a lock-in amplifier (Model SR830, Stanford instruments) synchronized with the mechanical chopper. The chopper was set to block two out of three pump pulses (333 Hz). At each delay setting, the lock-in amplifier signal was acquired for three seconds, corresponding to an average over 3000 laser pulses. Ten back-to-back scans were averaged for each kinetic trace. Traces were fit to sums of exponentials convoluted with a Gaussian function with a full width at half-maximum of 200 fs to represent the instrument response function. Fitting was performed both for individual traces recorded at single wavelengths and for groups of traces recorded at multiple wavelengths using global nonlinear least squares fitting routines in the Igor Pro software package (v 6.3, Wavemetrics).

Transient absorption anisotropy measurements were made using the single wavelength setup described above. Signals with parallel ($I_{\parallel}$) and perpendicular ($I_{\perp}$) polarizations of pump and probe pulses were recorded in back-to-back scans and used to calculate the time-dependent anisotropy, $r(t)$, defined as

$$r(t) = \frac{I_{\parallel} - I_{\perp}}{I_{\parallel} + 2I_{\perp}} \tag{3.1}$$

Before evaluating $r(t)$, the perpendicular and parallel signals were scaled to have the same amplitude at delay times greater than 300 ps. At this time delay, perpendicular and parallel signals are equal because reorientation of $[Ru(bpy)_3]^{2+}$ occurs with a time constant of 50 ps in acetonitrile solution at room temperature.[9,25] This tail-matching procedure minimizes errors due to fluctuations in laser parameters that could distort the

amplitudes of sequentially measured TA signals. As an additional check, it was confirmed that the signal calculated as $I_{\parallel} + 2I_{\perp}$ after tail matching agrees with the signal recorded separately with magic angle polarizations.

TA sample solutions were held in a stationary fused silica cuvette with a path length of 1 mm. Exchanging the sample solution in the pumped volume was not required as the metal complexes relax completely during the 1 ms interval between laser pulses. Samples were checked for degradation by comparing UV/vis absorption spectra before and after TA measurements, but no changes in absorption were observed. Additionally, TA signals recorded for $[Ru(bpy)_3]^{2+}$ using a flowing sample cell gave identical signals.

3.3 Results

3.3.1. Steady-State Measurements

Absorption spectra of the four ruthenium(II) complexes in acetonitrile solution are compared in Figure 3.1. The spectra were scaled to match the literature molar absorption coefficients (ε) listed in Table 3.1. Absorption in the ^{1}MLCT band seen near 450 nm increases with the number of phen ligands, although all complexes have similar absorption cross sections near 480 nm. For $[Ru(bpy)_3]^{2+}$, maximum ^{1}MLCT absorption occurs at 451 nm and a strong ligand-centered (LC) band is seen with λ_{max} at 287 nm, while in $[Ru(phen)_3]^{2+}$ the maxima in these bands are at 445 and 262 nm, respectively. The absorption spectra of the tris complexes agree with those from previous reports.[1,26]

Maximum MLCT absorption by the heteroleptic complexes occurs at wavelengths intermediate between ones measured for the homoleptic complexes and shifts to shorter

wavelength as the number of phen ligands increases. The absorption spectra of the two heteroleptic complexes can be approximately reproduced by linear combinations of the tris-chelate spectra.

3.3.2. Emission Lifetimes

Emission decays at 600 nm were recorded for each metal complex by the TCSPC technique (Figure 3.2). Emission from each complex decays with a single lifetime (last column in Table 3.2), which decreases as the number of phen ligands increases. The lifetimes measured for the $n = 0$ and $n = 1$ complexes (n is the number of phen ligands) are in excellent agreement with previous values of 894 ns and 798 ns, respectively, measured for these complexes in room-temperature acetonitrile solution by Glazer et al.[30] Our measured lifetime of 440 ns for $[Ru(phen)_3]^{2+}$ agrees well with the lifetime of 420 ns reported by Sakuda et al.[31] for the same complex in deaerated acetonitrile at 298 K.

3.3.3. Transient Anisotropy Measurements

Transient anisotropy signals were recorded for all complexes following excitation at 480 nm with probing within the ESA band (370 nm for $[Ru(bpy)_3]^{2+}$ and $[Ru(bpy)_2(phen)]^{2+}$, and 350 nm for $[Ru(bpy)(phen)_2]^{2+}$ and $[Ru(phen)_3]^{2+}$), and at 450 nm, a wavelength near the ^{1}MLCT band absorption maximum (Figure 3.3). Excitation at 480 nm was chosen in order to compare with results of Wallin et al.[9] and because this wavelength reduces interference from the effects of excess vibrational energy as discussed in ref 9.

The anisotropy signals within the ESA band (open circles in Figure 3.3) are negative at all delay times, but the observed biphasic decays approximately mirror the dynamics seen in the positive anisotropy signals at 450 nm. The anisotropy at 450 nm for all complexes decays rapidly to a value of 0.1 in under 1 ps for each complex, while the negative anisotropy signals seen at 370 and 350 nm decay toward the baseline approaching a value of −0.05 by 1 ps. The anisotropy signals at all three probe wavelengths could be globally fit for each complex to a fast decay that is shorter than our experimental time resolution (<200 fs, see Table 3.2), followed by a slower decay with a time constant of between 30 and 100 ps. The latter decay can be seen in Figure 3.3, but was difficult to determine accurately due to the weak anisotropy signals at long delay times. Nevertheless, this component agrees reasonably well with a value of 50 ps reported earlier for $[Ru(bpy)_3]^{2+}$.[6,9]

3.3.4. Magic Angle TA Experiments

TA difference spectra recorded from 3 to 300 ps after 400 nm excitation are shown in Figure 3.4. For each complex, bleaching of the ^{1}MLCT band is observed near 450 nm as well as a strong peak below 400 nm that is assigned to ESA by the ^{3}MLCT excited state. While $[Ru(phen)_3]^{2+}$ only shows a broad ESA band with a maximum near 320 nm, the three complexes with bpy ligands show a peak ($[Ru(bpy)_3]^{2+}$, $[Ru(bpy)_2(phen)]^{2+}$) or a shoulder ($[Ru(bpy)(phen)_2]^{2+}$) at 370 nm. The 370 nm band grows in amplitude over the first 100 ps after photoexcitation. Finally, a weak positive ΔA signal is seen at wavelengths above 500 nm for all complexes.

The TA difference spectrum of $[Ru(bpy)_3]^{2+}$ (Figure 3.4) does not change after 100 ps as reported by Wallin et al.[9] For this reason, the transient difference spectra at delay times ≥100 ps agree with ones recorded with nanosecond time resolution.[27,32] At 300 ps, the ratio of the maximum ESA signal at 370 nm to the absolute value of the maximum bleach signal at 451 nm is 1.70. This value is in excellent agreement with the ratio of 1.74 reported by Yoshimura et al.[27] for $[Ru(bpy)_3]^{2+}$ excited at 532 nm. Somewhat smaller ratios of 1.5 and 1.2 are estimated from the spectra published in refs 33 and 9, respectively. It is worth noting that the TA spectrum published in Figure 2A of ref 9 for $[Ru(bpy)_3]^{2+}$ is shifted by ∼15 nm to shorter wavelengths compared to other spectra, including our own.

Several trends in the difference spectra are noted as the number of phen ligands is increased. First, absorption above 500 nm increases in strength. Second, the ESA band seen below 400 nm broadens and shifts to shorter wavelengths. Finally, the ratio of the maximum of the short wavelength ESA band to the maximum bleach signal decreases by nearly a factor of 3 from $[Ru(bpy)_3]^{2+}$ to $[Ru(phen)_3]^{2+}$ in good agreement with the trend seen in ns transient difference spectra for the tris chelate complexes.[13]

The signals recorded in single-wavelength TA measurements generally evolve biexponentially with a time constant of less than 200 fs and a second time constant of approximately 10 ps. The time constants determined from global fits to kinetic traces recorded at several wavelengths are summarized in Table 3.2. Figure 3.5 shows the signal evolution at probe wavelengths of 370 and 450 nm after excitation at 400 nm. The former

wavelength falls in the ESA band, while the latter one reveals the bleaching dynamics of the MLCT absorption band.

The time constants observed here for $[Ru(bpy)_3]^{2+}$ agree well with findings by Wallin et al.,[9] who observed a time constant of 300 fs and a second component of between 5 and 15 ps for this complex at 360 nm following excitation at 480 nm. As seen in Figure 3.5, the ESA signal at 370 from each of the three bpy-containing complexes grows substantially with a time constant of ~10 ps. Importantly, the amplitude of this component is largest for the mixed-ligand complexes. For $[Ru(bpy)_3]^{2+}$, the amplitude of the picosecond component is 0.6 mOD (10% of the total amplitude), while for $[Ru(bpy)_2(phen)]^{2+}$ and $[Ru(bpy)(phen)_2]^{2+}$, this component has amplitudes of 1.1 mOD (30%) and 1.0 mOD (44%), respectively. Strikingly, the signal for $[Ru(phen)_3]^{2+}$ at 370 nm (Figure 3.5) lacks this component and is constant from 1 ps onward. Broadband TA spectra (Figure S1) and kinetic traces (Figure S2) recorded for each complex with 480 nm excitation were essentially the same within experimental uncertainty as the signals obtained with 400 nm excitation. Table 3.2 summarizes the very similar lifetimes observed for both excitation wavelengths.

Excited state absorption spectra were calculated from the transient difference spectra and the ground state absorption spectrum of each complex. Because TA signals are proportional to the difference between the absorption cross section of each excited-state species and the ground state, the molar absorption coefficient of the ^{3}MLCT excited state of a complex containing n phen ligands, ε_n', can be calculated as

$$\varepsilon_n'(\lambda,t) = \Delta A(\lambda,t)\cdot\gamma + \varepsilon_n(\lambda,t) \qquad (3.2)$$

where $\Delta A(\lambda, t)$ is the measured signal from Figure 3.4, ε_n is the molar absorption coefficient of the ground state from Figure 3.1, and γ is a constant that depends on experimental parameters such as the pump pulse fluence and the steady-state sample absorbance at the pump wavelength. Because the difference spectra in Figure 3.4 were recorded from solutions having the same absorbance at the pump wavelength and with all other experimental parameters held constant, γ has the same value for all complexes. This value was determined by fitting the 300 ps $[Ru(bpy)_3]^{2+}$ signal using eq 3.2 to the ESA spectrum of the same complex recorded by Ohno et al. in 4:1 H_2O:CH_3CN solution.[34] The same value of γ was then used to calculate the ESA spectra of the remaining complexes at all other delay times. The results are shown in Figure 3.6. The excellent agreement between the spectrum for $[Ru(phen)_3]^{2+}$ at 300 ps (i.e., the fully thermalized ESA spectrum) calculated in this manner with the spectrum for the same complex shown in Figure 4-S of ref 34 confirms the soundness of this procedure. ESA spectra calculated in the same manner from the difference spectra recorded with 480 nm excitation are shown in Figure S3. No significant differences are noted for 480 nm vs 400 nm excitation.

The ESA spectra of the three bpy-containing complexes in Figure 3.6 all exhibit a strong band near 370 nm. No such band is seen for $[Ru(phen)_3]^{2+}$, and its ESA spectrum instead peaks below 300 nm with a broad shoulder between 350 and 400 nm. The ESA spectra of the heteroleptic complexes are roughly intermediate in intensity between those of the homoleptic complexes, except near 450 nm, where both tris-complexes show higher molar absorptivity than the mixed-ligand complexes.

3.4 Discussion

3.4.1. Steady-State Absorption Spectra

The LC band maxima occur at 287 and 262 nm in all four complexes, indicating that neighboring ligands do not influence the transition energies of the localized $^1\pi\pi^*$ transitions of each ligand.[15] On the other hand, the maximum in the ^{1}MLCT absorption band shifts slightly to shorter wavelengths as the number of phen ligands increases (Figure 3.1 and Table 3.1). In view of the evidence that excitation initially populates fully localized ^{1}MLCT states,[35,36] the greater molar absorptivity of the phen-containing complexes between 375 and 450 nm suggests that 400 nm excitation of the heteroleptic complexes preferentially excites phen-localized MLCT states. On the other hand, the molar absorption coefficient is similar for all complexes at 480 nm (Figure 3.1), suggesting that this wavelength is equally likely to excite any of the three ligands. If excited-state redistribution via ILET were to occur slowly enough, then it could be possible to observe the different Franck−Condon distributions at early times. This possibility will be addressed below when our conclusions about the distribution of ^{3}MLCT states on bpy vs phen ligands are presented.

3.4.2. Emission Lifetimes

Monoexponential luminescence decays are observed for each complex at room temperature (Figure 3.2). The emission lifetimes of the Heteroleptic complexes are intermediate between those of the tris-ligated complexes in agreement with previous observations for $[Ru(bpy)_2(phen)]^{2+}$[15,30,37] and $[Ru(bpy)(phen)_2]^{2+}$.[15] If ILET rates were

comparable to or slower than the rate of emission, then two distinct lifetimes would be observed due to emission from bpy- and phen-localized ^{3}MLCT states. The monoexponential lifetimes therefore indicate that ILET takes place much faster than emission. We assume that each of the three localized ^{3}MLCT states can undergo ILET by transferring the excess electron to another ligand or decay radiatively or nonradiatively to the electronic ground state. Assuming that the rate of ILET is much faster than the latter rates, then all three ^{3}MLCT states will be in equilibrium in amounts that are determined by the energy splitting between the two types of ligand-localized excited states. As shown in Supporting Information (SI), each complex undergoes excited state decay with a unique rate given by

$$k_n = \frac{(3-n)k_0 + nk_3 \exp(-\Delta E/k_b T)}{3-n+n\exp(-\Delta E/k_b T)} \qquad (3.3)$$

where n is the number of phen ligands, and $3 - n$ is the number of bpy ligands. In eq 3.3, ΔE is the energy of the reduced phen ligand minus the energy of the reduced bpy ligand. In this model, the excited-state decay rates of the two Heteroleptic complexes, k_1 and k_2, are linear combinations of the decay rates for $[Ru(bpy)_3]^{2+}$ (k_0) and $[Ru(phen)_3]^{2+}$ (k_3).

An excellent fit to the measured lifetimes is obtained for ΔE equal to 310 ± 60 cm^{-1} (Figure 3.7). This value roughly matches the energy difference determined by Blakley et al. from a photoselection study of Ru(II) complexes in ethanol at 77 K.[38] These investigators estimated that the π* orbital of phen is 240 cm^{-1} higher in energy than the π* orbital of bpy.[38] However, the agreement may be somewhat fortuitous in view of solvent effects on the ^{3}MLCT state energetics and lifetimes. The energy of the phen-localized excited state is predicted to lie 55 ± 20 cm^{-1} below the bpy-localized state (ΔE

= −55 cm^{-1}) when eq 3.3 is applied to emission lifetimes measured by Baggott et al.[15] for $[Ru(bpy)_{3-n}(phen)_n]^{2+}$ (n = 0 to 3) complexes in H_2O at 298 K.[15] The inversion of the two ^{3}MLCT states in H_2O is most likely a solvent effect. Emission lifetimes measured in independent laboratories and compiled in ref 1 confirm that the emission lifetime of the n = 0 complex is longer than that of the n = 3 complex in room-temperature acetonitrile solution, while the opposite trend holds in room-temperature aqueous solution. The emission lifetimes also vary in complex fashion with increasing temperature.[39] Regardless of these subtleties, analysis of the emission lifetimes using the kinetic model described in the SI strongly confirms that the splitting between bpy- and phen-localized ^{3}MLCT states is small.

3.4.3. Excited-State Dynamics: Time-Resolved Anisotropy

ILET rates were investigated previously for $[Ru(bpy)_3]^{2+}$ using a variety of methods. Malone et al.[6] deduced a 47 ps time constant as the time needed for ^{3}MLCT excitation to hop from one bpy ligand to another from a 12 ps decay component seen in the anisotropy signal. They also observed a second, slower component of 51 ps, which they assigned to rotational diffusion. Later, Wallin et al.[9] measured the time-dependent anisotropy for $[Ru(bpy)_3]^{2+}$ with higher time resolution and observed significantly faster decay components than the ones reported in ref 6. Wallin et al. fit their anisotropy signals to triexponential decays with time constants of 300 fs, 5 ps, and 50 ps. They showed that the time-resolved anisotropy signals from $[Ru(bpy)_3]^{2+}$ attain values 1 ps after excitation

consistent with complete randomization of the initially excited state over all ligands.[9] For this reason, they concluded that ILET most likely occurs in less than 300 fs.

The anisotropy signals (Figure 3.3) measured in this study are similar in both temporal evolution and amplitude to the ones in ref 9. In particular, the absolute value of $r(t)$ decreases dramatically for all four complexes on the subpicosecond time scale, suggesting that ILET is responsible for the observed ultrafast depolarization. The time-dependent anisotropy measurements provide clear evidence in favor of ultrafast ILET, but we propose that this initial high rate of ILET is not maintained throughout the long microsecond lifetime of the complex. Indeed, barriers to ILET in $[Ru(bpy)_3]^{2+}$ have been estimated to be approximately 1000 cm^{-1} on the basis of intervalence charge transfer absorption by the singly and doubly reduced complex.[40,41] Barriers of this magnitude suggest that ET cannot occur in hundreds of femtoseconds for the fully thermalized ^{3}MLCT state. The solution to these conflicting concepts is a model in which ILET first occurs at ultrafast rates when excess vibrational energy is present, but then slows down by orders of magnitude as this energy is dissipated. Support for the idea that ILET can take place at slower rates at longer times is provided by analysis of the magic angle TA signals as discussed next.

3.4.4. Excited-State Dynamics: Magic Angle TA Experiments

After the ^{3}MLCT state of each excited complex has moved randomly to one of the other ligands, further hopping of the excitation can no longer alter the anisotropy of the ensemble, and is therefore unobservable. This makes it impossible to use time-resolved

anisotropy measurements to observe hopping after ~1 ps, the time required for initial depolarization. Magic angle TA signals, although they cannot be used to observe ILET between identical ligands, can report on population transfer between different ligands before excited state equilibrium is established. In the following, we present evidence that bpy- and phen-localized excited states have distinct ESA spectra that make it possible to differentiate between these states. Additionally, relatively slow changes occurring with a time constant of between 10 and 20 ps reveal that excited-state equilibration of the ^{3}MLCT states created by photoexcitation is established slowly.

The ESA spectrum derived for $[Ru(phen)_3]^{2+}$ shows only weak absorption at 370 nm compared to all of the bpy containing complexes (Figure 3.6). Transient absorption at 370 nm by $[Ru(bpy)_3]^{2+}$ has been assigned to a reduced bpy ligand,[42,43] consistent with localization of the excited electron of the ^{3}MLCT state on a single ligand: $[Ru^{3+}(bpy)_2(bpy^{\bullet-})]^{2+}$. The magic angle TA signals recorded for complexes containing at least one bpy ligand (Figures 3.4 and 3.5) exhibit a ~10 ps component that is seen most clearly as a rise in the ESA band near 370 nm (Figure 3.5). In contrast, the $[Ru(phen)_3]^{2+}$ signals are remarkably flat over the same time range, and the 10 ps component is not seen at any probe wavelength. The rising signals in Figure 3.5 could therefore be an indication of progressive population transfer from phen- to bpy-localized ^{3}MLCT states.

The rise in the $[Ru(bpy)_3]^{2+}$ signal (Figure 3.5) complicates this interpretation because transfer of population between identical bpy ligands cannot change the magic angle TA signals. Picosecond time scale changes to magic angle TA signals from $[Ru(bpy)_3]^{2+}$[9,18,33] and other ruthenium(II) polypyridyl complexes[11,44,45] have been

assigned in the past to vibrational cooling (VC) dynamics. VC reflects the transfer of excess vibrational energy to the solvent from an impulsively formed excited state, a process that commonly occurs on the ~10 ps time scale for many molecular solutes in acetonitrile solution.[46,47]

Henry et al.[33] thoroughly studied a series of Ru(II) polypyridyl complexes by time-resolved resonance Raman spectroscopy and concluded that VC occurs with a characteristic time constant of 10 ps. Surprisingly, these authors found the VC dynamics to be largely independent of solvent and excitation wavelength. This contrasts with other solutes like the DNA nucleobases where VC occurs at remarkably different rates as the solvent is varied.[47] Henry et al. also observed similar rates for complexes in which the ^{3}MLCT state is localized on a single ligand type as for complexes where multiple low-energy ^{3}MLCT states are present. Henry et al. suggested that this last result indicates that the time to fully thermalize the ^{3}MLCT state is unaffected by localization dynamics.

Although changes to the Raman spectrum of the ^{3}MLCT states of ruthenium(II) polypyridyl complexes provide evidence of vibrational relaxation on the tens of picoseconds time scale,[33] the consequences of this relaxation for electronic spectra are uncertain. In their study of emission from $[Ru(bpy)_3]^{2+}$ by broadband femtosecond fluorescence upconversion, Cannizzo et al.[17] observed no changes to the shape of the emission spectrum after 200 fs. They attributed this striking absence of vibrational cooling effects on emission to impulsive intramolecular vibrational-energy redistribution (IVR) to low frequency modes that contribute negligibly to the shape of the spectrum.[17]

Our results for $[Ru(phen)_3]^{2+}$ suggest that VC may not be entirely responsible for changes in the TA signals. The time resolved spectra for this complex are remarkably constant after 1 ps (Figure 3.4) and show no obvious VC effects. The flat TA kinetic traces seen for this complex at probe wavelengths of 370 and 450 nm reinforce this point (Figure 3.5). These observations demonstrate that the phen-localized ^{3}MLCT state is unaffected by the events, whatever their precise nature, that cause the TA signals of bpy-localized ^{3}MLCT states to increase. One possibility is that the 10 ps process reflects a geometrical change by the reduced bpy ligand that is frustrated by the more rigid phen ligand.

Regardless of the precise reasons for the increase in the $[Ru(bpy)_3]^{2+}$ signals at 370 nm, the similar increases seen in Figure 3.5 for the mixed ligand complexes (n = 1, 2) cannot be due solely to intraligand changes of bpy-localized excited states. If only bpy-localized ^{3}MLCT states are populated in all complexes, and if the VC (or other intraligand process) responsible for the signal growth is independent of the identity of the other ligands as suggested by the study of Henry et al.,[33] then all three of the bpy-containing complexes should give identical signals. On the other hand, if the final ^{3}MLCT states of the heteroleptic complexes were localized on both bpy and phen ligands, then the mixed-ligand complexes would not increase as much as those of $[Ru(bpy)_3]^{2+}$ due to the decrease in the number of bpy ligands.

In fact, the amplitude of the 10 ps decay component is greatest for the mixed-ligand complexes (Figures 3.4 and 3.5), suggesting strongly that the intraligand relaxation that takes place in $[Ru(bpy)_3]^{2+}$ is accompanied by at least some degree of population

transfer from phen- to bpy-localized ^{3}MLCT states in the n = 1 and n = 2 complexes. In the next section, we show that a careful analysis of the TA spectral amplitudes can be used to separate vibrational cooling dynamics from ILET dynamics, even though both processes take place on overlapping time scales.

3.4.5. Time-Dependent Localization on bpy

Assuming that ESA by an individual complex is dominated by absorption of its single reduced ligand, then the molar absorption coefficients describing ESA by the ensemble of the two mixed ligand complexes (ε_n', n = 1, 2) can be approximated as a linear combination of the ESA spectra of the two tris complexes, $[Ru(bpy)_3]^{2+}$ (ε_0') and $[Ru(phen)_3]^{2+}$ (ε_3'):

$$\varepsilon_n'(\lambda,t) = \chi(t)\cdot\varepsilon_0(\lambda,t) + (1-\chi(t))\cdot\varepsilon_3'(\lambda,t) \qquad (3.4)$$

In eq 3.4, $\chi(t)$ is the fraction of all excited states in the ensemble of photoexcited complexes that are localized on bpy at time t after photoexcitation. For example, when χ equals unity all ^{3}MLCT states are localized on bpy ligands and the signal is identical to that of $[Ru(bpy)_3]^{2+}$. On the other hand, when χ equals zero the signal equals that of $[Ru(phen)_3]^{2+}$. Importantly, the excited state absorption cross sections in eq 3.4 depend on time and are obtained using eq 3.2. By using time dependent absorption cross sections, eq 3.4 correctly accounts for the intraligand dynamics responsible for the time-dependent changes in the absorption by the bpy-localized ^{3}MLCT state described in the previous section.

Figure 3.8 compares experimental ESA spectra for the n = 1 and n = 2 complexes obtained with 400 nm excitation at several delay times with linear combinations

calculated with eq 3.4 using various χ values. The smaller of the two values of χ used to model the 3 ps spectra was chosen by assuming that the probability of forming a bpy- vs phen-localized ^{3}MLCT state is proportional to the absorption cross section of each ligand. In this scenario, which we call the Franck−Condon model, the percentage of ^{3}MLCT states localized on bpy (%bpy) varies with excitation wavelength. Values calculated for 400 and 480 nm are listed in Table 3.3. The low χ value reflects the fact that the phen ligand is expected to be excited preferentially at 400 nm due to its larger cross section.

A much better fit to the 3 ps spectra in Figure 3.8 is obtained with the "statistical" χ values (Table 3.3, fourth column). In this model, excited states are equally likely to be found on any of the three ligands. This is consistent with the anisotropy results indicating ultrafast redistribution of the initial excited state. The finding that the initial excited state has a significant percentage of phen-localized excited states agrees with DFT calculations of the n = 2 complex in solvent-free conditions by Bossert and Daniel showing that a significant fraction of the ^{1}MLCT and ^{3}MLCT excited states are localized on phen.[48] For both mixed ligand complexes, an even greater value of χ is needed to fit the 300 ps spectrum (Table 3.3, last column).

The finding that localization on bpy ligand(s) increases between 3 and 300 ps is borne out by the graphs in Figure 3.9. This figure shows best-fit values of χ determined by fitting eq 3.4 to the ESA spectra (Figure 3.6, results for 480 nm excitation are shown in Figure S3). The solid curves show fits to the single wavelength signals at 370 nm scaled using the same γ as in section 3.4. By 1 ps after excitation, the distribution of bpy localized excited states is clearly different from the Franck-Condon distribution

(horizontal solid lines in Figure 3.9) and the excited state of a given complex is equally likely to be found on any of the three ligands (statistical distribution). The subpicosecond growth in χ may stem from ultrafast rates of ILET at early times, as they match well with the time scales observed using anisotropy (Table 3.2), but may be difficult to discern from other processes occurring on ultrafast time scales.

Over the next few hundred picoseconds, the distribution of excited states gradually assumes the final Boltzmann populations shown by the dashed black lines in Figure 3.9. In both complexes, nearly half of the phen-localized excited states present at 1 ps have become bpy-localized by ~100 ps after excitation. Reasonably consistent dynamics are seen for excitation at both 400 and 480 nm, although it may take slightly longer to attain the Boltzmann equilibrium with the shorter-wavelength pump pulse. It is important to note that due to the rough equality of absorption coefficients for both tris complexes at 480 nm, this excitation wavelength is predicted to yield a Franck−Condon distribution that is indistinguishable from the statistical one. The results in Figure 3.9 provide support for the conclusion that localization occurs on multiple time scales.

No changes to the signals are seen after 100 ps, indicating that the excited states have achieved equilibrium by this time. The populations observed at 300 ps (83% bpy character for $[Ru(bpy)_2(phen)]^{2+}$, and 56% bpy character for $[Ru(bpy)(phen)_2]^{2+}$) correspond to a ΔE of 180 ± 40 cm^{-1}. This value is similar to the estimate of 310 ± 60 cm^{-1} determined from the crude model applied to emission lifetimes (section 4.2).

3.4.6. ILET Rates are Time-Dependent

The TA anisotropy signals (Figure 3.3) indicate that ILET takes place in hundreds of femtoseconds, while analysis of the magic angle kinetic traces and time-resolved spectra (Figures 3.4 and 3.5) provide evidence that ILET takes place in tens of picoseconds. A model in which ILET rates depend on the time elapsed after initial excitation can reconcile these apparently contradictory observations.

Rapid ILET is aided by the substantial excess energy deposited by the pump pulse. One measure of this excess energy is the Stokes shift of ~8000 cm^{-1} for 400 nm excitation of $[Ru(bpy)_3]^{2+}$. Excess vibrational energy allows activationless ILET to take place on an ultrafast time scale because available energy exceeds the barriers between the different ligand-localized ^{3}MLCT states. Over the next several picoseconds, the system dissipates excess energy by VC.

Papanikolas and co-workers first proposed that ILET among MLCT states could occur in both activated and activationless regimes. Their analysis of TA anisotropy signals recorded for the symmetrical osmium(II) tris bipyridine complex ($[Os(bpy)_3]^{2+}$) recorded at different pump wavelengths supported this picture by demonstrating that ILET occurs at faster rates as the excitation energy is increased.[49] Later, Miller and Moran investigated ILET in the same complex with higher time resolution of 25 fs.[50] These investigators reported that the TA anisotropy signals decay biexponentially with two time constants that are both less than 1 ps. The faster of the two time constants was assigned to activationless ILET, while the longer time constant was assigned to activated ILET. Consistent with the concept expressed in ref 49, Miller and Moran found that the

contribution of activationless ILET increased for excitation at higher energy (shorter wavelength).

Our model is rooted in this concept that ILET rates are greater when excess energy is present in the MLCT states.[49,50] However, while these previous investigators emphasized that rates increase at greater excitation energies, we generalize this observation and emphasize that ILET rates will be time dependent even for a fixed excitation wavelength that lies above the origin. This follows from the time-dependent exchange of energy between the ensemble of photoexcited complexes and the solvent. This energy exchange is what moves the ensembles of complexes dynamically between the limits of activationless and activated ILET. Our study is poorly suited to studying the fastest ILET dynamics, which may depend strongly on excitation wavelength, but the similar dynamics seen for excitation at 400 and 480 nm suggests that the evolution from the roughly statistical distribution of MLCT states to the final Boltzmann distribution at long times proceeds on similar time scales.

It is worth repeating that TA anisotropy experiments cannot observe continued hopping of the excitation after the initial depolarization takes place. This suggests to us that the "slow" time constants of 600−900 fs observed by Miller and Moran[50] and assigned by them to incoherent hopping in $[Os(bpy)_3]^{2+}$ are still much shorter than the time constants that characterize hopping by the fully thermalized ^{3}MLCT states. Indeed, Shaw et al. reported that ILET occurs with a time constant of 8.7 ps in $[Os(bpy)_3]^{2+}$.[8] We note that this value can be crudely reproduced using the Eyring-Polanyi equation

$$k_{ILET} = \frac{k_B T}{h} \exp\left(-\frac{\Delta G^{\ddagger}}{RT} \right) \tag{3.5}$$

where $\Delta G^{\ddagger}$ is the activation energy barrier between a pair of ^{3}MLCT states. Equation 3.5 predicts a rate of 8.3×10^{10} s^{-1} (τ = 12 ps) at 293 K using the previously estimated value of 875 cm^{-1} for $\Delta G^{\ddagger}$ of $[Os(bpy)_3]^{2+}$.[49,50] It thus appears that TA anisotropy measurements like the ones in ref 50 capture the faster portion of ILET dynamics, but miss the slower ILET that takes place during the remainder of the excited-state lifetime. Barriers for ILET in bpy-phen complexes are likely to be similar in magnitude to those reported for $[Os(bpy)_3]^{2+}$. For example, the barrier height for symmetric ET between bpy ligands is estimated to be approximately 1000 cm^{-1}.[40,41] Equation 3.5 predicts a lifetime of 22 ps in this case. This crude estimate suggests that ILET involving the fully thermalized excited states takes place on a time scale that overlaps that of vibrational cooling. We propose that the time of 10 to 20 ps required for the initially subpicosecond ILET rates to approach their final values happens to match the ultimate time scale for ILET by the fully thermalized MLCT states.

Based on the results of this study it appears that ILET rates change by several orders of magnitude from the instant of initial excitation until the MLCT states are fully thermalized. It is interesting that the range of time scales observed here for mixed bpy-phen complexes, which range from hundreds of femtoseconds (or faster) to tens of picoseconds, closely match the overall spread of lifetimes reported by individual studies in the past. Notably, magic angle TA experiments suggest that ILET requires at least several picoseconds,[6,8,10,11,49,51,52] while ILET is inferred to take place on a subpicosecond time scale from time-resolved anisotropy experiments.[9,50,53] The model outlined here suggests that ILET in ruthenium(II) metal complexes with nearly degenerate ligand

energies occurs on both slow and fast time scales. Magic angle experiments tend to emphasize the former, while TA anisotropy measurements can only observe the fastest ILET rates.

3.5 Conclusions

The excited-state dynamics of four bpy-phen ruthenium(II) complexes were studied by femtosecond transient absorption spectroscopy. The very different ESA spectrum of the $[Ru(phen)_3]^{2+}$ complex compared to the bpy-containing complexes made it possible to observe phen-to-bpy population transfer. ILET in each complex initially takes place at rates greater than 10^{12} s^{-1} between any pair of ligands, consistent with ultrafast depolarization seen in time-resolved anisotropy measurements. Ultrafast ILET causes the ^{3}MLCT state to be distributed statistically across all ligands no later than 1 ps after excitation when exciting at both 400 and 480 nm. Over the next several picoseconds, vibrational cooling dissipates the excess vibrational energy and ILET slows down, becoming an activated process. The rates for transfer between the various ligands gradually become differentiated, as the barriers become rate determining. For the bpy-phen complexes studied here, a Boltzmann distribution in which localization is somewhat favored on bpy is not established for up to 100 ps after excitation. At long times, ^{3}MLCT states localized on bpy ligands are somewhat more probable because the π^* orbital of bpy is estimated to lie 200−300 cm^{-1} lower in energy than the π^* orbital of phen. After the excited state has thermally equilibrated with the surroundings, hops to other ligands are

estimated to take place on the tens of picoseconds time scale using the Eyring-Polanyi equation and past estimates of the activation barriers.

The concept that ILET rates change by orders of magnitude in the first hundred picoseconds can reconcile the many disparate observations of the underlying rates in the literature. This picture may also be helpful for interpreting the often multiphasic ET behavior of transition metal photosensitizers.[54] More refined understanding of ILET can possibly be used to optimally direct a photoexcited electron to a desired ligand.

■ ASSOCIATED CONTENT

* Supporting Information

Transient absorption spectra, decay traces, and calculated excited state spectra for excitation at 480 nm are presented along with a description of the kinetic model used to fit emission lifetimes. The Supporting Information is available free of charge on the ACS Publications website at DOI: 10.1021/acs.jpca.5b01770.

■ AUTHOR INFORMATION

Corresponding Author

*E-mail: kohler@chemistry.montana.edu. Tel: +1 406-994-7931.

Present Addresses

†Wolfgang J. Schreier, Deutsches Patent- and Markenamt, Zweibrueckenstraße 12, 80331 Munich, Germany

‡Janice Lucon, Resodyn Corporation, 150 N. Main St, Suite 600, Butte, MT 59701

§Trevor Douglas, Department of Chemistry, Indiana University, Bloomington, IN 47405

Notes

The authors declare no competing financial interest.

■ ACKNOWLEDGMENTS

This research was made possible by funding from DOE-BES (FG02-07ER46477) and was supported in part by a research grant from the Alexander von Humboldt Foundation to Wolfgang J. Schreier.

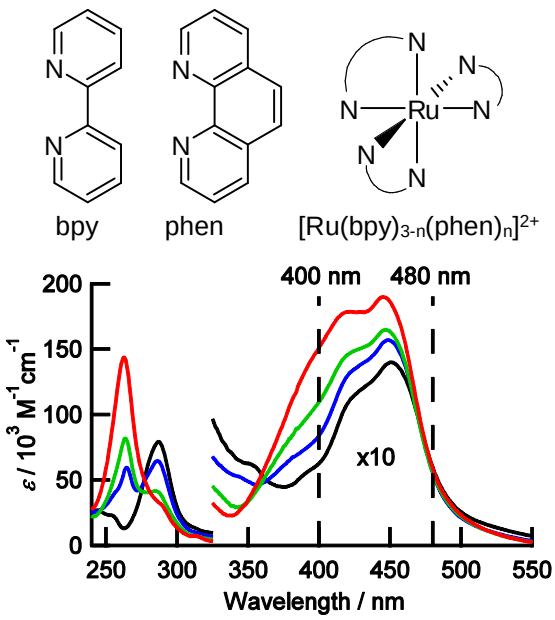

Figure 3.1. Top: Structures for the bidentate ligands 2,2'-bipyridine (bpy), 1,10-phenanthroline (phen) and the ruthenium complexes. Bottom: Molar absorption coefficient (ε) of $[Ru(bpy)_3]^{2+}$ (black), $[Ru(bpy)_2(phen)]^{2+}$ (blue), $[Ru(bpy)(phen)_2]^{2+}$ (green) and $[Ru(phen)_3]^{2+}$ (red) in acetonitrile solution. The spectra have been scaled using the ε values from Table 3.1. The dashed lines denote the pump wavelengths used in the transient absorption experiments.

Table 3.1. Wavelength of Maximum MLCT Absorption ($\lambda_{max,\ abs}$), emission ($\lambda_{max,\ em}$), and Molar Absorption Coefficient (ε) for the Indicated Complexes in Acetonitrile Solution

complex	$\lambda_{max,\ abs}$ (nm)	$\lambda_{max,\ em}$ (nm)	ε (M^{-1} cm^{-1})[a]
$[Ru(bpy)_3]^{2+}$	451	620	14,600[b] (452)
$[Ru(bpy)_2(phen)]^{2+}$	449	618	15,700[c] (449)
$[Ru(bpy)(phen)_2]^{2+}$	447	609	16,500[c] (448)
$[Ru(phen)_3]^{2+}$	445	600	19,000[d] (447)

[a] Measured at the wavelength (nm) shown in parentheses.
[b] Ref. 26.
[c] Ref. 27.
[d] Ref. 28.

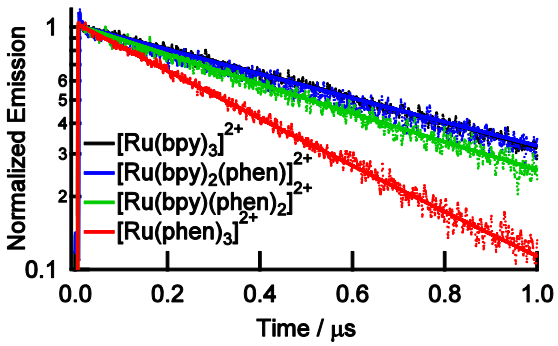

Figure 3.2. Normalized emission decays for the four ruthenium complexes at 600 nm after excitation with a 450 nm pulse. Each decay curve was fit to a single exponential convoluted with a separately measured IRF signal. Best-fit lifetimes are summarized in Table 3.2.

Table 3.2. Lifetimes in Acetonitrile Solution at Room Temperature[a]

Complex	anisotropy[b]	magic angle TA signals[c] 400 nm pump		480 nm pump		emission[d]	
	τ_r (fs)	τ_1 (fs)	τ_2 (ps)	τ_1 (fs)	τ_2 (ps)	τ_{em} (ns)	ϕ
$[Ru(bpy)_3]^{2+}$	100 ± 20	146 ± 7	9.2 ± 0.8	152 ± 10	13 ± 1	890 ± 16	0.062
$[Ru(bpy)_2(phen)]^{2+}$	140 ± 30	64 ± 6	8.3 ± 0.4	190 ± 20	10 ± 1	830 ± 15	0.066
$[Ru(bpy)(phen)_2]^{2+}$	300 ± 200	40 ± 60	10.1 ± 0.8	135 ± 70	13 ± 3	670 ± 10	0.059
$[Ru(phen)_3]^{2+}$	170 ± 60	130 ± 50	–	102 ± 16	–	440 ± 15	0.028

[a] Uncertainties are equal to one standard deviation.
[b] Determined from global fits of the anisotropy signals in Figure 3.
[c] Obtained by globally fitting transients at probe wavelengths of 350, 370, 450, 530, and 610 nm.
[d] Emission was detected at 600 nm with excitation at 450 nm.

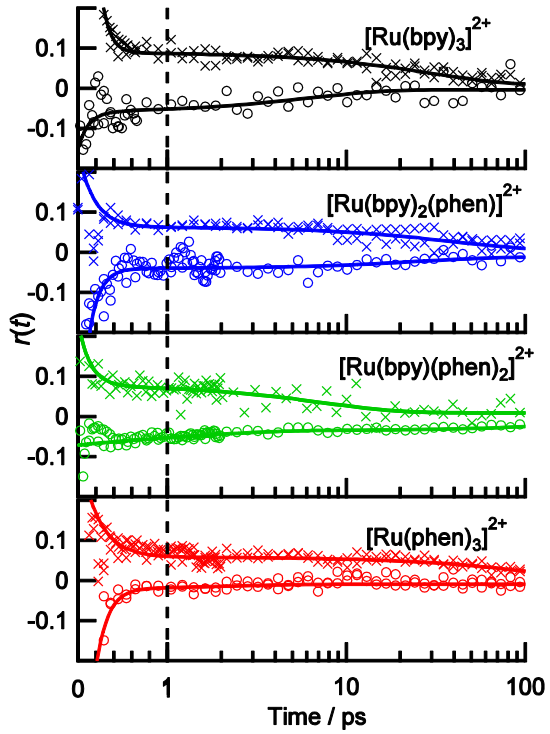

Figure 3.3. Time-resolved anisotropy signals, $r(t)$, for each ruthenium complex after excitation at 480 nm: $r(t)$ within the ESA band (370 nm for $[Ru(bpy)_3]^{2+}$ and $[Ru(bpy)_2(phen)]^{2+}$ and 350 nm for $[Ru(bpy)(phen)_2]^{2+}$ and $[Ru(phen)_3]^{2+}$) is shown by circles, while the anisotropy due to bleaching of the ^{1}MLCT band at 450 nm is shown by crosses. Solid lines are best-fit curves. The vertical dashed line indicates the change from a linear to a logarithmic time axis.

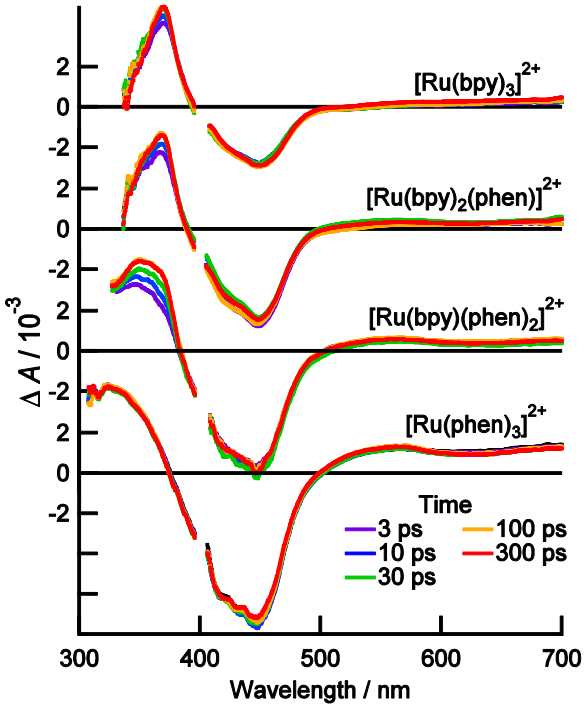

Figure 3.4. TA difference spectra at the indicated delay times for each complex in acetonitrile solution after excitation at 400 nm.

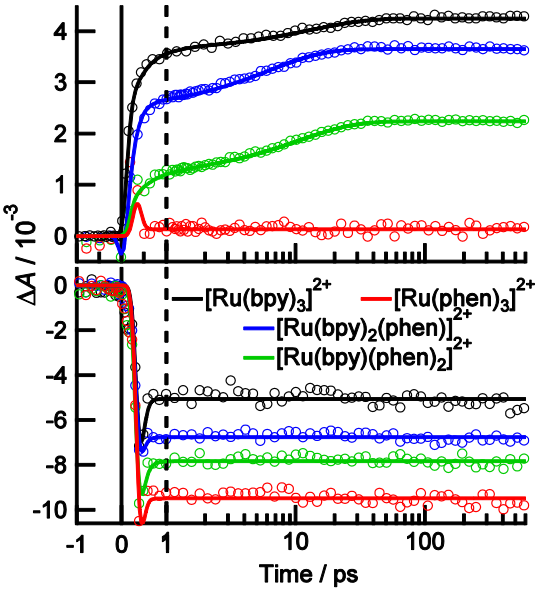

Figure 3.5. Transient absorption signals at 370 nm (top) and 450 nm (bottom) after excitation at 400 nm for $[Ru(bpy)_3]^{2+}$ (black), $[Ru(bpy)_2(phen)]^{2+}$ (blue), $[Ru(bpy)(phen)_2]^{2+}$ (green), and $[Ru(phen)_3]^{2+}$ (red) in acetonitrile solution. The vertical dashed line indicates the change from a linear to a logarithmic time axis.

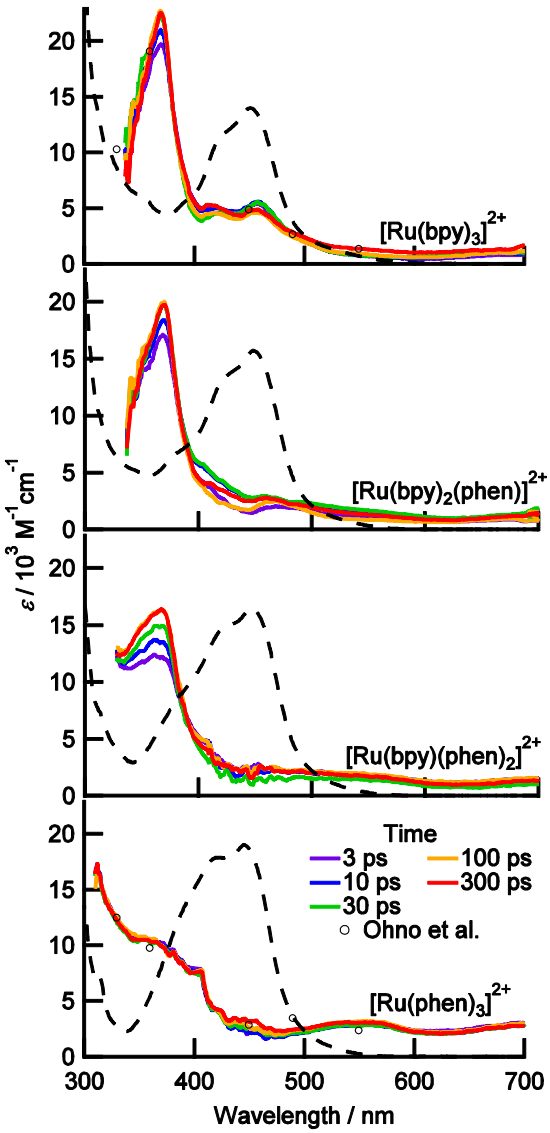

Figure 3.6. Excited-state absorption spectra for the four complexes at the indicated times after 400 nm excitation. The open circles shown nanosecond flash photolysis measurements for the two tris complexes from Ohno et al.[33] The ground-state absorption spectra are shown for comparison (black dashed curves).

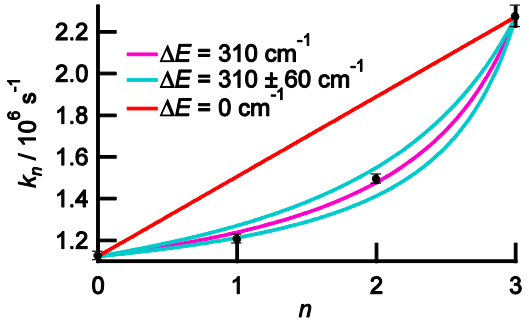

Figure 3.7. Excited-state decay rates (k_n) vs. n, the number of phenanthroline ligands (black circles). The magenta curve is the best fit using eq. 3.3. Cyan curves show the predicted lifetimes when ΔE, the splitting between bpy- and phen-localized ^{3}MLCT states, is increased or decreased by 60 cm^{-1} from the best-fit value of 310 cm^{-1}. The red curve represents the expected trend in emission lifetimes if there was no preference for localization on either type of ligand.

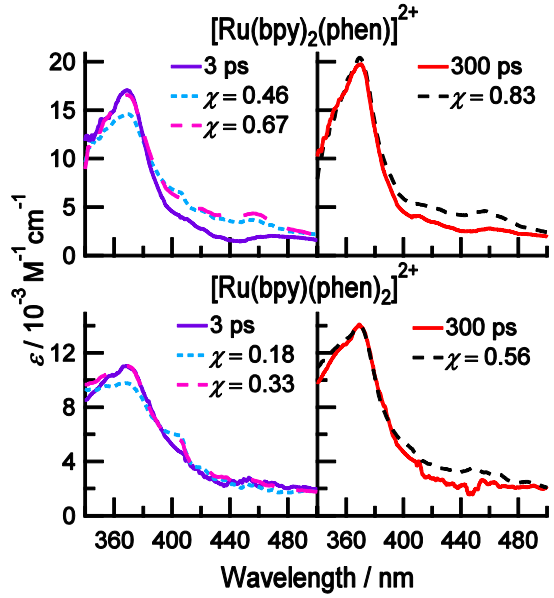

Figure 3.8. Excited-state absorption spectra at 3 ps and 300 ps (λ_{exc} = 400 nm) for the two mixed-ligand complexes (solid curves) compared with linear combinations of the excited-state spectra of the two tris complexes (dashed curves). The legend in each panel indicates the value of $\chi(t)$ (see eq. 3.4) used to generate the linear combinations.

Table 3.3. Excited State Localization in the Heteroleptic Complexes

	% bpy[a]			
Complex	FC_{400}[b]	FC_{480}[c]	Statistical	Boltzmann[d]
$[Ru(bpy)_2(phen)]^{2+}$	46	67	67	83
$[Ru(bpy)(phen)_2]^{2+}$	18	33	33	56

[a] Fraction of ^{3}MLCT states localized on the 2,2'-bipyridine (bpy) ligand, $\chi \times 100\%$.
[b] Franck-Condon distribution using ε_{400} values (M^{-1} cm^{-1}) of 6,550 and 15,800 for $[Ru(bpy)_3]^{2+}$ and $[Ru(phen)_3]^{2+}$, respectively.
[c] Franck-Condon distribution using ε_{480} values (M^{-1} cm^{-1}) of 6,230 and 6,170 for $[Ru(bpy)_3]^{2+}$ and $[Ru(phen)_3]^{2+}$, respectively.
[d] Boltzmann populations determined from fits to spectra in Figure 8.

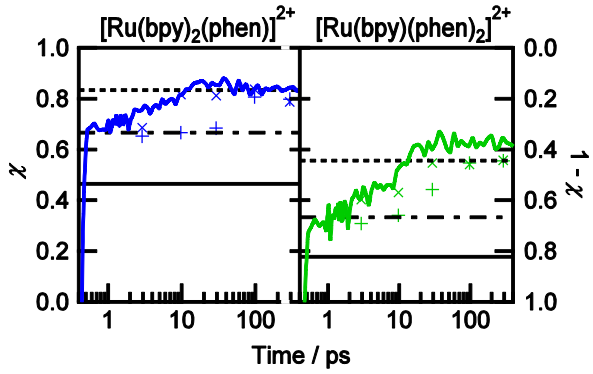

Figure 3.9. Fraction of bpy-localized ^{3}MLCT excited states (χ) vs. time for $[Ru(bpy)_2(phen)]^{2+}$ (blue) and $[Ru(bpy)(phen)_2]^{2+}$ (green). Solid curves are from fits of eq. 3.4 to the excited-state absorption measured at 370 nm (λ_{exc} = 400 nm). χ values shown by discrete points are from fits to broadband spectra at all wavelengths at the indicated delay times for excitation at 400 nm (+) and at 480 nm (×). Horizontal lines show the Franck-Condon distribution (solid, 400 nm excitation only), statistical (dot-dashed), and Boltzmann (dashed) distributions of localized states are shown as black lines.

■ REFERENCES

(1) Juris, A.; Balzani, V.; Barigelletti, F.; Campagna, S.; Belser, P. l; Von Zelewsky, A. Ru(II) Polypyridine Complexes: Photophysics, Photochemistry, Eletrochemistry, and Chemiluminescence. *Coord. Chem. Rev.* **1988**, *84*, 85–277.

(2) Damrauer, N. H.; Cerullo, G.; Yeh, A.; Boussie, T. R.; Shank, C. V.; McCusker, J. K. Femtosecond Dynamics of Excited-State Evolution in $[Ru(bpy)_3]^{2+}$. *Science* **1997**, *275*, 54–57.

(3) McCusker, J. K. Femtosecond Absorption Spectroscopy of Transition Metal Charge-Transfer Complexes. *Acc. Chem. Res.* **2003**, *36*, 876–887.

(4) Ardo, S.; Meyer, G. J. Photodriven Heterogeneous Charge Transfer with Transition-Metal Compounds Anchored to TiO_2 Semiconductor Surfaces. *Chem Soc Rev* **2009**, *38*, 115–164.

(5) Heimer, T. A.; DArcangelis, S. T.; Farzad, F.; Stipkala, J. M.; Meyer, G. J. An Acetylacetonate-Based Semiconductor-Sensitizer Linkage. *Inorg. Chem.* **1996**, *35*, 5319–5324.

(6) Malone, R. A.; Kelley, D. F. Interligand Electron Transfer and Transition State Dynamics in Ru(II)trisbipyridine. *J. Chem. Phys.* **1991**, *95*, 8970–8976.

(7) Cushing, J. P.; Butoi, C.; Kelley, D. F. Interligand Electron Transfer Dynamics in $Os(II)(bpy)_3$: Experimental Results and Model Calculations. *J. Phys. Chem. A* **1997**, *101*, 7222–7230.

(8) Shaw, G. B.; Brown, C. L.; Papanikolas, J. M. Investigation of Interligand Electron Transfer in Polypyridyl Complexes of Os(II) Using Femtosecond Polarization Anisotropy Methods: Examination of $Os(bpy)_3^{2+}$ and $Os(bpy)_2(Mab)^{2+}$. *J. Phys. Chem. A* **2002**, *106*, 1483–1495.

(9) Wallin, S.; Davidsson, J.; Modin, J.; Hammarström, L. Femtosecond Transient Absorption Anisotropy Study on $[Ru(bpy)_3]^{2+}$ and $[Ru(bpy)(py)_4]^{2+}$. Ultrafast Interligand Randomization of the MLCT State. *J. Phys. Chem. A* **2005**, *109*, 4697–4704.

(10) Hewitt, J. T.; Vallett, P. J.; Damrauer, N. H. Dynamics of the ^{3} MLCT in Ru(II) Terpyridyl Complexes Probed by Ultrafast Spectroscopy: Evidence of Excited-State Equilibration and Interligand Electron Transfer. *J. Phys. Chem. A* **2012**, *116*, 11536–11547.

(11) Ghosh, R.; Palit, D. K. Probing Excited State Charge Transfer Dynamics in a Heteroleptic Ruthenium Complex. *Phys Chem Chem Phys* **2014**, *16*, 219–226.

(12) Benniston, A.; Harriman, A. Controlling Electron Exchange in Molecular Assemblies. *Coord. Chem. Rev.* **2008**, *252*, 2528–2539.

(13) Kumar, C.; Barton, J.; Gould, I.; Turro, N.; Vanhouten, J. Energy Redistribution and Localization in the Excited-States of Ruthenium(II) Polypyridyl Complexes. *Inorg. Chem.* **1988**, *27*, 648–651.

(14) Chang, Y. J.; Xu, X.; Yabe, T.; Yu, S. C.; Anderson, D. R.; Orman, L. K.; Hopkins, J. B. Picosecond Raman Measurements of Electron Transfer in the Metal-to-Ligand Charge-Transfer Excited States of (1,10-Phenanthroline) Ruthenium(II) Complexes. *J. Phys. Chem.* **1990**, *94*, 729–736.

(15) Baggott, J.; Gregory, G.; Pilling, M.; Anderson, S.; Seddon, K.; Turp, J. Excited-States of Mixed-Ligand Chelate Complexes of Ruthenium(II) - a Re-Examination of the Evidence for Strong Interligand Coupling. *J. Chem. Soc.-Faraday Trans. Ii* **1983**, *79*, 195–210.

(16) Crosby, G.; Elfring, W. Excited-States of Mixed-Ligand Chelates of Ruthenium(II) and Rhodium(III). *J. Phys. Chem.* **1976**, *80*, 2206–2211.

(17) Cannizzo, A.; van Mourik, F.; Gawelda, W.; Zgrablic, G.; Bressler, C.; Chergui, M. Broadband Femtosecond Fluorescence Spectroscopy of $[Ru(bpy)_3]^{2+}$. *Angew. Chem. Int. Ed.* **2006**, *45*, 3174–3176.

(18) Tarnovsky, A. N.; Gawelda, W.; Johnson, M.; Bressler, C.; Chergui, M. Photexcitation of Aqueous Ruthenium(II)-Tris-(2,2‘-Bipyridine) with High-Intensity Femtosecond Laser Pulses. *J. Phys. Chem. B* **2006**, *110*, 26497–26505.

(19) Chang, C.-W.; Chou, C. K.; Chang, I.-J.; Lee, Y.-P.; Diau, E. W.-G. Relaxation Dynamics of Ruthenium Complexes in Solution, PMMA and TiO_2 Films: The Roles of Self-Quenching and Interfacial Electron Transfer. *J. Phys. Chem. C* **2007**, *111*, 13288–13296.

(20) Dattelbaum, D. M.; Kober, E. M.; Papanikolas, J. M.; Meyer, T. J. Application of Time-Resolved near-Infrared Spectroscopy (TRNIR) to the Metal-to-Ligand Charge Transfer (MLCT) Excited State(s) of. *Chem. Phys.* **2006**, *326*, 71–78.

(21) Sullivan, B. P.; Salmon, D. J.; Meyer, T. J. Mixed Phosphine 2,2’-bipyridine Complexes of Ruthenium. *Inorg. Chem.* **1978**, *17*, 3334–3341.

(22) Evans, I. P.; Spencer, A.; Wilkinson, G. Dichlorotetrakis(dimethyl sulphoxide)ruthenium(II) and Its Use as a Source Material for Some New ruthenium(II) Complexes. *J. Chem. Soc. Dalton Trans.* **1973**, 204–209.

(23) Szafran, Z.; Pike, R. M.; Singh, M. M. *Microscale Inorganic Chemistry: A Comprehensive Laboratory Experience*; 1 edition.; Wiley: New York, 1991.

(24) Laimgruber, S.; Schachenmayr, H.; Schmidt, B.; Zinth, W.; Gilch, P. A Femtosecond Stimulated Raman Spectrograph for the near Ultraviolet. *Appl. Phys. B* **2006**, *85*, 557–564.

(25) Henseler, A.; Vauthey, E. Picosecond Transient Grating Study of the Rotational Diffusion of a Ruthenium Complex in Solution. *Chem. Phys. Lett.* **1994**, *228*, 66–72.

(26) Kalyanasundaram, K. Photophysics, Photochemistry and Solar Energy Conversion with tris(bipyridyl)ruthenium(II) and Its Analogues. *Coord. Chem. Rev.* **1982**, *46*, 159–244.

(27) Yoshimura, A.; Hoffman, M.; Sun, H. An Evaluation of the Excited-State Absorption-Spectrum of $Ru(bpy)_3^{2+}$. *J. Photochem. Photobiol. -Chem.* **1993**, *70*, 29–33.

(28) Staniewicz, R. J.; Sympson, R. F.; Hendricker, D. G. Preparation and Investigation of the Spectral and Electrochemical Properties of Mixed-Ligand Ruthenium(II) Complexes Containing 1,8-Naphthyridines. *Inorg. Chem.* **1977**, *16*, 2166–2171.

(29) Hughes, H. P.; Martin, D.; Bell, S.; McGarvey, J. J.; Vos, J. G. Photophysical and Photochemical Properties of Dinuclear ruthenium(II) Complexes Containing 2,2'-bipyridine and 1,10-Phenanthroline Moieties. *Inorg. Chem.* **1993**, *32*, 4402–4408.

(30) Glazer, E. C.; Magde, D.; Tor, Y. Ruthenium Complexes That Break the Rules: Structural Features Controlling Dual Emission. *J. Am. Chem. Soc.* **2007**, *129*, 8544–8551.

(31) Sakuda, E.; Ando, Y.; Ito, A.; Kitamura, N. Long-Lived and Temperature-Independent Emission from a Novel Ruthenium(II) Complex Having an Arylborane Charge-Transfer Unit. *Inorg. Chem.* **2011**, *50*, 1603–1613.

(32) Müller, P.; Brettel, K. $[Ru(bpy)_3]^{2+}$ as a Reference in Transient Absorption Spectroscopy: Differential Absorption Coefficients for Formation of the Long-Lived 3MLCT Excited State. *Photochem. Photobiol. Sci.* **2012**, *11*, 632.

(33) Henry, W.; Coates, C. G.; Brady, C.; Ronayne, K. L.; Matousek, P.; Towrie, M.; Botchway, S. W.; Parker, A. W.; Vos, J. G.; Browne, W. R.; *et al.* The Early Picosecond Photophysics of Ru(II) Polypyridyl Complexes: A Tale of Two Timescales. *J. Phys. Chem. A* **2008**, *112*, 4537–4544.

(34) Ohno, T.; Yoshimura, A.; Prasad, D.; Hoffman, M. A Weak Delta-G-Degrees Dependence of Back Electron-Transfer Within the Geminate Redox Pairs Formed in the Quenching of Excited Ruthenium(II) Complexes by Methylviologen. *J. Phys. Chem.* **1991**, *95*, 4723–4728.

(35) Oh, D. H.; Boxer, S. G. Stark Effect Spectra of Ru(Diimine)$_3^{2+}$ Complexes. *J. Am. Chem. Soc.* **1989**, *111*, 1130–1131.

(36) Karki, L.; Hupp, J. T. Electroabsorption Studies of Metal-to-Ligand Charge Transfer in Ru(phenanthroline)$_3^{2+}$: Evidence for Intrinsic Charge Localization in the Initially Formed Excited State. *Inorg. Chem.* **1997**, *36*, 3318–3321.

(37) Caspar, J. V.; Meyer, T. J. Photochemistry of MLCT Excited States. Effect of Nonchromophoric Ligand Variations on Photophysical Properties in the Series Cis-Ru(bpy)$_2$L$_2^{2+}$. *Inorg. Chem.* **1983**, *22*, 2444–2453.

(38) Blakley, R.; Myrick, M.; Pittman, R.; Dearmond, M. Chromophoric Fine Tuning and the Interchromophoric Coupling Model in Ruthenium(II) Polypyridyl Complexes. *J. Phys. Chem.* **1990**, *94*, 4804–4809.

(39) Sun, H.; Hoffman, M. Z. Photophysics of Ruthenium(II)-Diimine Complexes in Water-Acetonitrile Mixed Solvents. *J. Phys. Chem.* **1993**, *97*, 11956–11959.

(40) Motten, A.; Hanck, K.; Dearmond, M. Electron-Spin-Resonance of the Reduction Products of [Fe(bpy)$_3$]$^{2+}$ and [Ru(bpy)$_3$]$^{2+}$. *Chem. Phys. Lett.* **1981**, *79*, 541–546.

(41) Heath, G.; Yellowlees, L.; Braterman, P. Ligand Ligand Inter-Valence Charge-Transfer Absorption in Reduced Ruthenium(II) Bipyridine Complexes. *Chem. Phys. Lett.* **1982**, *92*, 646–648.

(42) Bensasson, R.; Salet, C.; Balzani, V. Laser Flash Spectroscopy of Tris(2,2'-Bipyridine)ruthenium(II) in Solution. *J. Am. Chem. Soc.* **1976**, *98*, 3722–3724.

(43) Mahon, C.; Reynolds, W. L. Preparation of Sodium tris(2,2'-bipyridine)ferrate(-I). *Inorg. Chem.* **1967**, *6*, 1927–1928.

(44) Damrauer, N. H.; McCusker, J. K. Ultrafast Dynamics in the Metal-to-Ligand Charge Transfer Excited-State Evolution of [Ru(4,4'-Diphenyl-2,2'-Bipyridine)$_3$]$^{2+}$. *J. Phys. Chem. A* **1999**, *103*, 8440–8446.

(45) Henrich, J. D.; Zhang, H.; Dutta, P. K.; Kohler, B. Ultrafast Electron Transfer Dynamics in Ruthenium Polypyridyl Complexes with a π-Conjugated Ligand †. *J. Phys. Chem. B* **2010**, *114*, 14679–14688.

(46) Kovalenko, S. A.; Schanz, R.; Hennig, H.; Ernsting, N. P. Cooling Dynamics of an Optically Excited Molecular Probe in Solution from Femtosecond Broadband Transient Absorption Spectroscopy. *J. Chem. Phys.* **2001**, *115*, 3256.

(47) Middleton, C. T.; Cohen, B.; Kohler, B. Solvent and Solvent Isotope Effects on the Vibrational Cooling Dynamics of a DNA Base Derivative. *J. Phys. Chem. A* **2007**, *111*, 10460–10467.

(48) Bossert, J.; Daniel, C. Electronic Absorption Spectroscopy of $[Ru(phen)_2(bpy)]^{2+}$, $[Ru(phen)_2(dmbp)]^{2+}$, $[Ru(tpy)(phen)(CH_3CN)]^{2+}$ and $[Ru(tpy)(dmp)(CH_3CN)]^{2+}$ A Theoretical Study. *Coord. Chem. Rev.* **2008**, *252*, 2493–2503.

(49) Shaw, G. B.; Styers-Barnett, D. J.; Gannon, E. Z.; Granger, J. C.; Papanikolas, J. M. Interligand Electron Transfer Dynamics in $[Os(bpy)_3]^{2+}$: Exploring the Excited State Potential Surfaces with Femtosecond Spectroscopy. *J. Phys. Chem. A* **2004**, *108*, 4998–5006.

(50) Miller, S. A.; Moran, A. M. Nonlinear Optical Detection of Electron Transfer Adiabaticity in Metal Polypyridyl Complexes. *J. Phys. Chem. A* **2010**, *114*, 2117–2126.

(51) Cooley, L.; Bergquist, P.; Kelley, D. Determination of Exciton Hopping Rates in Ruthenium(II) Tris(bipyridine) Complexes by Picosecond Polarized Absorption-Spectroscopy. *J. Am. Chem. Soc.* **1990**, *112*, 2612–2617.

(52) Schoonover, J. R.; Dattelbaum, D. M.; Malko, A.; Klimov, V. I.; Meyer, T. J.; Styers-Barnett, D. J.; Gannon, E. Z.; Granger, J. C.; Aldridge, W. S.; Papanikolas, J. M. Ultrafast Energy Transfer between the ^{3}MLCT State of $[Ru^{II}(Dmb)_2(Bpy\text{-}an)]^{2+}$ and the Covalently Appended Anthracene. *J. Phys. Chem. A* **2005**, *109*, 2472–2475.

(53) Önfelt, B.; Lincoln, P.; Nordén, B.; Baskin, J. S.; Zewail, A. H. Femtosecond Linear Dichroism of DNA-Intercalating Chromophores: Solvation and Charge Separation Dynamics of $[Ru(Phen)_2dppz]^{2+}$ Systems. *Proc. Natl. Acad. Sci.* **2000**, *97*, 5708–5713.

(54) Benkö, G.; Kallioinen, J.; Korppi-Tommola, J. E. I.; Yartsev, A. P.; Sundström, V. Photoinduced Ultrafast Dye-to-Semiconductor Electron Injection from Nonthermalized and Thermalized Donor States. *J. Am. Chem. Soc.* **2002**, *124*, 489–493.

CHAPTER 4

PHOTOINDUCED ELECTRON TRANSFER OBSERVED IN A CLICK-FUNCTIONALIZED RUTHENIUM(II)-COBALT(II) SUPRAMOLECULAR COMPLEX

4.1 Introduction

Photoredox reactions such as those used for water-splitting are reactions involving electron or hole transfer from the sensitizer.[1] One of the most fundamental challenges in developing charge transfer systems is to enhance the yield and longevity of a charge-separated state, which can then perform redox reactions. Intermolecular photoredox systems in solution suffer in this regard, as an electron donor (D) and acceptor (A) must be at, or diffuse to, a short distance to undergo charge transfer, and so require either high concentrations or long excited-state lifetimes. Supramolecular systems known as donor-bridge-acceptor (DBA) molecules can remedy this issue by covalently linking the photosensitizer to a secondary functional group via a bridge (B).[2,3] This secondary group could be a catalytic center, a second sensitizer, or a repository for charges for use in multistep redox reactions.[4–12] The bridge linking the two centers allows for electron transfer to occur rapidly and consistently, allowing the sensitizer to be active even at low concentrations.

Charge-transfer in these DBA systems occurs through a combination of tunneling and hopping processes, that are distance-dependent.[13,14] The tunneling mechanism assumes that the bridge behaves as an energetic barrier between the donor and acceptor

groups, which the excited electron must tunnel across to achieve the charge-transfer state. This results in an exponential decrease in transfer rate (k) as the distance between the donor and acceptor groups (r_{DA}) becomes larger:

$$k = k_0 \exp(-\beta \cdot r_{DA}) \quad (4.1)$$

where k_0 is the theoretical rate constant for donor-acceptor pair in direct contact and β is an attenuation factor intrinsic to the molecular structure of the bridge. This attenuation factor is determined by the height of the energy barrier and the effective mass of the charge carrier across the bridge.[15,16] In systems where electron-transfer can occur along a π-conjugated bridge,[17] the attenuation factor is small ranging from 0.1 to 6 nm^{-1},[13] making this form of charge transfer the dominant mechanism in systems where donor-acceptor separation is less than ~4 nm.[18,19] On the other hand, charge hopping, where charge-transfer occurs over intermediate states localized along the bridge, dominates in systems with large donor-acceptor distance. The rate for hopping mechanisms depends less strongly on distance compared to tunneling mechanisms, and can be treated as a diffusive process; however, for this process to occur, the bridge is required to have low energy sites available for localization intermediate to the donor and acceptor sites.[13,20]

The underlying aspect of these DBA systems is the following. On the one hand, tethering the donor and acceptor groups together allows them to transfer charge more rapidly and consistently compared to free floating reactants in solution. On the other hand, coupling is sufficiently weak that the charges do not undergo recombination immediately upon formation. The DBAs can have the additional benefit of having separate photosensitizer and catalytic sites, which can be optimized individually, making

them simple and versatile. However, the bridge connecting the donor and acceptor must be able to connect many different types of reactive groups in a stable and robust way.

The Cu(I) catalyzed Huisgen cycloaddition between azide and alkyne moieties has recently been hailed as a simple and efficient means to form a bridge between donor and acceptor groups in a DBA photocatalysts.[21,22] This high yield "click" reaction, forming 1,2,3-triazole, is robust to a variety of synthetic conditions. The triazole bridge has been paired with many different porphyrins[23–25], boron-dipyrromethene[25–27], and ruthenium polypyridyl[21,26,28–35] photosensitizers and numerous secondary functional groups. The electron transfer rates of systems range from tens of picoseconds to hundreds of nanoseconds. In some cases, the triazole ring only acts to maintain a close distance between the donor-acceptor, whereby electron transfer takes place "through-space" directly from the donor to the acceptor.[35] In other cases, the triazole ring acts as a conductive wire, transferring the electron through conjugated π-bonds along the bridge ("through-bond").[24] The triazole bridge has been shown to have an attenuation factor β of approximately 2.8 nm^{-1},[36] which is similar to other conjugated ligands.[37,38]

The donor-acceptor pair used in this study is composed of three ruthenium(II) polypyridyl complexes and a cobalt(II) polypyridyl complex (Figure 4.1), abbreviated as $[Ru\text{-}Co]^{8+}$. Although the ruthenium centers act as the photosensitizer, three distinct mechanisms of quenching have been observed for pairs of Ru(II*)/Co(II) polypyridyl complexes previously, making it difficult to discern which is the donor and acceptor. These three quenching mechanisms can be outlined as:

$$\mathrm{Ru(II^*)/Co(II) \rightarrow Ru(III)/Co(I)} \qquad (4.2a)$$

$$\mathrm{Ru(II^*)/Co(II) \rightarrow Ru(I)/Co(III)} \quad (4.2b)$$

$$\mathrm{Ru(II^*)/Co(II) \rightarrow Ru(II)/Co(II^*)} \quad (4.2c)$$

The first mechanism (eq 4.2a) is oxidative electron transfer, where the excited electron initially localized on the ruthenium complex is transferred to an empty orbital on the cobalt center, which oxidizes the ruthenium sensitizer. The reductive electron transfer mechanism (eq 4.2b) involves an electron from cobalt being transferred to fill the hole formed from the excitation of ruthenium, reducing the sensitizer. The final quenching mechanism (eq 4.2c) is energy transfer, where the excited state is transferred from the ruthenium complex to the cobalt complex. All three mechanisms have been observed for non-bonded pairs of Ru(II)/Co(II) polypyridyl complexes[39–41] and have been thought to also affect intramolecular[42–46] systems. In the intermolecular systems, the three quenching pathways can be promoted or suppressed by changing the ligands attached to each metal center, which affects the redox potential between the donor and acceptor.[39]

The mechanisms of excited-state quenching by cobalt(II) may also be obfuscated by spin-state relaxations in Co(II), which is d^7 and can exist in the ground state as either a low-spin doublet (^{2}Co(II)), or a high-spin quadruplet (^{4}Co(II)).[42,47,48] The relative energy of these two spin-states is dependent on the crystal field splitting energy ($10Dq$) of the ligands surrounding the metal. While bipyridine ligands have been shown to be relatively weak-field ligands, resulting in cobalt complexes with primarily high-spin centers,[49] the cobalt(II) bis-terpyridine complex has been observed to have roughly equal proportions of the two spin states at room temperature.[50] Together, the multitude of quenching

pathways and the equilibrium of cobalt spin-states has made assignments of excited state quenching between these two metal complexes very difficult.[42]

In this work, we studied the excited-state quenching processes in the $[Ru\text{-}Co]^{8+}$ complex (Figure 4.1) after exciting the ruthenium center. This quenching rate is compared to that of the intermolecular quenching between the precursors of the multimetal complex, $[Ru(bpy)_2(alk\text{-}phen)]^{2+}$ and $[Co(N_3\text{-}phen)_3]^{2+}$ (Figure 4.1). This comparison will give insight into the effectiveness of using a triazole bridge for electron transfer processes, and potentially offer ways to improve the electron transfer efficiencies of similar bridged systems.

4.2 Results

4.2.1 Steady-State UV/Visible/NIR Absorption Spectra

Absorption spectra of the metal complexes in acetonitrile solution are shown in Figure 4.2a. The absorbance maximum of the ruthenium-centered ^{1}MLCT band occurs at 449 nm. The overall spectral shape and position of this band is similar between $[Ru\text{-}Co]^{8+}$ and $[Ru(bpy)_2(alk\text{-}phen)]^{2+}$, but the intensity is three times greater in the former complex. The ^{1}MLCT transition for cobalt appears as a higher energy (317 nm) peak for $[Co(N_3\text{-}phen)_3]^{2+}$ and a shoulder for $[Ru\text{-}Co]^{8+}$; however, this band is quite red shifted compared to $[Co(phen)_3]^{2+}$ where it appears as a shoulder near 295 nm.[51]

Ligand-centered transitions are observed near 285 nm for all complexes. The phenanthroline ligand absorbs at 265 nm in both $[Ru(phen)_3]^{2+}$ and $[Co(phen)_3]^{2+}$.[52,53] Here, the modified N_3-phen ligand absorption band is red-shifted to approximately 285

nm in the $[Co(N_3\text{-phen})_3]^{2+}$ complex. The $[Ru\text{-}Co]^{8+}$ complex displays twin absorption bands at 284 nm. The longer wavelength band likely corresponds to the N_3-phen absorption, whereas the shorter wavelength band is due to bipyridine absorption.[52] This twin band can be approximated by a linear combination ($\varepsilon'_{Ru\text{-}Co}$) of the molar absorption coefficients at each wavelength for $[Ru(bpy)_2(alk\text{-}phen)]^{2+}$ (ε_{Ru}) and $[Co(N_3\text{-phen})_3]^{2+}$ (ε_{Co}):

$$\varepsilon'_{Ru-Co}(\lambda) = A \cdot \varepsilon_{Ru}(\lambda) + B \cdot \varepsilon_{Co}(\lambda) \qquad (4.3)$$

where *A* and *B* are constants which were adjusted to minimize the sum of squared residuals for wavelengths above 300 nm, with values of 2.79 and 1.12, respectively. The spectrum at wavelengths below 250 nm shows less agreement between $[Ru\text{-}Co]^{8+}$ and this linear combination (Figure 4.2a).

The complexes $[Co(N_3\text{-phen})_3]^{2+}$ and $[Ru\text{-}Co]^{8+}$ also show weak metal-centered (MC) absorption at 918 and 915 nm, respectively (Figure 4.3), attributed to a transition on cobalt. The $[Co(N_3\text{-phen})_3]^{2+}$ complex also displays other weak MC transitions at 656, 615, 538, and 440 nm, which are not observed in the multimetal complex due to the ^{1}MLCT absorption of the ruthenium centers.

4.2.2 Steady-State Emission Spectra

Steady state emission spectra for the ruthenium complexes upon 450 nm excitation are displayed in Figure 4.2b. The emission bands for $[Ru\text{-}Co]^{8+}$ and $[Ru(bpy)_2(alk\text{-}phen)]^{2+}$, which peak at 612 and 618 nm respectively, are assigned to the emission of the ^{3}MLCT state of the ruthenium center.[54] The slight blue shift observed for $[Ru\text{-}Co]^{8+}$ originated from the perturbation from the formation of the bridging triazole.[31]

The emission of $[Co(N_3\text{-phen})_3]^{2+}$ upon 317 nm excitation peaks at 470 nm, and is orders of magnitude weaker than the ruthenium complexes; However, this weak emission is still much more intense than the emission of $[Co(phen)_3]^{2+}$, which was not observed using either steady-state or TCSPC methods used here. The $[Ru\text{-}Co]^{8+}$ complex showed no signature of this cobalt emission at 470 nm when excited at 450 nm.

4.2.3 Emission Quantum Yields and Stern-Volmer Quenching

The emission quantum yield for $[Ru(bpy)_2(alk\text{-}phen)]^{2+}$ exciting at 450 nm was found to be 0.064 ± 0.008, which is lower than the 0.080 quantum yield reported by Sun et. al.[31] in methanol, however it is very similar to $[Ru(bpy)_2(phen)]^{2+}$ which has a quantum yield of 0.060.[55] The quantum yield for the multimetal complex is reduced to 0.049 ± 0.004.

The emission intensity integrated over all wavelengths (M) for $[Ru(bpy)_2(alk\text{-}phen)]^{2+}$ after 450 nm excitation decreases with increasing concentration of $[Co(N_3\text{-}phen)_3]^{2+}$ from 0 to 30 μM, shown in Figure 4.4. The intermolecular quenching rate constant (k_q) is obtained from the Stern-Volmer relation:

$$\frac{M^0}{M} = 1 + k_q \tau_0 [Q] \qquad (4.4)$$

where M^0 is the integrated emission intensity without the $[Co(N_3\text{-phen})_3]^{2+}$ quencher (Q), and τ_0 is the emission lifetime of unquenched $[Ru(bpy)_2(alk\text{-phen})]^{2+}$ (see next section). The resulting quenching rate constant was determined to be $(3.6 \pm 2.8) \times 10^9$ M^{-1} s^{-1} (Figure 4.4b).

4.2.4 Time-Resolved Emission Lifetimes

To obtain the emission lifetimes for the ruthenium complexes, time-resolved emission was recorded for $[Ru(bpy)_2(alk\text{-}phen)]^{2+}$ and $[Ru\text{-}Co]^{8+}$ (Figure 4.5) using the TCSPC technique (section 2.2), exciting at 450 nm. The emission decay for $[Ru(bpy)_2(alk\text{-}phen)]^{2+}$ at 610 nm could be modeled with a single exponential decay with a lifetime of 990 ns, while the decay of $[Ru\text{-}Co]^{8+}$ required fitting with a bi-exponential function with lifetimes of 890 and 140 ns, with relative amplitudes of 60% and 40%, respectively (Table 4.1). The emission band at any moment matches the steady-state spectrum shown in Figure 4.2b. The 990 ns lifetime for $[Ru(bpy)_2(alk\text{-}phen)]^{2+}$ is shorter than the 1.30 μs lifetime reported by Sun, et. al. in acetonitrile solution; however, it matches well with the 961 ns lifetime reported for the complex in methanol.[31]

The biphasic decay for $[Ru\text{-}Co]^{8+}$ can be compared to the emission decay signals of a supramolecular triad of $[\{Ru(II)(bpy)_2(bpy\text{-}terpy)\}Co(II)]^{6+}$ (bpy = 2,2'bipyridine, bpy-terpy = 4'-(4-(2-(4'-methyl-2,2'-bipyridyl-4-yl)ethyl)phenyl)-2,2':6',2''-terpyridine)[42] In this system, the biexponential decay rates were observed to be 30 ns and 855 ns, with relative amplitudes of 93% and 7%, respectively. Although the long lifetimes for both complexes are similar, the short lifetime for the $[Ru\text{-}Co]^{8+}$ complex has a much smaller amplitude and displays slower kinetics.

Time-resolved emission signals at 455 nm were also collected for $[Co(N_3\text{-}phen)_3]^{2+}$, exciting at 317 nm. The emission can be well described by a single exponential decay with a lifetime of 6.7 ns. Similar emission for the $[Co(phen)_3]^{2+}$ complex was not observed under identical experimental conditions.

4.2.5 Broadband and Single Wavelength TA Experiments

Transient absorption spectra at selected delay times and decay signals at selected wavelengths for all polypyridyl complexes in acetonitrile solution upon 400 nm excitation are shown in Figures 4.6 and 4.7, respectively. Both $[Ru(bpy)_2(alk\text{-}phen)]^{2+}$ and $[Ru\text{-}Co]^{8+}$ complexes display nearly identical difference spectra, with an excited state absorption at 370 nm and a ground-state bleach at 450 nm. Transient signal spikes were observed on the time scale of the instrument response time of 200 fs (Figure 4.7), although these ultrafast signals are attributable to either ^{1}MLCT → ^{3}MLCT intersystem crossing on the ruthenium center or to the solvent. However, signals for both complexes are constant between 1 ps and 3 ns. The $[Co(N_3\text{-}phen)_3]^{2+}$ transient absorption signals are quite different and much weaker, showing an excited state absorption maximum at 480 nm, which decays exponentially with a lifetime of 3.3 ± 0.9 ps.

4.3 Discussion

4.3.1 Steady-State UV/Visible/NIR Absorption

The ground state absorption spectrum of the $[Ru\text{-}Co]^{8+}$ complex can be modeled by a linear combination of the $[Ru(bpy)_2(alk\text{-}phen)]^{2+}$ and $[Co(N_3\text{-}phen)_3]^{2+}$ absorption spectra (dashed line in Figure 4.2a). In particular, there is good agreement for the ruthenium ^{1}MLCT band at 450 nm, indicating that the potential energy landscape is virtually unchanged when linking the Ru complex to the Co complex. The higher energy ligand-centered absorption bands show less agreement between complexes, likely as a result of the formation of triazole bridge.[56] Similar spectral changes were observed by

Sun et al.[31]{Sun, 2012} upon the formation of a triazole bridge on $[Ru(bpy)_2(alk\text{-}phen)]^{2+}$.

The ligand centered absorption bands for the $[Co(N_3\text{-}phen)_3]^{2+}$ complex are significantly red shifted compared to the unmodified complex, $[Co(phen)_3]^{2+}$, as is the ^{1}MLCT band.[51] While previous studies have indicated that similar red shifts can occur in cobalt polypyridyl complexes if the cobalt center is oxidized to Co(III),[51,57] analysis of d-d transitions at NIR wavelengths (Figure 4.3) maintain that both the $[Co(N_3\text{-}phen)_3]^{2+}$ and $[Ru\text{-}Co]^{8+}$ complexes contain only Co(II). Absorption maxima at 918 nm for $[Co(N_3\text{-}phen)_3]^{2+}$ and 915 nm for the $[Ru\text{-}Co]^{8+}$ complex are both similar to peaks found at 909 nm by Palmer[49] for $[Co(bpy)_3]^{2+}$, or at 885 nm by Creutz[40] for $[Co(phen)_3]^{2+}$. In both studies, these MC transitions near 900 nm were identified as the d-d transition, $^4T_1(F) \rightarrow {}^4T_2(F)$ for the d^7 complex. These bands are inconsistent with a d^6 ligand-field description, as $[Co(phen)_3]^{3+}$ displays an absorption band at 705 nm.[58] Using other metal-centered transitions shown in Figure 4.3, the Racah B parameter and *Dq* splitting parameter for $[Co(N_3\text{-}phen)_3]^{2+}$ were found to be 820 ± 10 cm^{-1} and 1230 ± 50 cm^{-1}, respectively, indicating the ground states of both complexes are Co(II) and purely high-spin.

Although the MC transition bands labeled for $[Co(N_3\text{-}phen)_3]^{2+}$ in Figure 4.3 are not easily observable for the $[Ru\text{-}Co]^{8+}$ complex due to the much stronger ruthenium-centered ^{1}MLCT band, the close matching of the NIR peak at 915 nm indicates that the ligand environment around cobalt is likely unchanged. The red shifts observed for ligand and ^{1}MLCT bands of $[Co(N_3\text{-}phen)_3]^{2+}$ compared to $[Co(phen)_3]^{2+}$ therefore correspond

to lower energies of the reduced and excited states of the N_3-phen ligand compared to phenanthroline.

4.3.2 Intermolecular Quenching Processes

The quenching of $[Ru(bpy)_2(alk\text{-}phen)]^{2+}$ emission by $[Co(N_3\text{-}phen)_3]^{2+}$ was shown to have a quenching rate constant of $(3.6 \pm 2.8) \times 10^9$ M^{-1} s^{-1}, which is within a factor of ten of the Stokes-Einstein diffusion limit of 1.93×10^{10} M^{-1} s^{-1} in acetonitrile,[59,60] indicating that the barrier for the quenching process is very small. A more accurate theoretical limit can be determined using the Smoluchowski diffusion equation for diffusion-influenced charged particles:[59]

$$k_q = \frac{4\pi \cdot N_A (D_{Ru} + D_{Co}) \beta \cdot k_{rxn}}{\left(k_{rxn} + 4\pi (D_{Ru} + D_{Co}) \beta \cdot \exp\left(\frac{V(r)}{k_B T} \right) \right)} \tag{4.5a}$$

$$\beta^{-1} = \int_{2R}^{\infty} \frac{\exp\left(\frac{V(r)}{k_B T} \right)}{r^2} dr \tag{4.5b}$$

$$V(r) = \frac{Z_{Ru} Z_{Co} e^2}{4\pi\varepsilon \cdot r} \tag{4.5c}$$

where k_q is the total quenching rate, k_{rxn} is the intrinsic rate of quenching of a donor-acceptor encounter-pair, D is the diffusion constant for either ruthenium or cobalt, which was estimated using the Stokes-Einstein diffusion equation[61] for spherical particles with a radius (R) of 12 Å, corresponding to an average of crystal structure radii.[62–64] The interaction potential $V(r)$ is assumed to be purely columbic, with both complexes having +2 charge (Z). In the limit that k_{rxn} goes to infinity, the total rate approaches 4.3×10^9 M^{-1}

s^{-1}, which is within error of the observed $(3.6 \pm 2.8) \times 10^9$ M^{-1} s^{-1} rate, indicating that the quenching process for the encounter-pair is likely barrierless.

The observed intermolecular quenching rate for $[Ru(bpy)_2(alk\text{-}phen)]^{2+}$ and $[Co(N_3\text{-}phen)_3]^{2+}$ is faster than many other pairs of ruthenium and cobalt polypyridyl complexes, which have been observed to have rate constants ranging from 6×10^7 to 4×10^9 M^{-1} s^{-1}.[39,42,65] A model for this intermolecular quenching processes was introduced by Krishnan et al.[66] which relates the total quenching rate to the redox potential for oxidative electron-transfer quenching, forming $[Ru(L_1)_3]^{3+}$ and $[Co(L_2)_3]^{+}$, where L_1 and L_2 are modified bipyridine or phenanthroline ligands. The intermolecular quenching rate in this model was determined by three competitive processes which are oxidative (k_{ox}), reductive (k_{red}), or energy transfer (k_{en}) quenching. The rate of each individual process is determined by kinetic measurements of diffusion, ion self-exchange reactions, and overall quenching rates for many pairs of complexes. Using this model,[66] the observed 3.6×10^9 M^{-1} s^{-1} quenching rate for the $[Ru(bpy)_2(alk\text{-}phen)]^{2+}/[Co(N_3\text{-}phen)_3]^{2+}$ pair corresponds to a net cell potential (ΔE_0) of +0.1 V (Figure 4 in reference [66]) for the formation of $[Ru(bpy)_2(alk\text{-}phen)]^{3+}/Co(N_3\text{-}phen)_3]^{+}$, making oxidative quenching the major quenching pathway. Although there is significant uncertainty in the measured quenching rate, the reductive quenching pathway can be ruled out as it is in general much slower than either oxidative or energy transfer quenching due to a significant conformational barrier for the transition from Co(II) to Co(III).[67,68] The model by Krishnan suggests that energy transfer quenching is also a negligible process, which is

confirmed by the absence of any emission near 470 nm, where excited $[Co(N_3\text{-phen})_3]^{2+}$ emits.

4.3.3 Intramolecular Quenching Processes

The $[Ru\text{-}Co]^{8+}$ complex is assumed to undergo an oxidative quenching pathway analogous to the non-bonded system (section 4.3.2), as the formation of the triazole bridge is not expected to modify the electronic structure of the ruthenium or cobalt centers (section 4.3.1). However, unlike the intermolecular quenching mechanism which displayed rapid transfer limited only by diffusion, the intramolecular quenching process appears to occur with a much slower timescale.

Transient absorption spectra (Figure 4.6) indicate that quenching of the ruthenium centered ^{3}MLCT state does not occur in the first three nanoseconds after excitation, as the 370 nm peak attributed to a reduced bpy ligand is observed to be constant. If electron-transfer to the cobalt center takes place, then the 370 nm peak would decrease alongside the formation of a peak near 640 nm corresponding to the reduced cobalt center.[41] Neither signature is observed.

The slow decay of the ruthenium centered ^{3}MLCT state can also be observed in the time-resolved emission signals of the $[Ru\text{-}Co]^{8+}$ complex (Figure 4.5). These emission signals reveal evidence of quenching, as the overall excited state lifetime of the $[Ru\text{-}Co]^{8+}$ complex is shorter than that of the $[Ru(bpy)_2(alk\text{-}phen)]^{2+}$ complex. However, the emission signal requires a biexponential fit with two distinct lifetimes (Table 4.1), which necessitates a more complex mechanism than the single electron-transfer reaction used to describe the intermolecular case. This biphasic decay for the $[Ru\text{-}Co]^{8+}$ complex

can be modeled as either a significant back electron transfer process, or as two separate quenching processes acting on different excited states of $[Ru\text{-}Co]^{8+}$. Possible candidates for these different quenching processes are discussed below; although for two distinct lifetimes to be observable, the different states need to be unable to interconvert on the timescale of emission. States that are able to interconvert faster than the decay lifetime produce a single exponential lifetime, as in the case of $[Ru(bpy)_{3-n}(phen)_n]^{2+}$ discussed in Chapter 3. Another possibility is that the observed 890 ns lifetime is from excess $[Ru(bpy)_2(alk\text{-}phen)]^{2+}$ in the solution;[47] however, this is unlikely as there were no traces of contamination in the sample during HPLC separation prior to TCSPC measurements.

Multiple conformational isomers of the $[Ru\text{-}Co]^{8+}$ complex exist, as there are two rotational degrees of freedom around each of the single bonds at the 1 and 4 positions of the triazole bridge (Figure 4.1). It is possible that these different isomers could have different quenching lifetimes, as they may have different distances separating the ruthenium and cobalt centers. A study by de Miguel et. al.[23] demonstrated that decreasing the donor-acceptor distance in a triazole linked dyad of zinc(II)-porphyrin and buckminsterfullerene resulted in a change of the electron-transfer mechanism from a through-bond to a through-space process, which resulted in much faster rates of charge-separation in toluene solutions. In this dyad, the donor-acceptor distance was reduced by folding the conjugated bridge until the donor and acceptor were close together, allowing the frontier orbitals of the donor-acceptor pair to overlap directly. In the case of $[Ru\text{-}Co]^{8+}$, rotations along the 1,4-positions of the triazole bridge result in a nominal folding angle of ± 36 degrees, assuming the pentagonal ring of the triazole has bond angles of

108 degrees.[69] This angle is fairly small, and is not enough to drastically reduce the distance between the ruthenium and cobalt centers, making it is unlikely that the two lifetimes are from through-space and through-bond processes.

It is possible that quenching could occur both through inter- and intramolecular pathways for the $[Ru\text{-}Co]^{8+}$ complex, resulting in two separate decay lifetimes. However, changing the concentration of $[Ru\text{-}Co]^{8+}$ from 3.3 to 1.4 μM showed no significant variation in lifetimes or relative amplitudes of the two exponential decays, indicating that the effect of intermolecular quenching is negligible. It is possible that intermolecular quenching still could occur at higher concentrations, but even diffusion limited intermolecular quenching of ruthenium complexes becomes difficult to observe at low micromolar concentrations, as was the case for $[Co(N_3\text{-phen})_3]^{2+}$ (Figure 4.4b). The two lifetimes observed are therefore not from an intermolecular quenching process, but are intramolecular in origin.

Two separate quenching pathways could be observed in the case that the $[Ru\text{-}Co]^{8+}$ complex undergoes multiple excitations on different ruthenium centers. One excited state could be quenched by the cobalt center, resulting in the short lifetime, while secondary excited ruthenium centers on the same supramolecular complex would be unquenched and display lifetimes similar to $[Ru(bpy)_2(alk\text{-}phen)]^{2+}$. This has been hypothesized by Lombard et al. to describe other ruthenium cobalt supramolecular donor-acceptor molecules that show small amounts of long-lived emission.[42] However, in the case of $[Ru\text{-}Co]^{8+}$, 60% of the emission signal amplitude occurs from the long-lived state (Table 4.1). This would correspond to 60% of the emitting states originating from second

or third excitations on the same $[Ru\text{-}Co]^{8+}$ complex; in other words, the $[Ru\text{-}Co]^{8+}$ sample would require a population inversion, where the majority of ruthenium centers are in the excited ^{3}MLCT state. Although this is not impossible, it is unlikely to occur in the TCSPC setup, where excitations are low such that at most a single emitted photon is detected after each excitation pulse (section 2.2.1).

There are numerous electronic configurations that are possible for cobalt in polypyridyl complexes, where Co(III) and Co(II) can exist as either high-spin or low-spin.[39,50] These different electronic states can undergo spin-relaxation processes upon excitation or electron-transfer, producing multiple excited state lifetimes. This has been observed for the polypyridyl bimetallic complex, $[(bpy)_2{}^1Ru(II)(tpphz)^1Co(III)(bpy)_2]^{5+}$ (tpphz = tetrapyrido[3,2-a:2’,3’-c:3’’,2’’-h:2’’’,3’’’-j]phenazine) which undergoes an oxidative electron transfer forming ^{2}Ru(III) and low-spin ^{2}Co(II), followed by spin-relaxation to high-spin ^{4}Co(II).[48] In this case, the process of spin-relaxation was complete on a time scale of 10 ps. Similar spin-relaxation mechanisms have been hypothesized to occur following the photochemical reduction of $[Co(phen)_3]^{3+}$ by oxalate;[70] although in this case, the lifetime of the low-spin intermediate is short enough to make the reaction indistinguishable from a mechanism directly populating the high-spin state. However, steady-state absorption of the $[Ru\text{-}Co]^{8+}$ complex indicated that the ground state of the cobalt center exists purely as high-spin ^{4}Co(II) (section 4.3.1). Upon oxidative quenching of the ruthenium complex, Co(I) would be formed, which does not have the complication of spin relaxation, as for d^8 complexes the high-spin and low-spin forms are equivalent. It is possible that energy transfer quenching producing $[Ru(II)\text{-}Co(II^*)]^{8+}$ could occur,

which would undergo spin-state relaxation. However, the Co(II*) excited state would display an emission band near 470 nm, which was not observed.

Perhaps the most likely explanation for the biphasic decay of the $[Ru\text{-}Co]^{8+}$ emission is a substantial back electron transfer process to the ruthenium centered ^{3}MLCT state. This mechanism stems from the fact that the reduction potentials for Co(II/I) and Ru(III/II*) in polypyridyl complexes are respectively around -0.9 and +0.9 V,[39] resulting in a charge-separated state that is isoenergetic with the ruthenium centered ^{3}MLCT state. To describe the forward and back electron-transfer processes, a three state model was constructed (Figure 4.8a) consisting of the ground state ($[Ru(II)\text{-}Co(II)]^{8+}$, *GS*), the ^{3}MLCT excited state ($[Ru(II^*)\text{-}Co(II)]^{8+}$, *ES*), and the charge-separated state ($[Ru(III)\text{-}Co(I)]^{8+}$, *CS*). These three states were linked via four kinetic parameters for electron-transfer to cobalt (k_{ET}), the back electron transfer (k_{BET}), and relaxation to the ground state from either the ruthenium localized excited state ($k_{r\text{-}Ru}$) or the charge-separated state ($k_{r\text{-}Co}$). These could be represented as a set of ordinary differential equations, shown in matrix form as:

$$\begin{pmatrix} \frac{dES(t)}{dt} \\ \frac{dCS(t)}{dt} \\ \frac{dGS(t)}{dt} \end{pmatrix} = \begin{pmatrix} -(k_{ET} + k_{r-Ru}) & k_{BET} & 0 \\ k_{ET} & -(k_{BET} + k_{r-Co}) & 0 \\ k_{r-Ru} & k_{r-Co} & 0 \end{pmatrix} \begin{pmatrix} ES(t) \\ CS(t) \\ GS(t) \end{pmatrix} \qquad (4.6a)$$

As 450 nm excitation is only absorbed by the ruthenium centers, the initial condition for the dynamic system consisted only of excited states in the $[Ru(II^*)\text{-}Co(II)]^{8+}$ state, represented as:

$$\begin{aligned} ES(0) &= 1 \\ CS(0) &= 0 \\ GS(0) &= 0 \end{aligned} \tag{4.6b}$$

Analytical solutions for the time dependent populations of each state could be solved using the eigenvalues (λ_i) and eigenvectors ($\mathbf{v}_i$) of the transition rate matrix:

$$\begin{pmatrix} ES(t) \\ CS(t) \\ GS(t) \end{pmatrix} = \sum_i c_i \exp(\lambda_i \cdot t)\mathbf{v}_i \tag{4.7}$$

Where c_i are constants determined by the initial conditions. The emission lifetime signal of [Ru-Co]$^{8+}$ was fit with the modeled *ES*(*t*) state convoluted with the IRF from the TCSPC, as the [Ru(II*)-Co(II)]$^{8+}$ appeared to be the only emitting state, while the *CS*(*t*) state was assumed to be dark.

Although four kinetic parameters (k_{ET}, k_{BET}, $k_{r\text{-}Ru}$, $k_{r\text{-}Co}$) are more than necessary to describe the biexponential emission signal, the relaxation rate from the ruthenium center can be assumed to be the same as for unbridged [Ru(bpy)$_2$(alk-phen)]$^{2+}$, as both the excited and ground state transitions are nearly identical, implying that the excited ^{3}MLCT state is perturbed only slightly by the formation of triazole. Sun et al.[31] also observed that the emission lifetime of [Ru(bpy)$_2$(alk-phen)]$^{2+}$ was the same after the formation of a triazole bridge, which supports this assumption. Simpler models with no relaxation from the charge-separated state ($k_{r\text{-}Co} = 0$) drastically increase the intrinsic emission rate of the ruthenium complexes ($k_{r\text{-}Ru} = 2.28 \times 10^6$ s^{-1}), making them physically unreasonable.

Fitting the emission decay of $[Ru\text{-}Co]^{8+}$ with the three state model (Figure 4.8b) resulted in a k_{ET} of $(2.4 \pm 0.4) \times 10^6$ s^{-1}, and k_{BET} of $(3.35 \pm 0.64) \times 10^6$ s^{-1}. These rates can be used to obtain a difference in energies (ΔG) from the relation:

$$\Delta G = -k_B T \cdot \ln\left(\frac{k_{ET}}{k_{BET}}\right) \tag{4.8}$$

which results in an energy difference of 9 ± 3 meV between $[Ru(II^*)\text{-}Co(II)]^{8+}$ and $[Ru(III)\text{-}Co(I)]^{8+}$, indicating the charge-separated state is slightly higher in energy. This disagrees with the intermolecular system (section 4.3.2), which was modeled to have a charge separated state that was around 100 meV lower in energy. Although it is possible that the redox potential between the metal states could change upon the formation of the triazole bridge, there are other possible phenomena that could impact the accuracy of this model. However, the overall observation is that electron transfer is both slow and less favorable in the intramolecular case when compared to the intermolecular charge transfer reaction.

4.3.4 Comparison of Intra- and Intermolecular Quenching

Intramolecular electron-transfer in $[Ru\text{-}Co]^{8+}$ was observed to be slow and less energetically favorable when compared to the intermolecular charge transfer process between the precursor complexes $[Ru(bpy)_2(phen)]^{2+}$ and $Co(N_3\text{-}phen)_3]^{2+}$. The reason for this reduction in charge transfer capability is likely the result of the formation of the triazole bridge linking the metal centers, rather than from changes in the redox potential of the individual metal centers. There are several characteristics of the bridge that have potential to detract from the electron-transfer process.

As observed in Chapter 3, localization of the excited ^{3}MLCT electron on phenanthroline requires slightly more energy than localizations on bipyridine (~200-300 cm^{-1}). The resulting population of excited ^{3}MLCT states on the ruthenium centers of [Ru-Co]$^{8+}$ would favor localization on peripheral bpy ligands, rather than on the bridging phen ligand. Although ILET would allow the localized state to transfer between the three ligands with ~22 ps timescales (section 3.4.6), at any given moment the population localized on phenanthroline would be less than expected for a homoleptic ruthenium complex. The decreased ^{3}MLCT population localized on phenanthroline would reduce the number of through-bond electron transfer processes across the bridge. This would not explain the slow reaction rate for electron-transfer, as ILET occurs much faster than the observed rates of electron-transfer, but it could be responsible for the low (40%) amplitude of the quenching process. Analogous reductions in photocatalytic efficiency have been observed for other donor-bridge-acceptor systems, when lowering the ^{3}MLCT energy of peripheral ligands on a metal photosensitizer complexes.[71,72] This effect would disappear in the intermolecular case, where all three ligands on $[Ru(bpy)_2(alk\text{-}phen)]^{2+}$ have the possibility to be quenched by the $[Co(N_3\text{-}phen)_3]^{2+}$ complex.

One possible cause of the slow electron transfer rate observed in [Ru-Co]$^{8+}$ is that the triazole bridge separates the ruthenium and cobalt centers, resulting in prohibitively long distances for electron transfer.[11] However, 1,2,3-triazole has been estimated to have an attenuation factor of about 2.8 nm^{-1},[36–38] making it similar to other π-conjugated bridge systems.[19] These conjugated systems typically display much faster electron transfer dynamics when compared to non-conjugated bridges. It is therefore surprising

that $[Ru\text{-}Co]^{8+}$ shows slower rates than a similar Ru(II)-Co(II) complex studied by Lombard et al.[42] which contained a bridge of a similar distance that was not fully conjugated. It is possible that the system observed by Lombard was able to undergo more reorientation, allowing the ruthenium and cobalt centers to come into contact. However, other studies with closely-linked Ru(II)-Co(II) metal centers show electron transfer rates are orders of magnitude faster,[73] indicating that the rates observed by Lombard et al. are likely for metal centers that are separated by the bridge. The unexpectedly slow rates of electron transfer observed for $[Ru\text{-}Co]^{8+}$ cannot be explained by metal center separation distance alone, as the rates would be in general much faster in the conjugated bridge than in a non-conjugated bridge system.

Although π-conjugation does enhance the rates of electron-transfer in many cases, the precise structure of the molecular bridge can sometimes inhibit the effects of conjugation. The simplest example of this is the calculated difference in electron transfer rate between cis- and trans-isomerizations of a double bond. In the case of azobenzene, the cis- isomer has been estimated to be several orders of magnitude less conductive than the trans- isomer,[74] although experimental measurement of this effect has proven difficult.[75] Significant decreases in transfer rates have also been calculated as a result of quantum interference from either cross-conjugation[76–78] or from multiple electronic transfer routes within conjugated ring structures.[76,79–82] As an experimental example, Arroyo et al. demonstrated that modifying the bond structure on a benzene ring from para- to meta-substitution, the conductance across the bridge decreased by an order of magnitude.[83] This disagrees with a simple tunneling mechanism, as bonds at the meta-

position of the benzene would make the bridge shorter than the para-substituted isomer, increasing the theoretical transfer rate.

In $[Ru\text{-}Co]^{8+}$, the triazole bridge connects each metal center via the 5-position of phenanthroline (Figure 4.1). It is possible that the selection of this bridging location results in a structurally slowed electron-transfer process, similar to those stated above. This concept is substantiated by DFT calculations on complexes of ruthenium with phenanthroline ligands. Zheng et al. observed that although the LUMO in $[Ru(phen)_3]^{2+}$ is localized on the phenanthroline ligand, the electron density of this orbital does not extend to the 5 or 6 positions, even with the addition of electron withdrawing or donating groups at these locations.[84] Bossert et al. confirmed this observation, as simulations of 448 nm excitation on $[Ru(phen)_2(bpy)]^{2+}$ resulted in an excited-state isosurface that displayed no density at the 5 or 6 positions on the phenanthroline ligands.[85] If the excited ^{3}MLCT state does not extend to the 5-position of the phenanthroline ligand, then it is possible that linking the triazole at this position produces an electronic disconnect, similar to a non-conjugated bridge, resulting in a slow rate of electron transfer.

The limited effect of extending conjugation at the 5-position of phenanthroline can be seen in emission spectra for modified $[Ru(bpy)_2(phen)]^{2+}$ complexes, appending phenylacetylene groups to the 3-, 4- and 5- positions on the phenanthroline ligand.[55] While substitution on the 3- and 4- positions red-shifted the emission of the complex, an indication of extended conjugation, substitution on the 5-position was identical to the unsubstituted phenanthroline ligand. Thus modifications at the 5- position prohibit conjugation to interact with the phenanthroline localized ^{3}MLCT state. The emission of

$[Ru\text{-}Co]^{8+}$ is also very similar compared to $[Ru(bpy)_2(alk\text{-}phen)]^{2+}$, indicating that interaction is small in this case as well. Were the triazole bridge to be linked at the 4-position of the phenanthroline ligand, faster rates of electron transfer would be expected, due to enhanced interaction between the conjugated bridge with the excited ^{3}MLCT state.

4.4 Conclusions

The donor-bridge-acceptor complex $[Ru\text{-}Co]^{8+}$ demonstrates electron transfer from a ruthenium photosensitizer to a covalently linked cobalt catalyst via a 1,2,3-triazole bridge. While this electron transfer process is able to proceed on a timescale of hundreds of nanoseconds, it is a relatively minor pathway compared to decay via phosphorescence of the ^{3}MLCT state of the ruthenium centers. This is attributable to either a significant back electron-transfer process or as a result of electron trapping on lower energy non-bridged ligands on the ruthenium centers. In either case, the lower electron-transfer efficiency observed would result in a lower overall efficiency of photocatalysis.

The observed electron transfer lifetime is also slower than expected when comparing $[Ru\text{-}Co]^{8+}$ to both other ruthenium-cobalt systems or to the intermolecular quenching rate of the precursor metal complexes. Although the triazole bridge is assumed to offer a fast electron transfer pathway by means of tunneling through π-conjugated bonds, it appears to be limited by the attachment position on the phenanthroline ligands, which display minimal electronic interaction between the ligands and the bridge. Changing the attachment position of the bridging triazole on the phenanthroline ligand may drastically increase the electron-transfer rates.

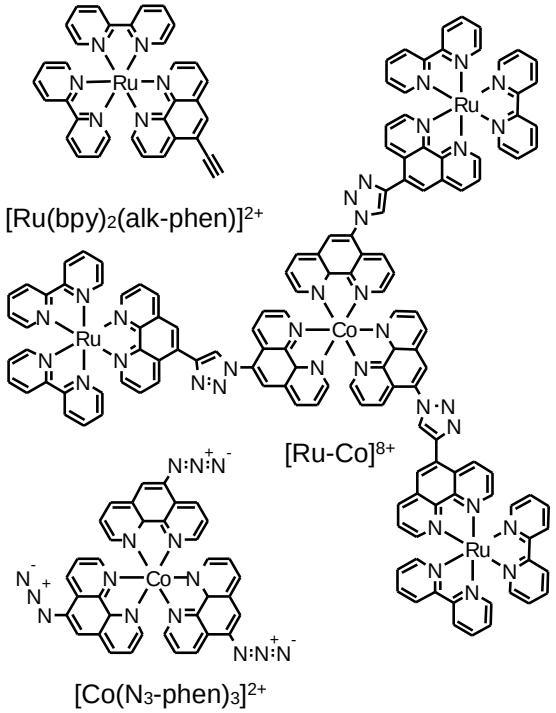

Figure 4.1. Structures of each molecule investigated.

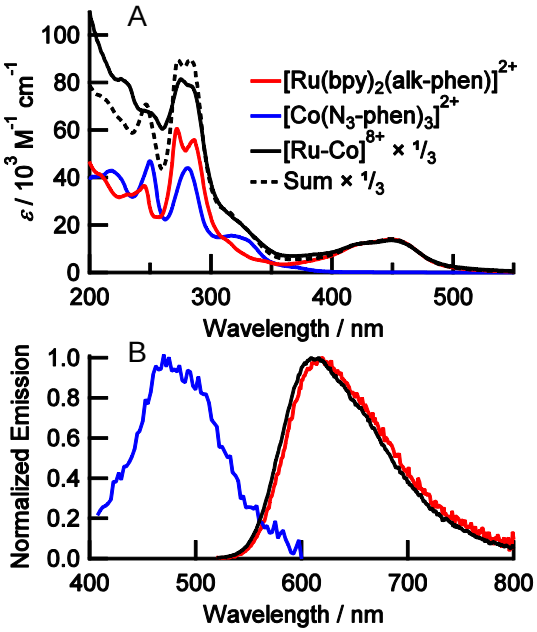

Figure 4.2. (A) Molar absorption coefficients (ε) for each complex (solid lines), as well as a sum of the precursor complexes approximating the $[Ru\text{-}Co]^{3+}$ complex. (B) Normalized emission for each complex.

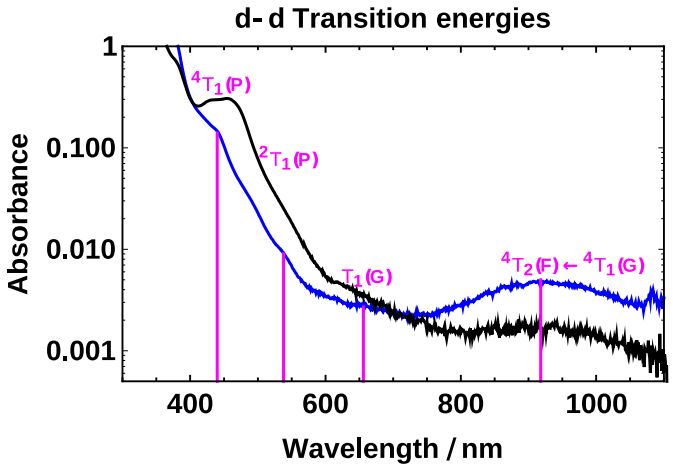

Figure 4.3. The near infrared absorption spectra for $[Co(N_3\text{-phen})_3]^{2+}$ (blue) and [Ru-Co]$^{2+}$ (black). The transitions used to predict the spin and charge state are shown in magenta, with their assigned transitions.

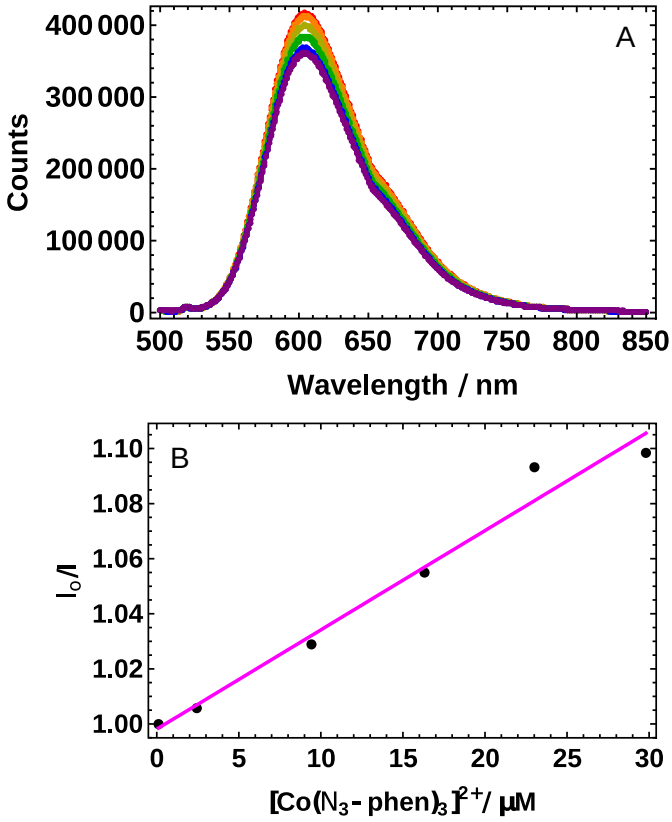

Figure 4.4. The intermolecular quenching constant (k_q), was determined by fitting the emission of uncorrected $[Ru(bpy)_2(alk\text{-}phen)]^{2+}$ decrease with the addition of small amounts of $[Co(N_3\text{-}phen)_3]^{2+}$. (A) The observed emission decreases. (B) The resulting Stern-Volmer plot.

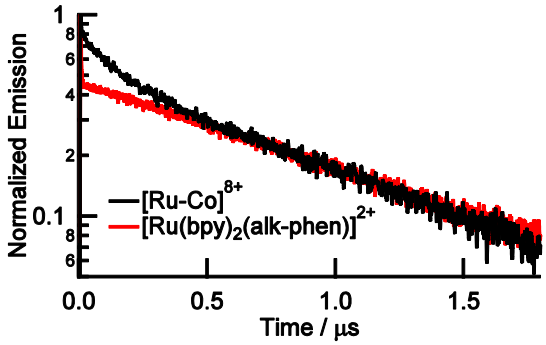

Figure 4.5. Normalized emission decays at 610 nm for $[Ru(bpy)_2(alk\text{-}phen)]^{2+}$ and $[Ru\text{-}Co]^{8+}$ in deaerated acetonitrile after excitation with a 450 nm pulse. Each decay was reconvoluted with a measured IRF signal (not shown).

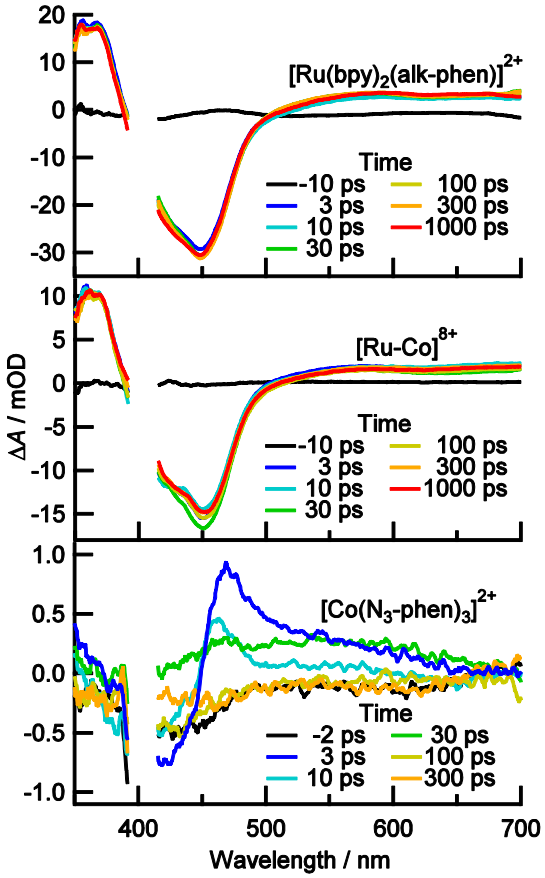

Figure 4.6 Time-resolved absorption difference spectra of each complex in acetonitrile after excitation with a 400 nm pump pulse.

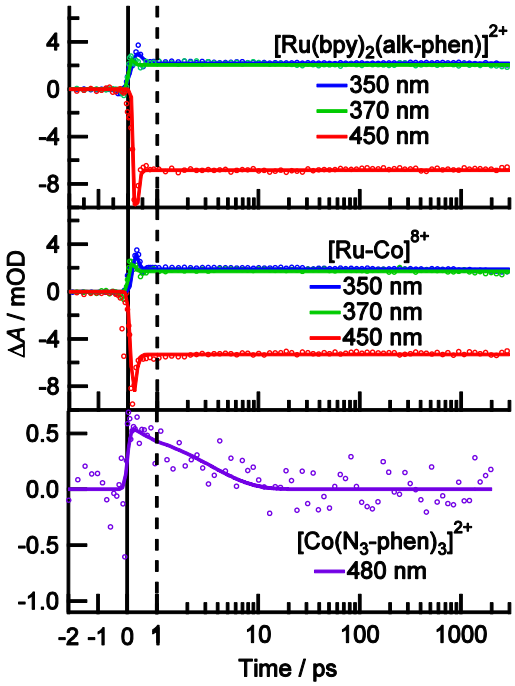

Figure 4.7 Transient absorption signals at the indicated wavelengths for each complex after excitation with a 400 nm pulse. The vertical dashed lines indicate a transition from a linear to logarithmic time axis.

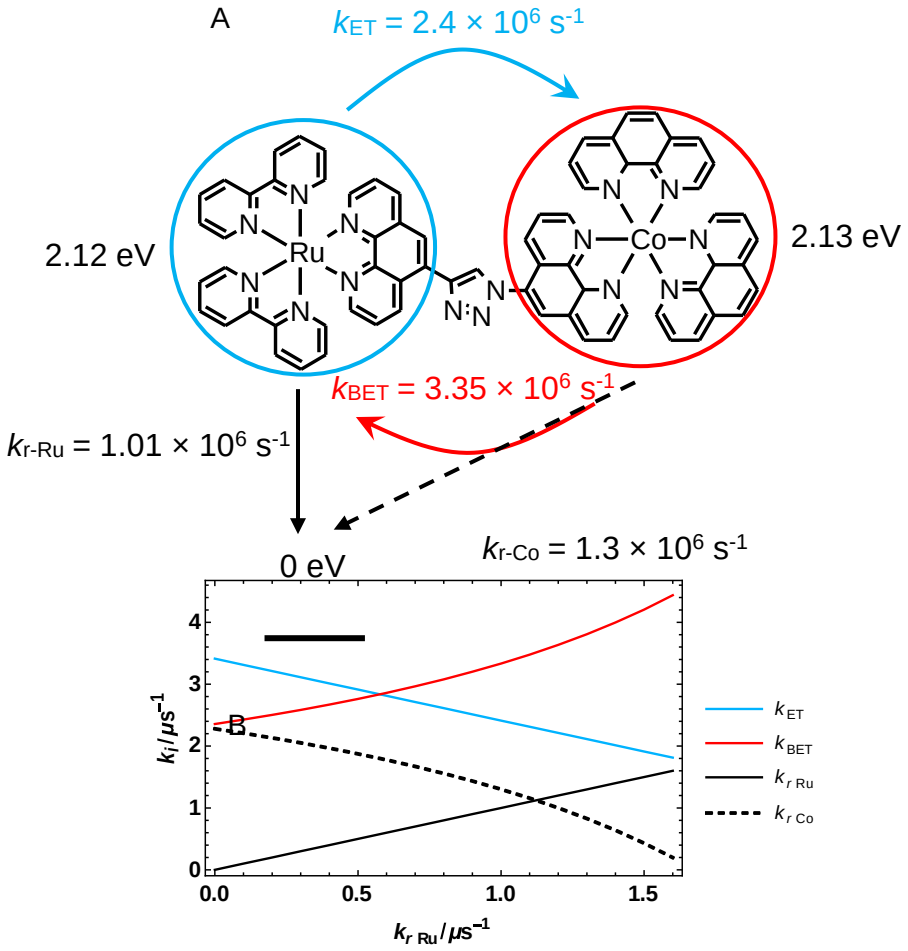

Figure 4.8. The two excited state model proposed to explain the emission lifetime data: (A) The model, fit using the assumption that the excited state on Ruthenium is the same as the unbridged $[Ru(bpy)_2(phen)]^{2+}$. (B) The effect that varying the intrinsic relaxation rate of the ruthenium center has on the other parameters.

Table 4.1. MLCT absorption and emission for the metal complexes.

Complex	$\lambda_{max,\ abs}$ (nm)	$\lambda_{max,\ em}$ (nm)	ε (M^{-1} cm^{-1})[a]	Φ_{em} [b]	τ_{em} (ns) [c]
$[Ru(bpy)_2(alk\text{-}phen)]^{2+}$	450	618	14000	0.064	990
$[Co(N_3\text{-}phen)_3]^{2+}$	317	470	15500	-	7
$[Ru\text{-}Co]^{8+}$	450	612	41000	0.049	890 (60%) 140 (40%)

[a]Measured at $\lambda_{max,\ abs}$. [b]Compared to $[Ru(bpy)_3]^{2+}$, Φ_{em} = 0.062. [c]Lifetimes observed at 455 nm for $[Co(N_3\text{-}phen)_3]^{2+}$, and at 610 nm for $[Ru(bpy)_2(alk\text{-}phen)]^{2+}$ and $[Ru\text{-}Co]^{8+}$, exciting at $\lambda_{max,\ abs}$.

■ REFERENCES

(1) Prier, C. K.; Rankic, D. A.; MacMillan, D. W. C. Visible Light Photoredox Catalysis with Transition Metal Complexes: Applications in Organic Synthesis. *Chem. Rev.* **2013**, *113*, 5322–5363.

(2) Lemmetyinen, H.; Tkachenko, N. V.; Efimov, A.; Niemi, M. Photoinduced Intra- and Intermolecular Electron Transfer in Solutions and in Solid Organized Molecular Assemblies. *Phys Chem Chem Phys* **2011**, *13*, 397–412.

(3) Fujitsuka, M.; Kim, S. S.; Lu, C.; Tojo, S.; Majima, T. Intermolecular and Intramolecular Electron Transfer Processes from Excited Naphthalene Diimide Radical Anions. *J. Phys. Chem. B* **2015**, *119*, 7275–7282.

(4) Gilbert, M.; Albinsson, B. Photoinduced Charge and Energy Transfer in Molecular Wires. *Chem. Soc. Rev.* **2015**, *44*, 845–862.

(5) Wenger, O. S. Long-Range Electron Transfer in Artificial Systems with d^6 and d^8 Metal Photosensitizers. *Coord. Chem. Rev.* **2009**, *253*, 1439–1457.

(6) Kuchi, V.; Oliver, A. M.; Paddon-Row, M. N.; Howe, R. F. Long-Lived Charge Separation in a Donor–acceptor Dyad Adsorbed in Mesoporous MCM-41. *Chem. Commun.* **1999**, 1149–1150.

(7) Bixon, M.; Jortner, J.; Verhoeven, J. Lifetimes for Radiative Charge Recombination in Donor-Acceptor Molecules. *J. Am. Chem. Soc.* **1994**, *116*, 7349–7355.

(8) Wiberg, J.; Guo, L.; Pettersson, K.; Nilsson, D.; Ljungdahl, T.; Martensson, J.; Albinsson, B. Charge Recombination versus Charge Separation in Donor-Bridge-Acceptor Systems. *J. Am. Chem. Soc.* **2007**, *129*, 155–163.

(9) Glover, S. D.; Goeltz, J. C.; Lear, B. J.; Kubiak, C. P. Inter- or Intramolecular Electron Transfer between Triruthenium Clusters: We'll Cross That Bridge When We Come to It. *Coord. Chem. Rev.* **2010**, *254*, 331–345.

(10) Herrero, C.; Quaranta, A.; Leibl, W.; Rutherford, A. W.; Aukauloo, A. Artificial Photosynthetic Systems. Using Light and Water to Provide Electrons and Protons for the Synthesis of a Fuel. *Energy Environ. Sci.* **2011**, *4*, 2353.

(11) Wenger, O. S. How Donor−Bridge−Acceptor Energetics Influence Electron Tunneling Dynamics and Their Distance Dependences. *Acc. Chem. Res.* **2011**, *44*, 25–35.

(12) Arrigo, A.; Santoro, A.; Indelli, M. T.; Natali, M.; Scandola, F.; Campagna, S. On the Effect of the Nature of the Bridge on Oxidative or Reductive Photoinduced Electron Transfer in Donor–bridge–acceptor Systems. *Phys Chem Chem Phys* **2014**, *16*, 818–826.

(13) Wielopolski, M. Molecule-Assisted Transport of Charges and Energy Across Donor–Wire–Acceptor Junctions. In *Testing Molecular Wires*; Springer Berlin Heidelberg: Berlin, Heidelberg, 2010; pp. 27–54.

(14) Weiss, E. A.; Wasielewski, M. R.; Ratner, M. A. Molecules as Wires: Molecule-Assisted Movement of Charge and Energy. In *Molecular Wires and Electronics*; Springer Berlin Heidelberg: Berlin, Heidelberg, 2005; Vol. 257, pp. 103–133.

(15) Salomon, A.; Cahen, D.; Lindsay, S.; Tomfohr, J.; Engelkes, V. B.; Frisbie, C. D. Comparison of Electronic Transport Measurements on Organic Molecules. *Adv. Mater.* **2003**, *15*, 1881–1890.

(16) Joachim, C.; Magoga, M. The Effective Mass of an Electron When Tunneling through a Molecular Wire. *Chem. Phys.* **2002**, *281*, 347–352.

(17) Hu, Y.; Zhu, Y.; Gao, H.; Guo, H. Conductance of an Ensemble of Molecular Wires: A Statistical Analysis. *Phys. Rev. Lett.* **2005**, *95*.

(18) Choi, S. H.; Risko, C.; Delgado, M. C. R.; Kim, B.; Brédas, J.-L.; Frisbie, C. D. Transition from Tunneling to Hopping Transport in Long, Conjugated Oligo-Imine Wires Connected to Metals. *J. Am. Chem. Soc.* **2010**, *132*, 4358–4368.

(19) Schubert, C.; Margraf, J. T.; Clark, T.; Guldi, D. M. Molecular Wires – Impact of π-Conjugation and Implementation of Molecular Bottlenecks. *Chem Soc Rev* **2015**, *44*, 988–998.

(20) Chiorboli, C.; Indelli, M. T.; Scandola, F. Photoinduced Electron/Energy Transfer Across Molecular Bridges in Binuclear Metal Complexes. In *Molecular Wires and Electronics*; Springer Berlin Heidelberg: Berlin, Heidelberg, 2005; Vol. 257, pp. 63–102.

(21) Zabarska, N.; Stumper, A.; Rau, S. CuAAC Click Reactions for the Design of Multifunctional Luminescent Ruthenium Complexes. *Dalton Trans.* **2016**, *45*, 2338–2351.

(22) Ladomenou, K.; Nikolaou, V.; Charalambidis, G.; Coutsolelos, A. G. "Click"-Reaction: An Alternative Tool for New Architectures of Porphyrin Based Derivatives. *Coord. Chem. Rev.* **2016**, *306*, 1–42.

(23) de Miguel, G.; Wielopolski, M.; Schuster, D. I.; Fazio, M. A.; Lee, O. P.; Haley, C. K.; Ortiz, A. L.; Echegoyen, L.; Clark, T.; Guldi, D. M. Triazole Bridges as Versatile Linkers in Electron Donor–Acceptor Conjugates. *J. Am. Chem. Soc.* **2011**, *133*, 13036–13054.

(24) Natali, M.; Ravaglia, M.; Scandola, F.; Boixel, J.; Pellegrin, Y.; Blart, E.; Odobel, F. Long-Range Charge Separation in a Ferrocene–(Zinc Porphyrin)–Naphthalenediimide Triad. Asymmetric Role of 1,2,3-Triazole Linkers. *J. Phys. Chem. C* **2013**, 130912075807001.

(25) Ganapathi, E.; Madhu, S.; Ravikanth, M. Synthesis and Properties of Triazole Bridged BODIPY-Conjugates. *Tetrahedron* **2014**, *70*, 664–671.

(26) Farràs, P.; Benniston, A. C. Bodipy-ruthenium(II) Tris-Bipyridyl Dyads for Homogeneous Photochemical Oxidations. *Tetrahedron Lett.* **2014**, *55*, 7011–7014.

(27) Guo, S.; Ma, L.; Zhao, J.; Küçüköz, B.; Karatay, A.; Hayvali, M.; Yaglioglu, H. G.; Elmali, A. BODIPY Triads Triplet Photosensitizers Enhanced with Intramolecular Resonance Energy Transfer (RET): Broadband Visible Light Absorption and Application in Photooxidation. *Chem. Sci.* **2013**, *5*, 489–500.

(28) Benson, M. C.; Ruther, R. E.; Gerken, J. B.; Rigsby, M. L.; Bishop, L. M.; Tan, Y.; Stahl, S. S.; Hamers, R. J. Modular "Click" Chemistry for Electrochemically and Photoelectrochemically Active Molecular Interfaces to Tin Oxide Surfaces. *Acs Appl. Mater. Interfaces* **2011**, *3*, 3110–3119.

(29) Baron, A.; Herrero, C.; Quaranta, A.; Charlot, M.-F.; Leibl, W.; Vauzeilles, B.; Aukauloo, A. Efficient Electron Transfer through a Triazole Link in Ruthenium(II) Polypyridine Type Complexes. *Chem. Commun.* **2011**, *47*, 11011.

(30) Baron, A.; Herrero, C.; Quaranta, A.; Charlot, M.-F.; Leibl, W.; Vauzeilles, B.; Aukauloo, A. Click Chemistry on a Ruthenium Polypyridine Complex. An Efficient and Versatile Synthetic Route for the Synthesis of Photoactive Modular Assemblies. *Inorg. Chem.* **2012**, *51*, 5985–5987.

(31) Sun, Y.; Chen, Z.; Puodziukynaite, E.; Jenkins, D. M.; Reynolds, J. R.; Schanze, K. S. Light Harvesting Arrays of Polypyridine Ruthenium(II) Chromophores Prepared by Reversible Addition–Fragmentation Chain Transfer Polymerization. *Macromolecules* **2012**, *45*, 2632–2642.

(32) Sheth, S.; Baron, A.; Herrero, C.; Vauzeilles, B.; Aukauloo, A.; Leibl, W. Light-Induced Tryptophan Radical Generation in a Click Modular Assembly of a Sensitiser-Tryptophan Residue. *Photochem. Photobiol. Sci.* **2013**, *12*, 1074.

(33) Herrero, C.; Batchelor, L.; Baron, A.; El Ghachtouli, S.; Sheth, S.; Guillot, R.; Vauzeilles, B.; Sircoglou, M.; Mallah, T.; Leibl, W.; *et al.* Click Chemistry as a Convenient Tool for the Incorporation of a Ruthenium Chromophore and a Nickel-Salen Monomer into a Visible-Light-Active Assembly. *Eur. J. Inorg. Chem.* **2013**, 494–499.

(34) Herrero, C.; Quaranta, A.; El Ghachtouli, S.; Vauzeilles, B.; Leibl, W.; Aukauloo, A. Carbon Dioxide Reduction via Light Activation of a ruthenium–Ni(cyclam) Complex. *Phys. Chem. Chem. Phys.* **2014**, *16*, 12067.

(35) Fang, Z.; Ito, A.; Luo, H.; Ashford, D. L.; Concepcion, J. J.; Alibabaei, L.; Meye, T. J. Polypyridyl Ru(II)-Derivatized Polypropylacrylate Polymer with a Terminal Water Oxidation Catalyst. Application of Reversible Addition-Fragmentation Chain Transfer Polymerization. *Dalton Trans.* **2015**, *44*, 8640–8648.

(36) Sayed, S. Y.; Bayat, A.; Kondratenko, M.; Leroux, Y.; Hapiot, P.; McCreery, R. L. Bilayer Molecular Electronics: All-Carbon Electronic Junctions Containing Molecular Bilayers Made with "Click" Chemistry. *J. Am. Chem. Soc.* **2013**, *135*, 12972–12975.

(37) Kondratenko, M.; Stoyanov, S. R.; Gusarov, S.; Kovalenko, A.; McCreery, R. L. Theoretical Modeling of Tunneling Barriers in Carbon-Based Molecular Electronic Junctions. *J. Phys. Chem. C* **2015**, *119*, 11286–11295.

(38) Devaraj, N. K.; Decreau, R. A.; Ebina, W.; Collman, J. P.; Chidsey, C. E. D. Rate of Interfacial Electron Transfer through the 1,2,3-Triazole Linkage. *J. Phys. Chem. B* **2006**, *110*, 15955–15962.

(39) Creutz, C.; Sutin, N. Photogeneration and Reactions of Cobalt(I) Complexes. *Coord. Chem. Rev.* **1985**, *64*, 321–341.

(40) Creutz, C.; Sutin, N. Electron-Transfer Reactions of Excited States. Reductive Quenching of the tris(2,2'-bipyridine)ruthenium(II) Luminescence. *Inorg. Chem.* **1976**, *15*, 496–499.

(41) Kirch, M.; Lehn, J.-M.; Sauvage, J.-P. Hydrogen Generation by Visible Light Irradiation of Aqueous Solutions of Metal Complexes. An Approach to the Photochemical Conversion and Storage of Solar Energy. *Helv. Chim. Acta* **1979**, *62*, 1345–1384.

(42) Lombard, J.; Boulaouche, R.; Amilan Jose, D.; Chauvin, J.; Collomb, M.-N.; Deronzier, A. Synthesis and Properties of Trinuclear Polypyridyl Complexes Ru(II)–Co(II)–Ru(II) and Ru(II)–Co(III)–Ru(II): Their Photoinduced Interconversion. *Inorganica Chim. Acta* **2010**, *363*, 234–242.

(43) Fihri, A.; Artero, V.; Razavet, M.; Baffert, C.; Leibl, W.; Fontecave, M. Cobaloxime-Based Photocatalytic Devices for Hydrogen Production. *Angew. Chem. Int. Ed.* **2008**, *47*, 564–567.

(44) Horvath, R.; Lombard, J.; Leprêtre, J.-C.; Collomb, M.-N.; Deronzier, A.; Chauvin, J.; Gordon, K. C. Excited-State Spectroscopic Investigations of Multinuclear Complexes Based on $[Ru(bpy)_3]^{2+}$ Moieties Connected to 2,2′-Bipyridine and 2,2′;6′,2″-Terpyridine Ligands. *Dalton Trans.* **2013**, *42*, 16527.

(45) Mukherjee, A.; Kokhan, O.; Huang, J.; Niklas, J.; Chen, L. X.; Tiede, D. M.; Mulfort, K. L. Detection of a Charge-Separated Catalyst Precursor State in a Linked Photosensitizer-Catalyst Assembly. *Phys. Chem. Chem. Phys.* **2013**, *15*, 21070.

(46) Li, C.; Wang, M.; Pan, J.; Zhang, P.; Zhang, R.; Sun, L. Photochemical Hydrogen Production Catalyzed by Polypyridyl Ruthenium–cobaloxime Heterobinuclear Complexes with Different Bridges. *J. Organomet. Chem.* **2009**, *694*, 2814–2819.

(47) Song, X.; Lei, Y.; Vanwallendal, S.; Perkovic, M.; Jackman, D.; Endicott, J.; Rillema, D. Photoinduced Electron-Transfer Processes Involving Covalently Linked Ruthenium and Cobalt Polypyridyl Complexes - Comparison of Electronic Coupling in Bridged and Nonbridged Ruthenium and Cobalt Complexes. *J. Phys. Chem.* **1993**, *97*, 3225–3236.

(48) Canton, S. E.; Kjær, K. S.; Vankó, G.; van Driel, T. B.; Adachi, S.; Bordage, A.; Bressler, C.; Chabera, P.; Christensen, M.; Dohn, A. O.; *et al.* Visualizing the Non-Equilibrium Dynamics of Photoinduced Intramolecular Electron Transfer with Femtosecond X-Ray Pulses. *Nat. Commun.* **2015**, *6*, 6359.

(49) Palmer, R.; Piper, T. 2,2’-Bipyridine Complexes .i. Polarized Crystal Spectra of Tris(2,2’-Bipyridine)copper(II) -Nickel(II) -Cobalt(II) -Iron(II) and -Ruthenium(II). *Inorg. Chem.* **1966**, *5*, 864-.

(50) Kremer, S.; Henke, W.; Reinen, D. High-Spin-Low-Spin Equilibriums of cobalt(II) in the Terpyridine Complexes $Co(terpy)_2X_2 \cdot nH_2O$. *Inorg. Chem.* **1982**, *21*, 3013–3022.

(51) Yamasaki, K.; Hara, T.; Yasuda, M. Absorption Spectra of Cobalt Complexes with 1,10-Phenanthroline. *Proc. Jpn. Acad.* **1953**, *29*, 337–341.

(52) Fabian, R. H.; Klassen, D. M.; Sonntag, R. W. Synthesis and Spectroscopic Characterization of Ruthenium and Osmium Complexes with Sterically Hindering Ligands. 3. Tris Complexes with Methyl-and Dimethyl-Substituted 2,2’-bipyridine and 1,10-Phenanthroline. *Inorg. Chem.* **1980**, *19*, 1977–1982.

(53) Ruminski, R.; Petersen, J. Tris(2,2'-Bipyrimidine)cobalt(III,II,I) - a Cobalt Polyazine Electrochemical System with Large Storage Capabilities. *Inorganica Chim. Acta-Artic. Lett.* **1984**, *88*, 63–66.

(54) Juris, A.; Barigelletti, F.; Balzani, V.; Belser, P.; Von Zelewsky, A. Luminescence of Ruthenium(II) Tris Chelate Complexes Containing the Ligands 2,2'-bipyridine and 2,2'-biisoquinoline. Behavior of the $Ru(bpy)^{2+}$ and $Ru(Bpy)_2^{2+}$ Emitting Units. *Inorg. Chem.* **1985**, *24*, 202–206.

(55) Glazer, E. C.; Magde, D.; Tor, Y. Ruthenium Complexes That Break the Rules: Structural Features Controlling Dual Emission. *J. Am. Chem. Soc.* **2007**, *129*, 8544–8551.

(56) Schofield, K.; Grimmett, M. R.; Keene, B. R. T. *Heteroaromatic Nitrogen Compounds: The Azoles*; CUP Archive, 1976.

(57) Gajardo, F.; Loeb, B. Spectroscopic and Electrochemical Properties of a Series of Substituted Polypyridine Co(II)/Co(III) Couples and Their Potentiality as Mediators for Solar Cells. *J. Chil. Chem. Soc.* **2011**, *56*, 697–701.

(58) Krist, K.; Gafney, H. An Analysis of the Mechanistic Pathways in the Reversible Photoinduced Reactions Between $Ru(bpy)_3^{2+}$ and $Co(phen)_3^{3+}$ by Flash-Photolysis Techniques. *J. Phys. Chem.* **1982**, *86*, 951–958.

(59) Steinfeld, J. I.; Francisco, J. S.; Hase, W. L. *Chemical Kinetics and Dynamics*; 2 edition.; Pearson: Upper Saddle River, N.J, 1998.

(60) Smallwood, I. M. *Handbook of Organic Solvent Properties*; Arnold ; Halsted Press: London : New York, 1996.

(61) Einstein, A. A new determination of the molecular dimensions. *Ann. Phys.* **1906**, *19*, 289–306.

(62) Masuda, Y.; Yamatera, H. Rotational Motions of the Tris (1,10-Phenanthroline) and Tris (2,2'-bipyridine) Complexes of Ruthenium(II) and Cobalt(III) Ions in Solution. *J. Phys. Chem.* **1984**, *88*, 3425–3431.

(63) Harrowfield, J.; Sobolev, A. The Crystal-Structure of Tris(2,2'-Bipyridine)ruthenium(ii) Perchlorate. *Aust. J. Chem.* **1994**, *47*, 763–767.

(64) Váhovská, L.; Potoèòák, I. Crystal Structures of Fe(II) and Co(II) Complexes with N-Donor Bidentate Ligands. *Mater. Struct. Chem. Biol. Phys. Technol.* **2012**, *19*, 102–104.

(65) Deponti, E.; Luisa, A.; Natali, M.; Iengo, E.; Scandola, F. Photoinduced Hydrogen Evolution by a Pentapyridine Cobalt Complex: Elucidating Some Mechanistic Aspects. *Dalton Trans* **2014**, *43*, 16345–16353.

(66) Krishnan, C. V.; Brunschwig, B. S.; Creutz, C.; Sutin, N. Homogeneous Catalysis of the Photoreduction of Water. 6. Mediation by Polypyridine Complexes of ruthenium(II) and cobalt(II) in Alkaline Media. *J. Am. Chem. Soc.* **1985**, *107*, 2005–2015.

(67) Szalda, D. J.; Creutz, C.; Mahajan, D.; Sutin, N. Electron-Transfer Barriers and Metal-Ligand Bonding as a Function of Metal Oxidation State. 2. Crystal and Molecular Structures of tris(2,2'-bipyridine)cobalt(II) Dichloride-2-Water-Ethanol and tris(2,2'-bipyridine)cobalt(I) Chloride-Water. *Inorg. Chem.* **1983**, *22*, 2372–2379.

(68) Nozaki, K.; Yoshimura, A.; Ohno, T. Photoinduced ET and Back-ET in Bimetallated Compounds of Ru(II)-Rh(III) and Ru(II)-Co(III). *J. Chem. Sci.* **1993**, *105*, 495–503.

(69) Palmer, M. H.; Hoffmann, S. V.; Jones, N. C.; Head, A. R.; Lichtenberger, D. L. The Electronic States of 1,2,3-Triazole Studied by Vacuum Ultraviolet Photoabsorption and Ultraviolet Photoelectron Spectroscopy, and a Comparison with Ab Initio Configuration Interaction Methods. *J. Chem. Phys.* **2011**, *134*, 84309.

(70) Vuik, C. P. J.; Kane-Maguire, N. A. P.; Langford, C. H. Ligand Field Photochemistry of Cobalt(III) Phenanthroline and Bipyridyl Complexes. *Can. J. Chem.* **1975**, *53*, 3121–3127.

(71) Rau, S.; Walther, D.; Vos, J. G. Inspired by Nature: Light Driven Organometallic Catalysis by Heterooligonuclear Ru(II) Complexes. *Dalton Trans.* **2007**, 915.

(72) Schulz, M.; Karnahl, M.; Schwalbe, M.; Vos, J. G. The Role of the Bridging Ligand in Photocatalytic Supramolecular Assemblies for the Reduction of Protons and Carbon Dioxide. *Coord. Chem. Rev.* **2012**, *256*, 1682–1705.

(73) López, A. M.; Natali, M.; Pizzolato, E.; Chiorboli, C.; Bonchio, M.; Sartorel, A.; Scandola, F. A Co(II)–Ru(II) Dyad Relevant to Light-Driven Water Oxidation Catalysis. *Phys. Chem. Chem. Phys.* **2014**, *16*, 12000–12007.

(74) Zhang, C.; Du, M.-H.; Cheng, H.-P.; Zhang, X.-G.; Roitberg, A. E.; Krause, J. L. Coherent Electron Transport through an Azobenzene Molecule: A Light-Driven Molecular Switch. *Phys. Rev. Lett.* **2004**, *92*.

(75) Wang, Y.; Cheng, H.-P. Electronic and Transport Properties of Azobenzene Monolayer Junctions as Molecular Switches. *Phys. Rev. B* **2012**, *86*.

(76) Guédon, C. M.; Valkenier, H.; Markussen, T.; Thygesen, K. S.; Hummelen, J. C.; van der Molen, S. J. Observation of Quantum Interference in Molecular Charge Transport. *Nat. Nanotechnol.* **2012**, *7*, 305–309.

(77) Solomon, G. C.; Andrews, D. Q.; Hansen, T.; Goldsmith, R. H.; Wasielewski, M. R.; Van Duyne, R. P.; Ratner, M. A. Understanding Quantum Interference in Coherent Molecular Conduction. *J. Chem. Phys.* **2008**, *129*, 54701.

(78) Phelan, N. F.; Orchin, M. Cross Conjugation. *J Chem Educ* **1968**, *45*, 633.

(79) Maiti, S. K. Molecular Wires: Tuning of Electron Transport. *Solid State Commun.* **2008**, *145*, 126–131.

(80) Walczak, K. The Role of Quantum Interference in Determining Transport Properties of Molecular Bridges. *Open Chem.* **2004**, *2*.

(81) Ma, X.; Yan, L.; Wang, X.; Guo, Q.; Xia, A. Spectral and Intramolecular Charge Transfer Properties in Terminal Donor/acceptor-Substituted All-Trans-A,ω-Diphenylpolyenes and A,ω-Diphenylpolyynes. *Phys. Chem. Chem. Phys.* **2011**, *13*, 17273.

(82) Walter, D.; Neuhauser, D.; Baer, R. Quantum Interference in Polycyclic Hydrocarbon Molecular Wires. *Chem. Phys.* **2004**, *299*, 139–145.

(83) Arroyo, C. R.; Frisenda, R.; Moth-Poulsen, K.; Seldenthuis, J. S.; Bjørnholm, T.; van der Zant, H. S. Quantum Interference Effects at Room Temperature in OPV-Based Single-Molecule Junctions. *Nanoscale Res. Lett.* **2013**, *8*, 1.

(84) Zheng, K. C.; Wang, J. P.; Liu, X. W.; Shen, Y.; Yun, F. C. Studies of Substituent Effects on the Electronic Structure and Related Properties of $[Ru(phen)_3]^{2+}$ with DFT Method. *J. Mol. Struct. THEOCHEM* **2002**, *577*, 95–105.

(85) Bossert, J.; Daniel, C. Electronic Absorption Spectroscopy of $[Ru(phen)_2(bpy)]^{2+}$, $[Ru(phen)_2(dmbp)]^{2+}$, $[Ru(tpy)(phen)(CH_3CN)]^{2+}$ and $[Ru(tpy)(dmp)(CH_3CN)]^{2+}$ A Theoretical Study. *Coord. Chem. Rev.* **2008**, *252*, 2493–2503.

CHAPTER 5

CERIUM OXIDE NANOPARTICLES: STABILIZATION AND PHOTOPHYSICAL PROPERTIES

5.1 Introduction

Cerium(IV) Oxide (CeO_2) is a rare earth metal oxide that is used as a catalyst or as a non-inert support for other catalytic reactions.[1] Its most common application is in three-way catalysts where it acts as a repository for O_2, as it can stably lose or regain oxygen in the lattice structure, forming CeO_{2-x}, due to the ability of cerium to readily convert between Ce^{3+} and Ce^{4+}. This process, called oxygen storage capacity (OSC), has been found to be completely reversible, and has made CeO_2 an intriguing potential catalyst for repeatable redox processes. Perhaps most impressively, it has been shown to be able to thermochemically catalyze water splitting, forming H_2 and O_2 gas.[2]

In recent years, CeO_2 has gained some attention as a potential photocatalyst for the production of O_2,[3,4] or the degradation of waste water compounds[5–7], similar to TiO_2. Although the activity of oxygen production in CeO_2 is less when compared to TiO_2 when irradiated by UV-light, bulk CeO_2 has a significantly smaller band gap energy, which allows it to be activated by visible light.[6,8]

CeO_2 can be described as a direct band gap semiconductor with a valence band composed of O 2p orbitals, and a conduction band created from Ce5d orbitals with a band gap of > 6 eV.[9–11] There is a second band made of Ce4f orbitals located 2.8 eV above the valence band, which has been described as either a set of localized states,[11–14] or a

delocalized conduction band.[15–18] The discrepancy in the description of this band primarily stems from contributions of Ce^{3+} present in CeO_2, where Ce4f states can be treated like conduction bands in pure CeO_2, but localized states form when Ce^{3+} or defects are present.[9] Tuller et al. showed that electron transfer between Ce^{3+} and Ce^{4+} can occur in CeO_{2-x} crystallites when $x > 0.01$,[19,20] indicating that the localized description makes more sense for crystals with significant amounts of Ce^{3+}. This electron hopping process has a thermal activation barrier of 0.4 eV, which increases to 0.5 eV in $CeO_{1.75}$. A study by Griffiths et al.[21] confirmed this transition energy, as reducing powdered CeO_2 with H_2 gas resulted in the formation of an absorption band centered around 1.847 eV. This transition corresponds to a photo-initiated electron transfer, which according to Marcus theory is four times the thermal energy barrier, given that the initial and final states are isoenergetic. This charge transfer "hopping" process has since been described by several computational studies to be a localized 4f electron.[22,23]

The energy of the Ce4f band in bulk pure CeO_2 is 2.8 eV above the O2p band.[24–26] However, the majority of research has been devoted to CeO_2 nanoparticles, for which confinement effects and Ce^{3+} sites can increase the observed band gap energy, blue shifting absorbance. In general, nanoparticle size and surface functionalities offer the ability to tune photochemical and redox properties, although these properties depend strongly on the precise synthetic method used to prepare them.[27–29] As a result, the proposed uses of CeO_2 nanoparticles sometimes appear to contradict each other.[30]

Irradiation of CeO_2 with visible or UV light results in the creation of an electron in the Ce4f conduction band and a corresponding hole in the O2p valence band (Figure

5.1). The electron (e^-) has been observed to reduce O_2 adsorbed on the surface of the nanoparticle, producing superoxide ($O_2^{\cdot -}$)[6,18,31,32] and can also break apart H_2O_2 into OH^- and $OH^{\cdot}$.[5] The hole (h^+) formed during excitation is much more reactive and has been estimated to have a reduction potential of +2.5 to +2.7 V vs NHE.[18,32,33] It has been observed to form $OH^{\cdot}$,[27,31,32] as well as directly degrade organic molecules such as methylene blue[5,32] or toluene.[31] Irradiating CeO_2 also has been shown to produce O_2 gas, which has been ascribed to holes splitting water at the surface[3,34,35]; however, with oxygen storage capacity as one of the primary uses of CeO_2, it is quite possible that the oxygen produced during excitation may originate from the lattice of the CeO_2 nanoparticle itself. Although the direct removal of ½ O_2 from O^{2-} lattice sites in CeO_2 experimentally requires 3.9-4.7 eV,[36] computational studies by Skorodumova et al.[37] have indicated that this energy is lowered to 0.26 eV in the presence of nearby Ce^{3+} sites in the lattice, while other computational studies have indicated that nanoparticle defects can also lower this energy substantially.[9]

Although the above photochemical reactions at the surface have been observed previously, the photophysical behavior of holes and electrons in excited CeO_2 nanoparticles remain uncertain. In particular, electron-hole recombination processes have remained largely unknown, although this reaction is assumed to limit the catalytic ability of the nanoparticles in several cases.[5,34] In this study, we observe this recombination process in commercial CeO_2 nanoparticles from Sigma Aldrich and STREM Chemicals Inc., which have listed diameters of < 25 nm and 8 nm, respectively. The formation and decay of trapped holes was observed using transient absorption spectroscopy, as well as

long term photochemical changes in nanoparticles using a photoreactor. A large portion of the research was also devoted to characterizing the colloidal stability of the commercial nanoparticles, in order to create solutions concentrated enough to analyze with transient absorption, as well as compare to other studies.

5.2 Results

5.2.1 Colloidal Stability of Nanoparticles

Both Sigma Aldrich and STREM nanoparticles, prepared using procedures outlined in Chapter 2.4.5 were observed to be stable in basic conditions, with no observable pH or visible absorption changes in solutions kept at pH > 10, and having only very minor decreases in absorption over several weeks at pH's from 8-9. At pH < 7.4, the nanoparticles rapidly agglomerated, forming a large powdery white precipitate, leaving no nanoparticles in the supernatant after 3 days, determined from visible absorption. The agglomeration process was observed using changes in UV-visible absorption spectra, where a peak at ~300 nm decreased as the nanoparticles settled, while also undergoing a slight red shift (Figure 5.2). Exploratory analysis via a two-level fractional factorial design experiment (method 2_V^{5-1})[38] investigated the rate of agglomeration for nanoparticles with respect to nanoparticle concentration, pH, ionic strength (using [NaCl]), sonication, and aging. Although ionic strength had no observable effect on the agglomeration rate, all other parameters demonstrated effects, which are discussed below.

The rate of agglomeration was observed to be biphasic (Figure 5.2, inset), with a fast reaction occurring over minutes, followed by a slower reaction that took several hours to days, depending on conditions. Both processes were observed by the disappearance of the colloidal CeO_2 peak at ~300 nm, which could be fit with a linear decay. This would imply a zero-order kinetic process for the overall reaction; however, the formation of agglomerates in solution increases the scattering of a sample, which in turn would increase the perceived absorption at 300 nm, making assignments of agglomeration kinetics based on this fitting alone inaccurate. Changing the mass of CeO_2 added to solutions was observed to proportionally increase the agglomeration rate, indicating agglomeration had a reaction order of 0.95 ± 0.06 with respect to the initial concentration of CeO_2.

Changing the pH of solutions had no observed effect on the kinetics of the fast reaction, however it did affect the rate of agglomeration in the second slower process, doing so in a very nonlinear fashion. In all cases the agglomeration rate increased with decreasing pH, which disagrees with some reports that indicate nanoparticles display enhanced stability at low pH.[29,34] The reaction order for this second agglomeration process with respect to $[H^+]$, calculated from pH measurements, was found to be 0.4 ± 0.9. The large variation in $[H^+]$ dependence was able to be described as a result of sonicating the solution (Figure 5.3), where samples that were sonicated for 10 minutes demonstrated a dependence of the agglomeration rate on $[H^+]$, while those that were not sonicated showed much weaker dependence. Specifically, solutions that were sonicated had reaction orders with respect to $[H^+]$ of 1.1 ± 0.4, while solutions that were not

sonicated had reaction orders of 0.2 ± 0.4. Thus solutions that were not sonicated agglomerated at rates weakly dependent of pH, while sonicated solutions agglomerated significantly more quickly at low pH conditions then they did at higher pH conditions.

As the experimental design determining the interaction between sonication and pH was a 5-1 fractional factorial design, this negative two-factor interaction could equivalently or partially be described as a positive three-factor interaction between the age, ionic strength, and concentration of nanoparticles in solution.[38] That is, the rate of the agglomeration reaction may become faster if the solution age and the concentrations of [CeO_2] and [NaCl] are all increased. While increasing the concentration of CeO_2 did show an increase in reaction rate, aging the solution had the effect of generally slowing down the reaction rate, and there was not a significant interaction observed between aging and initial concentration (i.e. Aged solutions displayed decreases in the rate of agglomeration that were proportional to the initial rate for both high and low CeO_2 concentrations). Ionic strength did not show any interactions with other variables, and had no observed effect on the reaction rate by itself. It is unlikely to observe a three-factor interaction process when neither one- nor two-factor effects are observable. Thus the interaction between pH and sonication is likely the only strong interaction between parameters out of the ones analyzed, while this three-factor interaction is negligible.

Short (≤ 30 minute) applications of sonication were found to reverse the process of agglomeration and increase the absorption peak at 300 nm (Figure 5.4), as well as decrease the pH of solutions by 0.2, compared to unsonicated samples. Surprisingly, extending the time of sonication reversed this process, showing decreases in the 300 nm

peak and increasing the rate of agglomeration. However, it is important to note that prolonged use of the sonicator caused the sample to heat by roughly 10 ºC. This heat may be the cause of agglomeration in the nanoparticle solution, as previous studies have shown that increasing the temperature of a solution will stimulate agglomeration processes.[39–41]

The pH of solutions in which agglomeration occurred increased over time, although at very low pH this was difficult to observe as the liquid junction potential for pH probes changes due to high concentrations of H^+ ions present in solution.[42] STREM nanoparticles displayed slightly faster agglomeration kinetics than Sigma Aldrich, which could be an indication that nanoparticle size is important in the agglomeration process. However, both types of nanoparticles demonstrated stability in similar pH ranges, indicating that the chemical reactions involved in agglomeration are likely the same for the two samples of nanoparticles.

Many sources in literature[29,34] suggest that CeO_2 nanoparticles near neutral pH conditions are unstable, but can be stabilized at pH ~1, particularly for nanoparticles originating from $Ce(NO_3)_3$ precursors. Adding nitrate to a solution of nanoparticles has also been observed to aid in the dispersal of nanoparticles at low pH.[43] However, colloidal solutions of the commercial nanoparticles used here were unstable at pH 1, even with the addition of nitrate. After filtering solutions with 200 nm pore size filters, there was no difference between nanoparticle solutions and solutions containing only nitric acid (Figure 5.5), indicating that all nanoparticles in these solutions had formed agglomerates greater than 200 nm in size. Nitrate has an absorption maximum at 300

nm,[44] which is very similar in shape to nanoceria, and may be mistaken in some cases. However, Nabavi et al.[29] also demonstrated that the preparation methods used to make CeO_2 nanoparticles greatly affect the ability of nitrate to bind to the surface. They showed that nanoparticles synthesized with $Ce(NO_3)_3$ precursors contained nitrate on every surface cerium atom, although titrating the nanoparticles with a base removed the surface nitrates; above pH 11, an irreversible reaction occurred, eliminating nitrate binding sites. They attribute this to a rearrangement of bidentate binding sites on the surface into tridentate sites. However, the bond valence model which they use to describe this process contained only Ce^{4+} atoms on the surface, while it has been shown that the surface of CeO_2 nanoparticles may contain significant Ce^{3+} sites.[45,46] These reduced sites could perhaps alter nitrate binding, however such phenomena would require investigation.

5.2.2 pH Titration

Titrating solutions of Sigma Aldrich and STREM nanoparticles further elucidated the dependence of agglomeration processes on pH. Basic solutions containing nanoparticles were found to slowly decrease in pH when titrated with 1 M perchloric acid, reaching a buffer-like region over the pH range of 7.4-6.8, as seen in Figure 5.6. At the endpoint of this buffer region agglomerates were observed to form rapidly, which raised the pH of the solution. After this agglomeration process appeared to be completed, indicated by achieving a constant pH of 7.6, continued additions of perchloric acid rapidly decreased the pH. Retitrating the acidic solutions with KOH showed that the agglomeration was irreversible and involved a reaction with the perchloric acid, as the

agglomerates remained as an insoluble mass, and the moles of KOH required to return the solution to basic pH was much less than for solutions without CeO_2 present.

The buffer region could be modeled as a series of acid/base reactions in equilibrium, adapting a procedure by Morales.[47]

$$HClO_4 \leftrightarrow H^+ + ClO_4^- \quad (5.1a)$$

$$H^+ + KOH \leftrightarrow K^+ + H_2O \quad (5.1b)$$

$$H^+ + CeO^- \leftrightarrow CeOH \quad (5.1c)$$

The exact protonation reaction that occurs on the surface of CeO_2 is not known, and so the designations CeOH and CeO^- in equation 5.3 are only representations that a negative site on the surface can be neutralized by a proton. However, a model of different surface sites by Nabavi et al.[29] suggests that the most likely candidate for this reaction is the protonation of an O^{2-} ion bound to three different Ce^{4+} atoms on the surface.

There are two incorrect mathematical assumptions made here, which are that the deprotonated reaction sites (Represented as CeO^- in eq. 5.1c) behave as individual ions in solution, when they are in fact a connected surface structure, and that the reaction is at equilibrium during the entire titration. In reality, the surface sites on the nanoparticle may have slight variations in pKa due to differences in local surface structure, and protonating one surface site may alter the pKa of nearby sites.[48] However, the effects of these inter-site interactions may be small, and would require a sophisticated model of the nanoparticle surface to be properly understood.

The assumption that the solution is at equilibrium during each step of the titration is also incorrect, as the nanoparticles displayed very slow reaction kinetics at high pH.

Reactions that are too slow to reach equilibrium during a titration will also cause equivalence points to appear as gradual rather than sharp changes in pH, which can be seen in the titration data at pH values > 8 in Figure 5.6. These pH values correspond to allowing the solution 5 minutes to react after each addition of perchloric acid, although a more accurate titration curve could be created by extending this reaction time. Equilibration time did not appear to be an issue near neutral or acidic pH, indicating that the acid/base reaction is able to achieve equilibrium within 5 minutes at lower pH. The three reactions (eq 5.1) had corresponding equilibrium constants:

$$K_{\mathrm{HClO_4}} = \frac{[\mathrm{H^+}][\mathrm{ClO_4^-}]}{[\mathrm{HClO_4}]} \tag{5.2a}$$

$$K_{\mathrm{KOH}} = \frac{[\mathrm{H^+}][\mathrm{KOH}]}{[\mathrm{K^+}]} \tag{5.2b}$$

$$K_{\mathrm{CeO}} = \frac{[\mathrm{H^+}][\mathrm{CeO^-}]}{[\mathrm{CeOH}]} \tag{5.2c}$$

It is important to note that the K_{KOH} is not a typical representation of an equilibrium constant for a base, but was rearranged into an acidic form so as to easily solve for $[\mathrm{H^+}]$. This transformation for KOH was performed using the equilibrium for the self-ionization of water:

$$K_{\mathrm{w}} = [\mathrm{H^+}][\mathrm{OH^-}] \tag{5.3}$$

Each reaction also had to obey the conservation of mass, where the total concentration of any component was equal to the sum of all forms it could exist as in the model:

$$[\mathrm{HClO_4}]_{tot} = [\mathrm{HClO_4}] + [\mathrm{ClO_4^-}] \tag{5.4a}$$

$$[\mathrm{KOH}]_{tot} = [\mathrm{K^+}] + [\mathrm{KOH}] \tag{5.4b}$$

$$[CeO]_{tot} = [CeO^-] + [CeOH] \quad (5.4c)$$

As a note, the $[CeO]_{tot}$ concentration in this equation is the concentration of only those surface sites being protonated, and not the concentration of the total cerium nanoparticles. The entire solution had to obey the conservation of charge, where the total concentration of negative and positive ions in solution were equal:

$$[OH^-] + [ClO_4^-] + [CeO^-] = [H^+] + [K^+] \quad (5.5)$$

The system of equations (eq. 5.2 - 5.5) could then be combined into a single equation:

$$\frac{[KOH]_{tot}}{\frac{K_{KOH}}{[H^+]} + 1} + [H^+] = \frac{K_w}{[H^+]} + \frac{[CeO]_{tot}}{1 + \frac{[H^+]}{K_{CeO_2}}} + \frac{[HClO_4]_{tot}}{1 + \frac{[H^+]}{K_{HClO_4}}} \quad (5.6)$$

Where $-\log([H^+])$ was numerically plotted as a function of $[HClO_4]_{tot}$, (black line in Figure 5.6) representing the two axes plotted in a titration curve. K_{CeO_2} was fit to $10^{-7.17}$, while the other equilibrium constants K_{KOH}, K_w and K_{HClO_4} were assigned literature values of $10^{-16.25}$, $10^{-13.9965}$ and $10^{2.75}$, respectively.[49] Both $[HClO_4]_{tot}$ and $[KOH]_{tot}$ are known as they represent the total amount of acid or base added to the solution, however each was scaled based on the total volume of the titration solution, which changed slightly as titrant was added.

The region from pH 8-10 is not accurately modeled, which is likely the result of slow surface reactions that do not reach equilibrium on the timescale of the titration. Nabavi et al.[29] predicted that there should be a protonation reaction on surface Ce-OH groups with a pKa of 10.4, which would appear as a second buffer region around that pH. However, using a titration process to identify this buffer region would likely take several hours or days to reach equilibrium at each pH point. The more obvious buffer region was

found to have a pKa of 7.3, which does not match any of the pKa's predicted by the model Nabavi uses for surface oxide sites; however, upon the formation of aggregates at the end of this region, it is likely that the completion of this reaction results in a net zero charge on the surface. It is important to note that this is very near the isoelectric point observed for CeO_2, which has been observed to range from pH 6.7-8.6 at 25 ^{o}C.[50]

There is a linear relationship between mass of dissolved nanoparticles and the amount of reactant required to titrate this buffer region (Figure 5.6, inset), indicating that roughly 0.675 mmol/g, or 11.6 ± 0.1% of the total CeO_2 formula units are reactive sites in this region. The calculated percentage of reactive sites in Sigma Aldrich particles is decreased by nearly half compared to STREM. This is likely to be a result of the larger average size of Sigma Aldrich nanoparticles, discussed in section 5.2.5, because smaller particles would have a larger surface area to volume ratio, corresponding to an increase in the surface site to total mass ratio. However, this difference could also be an artifact from the generally slower agglomeration kinetics observed for Sigma Aldrich particles.

5.2.3 Citrate Capped Nanoparticles

Citrate has been used previously to improve the dispersal of CeO_2 nanoparticles in neutral and basic solutions.[41,51–53] Additions of citrate to solutions of either Sigma Aldrich and STREM nanoparticles yielded stable colloidal solutions at pH levels as low as 5 for several days. Agglomeration was still observed to occur in solutions at pH 2.6, where the kinetics resembled that of nanoparticle solutions without added citrate. However, the agglomeration process could be reversed if acidic solutions were brought back to pH 5.7 (Figure 5.7). This is still lower than the pH at which bare nanoparticles

rapidly agglomerate, which was observed at the end of the buffer region (pH 6.8) in section 5.2.2, indicating that citrate aids in the stability of nanoparticles near neutral pH. In addition to preventing agglomeration near neutral conditions, the introduction of citrate into nanoparticle solutions also enabled much larger yields of nanoparticles filtered through 200 nm syringe filters after being left for several days (Figure 5.8), indicating that a significant number of nanoparticles that may have been initially flocculated were broken apart into either smaller clusters or individual particles by citrate. This is in contrast to bare nanoparticles, which show a slow agglomeration over several days.

The addition of citrate did not affect the absorption spectrum of unagglomerated nanoparticles. The absorption maximum for a freshly prepared pair of samples with and without citrate was observed to be 282 nm (Figure 5.8), and the direct band gap for each was calculated to be 3.67 eV (section 2.5.4, Figure 5.8 inset). This is a good indication that although the citrate molecules bind to the surface, they do not alter the electronic transitions of the nanoparticles.

5.2.4 UV Irradiation Experiments

Solutions of Sigma Aldrich nanoparticles were irradiated in a photoreactor using 254 nm light with a radiant power of 27 mW over a 1 cm quartz cuvette, described in section 2.4.6. To observe the dependence of observed photoproducts on pH, nanoparticle solutions with pH 2.6, 7.5, 9.5 and 10.5 were prepared using KOH. Some of these solutions also contained citrate, as described below.

Irradiation of bare Sigma Aldrich nanoparticles in acidic (pH 2.6) conditions produced aqueous Ce^{3+}, observed by narrow absorption peaks at 221, 239, and 253 nm (Figure 5.9a).[54] Although Ce^{3+} also has absorption bands at 211 and 297, these bands are weak in comparison and are obscured by the absorbance of the perchlorate and nanoparticles in solution. The CeO_2 peak at 300 nm (Figure 5.9b) was observed to disappear, at a rate faster than that observed for nanoparticle agglomeration in the dark. While agglomeration processes red shift this absorption peak (Figure 5.2), the irradiated sample demonstrated an initial blue shift. This shift could be fit to a change in the direct bandgap transition energy from 3.30 eV to 3.52 eV within the first 50 minutes of irradiation, after which it remained constant (Figure 5.10b). This coincided with the formation of a weak absorption band at 740 nm (Figure 5.10c and Figure 5.11a), which likely corresponds to the Ce^{3+}/Ce^{4+} charge transfer band observed by Griffiths et al.[21] Although Griffiths observed a much broader absorbance band, this discrepancy is likely a result of the high temperatures at which their experiments were performed (> 480 ^{o}C), compared with room temperature observations here.

Irradiating bare Sigma Aldrich nanoparticles in basic solutions (pH 10.5) resulted in a minor decrease in the absorption band amplitude, as seen in Figure 5.12a. This decrease was not accompanied by the development of aqueous Ce^{3+} peaks at 253 nm, nor was there a noticeable shift in the absorbance maximum; the calculated bandgap is constant at 3.3 eV. Nanoparticles in the dark did not undergo any noticeable spectral development (Figure 5.12b).

Citrate coated Sigma Aldrich nanoparticles showed enhanced stability compared to bare nanoparticles when irradiated under the same conditions (pH 10.5), seen as a slight decrease in absorption at 300 nm (Figure 5.12c). There is a substantial growth and subsequent decay of an absorption peak at 260 nm, although this is attributable to the photochemical degradation of citrate, as it was observed for solutions only containing citrate as well (Figure 5.13). The mechanism of this degradation has been well characterized by Kuyper,[55] as a reaction between citrate and dissolved oxygen in solution, forming 1,3-acetonedicarboxylic acid. This photoproduct is the observed intermediate absorbing at 260 nm, which further reacts with dissolved oxygen to produce formate, formic acid and carbon dioxide. If solutions are purged with nitrogen before irradiation, the absorption at 260 nm disappears, as is the case for solutions of citrate coated nanoparticles irradiated at pH 9.5.

Solutions of Sigma Aldrich nanoparticles and citrate at pH 9.5 showed much greater spectral changes upon irradiation than the pH 10.5 solutions did. The reason for this is that the experiment at pH 9.5 was performed for a nitrogen purged solution that had been prepared 10 days earlier. As mentioned in section 5.2.1, nanoparticles below pH 10 slowly agglomerate over days or weeks, which was observed as an increase in scattering of the sample. Irradiation decreased this scattering, indicating that UV-light is able to break apart agglomerated nanoparticles. To observe spectral changes in the absorption band at 300 nm, the effect of scattering also had to be considered. This correction was done by subtracting the absorbance at 500 nm from the absorbance at 300 nm, as the decreases observed at 500 nm are assumed to be primarily from reductions in

scattering. This subtraction at different irradiation times is shown in the inset of Figure 5.14a, relative to the corrected absorbance at the start of irradiation. The decay process observed is similar to the decay process seen at pH 10.5 (Figure 5.12c), although there is also a small growth in the 300 nm peak that occurs after 100 minutes of irradiation, which is attributed to breaking up agglomerates. A slight red shift in the absorption band maximum was observed over the course of irradiation; however, it is likely that the red shift observed is actually an artifact of reduced scattering in the sample. Modeling the band gap energy for this transition indicated that the bandgap increased from 3.48 eV to 3.57 eV. This shift in band gap was accompanied by the formation of a peak at 740 nm (Figure 5.11c), identical to the one formed for the pH 2.6 sample during irradiation. There is also a small peak that emerges at 250-260 nm; although it is possible this is from the formation of $Ce^{3+}_{(aq)}$, a more likely explanation is that it is the result of minor degradation of citrate due to a small amount of residual oxygen in the cuvette after nitrogen purging.

At the end of the irradiation process, UV-vis spectra of the pH 9.5 sample were taken to observe dark reactions that could occur. Using the same correction for scattering as before, the absorption band at 300 nm is observed to make a full recovery while scattering remains minor (Figure 5.14b). The absorption at 740 nm and the calculated band gap both begin to return to original values (Figure 5.15b & 5.15c), although each appears to do so more slowly than the 300 nm peak recovery.

Figure 5.16a shows the spectral changes from irradiating citrate-coated Sigma Aldrich nanoparticles in neutral solutions (pH 7.5), demonstrating very different spectral

evolution than either acidic or basic solutions. The peak at 300 nm disappeared, following distinctly second-order kinetics (Figure 5.16a, inset). A new peak is observed to form with a maximum absorbance of 270 nm, which is different from absorption bands for either aqueous Ce^{3+} or citrate photoproducts. The formation of this new peak was also not a simple continuous shift in wavelength from the 300 nm maximum, suggesting that it is not similar to band shifts caused by agglomeration. After irradiation stopped, the 270 nm peak did not rapidly return to the initial state, although monitoring the absorption of the same solution three weeks later displayed a peak at 300 nm, indicating a slow recovery. Modeling the direct bandgap at different irradiation times results in a distinctly biphasic increase in bandgap energy over time (Figure 5.17b). An initial rapid increase in bandgap, similar to observations for both pH 9.5 and pH 2.6 solutions, is accompanied by the development of the Ce^{3+}/Ce^{4+} CT band at 740 nm. After ~50 minutes, both the band gap and the 740 absorbance appear to level off, but while the 740 nm absorbance remains constant, the band gap increases again after 100 minutes. This is in sharp contrast to the band gap change at pH 9.5, where both the calculated band gap and the absorbance at 740 nm remained constant after ~150 minutes.

Spectral changes were observed for STREM nanoparticles irradiated in pH 6.6 solutions (Figure 5.16b). These changes appeared similar to the Sigma Aldrich solution at pH 7.5, although in this case the solution was not purged with nitrogen, so absorbance at 260 nm indicating citrate degradation was observed as well. Irradiation of the STREM solution was stopped after 100 minutes, and the absorbance of the sample was observed

to increase in the dark. However, the spectrum was unable to return to the initial absorbance after 24 hours.

5.2.5 Transmission Electron Microscopy

Transmission electron microscopy (TEM) images were taken of both Sigma Aldrich and STREM nanoparticles in basic solution (pH 11), in order to obtain an accurate distribution of nanoparticle sizes. The Sigma Aldrich nanoparticles (Figure 5.18a) have rectilinear shapes, with straight edges and corners, indicating that they are likely nanocrystalline particles, as amorphous particles would necessarily be less structured. The average size of the nanoparticles was estimated using an in-house algorithm written in Mathematica, which optimized circles around connected-components in a binary rendition of the TEM images, created using a local adaptive threshold technique.[56] The diameter of the fitted circle was recorded as the average size of each nanoparticle. Sigma Aldrich nanoparticles show typical diameters of 20 nm, agreeing well with the stated size of < 25 nm; however, there are a significant number of very large nanoparticles, skewing the mean diameter to 37 nm. The Sigma Aldrich nanoparticles show some agglomeration, forming branched structures in Figure 5.18a, although these branches could be an indication that binding between nanoparticles is not very strong. STREM nanoparticles on the other hand, were only found in dense clusters (Figure 5.18b), indicating adhesive forces between nanoparticles are likely stronger. These large agglomerates made it difficult to obtain accurate sizes for the individual nanoparticles, although examining the smaller structures within each cluster, an average

diameter of ~ 10 nm could be estimated, although the clusters themselves were roughly 120 nm in size.

Micrometer sized crystallites of Sigma Aldrich nanoparticles can be seen in Figure 5.19, and are the result of prolonged agglomeration. Although the scaling was not recorded for this image, the relative size can be seen compared to the copper grid scaffolding used to hold samples in the TEM, which they appear to adhere to. The crystalline structure they form is stellated, indicating that agglomeration processes likely has preferential surfaces for adhesion.

Sigma Aldrich nanoparticles that were coated in citrate showed less agglomeration and had many fewer large crystallites (Figure 5.20a), although some clustering was still present. The most common size was still 20 nm, while the mean was 21.5 nm. The absence of nanoparticles larger than 60 nm in diameter is a conformation that citrate does in fact break apart agglomerated nanoparticles, as nanoparticles of this size would still be able to fit through the 200 nm pore filter used to remove largescale nanoparticles, so would still be present if citrate only coated the surface. Interestingly, there was also a distinct ring around the perimeter of the nanoparticle cluster. A similar ring is much less intense in the uncoated particles (Figure 5.18a), indicating that perhaps it is only an artifact of dried salt surrounding the nanoparticles.

A duplicate of the sample in Figure 5.20a was irradiated for 8.5 hours at pH 6.6 before observing the nanoparticles using TEM (Figure 5.20b). Unfortunately, this irradiation was not performed under deaerated conditions, so citrate was degraded in the process. This can be confirmed by observing that the nanoparticles do not have a dark

ring surrounding them. Many of the nanoparticles lost their original shape, displaying rounded or blemished surfaces. Although the most common size was now 10 nm, there also appeared to be formations of larger clusters, shifting the mean diameter to 25 nm. These larger clusters are likely the result of agglomerates forming after the citrate coating had degraded.

5.2.6 Transient Absorption Spectroscopy

Transient absorption signals were observed for citrate-coated nanoparticles at pH 10.5 and pH 6.4, exciting the solutions using 305 nm laser pulses. The pump energy was kept fairly low, with energies of 0.25-1.1 μJ per pulse and a FWHM diameter of ~500 μm, in order to reduce multiple excitations of individual nanoparticles. The transient absorption signals are rather weak as a result, and were also compounded by significant scattering of the pump pulse. Scattered light was reduced using bandpass filters at each wavelength observed.

Seen in Figure 5.21, citrate-coated Sigma Aldrich nanoparticles at pH 10.5 displayed a weak bleach signal at 280 and 320 nm, while displaying excited state absorption at wavelengths from 340 to 380 nm. Both the bleach and excited state absorption signals could be globally fit to a single second order decay rate of 140 ± 40 ps. The excited state signals also displayed a rise time, which was modeled with a first-order kinetic lifetime of 600 ± 150 fs. Slightly faster transient signals were observed for STREM nanoparticles at pH 10.5 (Figure 5.22), which had a second-order decay lifetime of 90 ± 40 ps. The rise of the excited state was substantially slower in the STREM solution, with a lifetime of 2.3 ± 0.6 ps.

Transient absorption by Sigma Aldrich nanoparticles at pH 6.4 showed distinctly slower decay kinetics at 350 nm (Figure 5.23), which were fit to a second order decay lifetime of 240 ± 20 ps. The excitation kinetics were essentially the same, with a rise time of 700 ± 100 fs. Transient absorption signals at 620 nm for Sigma Aldrich nanoparticles at both pH 10.5 and 6.4 were identical to signals from neat water.

5.3 Discussion

5.3.1 Agglomeration of Nanoparticles

As the rate of the agglomeration reaction was first order with respect to the concentration of CeO_2, the slow step in the agglomeration process likely involves modification of the surface of a single nanoparticle. The variation of $[H^+]$ dependence indicates that only some of these surface changes involve a proton. Sonication, which breaks apart loosely bound nanoparticles, appears to expose surfaces that react with protons. For freshly prepared solutions, there appears to be a second surface process, which may be from some unknown ions bound to the surfaces of the dried nanoparticles as received by the manufacturer. After the initial modification of a single nanoparticle surface, it would appear that the process of two (or more) nanoparticles adhering together to form an agglomerate occurs relatively rapidly.

The increase in pH observed with the formation of agglomerates indicates a surface protonation mechanism is involved in agglomeration. This makes sense in basic solutions, as CeO_2 nanoparticles have surface bound hydroxide or oxide groups,[29] which when protonated would neutralize the overall surface charge. Without this electrostatic

repulsion between nanoparticles, agglomerates could form due to van der Waals attraction.[57] It is rather surprising to observe similar agglomeration at pH's significantly below the isoelectric point, as nanoparticles should initially have positive surface charges. Protonating this surface would only increase the surface charge, which would not promote agglomeration. However, given the observation that both Sigma Aldrich and STREM nanoparticles do agglomerate readily at pH 1, it would appear that they still have a significant negative surface charge. This can perhaps be explained using observations by Nabavi et al.[29] who demonstrated that titrating CeO_2 nanoparticles to highly basic conditions (pH > 11) causes them to undergo an "irreversible" reaction with hydroxide, which presumably adsorbed to the surface. Retitrating these nanoparticles to acidic conditions (pH 3) was not observed to release the hydroxide ions immediately, although hydroxide release was observed via an increase in pH of the solution after 40 days. It is possible that the Sigma Aldrich and STREM nanoparticles observed in this study also have excess hydroxide ions on the surface, as a result of synthetic methods, that are very slow to release, resulting in agglomeration at low pH due to decreased surface charges.

5.3.2 Improved Colloidal Stability of Nanoparticles by Citrate

In general, surface coatings prohibit the agglomeration of nanoparticles by creating a net surface charge, which electrostatically repels nanoparticles, as well as provides a steric barrier between nanoparticles. Citrate has been observed to enhance nanoparticle stability in several previous studies, where it has been used to coat both TiO_2 and CeO_2 nanoparticles.[41,43,51,53] At neutral pH, citrate has several deprotonated

carboxylic acid groups (pKa's: 3.13, 4.76, 6.39), which likely bind to the CeO_2 surface, resulting in an overall negative surface charge. Similar carboxylate groups have been used extensively to attach photosensitizers to the surface of TiO_2,[58–60] and several studies have determined that carboxylate groups can adhere to CeO_2 surfaces.

An investigation by Lu et al.[61] using sum frequency generation observed that acetate attaches to the surface of CeO_2 using both oxygens in the carboxylate moiety, either as a bidentate ligand on a single surface cerium atom, or bridging two cerium atoms on the same surface. Both forms of complexation have been modeled using DFT methods to have a binding energy of ~-45 kcal/mol in the gas phase, although the bridged form is slightly more favorable. In a separate study by Vlasova et al.[62] adsorption of benzoic acid derivatives on aqueous CeO_2 nanoparticles was monitored by changes in UV spectra. The binding in these cases was shown to be competitive with other ions in solution, indicating that the interaction is at least partially ionic in nature. It was also observed that the binding had a correlation with the pKa of the carboxylic acid group involved, where compounds with a lower pKa showed greater binding affinities.

The three carboxylate groups on citrate have different pKa's, indicating that the binding affinity of each carboxylate is probably not equivalent, and the observable binding affinity would vary depending on pH. However, the polydentate nature of citrate likely enhances the total binding affinity of the molecule. Polyacrylic acid (PAA), which has many more carboxylic acid groups, was observed by Ivanov et al.[41] to have higher binding affinity to CeO_2 nanoparticles than citric acid, indicated by increasing the temperature of coated nanoparticle solutions until agglomerates were observed. Aside

from the carboxylate groups, the hydroxyl moiety on citrate may have some affinity to the CeO_2 surface, but it is probably not crucial for surface binding, as the OH would not deprotonate even in high pH solutions, and thus confined to hydrogen bonding or dipole attraction mechanisms.

As the titration data in section 5.2.2 indicated that rapid agglomeration occurs at the completion of the reaction at pH 7.3, it is expected that citrate binds to the surface groups involved in this reaction, preventing the protonation that would otherwise occur. The loss of stability below pH 5 is likely a result of the carboxylate groups becoming protonated and losing affinity to these surface sites.

Theoretically, the surface of CeO_2 in basic solutions should be negatively charged, which would electrostatically repel the citrate anion. This would limit binding that occurs between the two. However, freshly prepared nanoparticles demonstrate different agglomeration kinetics after their initial dispersal in water, lasting for several minutes (Figure 5.2). This may be an indication that surface charges on nanoparticles are slow to equilibrate to changes in the environment. A similar slow reaction mechanism was used to explain the poor fit of the titration curve in section 5.2.2 (Figure 5.6), as the fitted model assumed that equilibrium had been achieved for each measured point. Citrate was only added to freshly prepared solutions of nanoparticles, so it is possible that citrate binds to the nanoparticle surface before the surface has developed a significant charge. It would be interesting to test whether bare nanoparticles that have been equilibrated in basic solutions have similar affinities to citrate as freshly prepared solutions do.

Although the stabilizing effects of citrate can be confirmed by several means (i.e. preventing agglomeration at neutral pH, increasing the number of nanoparticles that are less than 200 nm in diameter, and enhancing the robustness of nanoparticles to irradiation), it is not certain how many citrate ions are bound to the surface of the nanoparticles. As citrate is able to break apart larger agglomerates into smaller particles, which in turn have more surface area, there may be some equilibrium that is achieved between the formation of large nanoparticles and the surface coverage of citrate. A study by Trujillo-Reyes et al.[52] found that increasing the molar ratio of Citrate:CeO_2 in aqueous solution from 3:1 to 7:1 decreased the average sizes of nanoparticles observed by TEM from 8 nm to 4.5 nm. In solutions with high concentrations of citrate, the nanoparticles were observed to have a dark amorphous ring around them, ascribed to a dense layer of citrate. This ring is several nanometers thick, indicating that citrate would need to form more than a single layer on the surface of the nanoparticle.

TEM measurements in this study indicate that although agglomerates larger than ~60 nm are broken apart by the addition of citrate, the median size of nanoparticles was unchanged, indicating that the surface coverage was not enough to break apart the fundamental crystallite size of 20 nm. TEM images show a large dark ring around nanoparticle clusters in samples with citrate present (Figure 5.20a), which is not seen in bare nanoparticle solutions (Figure 5.18a). These rings may be citrate layers, as Trujillo-Reyers suggests,[52] indicating that the surfaces are covered in a layer of citrate that is several nanometers thick. It is also possible that these rings may simply be an artifact of

drying the sample, concentrating citrate salts near the nanoparticles, while actual surface coverage in solution is significantly smaller.

5.3.3 Direct Band Gap Calculations and Comparisons to Literature

The pronounced blue shift in absorption spectra after irradiating samples at neutral pH (Figure 5.16a) is difficult to characterize, as the absorption band is quite broad and featureless. The absorption spectrum is visibly different from solvated Ce^{3+} or Ce^{4+} compounds, indicating that the absorption is probably from changes within the nanoparticle. To describe these changes in absorption, many previous studies have modeled the nanoparticles as direct semiconductors, calculating a direct band gap energy (E_G) from the UV-visible absorption spectrum using a Tauc plot.[63] Although treating CeO_2 as a semiconductor may seem surprising as one could expect it to have localized excitons similar to TiO_2,[64] most studies indicate the exciton Bohr radius in CeO_2 is 7-9 nm.[26,65,66] This larger exciton size can also be inferred by the low band gap energy (2.8 eV) for bulk CeO_2, [24–26] which is lower than either TiO_2 (3.20 eV for Anatase, 3.01 eV for Rutile, 3.13 eV for Brookite)[67] or ZnO (3.3 eV).[68] At any rate, this analysis provides a method to compare the absorption spectra collected here to other studies, as many do not depict absorption spectra or maxima, but do report the direct band gap energy.

Furthermore, there have been numerous studies claiming that band gap energy can be used to predict nanoparticle size.[65,69–76] Although these predictions can be confounded by the concentration of Ce^{3+} in nanoparticles,[66] there is fairly good agreement between different studies indicating that these estimates are still useful. There are two primary

models used to obtain the size of nanoparticles from the band gap energy. The first model is known as the effective mass approximation (EMA), which approximates the electronic band structure near an energetic minimum or maximum with a parabola.[77] The curvature of this parabola can be redefined as an effective mass for a free particle (m_e or m_h), where narrow wells in k-space correspond to light effective masses, while broad wells correspond to heavy effective masses. Essentially, as the semiconductor decreases in size, inter-band transition energies grow according to a particle-in-a-box description:

$$E_G = E_{G,B} + \frac{\hbar^2 \pi^2}{2R^2}\left(\frac{1}{m_e} + \frac{1}{m_h}\right) - \frac{1.8e^2}{\varepsilon R} \tag{5.6}$$

Where E_G is the band gap energy, and $E_{G,B}$ is the band energy for the bulk crystal. The second term on the right hand side of eq 5.6 is essentially the particle-in-a-box quantum energy, while the third term is an interaction term between the electron and hole via shielded coulombic interactions. The constants m_e and m_h are the effective masses for the electron and hole in the material, respectively. They are typically smaller than the real electron mass (m_r), and are related to the Bohr radius (a_B) of the exciton formed from absorption via the relation:

$$a_B = \frac{4\hbar^2 \pi \varepsilon (m_e + m_h)}{m_e m_h e^2} \tag{5.7}$$

which is the approximate size at which quantum confinement effects begin to occur in a material. For CeO_2, the effective masses for both electrons and holes are typically assumed to be 0.4 m_r.[78] Although this model does well for many semiconductors, CeO_2 is not particularly well described, as the valency of cerium atoms can change, which alters the properties of electronic bands in the nanoparticle. There have been several studies

indicating that as the proportion of Ce^{3+} increases in the nanoparticle, the observed band gap will increase as well, even if nanoparticles are the same size.[66,79,80]

The second (electrostatic) model that describes shifts in band gap with nanoparticle size was proposed by Tsunekawa[81] and describes the changes in the band gap energy as a function of Ce^{3+} percentage in the nanoparticle. These concentrations can be modeled using the crystal lattice parameters from electron diffraction,[82] and also with the average valency of cerium from XPS.[76] The resulting function of band gap to particle size is shown as:

$$E_G = E_{G,B} + 5.3R^{-2.17} \tag{5.8}$$

Where the radius R is in units of nanometers while band gap energies are in eV. The model assumes Ce^{3+} exists only on the surface of the nanoparticles, similar to other mechanistic models proposed for TiO_2, which link blue shifts in the absorption edge with negative surface charges.[64] These surface Ce^{3+} ions causes an electrostatic difference between the surface and interior, shifting the energy of the band gap. This model also predicts that the oxygens bound to surface Ce^{3+} are primarily O_2^{2-}, or equivalently $2(OH^-)$. If this is the case, then altering these surface sites could have significant effects on the band gap of nanoparticles.

It is important to note that these models both assume the absorption of the nanoparticles is from delocalized interband transitions, and not from individual contributions of localized states. Although the Ce4f band is thought to consist only of delocalized states in pure CeO_2,[15,16] several groups have observed bands in absorption or diffuse reflectance spectra that can be associated with transitions localized on low

coordination defects.[24,26,83] These transitions can be attributed to either Ce^{3+} or Ce^{4+} centers, and are described as a charge transfer from an oxygen 2p orbital to a cerium 4f orbital. Ce^{3+} transitions are typically observed around 250-265 nm, whereas localized O $\rightarrow$ Ce^{4+} transitions are observed near 280 nm. These localized transitions may alter the observed absorption spectrum, which could severely affect calculated band gap energies. However, in many cases the interband transition is sufficiently lower in energy[26,72,83,84] than observed localized transitions that effects they might have on the predicted band gap are negligible. It is possible that these localized transitions could become more significant as the size of the nanoparticle decreases or if considerable defect states exist in a nanoparticle.

A summary of predicted direct band gap energies and nanoparticle diameters measured using TEM is shown in Figure 5.24. The majority of measurements lie between the predictions of the EMA and electrostatic models assuming the band gap for bulk CeO_2 is 2.85 eV. However, there are a significant number of studies that indicate a much higher bulk band gap energy. These can be fit reasonably well with the EMA model, resulting in a new bulk bandgap energy of about 3.3 eV. The majority of studies that fit to this altered EMA model are studies where nanoparticles were calcined at high temperatures and have large nanoparticle diameters,[74,75,84–86] although Chen and Chang report similar sizes and bandgaps using synthetic methods at room temperature.[39,40] The band gap energy calculated from absorption and the mean diameter calculated from TEM images place the Sigma Aldrich nanoparticles analyzed in this study (black triangles in Figure 5.24) among those that require a higher intrinsic band gap, corresponding to the

bare nanoparticles, and citrate coated nanoparticles before and after irradiation. The solution of STREM nanoparticles showed a band gap of 3.285 eV, which is lower than even the bare Sigma Aldrich nanoparticles. However, it is not certain if the absorbance spectrum of the STREM solution is from the individual 8 nm diameter nanoparticles or from the large agglomerate structures.

As a side note, Figure 5.24 does not include studies that measured nanoparticle sizes from broadening of X-ray diffraction or Raman-scattering bands, as these measurements demonstrated less correlation to the direct band gap. A recent study by Lorilte et al.[87] identified that even mild agglomeration in nanoparticles can have significant effects on the line broadening observed in Raman bands, and the subsequent estimation of nanoparticle size. Agglomeration may also affect the perceived diameters from X-ray diffraction measurements, resulting in unreliable predictions of size. TEM does not suffer from the same issues with fitting, as nanoparticle sizes can be directly observed.

5.3.4 Modeling Shifts in Band Gap During Irradiation

Increases in the modeled band gap energy were observed for citrate coated Sigma Aldrich solutions at pH 9.5, 7.5 and bare nanoparticles at pH 2.6 throughout the period of irradiation (Figures 10, 15 & 17). Each consistently displayed a sharp rise in band gap energy that could be fit with an exponential lifetime of 20-30 minutes. This initial rise paralleled the appearance of an absorption band at 740 nm, which is likely due to electron transfer between Ce^{3+} and Ce^{4+} sites in the nanoparticle. Tuller et al.[19] found that this charge transfer process has a thermal barrier of 0.4 eV. According to Marcus theory,

the light-induced transition should have an energy four times the thermal barrier (1.6 eV), assuming that the initial and final localized states are on equivalent cerium atoms in the lattice. This 1.6 eV transition energy corresponds to 775 nm, which is close to the 740 nm band observed.

The absence of the 740 nm band prior to irradiation indicates that there is only Ce^{4+} present in nanoparticles initially, and the observed increase in this band can be related to an average increase in Ce^{3+} present in the nanoparticles. Similar reductions of Ce^{4+} to Ce^{3+} have been observed when irradiating nanoparticle samples with X-rays, where prolonged irradiation significantly reduces the average valence state of cerium.[88] While X-rays are certainly more energetic than the 254 nm UV light, it is possible the mechanism is similar. A separate study by Takeda and Mafune[85]{Takeda, 2014} showed that laser ablation at 1064 nm also induced an abnormal increase in Ce^{3+} in nanoparticles, resulting in a bandgap increase from 3.43 to 3.48 eV. However, they attribute this to localized heating that fractured the nanoparticles into small pieces, which contain more Ce^{3+} on the surface.

The fact that this 740 nm absorption band and the band gap energy change on the same timescale indicates that the increase in band gap energy is likely from the formation of Ce^{3+} within nanoparticles. Increases in band gap energy due to higher concentrations of Ce^{3+} have been observed before,[66] however the observation of the 740 nm band could be used as a nonintrusive indicator of changes in the average valence state in CeO_2 nanoparticles. Current methods rely on X-ray absorption spectroscopy,[88] X-ray

photoelectron spectroscopy[89] or chemical redox reactions[53] to obtain relative amounts of Ce^{3+} in nanoparticles, which all modify the sample.

At pH 2.6, the observed band gap change is much larger than the solutions irradiated at higher pH, yet the observed band at 740 nm is much smaller. The obvious answer to this discrepancy is that the Ce^{3+} atoms created by irradiation are free to exit the nanoparticle as aqueous Ce^{3+}, which appears in solution. The increase in band gap at the same time is from the decrease in nanoparticle size (Figure 5.10) due to this loss, although the true magnitude of this effect may be offset by the agglomeration processes that are simultaneously occurring in solution.

It is rather surprising, given the formation of Ce^{3+} in acidic conditions, that an aqueous Ce^{3+} peak is not observed at neutral conditions as well, as the hydrated Ce^{3+} ion is equally stable below pH 8.[90] It is possible that the adhesion of citrate to the surface of the nanoparticle affects the surface charge enough to prevent Ce^{3+} from exiting into solution. Another possibility is that the surface binding sites of CeO_2 change from pH 2.6 to 7.5. The model proposed by Nabavi et al. indicates that triply coordinated hydroxyl groups on the surface (Ce_3-$OH^{+0.5}$) are deprotonated to oxides (Ce_3-$O^{-0.5}$) above pH 5.5. These changes would produce the same effect of creating a negative charge at the surface, which would stabilize Ce^{4+} near the surface, making it more difficult for Ce^{3+} to exit the nanoparticle.

The formation of Ce^{3+} in the nanoparticle could be the result of two possible mechanisms: a reduction of Ce^{4+} by an excited electron, or by the ejection of oxygen (as ½ O_2) from the nanoparticle, which leaves behind two electrons after it is released.[9] Both

are possible, although direct reduction of Ce^{4+} by an excited electron would suffer from the possibility of recombination with the corresponding hole, returning to the initial Ce^{4+} ground state. This recombination is avoided in the case where the hole reacts at the surface of the nanoparticle, where it could potentially oxidize water.[34,35] However, the oxidation of water produces H^+, which would decrease the pH; in all cases of irradiating the Sigma Aldrich nanoparticles the pH was observed to increase. The latter mechanism of releasing oxygen would be much less likely to suffer from fast recombination, as the ejected oxygens would produce O_2 gas in a manner similar to reactions involved in OSC. Experiments using pulses of oxygen gas flowed across the surface of reduced CeO_2 have indicated that the reabsorption of oxygen occurs on a timescale of several seconds at temperatures > 500 K,[91,92] with a activation energy of 48.1 kJ/mol.[92] It is not surprising that at room temperatures this reaction would slow to minutes. The fact that the 740 nm absorption band partially recovers after irradiation indicates that Ce^{3+} is slowly being oxidized back to Ce^{4+}, which could be explained by the reabsorption of oxygen into the lattice structure.

While changes in cerium valence can describe the initial rise in band gap, irradiation at pH 7.5 (Figure 5.17) displayed a second increase after ~100 minutes. This did not have a corresponding change in the absorption at 740 nm, indicating that it is not from changing concentrations of Ce^{3+}. It is therefore likely an effect of exciton confinement due to decreases in average nanoparticle size. The 4.13 eV band gap at the end of irradiation corresponds to a nanoparticle diameter of 9.4 nm using the EMA model, which best fit the unirradiated Sigma Aldrich nanoparticles (Dot-Dashed line in

Figure 5.24). This agrees with TEM images of citrate coated CeO_2 after 8 hours of irradiation at pH 6.6, which show a significant number of nanoparticles with diameters around 10 nm (Figure 5.20b). Thus prolonged irradiation could be used to form smaller nanoparticles from initially larger particles.

In contrast to other irradiated solutions at lower pH, the solution of citrate coated Sigma Aldrich nanoparticles at pH 10.5 did not show any development in the 3.3 eV bandgap during irradiation, nor did it demonstrate a Ce^{3+}/Ce^{4+} CT band at 740 nm, indicating that at very high pH conditions, the pathway forming Ce^{3+} is suppressed or has a competitive back reaction. This lack of activity makes sense if the reactive sites for cerium reduction are located on the surface, as raising the pH would have the effect of deprotonating surface sites on the nanoparticle and decreasing the overall surface charge,[29] making it difficult for electrons to reach these reactive sites.

5.3.5 Ultrafast Kinetics and Photophysical Mechanisms

The excited state absorption band around 350 nm (Figure 5.21) is assigned to a trapped hole, which is a hole that has been localized to a specific location in the lattice structure. The most obvious location for this localization would be on the negatively charged oxygen atoms in the lattice.[93] This localization can equivalently be described as O^- small polarons, or localized deformations in the lattice structure that occur in the presence of a hole, localizing the hole in a potential well.[94] Absorption bands associated with trapped sites can occur through either intra- or interpolaron transitions.[95] Actual observations of intrapolaron transitions are rare, because in many cases the transitions are forbidden by symmetry. The more common case is interpolaron transitions, which is

essentially the process of a hole hopping from one localized state to another through the absorption of light. Thus holes caught in “deep traps” will require more energy to hop to a nearby site, and will consequently have a blue shifted absorption spectrum when compared to transitions from shallow traps.

The 350 nm absorption peak is significantly blue shifted from equivalent bands in TiO_2, [96] indicating that the hole traps are deeper in CeO_2 than in TiO_2. One explanation for this is the relatively high mobility of oxygens within the Ceria lattice.[97] This property allows them to be used for oxygen storage or in solid oxide fuel cells, but also may help in the nuclear displacement needed to form small polarons. A different possibility that could describe the blue shift is disorder on the surface of the nanoparticle.[98] This disorder would create very favorable traps compared to the bulk structure.[94] Given the additional facts that in basic solution, and with the addition of citrate, the surface potential of the nanoparticles is negatively charged, it would not be surprising if the holes are electrostatically attracted to the surface where they are subsequently trapped in local disordered sites.

The rise time of the 350 nm absorption band is likely from the cooling and trapping process of holes that are initially untrapped or only in shallow wells immediately following excitation. This fast kinetic process has been observed to happen in 20 nm diameter TiO_2 nanoparticles on timescales of 200 fs,[99] which is slightly faster than the dynamics observed for the 20 nm diameter citrate coated Sigma Aldrich nanoparticles (Figure 5.21). The rise time for trapped holes in 10 nm STREM nanoparticles is slower still (Figure 5.22), which is rather surprising assuming trapping occurs primarily at the

surface. If a nanoparticle is smaller the holes should be able to reach the surface and trap more quickly than in larger nanoparticles. One possible explanation is that the STREM nanoparticles are actually tightly bound agglomerates in solution, in which electrons are able to transfer seamlessly throughout the cluster. Such dense agglomeration is observed in TEM images (Figure 5.18b), where individual STREM nanoparticles are difficult to discern. However, for holes to travel throughout a large agglomerate there would have to be few internal defect sites that could act as traps. A separate explanation would be that STREM has more shallow traps, which are able to slow the movement of the hole, but do not result in a defined transition band. This is perhaps in the same vein as the first possibility as shallow holes could be formed by agglomeration processes.

The decay of the 350 nm band was observed to have second order kinetics, with a lifetime that appeared to vary with pump intensity (Figure 5.25). These attributes have been shown to correspond to the formation of multiple excitons in TiO_2 nanoparticles. A study by Rothenberger et al.[100] demonstrated that at low pump intensity, excitons formed in TiO_2 nanoparticles follow single order decay kinetics that had a constant lifetime, however at high pump intensity, the kinetics changed and became second order with lifetimes that decreased with increasing pump power. They were able to accurately model this change in decay kinetics by assuming a Poisson distribution of excitons formed per nanoparticle with an average that depended on pump energy, where each exciton undergoes a random walk process of recombination. Forming multiple excitons on a single nanoparticle decreased the overall lifetime, as there were more possible recombination pathways. According to their model, first order kinetics model the system

well as long as there are 0.5 excitons formed per nanoparticle on average, while second order processes are good approximations for averages above 30 excitons per nanoparticle.

To obtain the average number of photons absorbed by each CeO_2 nanoparticle, the ratio of the number of photons absorbed per particle in the pump beam was estimated using the following equation.

$$\frac{photons}{particles} = \frac{\int_t \frac{E_e}{h\nu}\left(1-10^{-A}\right)}{\left(\frac{A}{\varepsilon_{305}}\right)\left(\frac{MM}{\frac{4\pi}{3}r_{NP}^3 \cdot \rho}\right)} \tag{5.8}$$

Where E_e is the irradiance of the Gaussian pump pulses at 305 nm integrated over the duration of a single pulse (J/m^2), A is the absorbance of the sample, ε_{305} is the molar absorption coefficient of CeO_2 at the pump wavelength, assumed to be 3000 $M^{-1}cm^{-1}$,[101] ρ is the density of bulk CeO_2, r_{NP} is the radius of the nanoparticle taken from TEM data, and MM is the molar mass of CeO_2. Thus the numerator is the number of photons absorbed in a cylindrical Gaussian volume of the sample, while the denominator represents the concentration of nanoparticles in that same sample. For Sigma Aldrich nanoparticles, the average number of photons absorbed per particle varied from 1.05 to 4.66, depending on the absorption and pump power used on the sample. STREM nanoparticles, which were smaller in size, corresponded to 0.21-0.58 photons per particle.

In the case of Sigma Aldrich nanoparticles, the behavior predicted by Rothenberger et al.[100] would be primarily first order, with a small but significant population of nanoparticles decaying via a second order term. However, in all cases a

purely second order reaction model described the data more accurately, with a lifetime of 140 ± 40 ps. Fitting the decay process with a single exponential showed noticeable deviations from the raw signals (Figure 5.26). Applying the Akaike information criterion (AIC) or Bayesian information criterion (BIC)[102] indicated that second order kinetics has a relative likelihood 10^5-10^6 times more than first-order kinetics. The decay could be described with two exponential terms, resulting in lifetimes of 70 ± 20 ps and 1050 ± 240 ps. However, this fit offered no benefit when compared to the second order decay, with relative likelihoods for AIC and BIC respectively being 0.23 and 1.49 when compared to second order decay model. Given that the more complicated model did not describe the data any better, the simpler second order kinetic process was preferable.

In STREM nanoparticles, decreases in nanoparticle size lead to lower pump energy per nanoparticle for the same pump power, for which the Rothenberger model would predict purely first order kinetics. However, both AIC and BIC indicated that the second order kinetic description was still more representative, with respective likelihoods of 19.7 and 10.4 compared to the first order kinetic model. The lower likelihood indicates that the two models are much more equivalent at describing the STREM signal decay than was the case for Sigma Aldrich nanoparticles. It is not certain if this is the result of the differences in the number of excitons present in each nanoparticle, or simply smaller signal to noise ratio. In this case, more data would need to be collected to accurately discern the two possibilities.

Although second order kinetics would imply that there are multiple excitons on individual nanoparticles,[100] Sigma Aldrich nanoparticles analyzed at different pump

intensities did not show decreasing lifetimes with increased pump power. In fact, decay processes appear to become longer with increasing pump fluence (Figure 5.25). This disagrees with the multiple exciton model used for TiO_2, as forming more excitons in a single nanoparticle increases the likelihood of recombination, which results in faster decay kinetics.[100,103] The reversal of this trend in CeO_2 could be an indication that a different process is responsible for the observed second order kinetics.

CeO_2 differs notably from TiO_2 in that cerium atoms can change valence states between Ce^{3+} and Ce^{4+} with relative ease compared to titanium, which is predominantly Ti^{4+}. In TiO_2, excited electrons can exist as a delocalized electron in the conduction band or a localized polaron, where the two states have similar energies.[104,105] However, transient absorption signals at 620 nm should observe signals for a delocalized/free electron,[99] were no different from transient absorption signals for pure water, indicating that there was no signal from exciting the nanoparticles. This would indicate that delocalized electronic states are not significant in CeO_2, which agrees with the description by Tuller et al. who determined that conduction through CeO_2 is exclusively from localized electron hopping from Ce^{3+} to adjacent Ce^{4+}.[19] The transition band for this hopping process was observed in steady state irradiation experiments with an absorption maximum at 740 nm, and would be predicted to appear in the transient absorption at this same region.

The possibility that both holes and electrons are much more deeply trapped in CeO_2 than TiO_2 could indicate that the small polarons they form diminish the electronic attraction between the two charge carriers at larger distances. Thus their recombination

may behave as two isolated polarons annihilating each other, rather than the bound state observed between electrons and holes in a typical exciton. If both charge carriers behaved independently, their interactions would result in the second-order kinetics observed.

With no signals at 620 nm even at early times after excitation, the trapping of electrons would need to be complete in less than a picosecond. This is not too surprising, as the majority of cerium atoms in the nanoparticles are Ce^{4+},[53,88] making electron traps common throughout the nanoparticle. Electrons are still able to reach the surface, as several studies have indicated that superoxide (O_2^-) is produced by irradiating CeO_2 in the presence of Oxygen.[6,106] However, the movement of electrons in CeO_2 could be quite different from TiO_2 if they are exclusively in trapped states.

Without the direct observation of trapped electrons, it is uncertain exactly how much of the decay of the trapped hole transient signal is due to photochemical product formation and how much is from reforming the ground state. However, CeO_2 is generally less active than TiO_2 under UV irradiation, as observed in the slow rates of degrading pollutant analogues.[4,107] As TiO_2 has a quantum yield of photoproducts on the surface of ~0.1,[108–112] CeO_2 would be expected to even lower yields of such decay processes, so the majority of the signal decay is likely from recombination dynamics. This decay lifetime was observed to be significantly longer in neutral solutions compared to basic solutions (Figure 5.23). This is surprising, considering that lowering the pH forms more Ce^{3+} sites,[14] which can be regarded as recombination centers for holes, and would be expected to speed up recombination processes. However, this is under the assumption that pure

CeO_2 behaves like an intrinsic semiconductor, where conduction and valence bands have equal populations of electrons or holes, respectively.

Many studies have found that at high temperatures and low oxygen environments, which promote oxygen vacancies and Ce^{3+} centers, CeO_2 behaves as an n-type semiconductor.[113] However, several studies have indicated that at temperatures lower than 700 ^oC or at oxygen conditions above one atmosphere, CeO_2 actually behaves as a p-type semiconductor.[113–115] Together, these studies would imply that CeO_2 nanoparticles containing only Ce^{4+} should be treated as a p-type semiconductor, which transitions to an n-type semiconductor upon reduction or by loss of oxygen (i.e. forming CeO_{2-x}). Thus at room temperature, the Sigma Aldrich nanoparticles should behave like a p-type semiconductor. In a p-type semiconductor, there are more holes present than electrons, which means the recombination rate is primarily determined by the ability of the excited electron to reach a recombination center where a hole is already present.[116] The movement of the corresponding excited hole becomes less important, as there are other holes present in p-type materials and so would have a much higher chance of recombining once the electron has reached a recombination center. The formation of Ce^{3+}, via lowering pH, reduces the number of holes present in trap sites making it less likely for the electron to encounter an unfilled trap site, which consequently increases the recombination lifetime. As a result of lengthening this recombination lifetime, slower photochemical processes can begin to occur, as evidenced by the increased reactivity of nanoparticles irradiated at lower pH (Figure 5.9, 5.12, 5.14 & 5.16). It is important to note that changing the pH would primarily effect the surface of the nanoparticle, so the

observed changes in recombination rates are probably due to modifications of traps located near the surface.

The recombination lifetime observed at pH 10.5 appeared to decrease over the course of several hours (Figure 5.27). This was not an effect of prolonged irradiation, as the trend was observed for a duplicate sample that had been kept in the dark, indicating that at high pH, a dark reaction slowly oxidizes cerium Ce^{3+} to Ce^{4+} within the nanoparticle after initial dispersion. The slow kinetics for this equilibrium reaction agree with the titration analysis (Section 5.2.2) which indicated the presence of a reaction above pH 8 that was much slower than the 5-minute timescale used for the additions of acid. The slow equilibration may also account for the initial decrease of the 300 nm band in the steady state irradiated solution at pH 10.5 (Figure 5.12c), where the observed decay appears to taper off as the solution ages. However, it is not certain if this is due to the nanoparticle surface not being at equilibrium with the surrounding solution, or whether the decay is observable after equilibrium is achieved. To discern this difference, a sample would need to be prepared that had achieved equilibrium before irradiation was initiated.

In summary, the transient absorption data indicate that both electrons and holes are more deeply trapped in CeO_2 than in TiO_2. This trapping is dependent on the valence of cerium atoms, where the presence of surface Ce^{3+} sites slows down recombination. The excited states formed at neutral pH are longer lived than at basic pH, and could allow for more photoinduced reactivity at the surface of nanoparticles, which could explain their photodegradation in acidic solutions.

5.4 Conclusion

Cerium oxide nanoparticles from two commercial sources were analyzed using ultrafast transient absorption and using a photoreactor to determine the photophysical and photodegradation processes. Observations of charge transfer bands for both electrons and holes indicate that both charge carriers exist as small polarons which appear to be more deeply trapped than in other metal oxides, challenging previous descriptions of delocalized charge carriers in CeO_2. The small size of the polarons around both electrons and holes also limits the excitonic description of the charge carrier pair, resulting in second order recombination kinetics even at low light intensity.

It was found that pH plays an important role in photoreactivity, where raising the pH increases the recombination rate of excited electrons and holes, limiting the activity of the nanoparticles. At pH below 10, the nanoparticles were observed to undergo photochemical reduction of Ce^{4+} to Ce^{3+}, presumably accompanied by releasing O_2 gas from the lattice structure, although this was not directly monitored. At pH 2.6, the Ce^{3+} that is formed is released as an aqueous ion. However, at neutral conditions (pH 7.5), Ce^{3+} remains inside the nanoparticle, reaching a critical concentration at which point the nanoparticle begins to break apart. At pH 9.5, the formation of Ce^{3+} is still observed, yet nanoparticle fracturing becomes negligible, making this system ideal for photocatalytic redox chemistry. Photoinduced fracturing was also observed for agglomerated nanoparticles, demonstrating that applied UV-light can be a useful means to redisperse nanoparticles from agglomerates. Agglomerates could also be broken up using

sonication, although sonication was observed to alter the surfaces of nanoparticles in acidic solutions, causing the nanoparticles to be more reactive with protons.

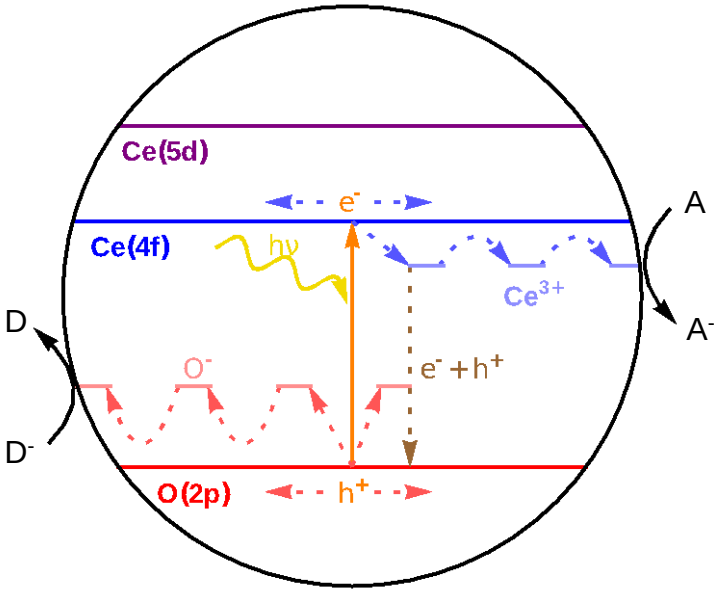

Figure 5.1 Diagram outlining the excited state processes in CeO_2. Upon excitation by UV or visible light ($h\nu$), an electron and hole are formed in the Ce4f and O2p bands, respectively. These can theoretically remain delocalized, or can localize on trap sites in the lattice. These charge carriers will be able to react with electron donors (D) or acceptors (A) if they make it to the surface; however, trap sites can facilitate electron-hole recombination via a Shockley-Read Hall mechanism, returning to the initial ground state.

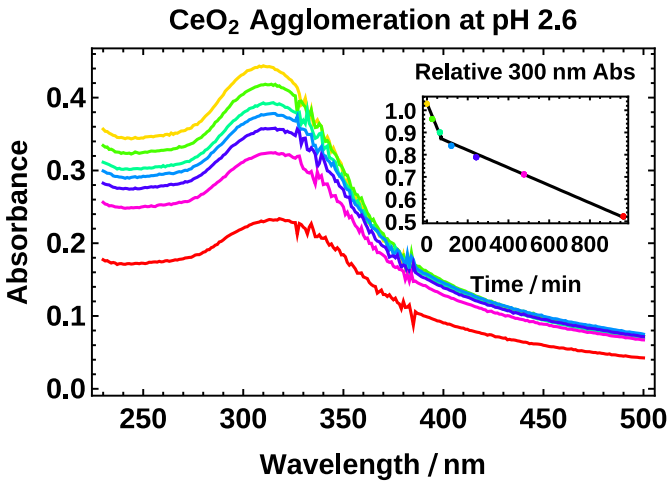

Figure 5.2. In acidic solutions, biphasic kinetics are observed for the decay of the absorption maximum at 300 nm, attributed to agglomeration. The rates of both processes could be fit as a zero order rate law.

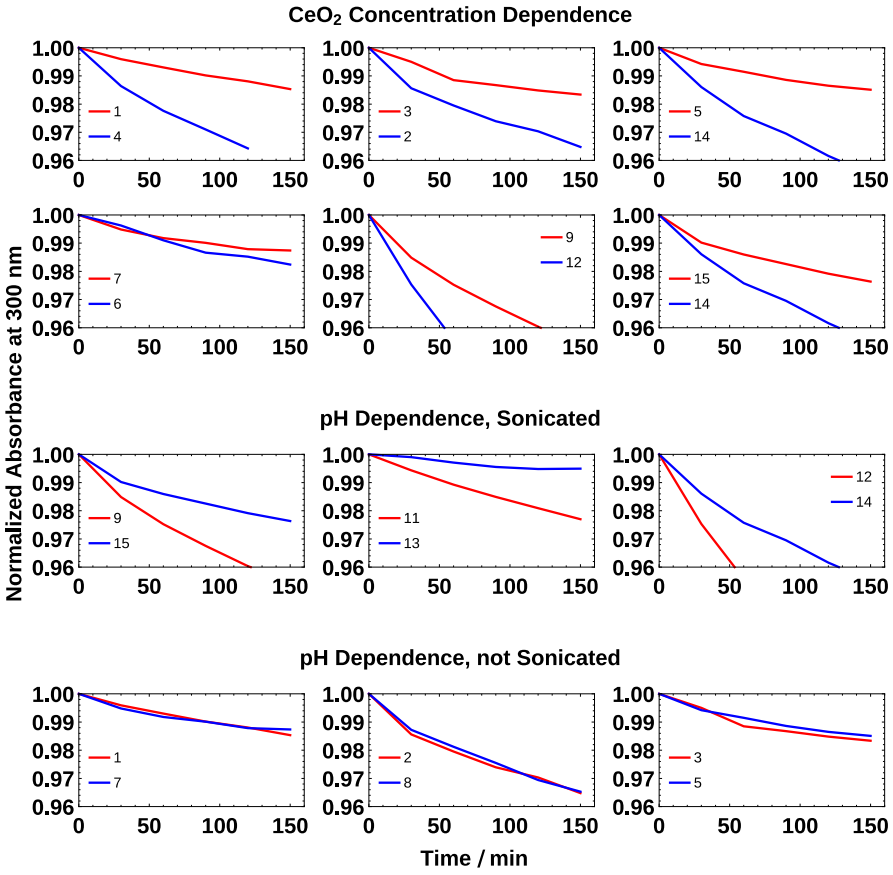

Figure 5.3 Normalized decays of absorbance as an indicator of agglomeration. Each plot is comparing solutions that were matched for each parameter in Table 5.1 except the ones indicated and ionic strength, which had no effect on the kinetics. The top six plots show the effect of CeO_2 concentration, where kinetics were faster at high concentration (blue lines) compared to low concentrations (red lines). The bottom six plots compare the effect of pH on decay rate, showing slower kinetics at high pH (blue lines) compared to low pH (red lines) after sonicating the solution, but the kinetics become independent of pH if sonication is omitted.

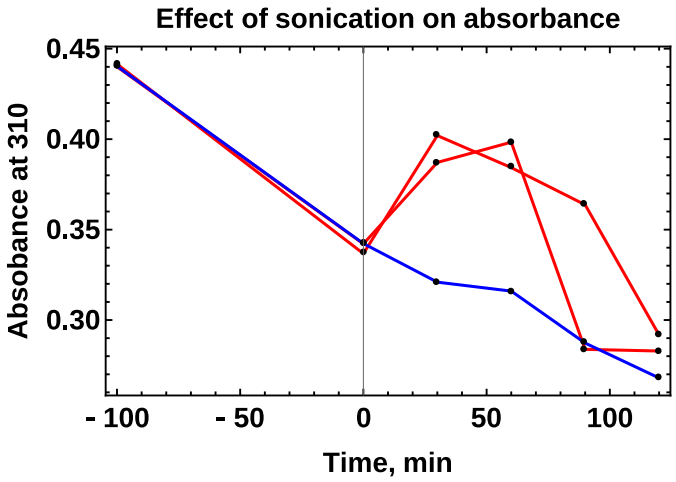

Figure 5.4. The effect of sonication on the absorption at 310 nm, which is related to the concentration of Sigma Aldrich CeO_2 nanoparticles dispersed in solution. Negative times are before the application of sonication. Sonicated samples (red) display an increase in absorbance after 30 minutes of sonication, attributable to breaking up large agglomerates. However, after 60 minutes of continuous sonication, the absorbance decreases more rapidly than unsonicated nanoparticles (blue).

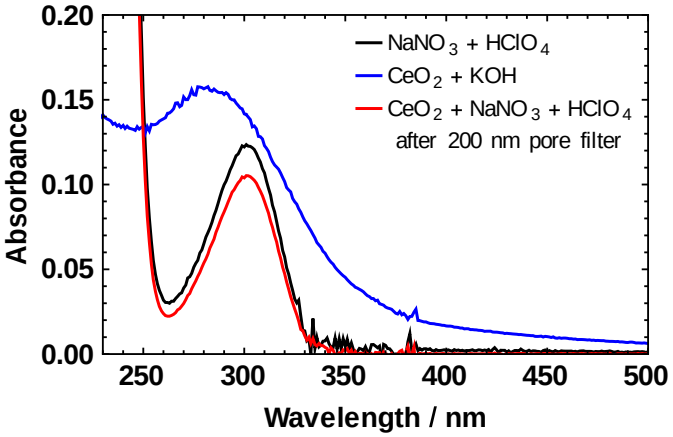

Figure 5.5 The absorbance of a filtered solution of Sigma Aldrich nanoparticles dispersed with nitrate in acidic solution (red) shows an identical spectrum to sodium nitrate (black), indicating that no nanoparticles were able to pass through the 200 nm pore filter. This would imply that all nanoparticles had agglomerated, and nitrate is unable to disperse CeO_2. The absorbance maximum of nitrate is at 300 nm, which may have been mistaken for the absorption band of CeO_2 (blue) in previous studies.

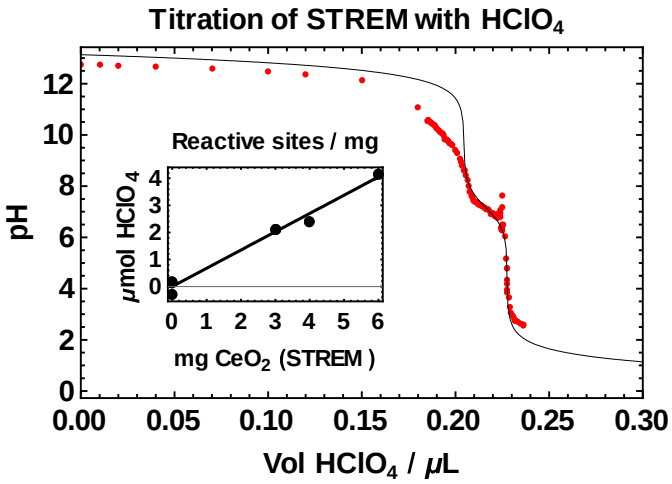

Figure 5.6. Titration of STREM nanoparticles. Inset shows the linear dependence of concentration with the mass of nanoparticles added, which indicates that only 11.6% of the surfaces sites react in the buffer region near pH 7. The curve above pH 8 appears very different from the model, the reasons for which are explained in the text.

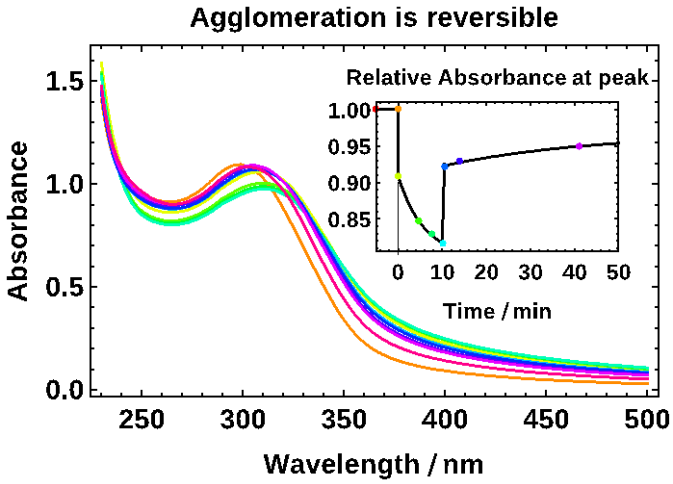

Figure 5.7 Sigma Aldrich nanoparticles with citrate were shown to be stable at pH 9.5, however lowering the pH to 2.6 (dashed line in inset) demonstrated an immediate red shift and decrease in the peak absorption with a rise in scattering. Raising the pH back to 5.7 (dotted line in inset) raised the absorption peak and began to decrease scattering. However, this was observed to still be incomplete after a day.

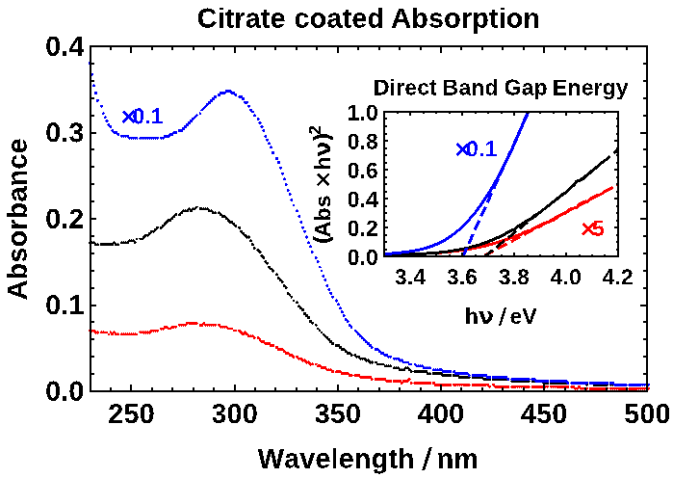

Figure 5.8 The absorption spectra for Sigma Aldrich nanoparticles in basic solution after filtering with 200 nm pore filters. Bare nanoparticles (red) display a low absorbance, indicating most nanoparticles were agglomerated. Nanoparticles coated with citrate and immediately filtered (black) so an increase in absorbance with no change in bandgap energy (inset). However, an enormous increase in absorption is observed when nanoparticles were allowed to equilibrate with the citrate coating (blue). However, this dispersal is also observed to shift the maximum and band gap slightly.

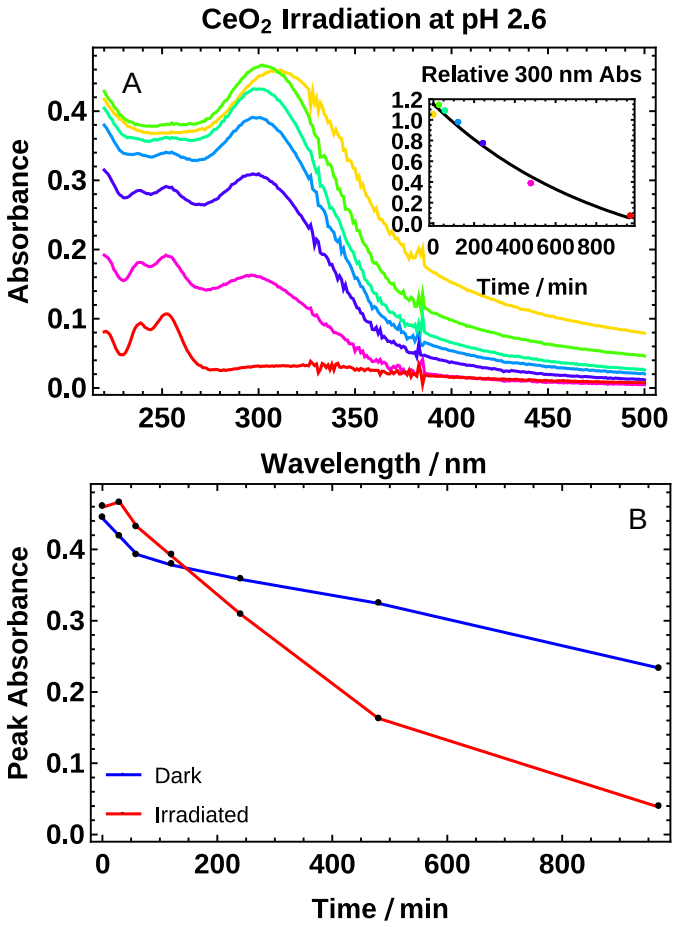

Figure 5.9 Irradiating Sigma Aldrich nanoparticle solutions at pH 2.6. (A) The absorption spectra show an initial blue shift upon irradiation, and decay while Ce^{3+} peaks at 239 and 253 nm emerge. The inset displays the kinetics of the 300 nm peak, which appear to be first order. (B) A comparison of the kinetics of dark and irradiated solutions of Sigma Aldrich nanoparticles, showing irradiation diminishes nanoparticle absorption more rapidly than the kinetics of agglomeration.

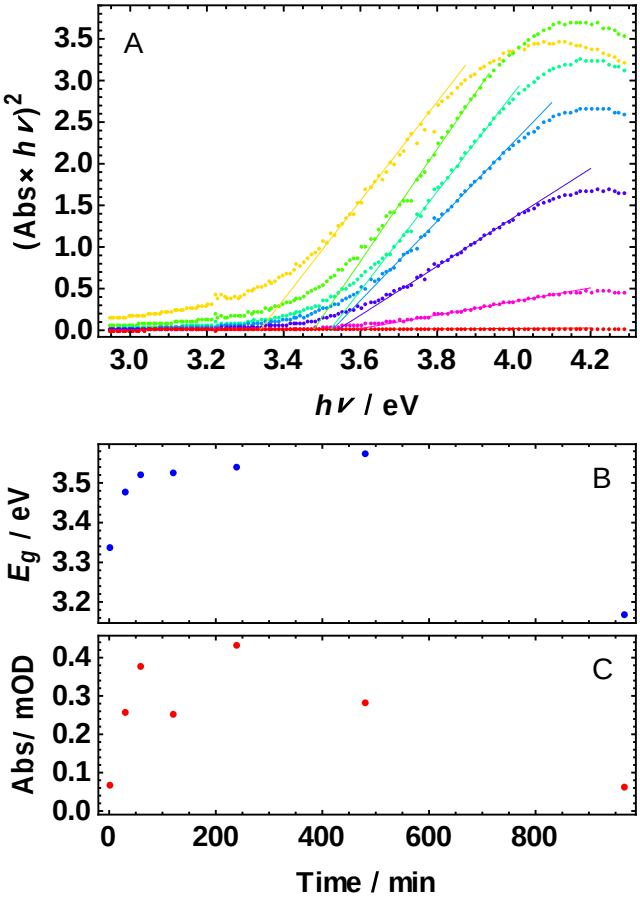

Figure 5.10 Changes in band gap energy and the absorbance at 740 nm for Sigma Aldrich nanoparticles irradiated at pH 2.6. (A) Tauc plots at each time used to calculate the direct band gap. (B) The change in band gap energy with irradiation time displays an initial rise, which remains roughly constant. (C) The corresponding change in 740 nm absorbance shows a similar trend to the bandgap, although displays more noise due to the solutions scattering.

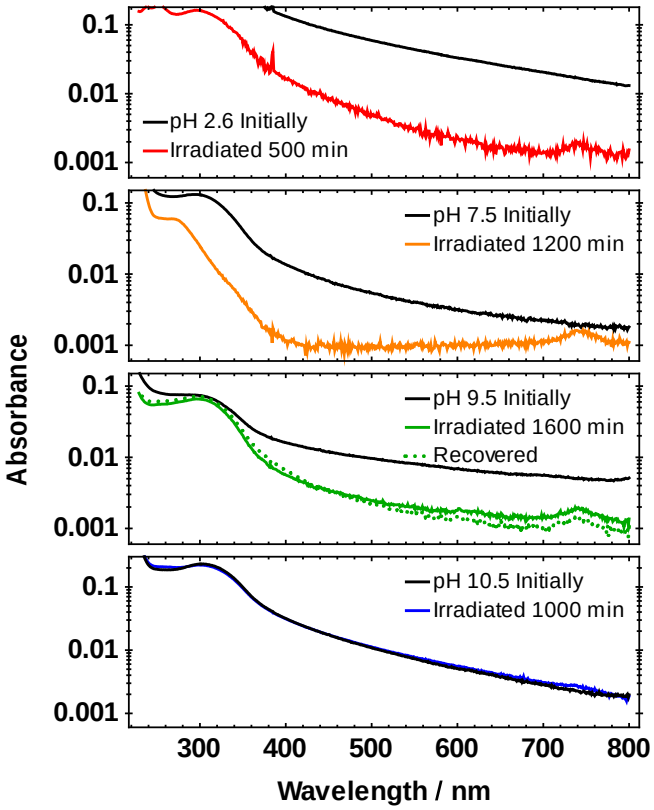

Figure 5.11 Near IR absorption of Sigma Aldrich nanoparticle solutions before (dotted lines) after (solid lines) irradiation. Solutions at pH 7.5, 9.5 and 10.5 all contain citrate. All solutions except pH 10.5 display the formation of a band at 740 nm. This is still observable in the pH 9.5 solution after the recovery of the 300 nm peak (dashed line).

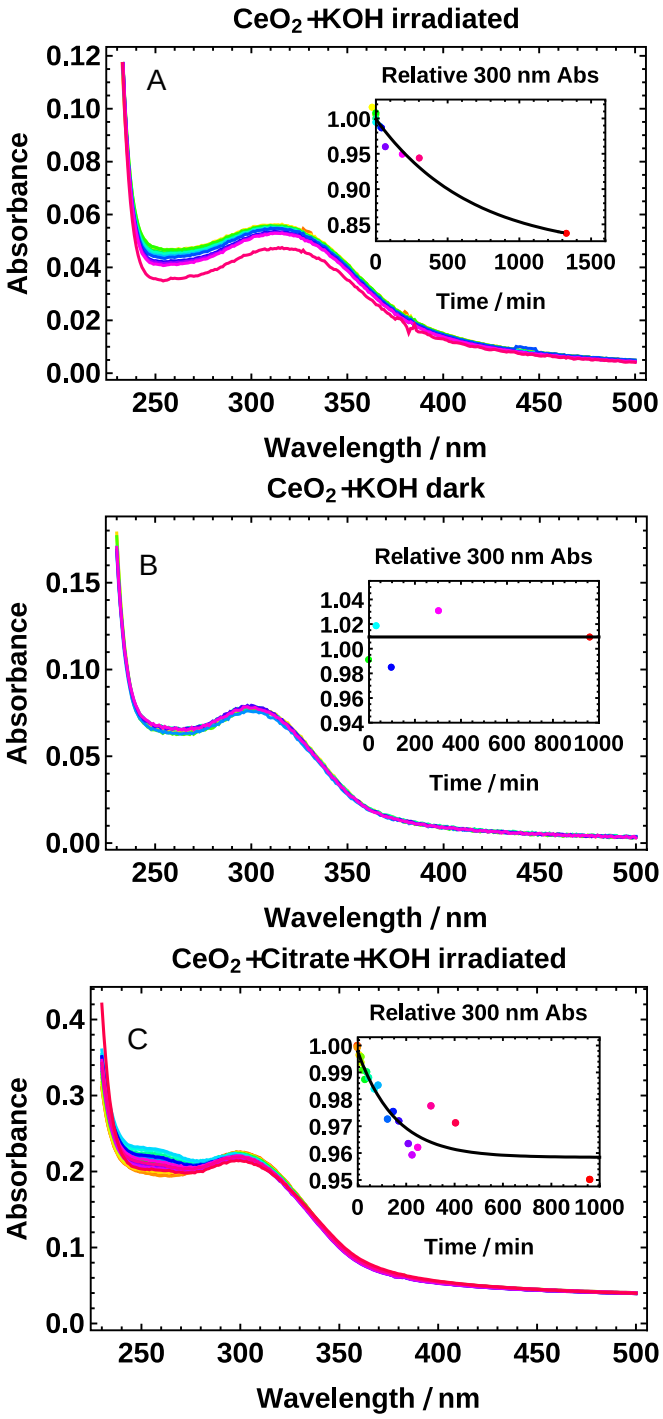

Figure 5.12 Irradiation of bare Sigma Aldrich CeO_2 nanoparticles at pH 10.5 (A) Bare nanoparticles show a decrease in absorption. (B) The corresponding unirradiated solution displays no spectral changes. (C) The addition of citrate reduces the effects of photodegradation, although citrate is observed to photochemically break down in the presence of dissolved O_2.

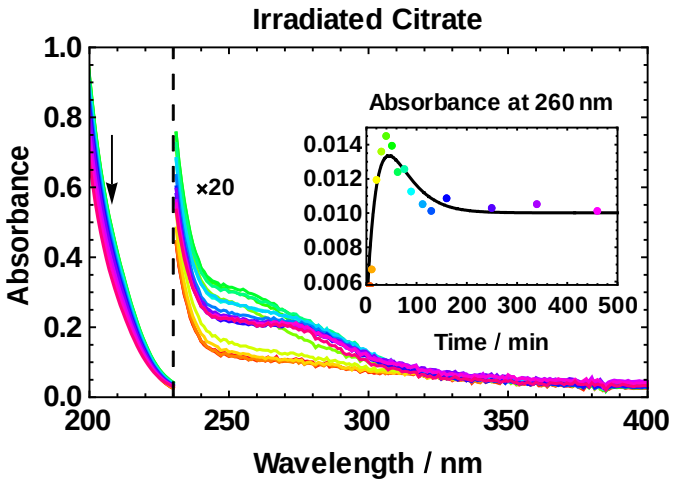

Figure 5.13 The absorption spectrum of citrate at pH 8.8 under irradiation in the presence of oxygen. The large shoulder at 220 nm is absorption due to citrate, which decreases during irradiation. At the same time, there is the emergence and subsequent decay (inset) of a small shoulder at 260 nm, corresponding to 1,3-acetonedicarboxylic acid.[55] This shoulder appears as a peak in the citrate coated CeO_2 spectrum; however, purging the solution with nitrogen prevents all observable degradation processes.

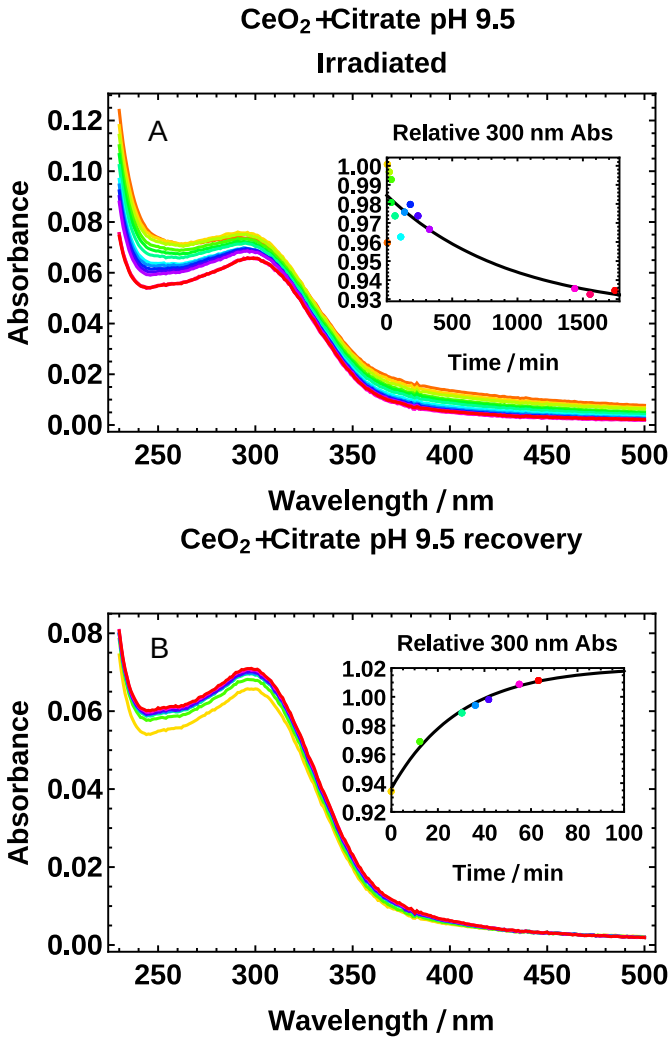

Figure 5.14 Irradiation of citrate coated Sigma Aldrich nanoparticles at pH 9.5 after purging with nitrogen gas. (A) There is a more substantial decrease in absorption at 300 nm than what was observed at pH 10.5, although much of this change is a result of decreasing scatter. (B) After irradiation is stopped, the 300 nm peak returns to its original absorbance value, however the scattering at long wavelengths does not return, indicating that irradiation irreversibly breaks apart large agglomerates.

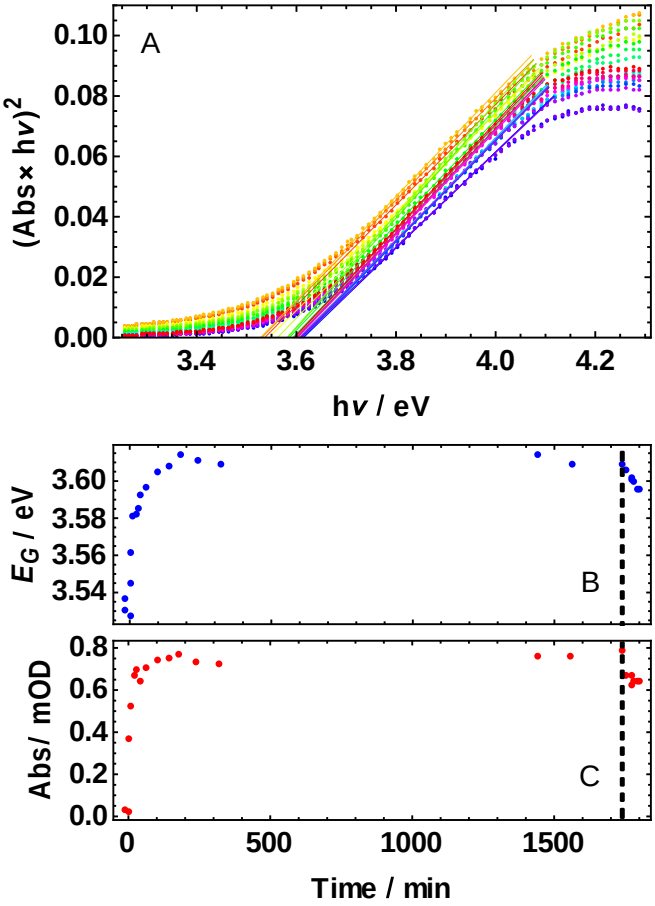

Figure 5.15 Changes in band gap and absorbance at 740 nm for the solution of citrate coated Sigma Aldrich nanoparticles at pH 9.5. (A) A Tauc plot used to model the direct band gap of the solution over the course of irradiation. (B) The band gap increases to a constant value upon irradiation. The dashed line indicates the end of irradiation, after which a relaxation process is observed. (C) The absorption of the band at 740 nm increases at roughly the same time scale.

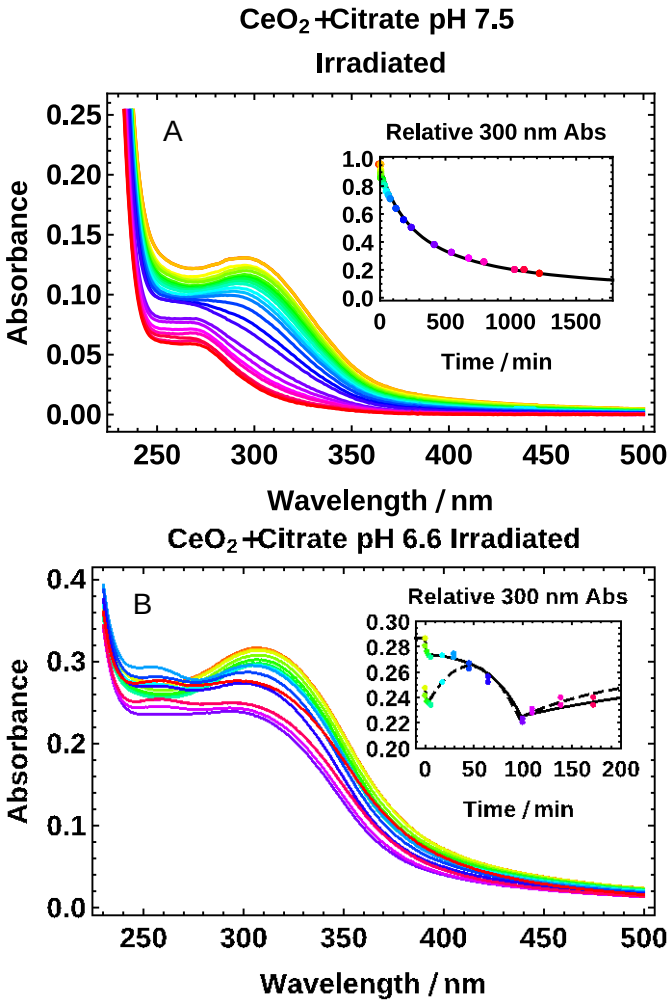

Figure 5.16 Irradiation of citrate coated CeO_2 nanoparticles at neutral pH. (A) Irradiation of a deaerated solution of citrate coated Sigma Aldrich nanoparticles at pH 7.5 displays a decay in the peak at 300 nm and the appearance of a new band at 270 nm. The inset displays the kinetics of this 300 nm absorbance, which are second order. (B) Irradiation of citrate coated STREM nanoparticles at pH 6.6 display a similar decrease in the 300 nm absorbance, although irradiation was halted after 100 minutes. In this case, the solution was not deaerated, so the degradation of citrate at 260 nm is observable. The absorption at 260 nm and 300 nm are shown in the inset.

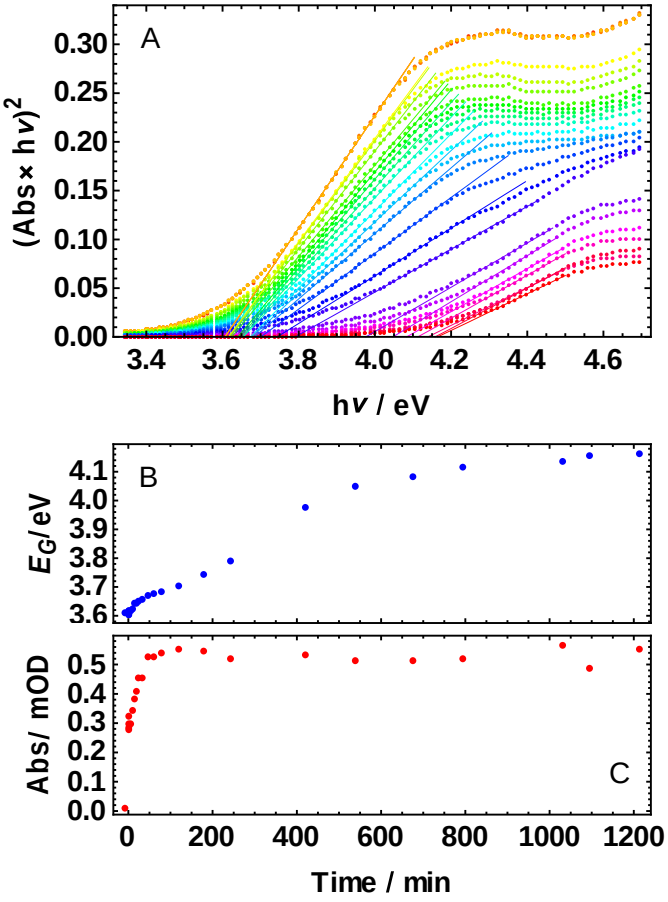

Figure 5.17 The modeled changes in band gap energy for citrate coated Sigma Aldrich nanoparticles irradiated at pH 7.5. (A) The Tauc plot used to calculate the band gap energy. (B) The change in band gap with irradiation time. An observed fast rise is observed, analogous to the pH 9.5 solution. (C) The absorbance of the band at 740 nm, which displays a rise matching with the initial increase in band gap. However, this absorption remains constant, while the band gap continues to increase after ~100 minutes.

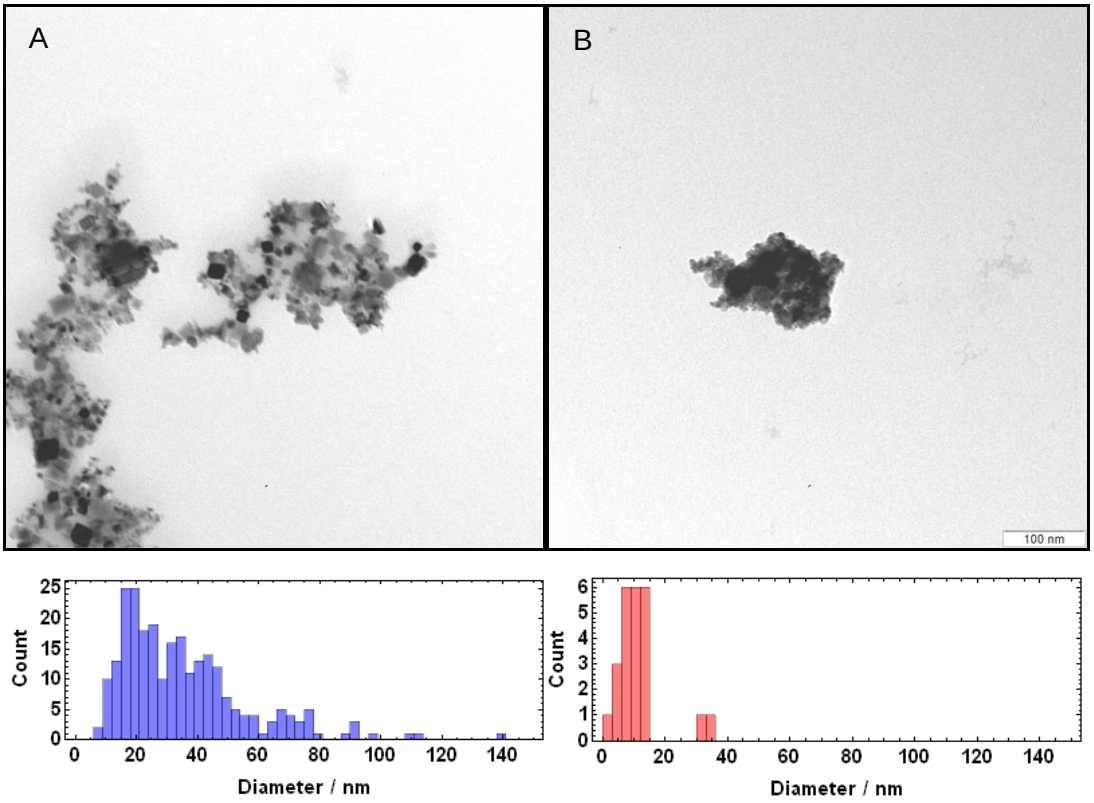

Figure 5.18 Transmission electron microscope (TEM) images of (A) Sigma Aldrich and (B) STREM nanoparticles prepared using basic solution (pH 10.5). Below each figure is the distribution of nanoparticle diameters calculated in the image. Both nanoparticles appear to agglomerate, although the STREM cluster is more densely packed, making the diameters of individual nanoparticles difficult to measure accurately.

Figure 5.19 TEM image of agglomerated Sigma Aldrich nanoparticles prepared at neutral pH. The sizes of each were not recorded, however the structures are on the 10-100 μm scale. The extended structures along the bottom and right are the copper wire grid used to hold the TEM samples.

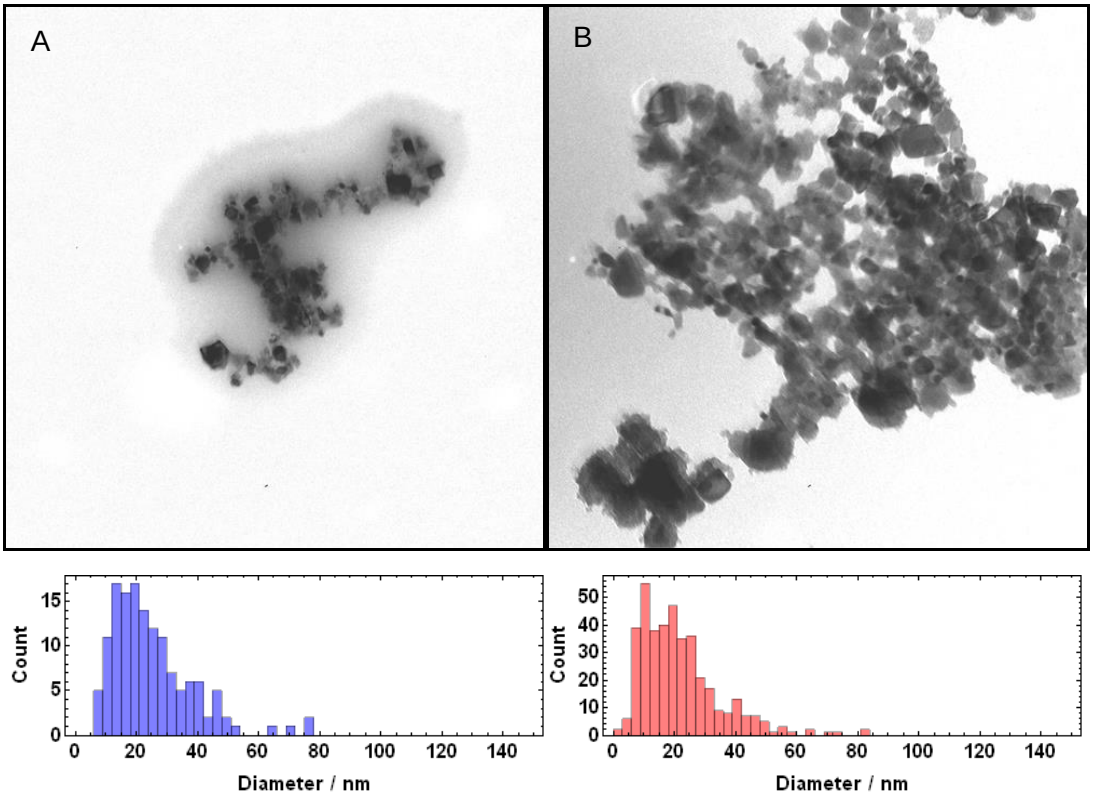

Figure 5.20 TEM images of citrate coated Sigma Aldrich nanoparticles at pH 6.6 (A) before irradiation, and (B) after irradiation with 254 nm light for 8.5 hours. Below each image is the respective size distribution in the image.

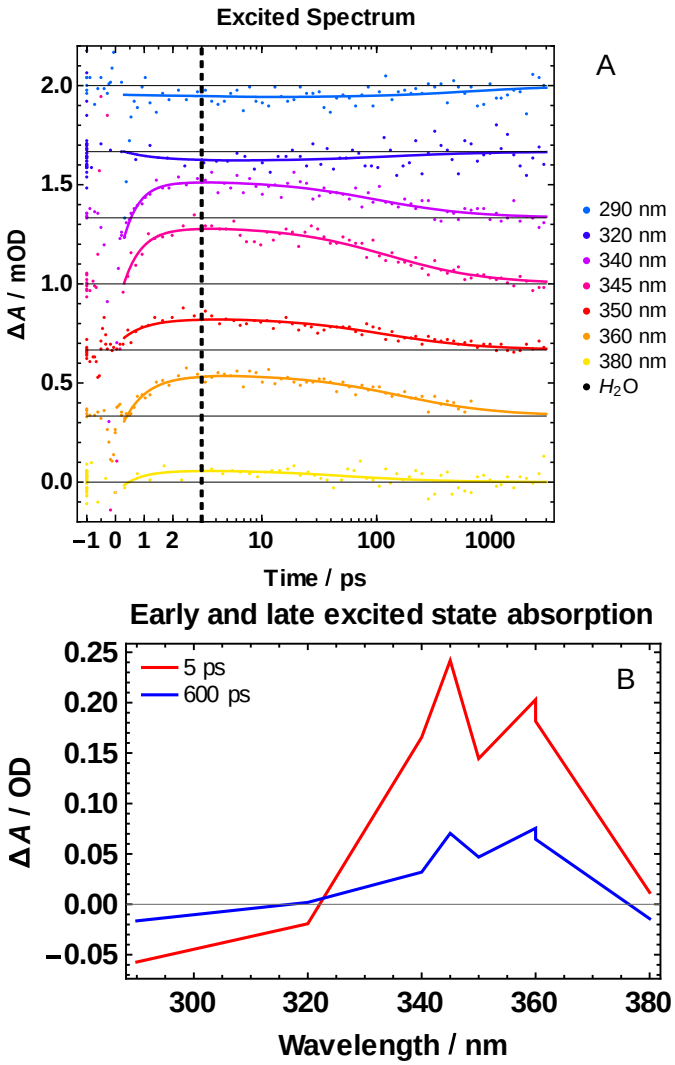

Figure 5.21 Transient absorption profiles of citrate coated Sigma Aldrich nanoparticles at pH 10.5. (A) Transient absorption signals could be globally fit to a rise and second order decay, showing a ground state bleach at 280 and 320 nm, with an excited state absorption at 340, 345, 350, 360, and 380 nm. The dashed line indicates a transition from linear to logarithmic time scales. (B) The resulting transient spectra at 5 and 600 ps.

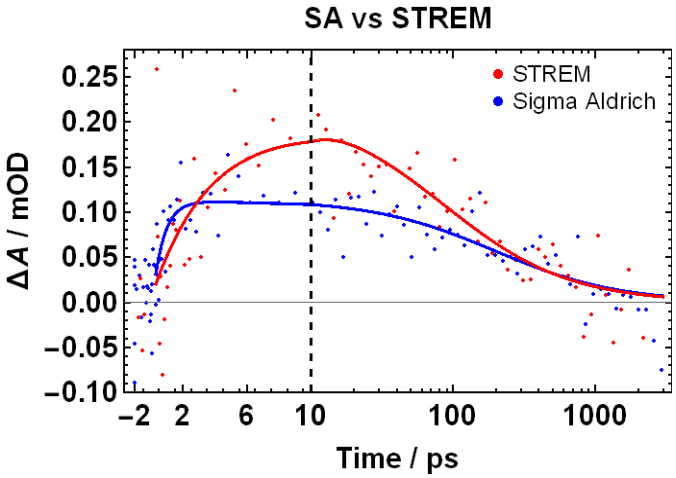

Figure 5.22 Transient absorption signals at 350 nm for citrate coated solutions of STREM and Sigma Aldrich nanoparticles at pH 10.5. The signal for the STREM sample shows a significantly slower rise time than Sigma Aldrich. The dashed line indicates a transition from linear to logarithmic time scales.

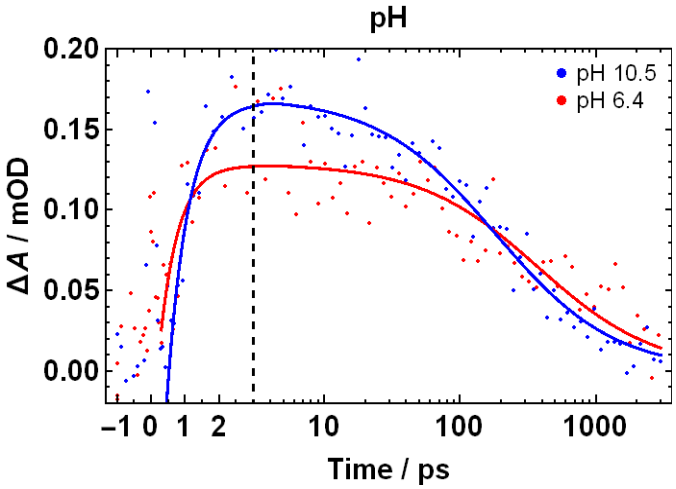

Figure 5.23 Transient absorption for citrate coated Sigma Aldrich nanoparticles at pH 10.5 and pH 6.4. The neutral solution shows a significantly faster decay process, although both have similar rise kinetics.

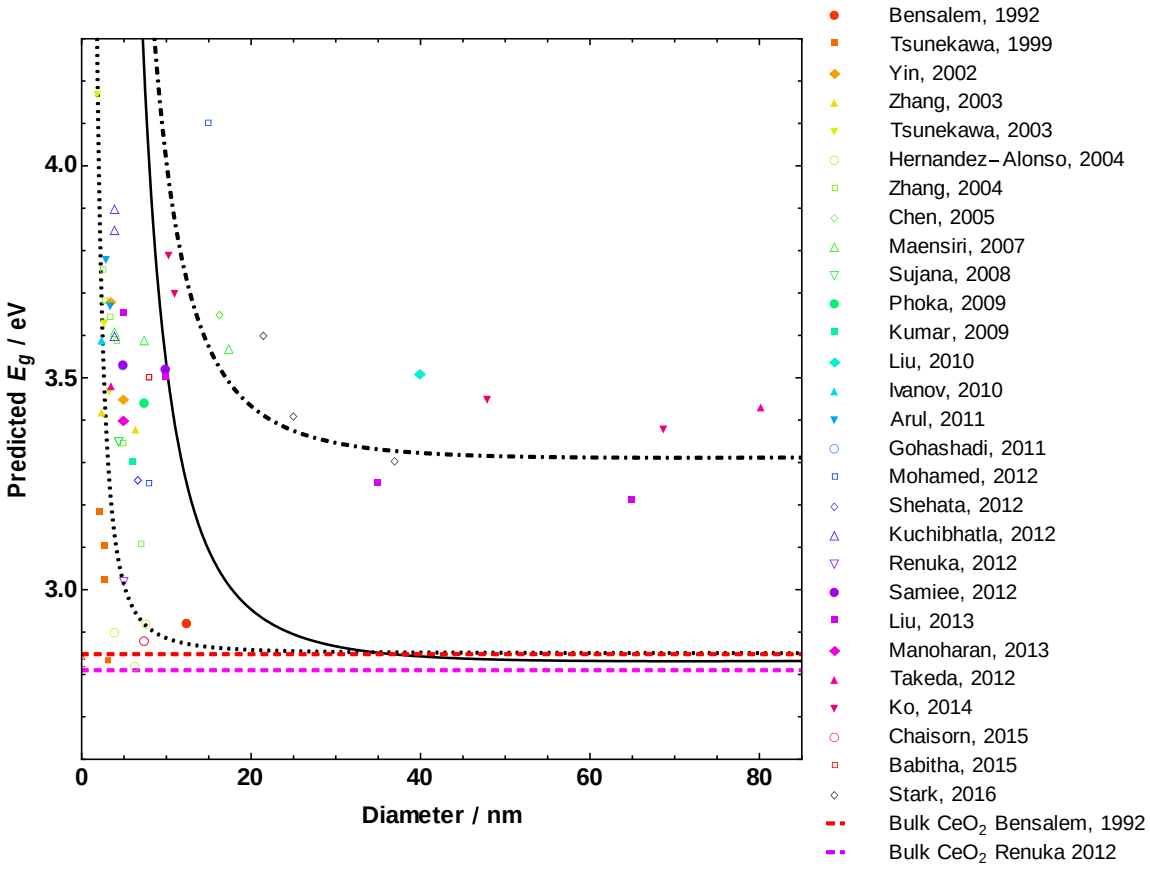

Figure 5.24 A comparative summary of studies correlating the diameter and direct band gap of CeO_2 nanoparticles. Individual publications on nanoparticles are displayed as colored markers, while observations of the band gap for bulk CeO_2 are shown as colored dashed lines, averaging 2.83 eV. The black lines indicate the different models used to describe the relationship between diameter and band gap. The EMA model (solid line) and electrostatic (dotted) lines appear to work in many cases, however there is a subset of nanoparticle observations which are better described by an EMA model with a bulk band gap of 3.3 eV (dot-dashed lines).[24,26,40,41,66,69,70,72–75,78,83–86,117–123]

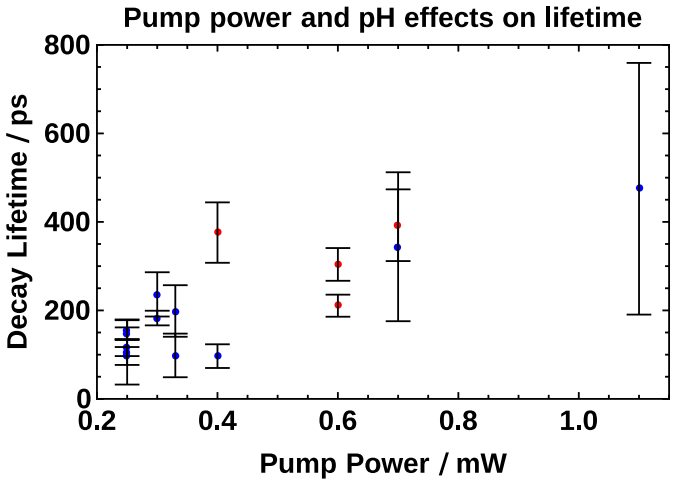

Figure 5.25 The relationship between fitted decay lifetimes and the pump power used in different transient absorption experiments. Blue dots are experiments performed at pH 10.5, while red dots indicate experiments at pH 6.4. The bars indicate the confidence range of twice the standard error.

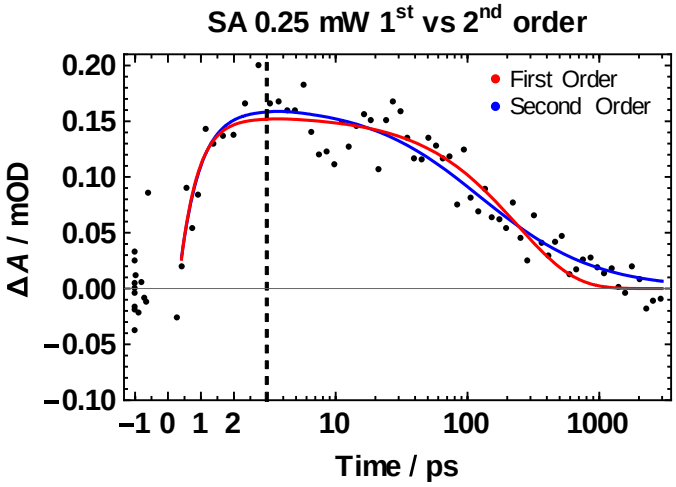

Figure 5.26 Transient absorption signal at 350 nm for citrate coated Sigma Aldrich nanoparticles at pH 10.5 exciting with 0.25 μJ pump pulses at 300 nm, fit with either first order (red) or second order (blue) decay kinetics.

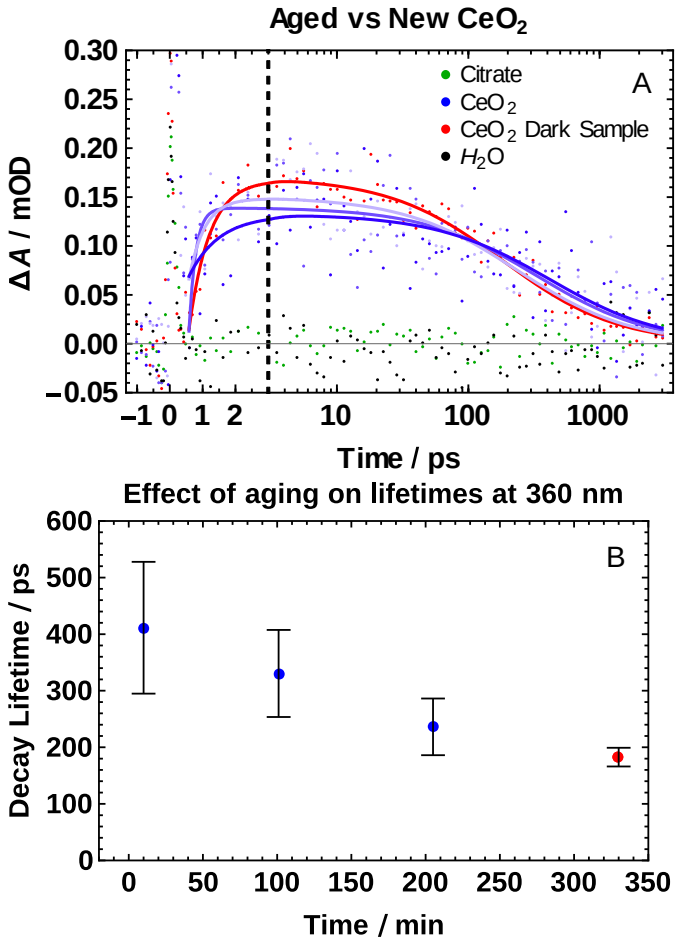

Figure 5.27 A decrease in the decay lifetime was observed for a solution of citrate coated Sigma Aldrich nanoparticles at pH 10.5, which was aged over the course of several hours. (A) The transient absorption signals of the solution collected at 100 minute intervals, shown in lighter shades of blue as the solution ages. (B) The fitted lifetimes are shown as dots, which display a clear trend, although there is significant uncertainty for measurements with long decay lifetimes, where two standard deviations are depicted as vertical bars. The red decay signal and corresponding red dot are from a duplicate sample that was not irradiated during the experiment.

Table 5.1 Fractional factorial design to determine the dependence of the agglomeration rate on concentration of CeO_2, Ionic strength, pH, Sonication, and solution age.

Sample	***[CeO_2] / mM***	***[NaCl] / M***	***pH***	***Sonicated / min***	***Age / hr***	***Rate / min^{-1}***
1	0.032	0.014	1.20	0	5	417
2	0.080	0.014	1.17	0	0	407
3	0.032	0.027	1.28	0	0	346
4	0.079	0.027	1.25	0	5	375
5	0.031	0.040	1.77	0	0	506
6	0.078	0.040	1.88	0	5	593
7	0.031	0.052	1.90	0	5	427
8	0.077	0.052	1.83	0	0	451
9	0.032	0.014	1.19	10	0	249
10	0.080	0.014	1.23	10	5	489
11	0.032	0.027	1.20	10	5	503
12	0.079	0.027	1.18	10	0	294
13	0.032	0.040	1.87	10	5	608
14	0.078	0.040	1.62	10	0	453
15	0.031	0.052	1.72	10	0	405
16	0.077	0.052	1.69	10	5	390

■ REFERENCES

(1) Montini, T.; Melchionna, M.; Monai, M.; Fornasiero, P. Fundamentals and Catalytic Applications of CeO_2-Based Materials. *Chem. Rev.* **2016**, *116*, 5987–6041.

(2) Abanades, S.; Flamant, G. Thermochemical Hydrogen Production from a Two-Step Solar-Driven Water-Splitting Cycle Based on Cerium Oxides. *Sol. Energy* **2006**, *80*, 1611–1623.

(3) Bamwenda, G. R.; Uesigi, T.; Abe, Y.; Sayama, K.; Arakawa, H. The Photocatalytic Oxidation of Water to O_2 over Pure CeO_2, WO_3, and TiO_2 Using Fe^{3+} and Ce^{4+} as Electron Acceptors. *Appl. Catal. Gen.* **2001**, *205*, 117–128.

(4) Hernández-Alonso, M. D.; Fresno, F.; Suárez, S.; Coronado, J. M. Development of Alternative Photocatalysts to TiO_2: Challenges and Opportunities. *Energy Environ. Sci.* **2009**, *2*, 1231.

(5) Pouretedal, H. R.; Kadkhodaie, A. Synthetic CeO2 Nanoparticle Catalysis of Methylene Blue Photodegradation: Kinetics and Mechanism. *Chin. J. Catal.* **2010**, *31*, 1328–1334.

(6) Ji, P.; Zhang, J.; Chen, F.; Anpo, M. Study of Adsorption and Degradation of Acid Orange 7 on the Surface of CeO_2 under Visible Light Irradiation. *Appl. Catal. B Environ.* **2009**, *85*, 148–154.

(7) Zhai, Y.; Zhang, S.; Pang, H. Preparation, Characterization and Photocatalytic Activity of CeO_2 Nanocrystalline Using Ammonium Bicarbonate as Precipitant. *Mater. Lett.* **2007**, *61*, 1863–1866.

(8) Ji, P.; Zhang, J.; Chen, F.; Anpo, M. Ordered Mesoporous CeO_2 Synthesized by Nanocasting from Cubic Ia3d Mesoporous MCM-48 Silica: Formation, Characterization and Photocatalytic Activity. *J. Phys. Chem. C* **2008**, *112*, 17809–17813.

(9) Ganduglia-Pirovano, M. V.; Hofmann, A.; Sauer, J. Oxygen Vacancies in Transition Metal and Rare Earth Oxides: Current State of Understanding and Remaining Challenges. *Surf. Sci. Rep.* **2007**, *62*, 219–270.

(10) Barreca, D.; Bruno, G.; Gasparotto, A.; Losurdo, M.; Tondello, E. Nanostructure and Optical Properties of CeO_2 Thin Films Obtained by Plasma-Enhanced Chemical Vapor Deposition. *Mater. Sci. Eng. C* **2003**, *23*, 1013–1016.

(11) Marabelli, F.; Wachter, P. Covalent Insulator CeO_2 - Optical Reflectivity Measurements. *Phys. Rev. B* **1987**, *36*, 1238–1243.

(12) Sun, C.; Li, H.; Chen, L. Nanostructured Ceria-Based Materials: Synthesis, Properties, and Applications. *Energy Environ. Sci.* **2012**, *5*, 8475.

(13) Zacherle, T.; Schriever, A.; De Souza, R. A.; Martin, M. *Ab Initio* Analysis of the Defect Structure of Ceria. *Phys. Rev. B* **2013**, *87*.

(14) Kumar, A.; Das, S.; Munusamy, P.; Self, W.; Baer, D. R.; Sayle, D. C.; Seal, S. Behavior of Nanoceria in Biologically-Relevant Environments. *Env. Sci Nano* **2014**, *1*, 516–532.

(15) Fujimori, A. Comment on "Spectroscopic Evidence for Localized and Extended f-Symmetry States in CeO_2." *Phys. Rev. Lett.* **1984**, *53*, 2518–2518.

(16) Wuilloud, E.; Delley, B.; Schneider, W.-D.; Baer, Y. Spectroscopic Study of Localized and Extended f-Symmetry States in CeO_2, CeN and $CeSi_2$. *J. Magn. Magn. Mater.* **1985**, *47*, 197–199.

(17) Skorodumova, N. V.; Ahuja, R.; Simak, S. I.; Abrikosov, I. A.; Johansson, B.; Lundqvist, B. I. Electronic, Bonding, and Optical Properties of CeO_2 and Ce_2O_3 from First Principles. *Phys. Rev. B* **2001**, *64*.

(18) Arul, N. S.; Mangalaraj, D.; Ramachandran, R.; Grace, A. N.; Han, J. I. Fabrication of CeO_2/Fe_2O_3 Composite Nanospindles for Enhanced Visible Light Driven Photocatalysts and Supercapacitor Electrodes. *J Mater Chem A* **2015**, *3*, 15248–15258.

(19) Tuller, H. L.; Nowick, A. S. Small Polaron Electron Transport in Reduced CeO_2 Single Crystals. *J. Phys. Chem. Solids* **1977**, *38*, 859–867.

(20) Tuller, H. L.; Nowick, A. S. Defect Structure and Electrical Properties of Nonstoichiometric CeO_2 Single Crystals. *J. Electrochem. Soc.* **1979**, *126*, 209–217.

(21) Griffiths, T. R.; Hubbard, H. V. S. A.; Davies, M. J. Electron Transfer Reactions in Non-Stoichiometric Ceria and Urania. *Inorganica Chim. Acta* **1994**, *225*, 305–317.

(22) Plata, J. J.; Márquez, A. M.; Sanz, J. F. Transport Properties in the CeO_{2-x} (111) Surface: From Charge Distribution to Ion-Electron Collaborative Migration. *J. Phys. Chem. C* **2013**, *117*, 25497–25503.

(23) Paier, J.; Penschke, C.; Sauer, J. Oxygen Defects and Surface Chemistry of Ceria: Quantum Chemical Studies Compared to Experiment. *Chem. Rev.* **2013**, *113*, 3949–3985.

(24) Bensalem, A.; Muller, J. C.; Bozon-Verduraz, F. Faraday Communications. From Bulk CeO2 to Supported Cerium–oxygen Clusters: A Diffuse Reflectance Approach. *J. Chem. Soc. Faraday Trans.* **1992**, *88*, 153–154.

(25) Tsunekawa, S.; Fukuda, T.; Kasuya, A. Blue Shift in Ultraviolet Absorption Spectra of Monodisperse CeO2-X Nanoparticles. *J. Appl. Phys.* **2000**, *87*, 1318–1321.

(26) Renuka, N. K. Structural Characteristics of Quantum-Size Ceria Nano Particles Synthesized via Simple Ammonia Precipitation. *J. Alloys Compd.* **2012**, *513*, 230–235.

(27) Ni, P.; Wei, X.; Guo, J.; Ye, X.; Yang, S. On the Origin of the Oxidizing Ability of Ceria Nanoparticles. *RSC Adv* **2015**, *5*, 97512–97519.

(28) Filtschew, A.; Hofmann, K.; Hess, C. Ceria and Its Defect Structure: New Insights from a Combined Spectroscopic Approach. *J. Phys. Chem. C* **2016**, *120*, 6694–6703.

(29) Nabavi, M.; Spalla, O.; Cabane, B. Surface Chemistry of Nanometric Ceria Particles in Aqueous Dispersions. *J. Colloid Interface Sci.* **1993**, *160*, 459–471.

(30) Karakoti, A. S.; Munusamy, P.; Hostetler, K.; Kodali, V.; Kuchibhatla, S.; Orr, G.; Pounds, J. G.; Teeguarden, J. G.; Thrall, B. D.; Baer, D. R. Preparation and Characterization Challenges to Understanding Environmental and Biological Impacts of Ceria Nanoparticles: Environmental and Biological Impacts of Nanoparticles. *Surf. Interface Anal.* **2012**, *44*, 882–889.

(31) Hernández-Alonso, M. D.; Hungría, A. B.; Martínez-Arias, A.; Fernández-García, M.; Coronado, J. M.; Conesa, J. C.; Soria, J. EPR Study of the Photoassisted Formation of Radicals on CeO_2 Nanoparticles Employed for Toluene Photooxidation. *Appl. Catal. B Environ.* **2004**, *50*, 167–175.

(32) Chaisorn, J.; Wetchakun, K.; Phanichphant, S.; Wetchakun, N. A Novel $CeO_2/InVO_4$ Composite with High Visible-Light Induced Photocatalytic Activity. *Mater. Lett.* **2015**, *160*, 75–80.

(33) Arul, N. S.; Mangalaraj, D.; Kim, T. W. Photocatalytic Degradation Mechanisms of CeO_2/Tb_2O_3 Nanotubes. *Appl. Surf. Sci.* **2015**, *349*, 459–464.

(34) Bamwenda, G. R.; Arakawa, H. Cerium Dioxide as a Photocatalyst for Water Decomposition to O_2 in the Presence of Ce^{4+} and Fe^{3+} Species. *J. Mol. Catal. Chem.* **2000**, *161*, 105–113.

(35) Primo, A.; Marino, T.; Corma, A.; Molinari, R.; García, H. Efficient Visible-Light Photocatalytic Water Splitting by Minute Amounts of Gold Supported on Nanoparticulate CeO_2 Obtained by a Biopolymer Templating Method. *J. Am. Chem. Soc.* **2011**, *133*, 6930–6933.

(36) Chiang, Y. M.; Lavik, E. B.; Blom, D. A. Defect Thermodynamics and Electrical Properties of Nanocrystalline Oxides: Pure and Doped CeO_2. *Nanostructured Mater.* **1997**, *9*, 633–642.

(37) Skorodumova, N. V.; Simak, S. I.; Lundqvist, B. I.; Abrikosov, I. A.; Johansson, B. Quantum Origin of the Oxygen Storage Capability of Ceria. *Phys. Rev. Lett.* **2002**, *89*.

(38) Box, G. E. P.; Hunter, J. S.; Hunter, W. G. *Statistics for Experimenters: Design, Innovation, and Discovery, 2nd Edition*; 2nd edition.; Wiley-Interscience: Hoboken, N.J, 2005.

(39) Chen, H.-I.; Chang, H.-Y. Synthesis of Nanocrystalline Cerium Oxide Particles by the Precipitation Method. *Ceram. Int.* **2005**, *31*, 795–802.

(40) Chen, H.-I.; Chang, H.-Y. Synthesis and Characterization of Nanocrystalline Cerium Oxide Powders by Two-Stage Non-Isothermal Precipitation. *Solid State Commun.* **2005**, *133*, 593–598.

(41) Ivanov, V. K.; Polezhaeva, O. S.; Shaporev, A. S.; Baranchikov, A. E.; Shcherbakov, A. B.; Usatenko, A. V. Synthesis and Thermal Stability of Nanocrystalline Ceria Sols Stabilized by Citric and Polyacrylic Acids. *Russ. J. Inorg. Chem.* **2010**, *55*, 328–332.

(42) Feldman, I. Use and Abuse of pH Measurements. *Anal. Chem.* **1956**, *28*, 1859–1866.

(43) Faure, B.; Salazar-Alvarez, G.; Ahniyaz, A.; Villaluenga, I.; Berriozabal, G.; De Miguel, Y. R.; Bergström, L. Dispersion and Surface Functionalization of Oxide Nanoparticles for Transparent Photocatalytic and UV-Protecting Coatings and Sunscreens. *Sci. Technol. Adv. Mater.* **2013**, *14*, 23001.

(44) Bravo, M.; Olivieri, A. C.; Oelckers, B. Nitrate Determination in Chilean Caliche Samples by UV-Visible Absorbance Measurements and Multivariate Calibration. *J. Chil. Chem. Soc.* **2009**, *54*, 93–98.

(45) Turner, S.; Lazar, S.; Freitag, B.; Egoavil, R.; Verbeeck, J.; Put, S.; Strauven, Y.; Van Tendeloo, G. High Resolution Mapping of Surface Reduction in Ceria Nanoparticles. *Nanoscale* **2011**, *3*, 3385.

(46) Reed, K.; Cormack, A.; Kulkarni, A.; Mayton, M.; Sayle, D.; Klaessig, F.; Stadler, B. Exploring the Properties and Applications of Nanoceria: Is There Still Plenty of Room at the Bottom? *Env. Sci Nano* **2014**, *1*, 390–405.

(47) Morales, D. A. Mathematical Modeling of Titration Curves. *J. Chemom.* **2002**, *16*, 247–260.

(48) Calatayud, M.; Maldonado, L.; Minot, C. Reactivity of $(TiO_2)_N$ Clusters (N = 1−10): Probing Gas-Phase Acidity and Basicity Properties. *J. Phys. Chem. C* **2008**, *112*, 16087–16095.

(49) Perrin, D. D. *Dissociation Constants of Inorganic Acids and Bases in Aqueous Solution,*; Butterworths: London, 1969.

(50) Kosmulski, M. *Chemical Properties of Material Surfaces*; CRC Press, 2001.

(51) Zholobak, N. M.; Ivanov, V. K.; Shcherbakov, A. B.; Shaporev, A. S.; Polezhaeva, O. S.; Baranchikov, A. Y.; Spivak, N. Y.; Tretyakov, Y. D. UV-Shielding Property, Photocatalytic Activity and Photocytotoxicity of Ceria Colloid Solutions. *J. Photochem. Photobiol. B* **2011**, *102*, 32–38.

(52) Trujillo-Reyes, J.; Vilchis-Nestor, A. R.; Majumdar, S.; Peralta-Videa, J. R.; Gardea-Torresdey, J. L. Citric Acid Modifies Surface Properties of Commercial CeO_2 Nanoparticles Reducing Their Toxicity and Cerium Uptake in Radish (Raphanus Sativus) Seedlings. *J. Hazard. Mater.* **2013**, *263*, 677–684.

(53) Stoianov, O. O.; Ivanov, V. K.; Shcherbakov, A. B.; Stoyanova, I. V.; Chivireva, N. A.; Antonovich, V. P. Determination of cerium(III) and cerium(IV) in Nanodisperse Ceria by Chemical Methods. *Russ. J. Inorg. Chem.* **2014**, *59*, 15–23.

(54) Wang, J.; Mei, Y.; Tanner, P. A. Luminescence Properties, Centroid Shift and Energy Transfer of Ce^{3+} in Aqueous Chloride Solutions. *J. Lumin.* **2014**, *146*, 440–444.

(55) Kuyper, A. C. The Oxidation of Citric Acid. *J. Am. Chem. Soc.* **1933**, *55*, 1722–1727.

(56) Sauvola, J.; Pietikäinen, M. Adaptive Document Image Binarization. *Pattern Recognit.* **2000**, *33*, 225–236.

(57) Dunphy Guzman, K. A.; Finnegan, M. P.; Banfield, J. F. Influence of Surface Potential on Aggregation and Transport of Titania Nanoparticles. *Environ. Sci. Technol.* **2006**, *40*, 7688–7693.

(58) Kalyanasundaram, K.; Grätzel, M. Applications of Functionalized Transition Metal Complexes in Photonic and Optoelectronic Devices. *Coord. Chem. Rev.* **1998**, *177*, 347–414.

(59) She, C.; Guo, J.; Irle, S.; Morokuma, K.; Mohler, D. L.; Zabri, H.; Odobel, F.; Youm, K.-T.; Liu, F.; Hupp, J. T.; *et al.* Comparison of Interfacial Electron Transfer through Carboxylate and Phosphonate Anchoring Groups †. *J. Phys. Chem. A* **2007**, *111*, 6832–6842.

(60) Wang, S.-W.; Wu, K.-L.; Ghadiri, E.; Lobello, M. G.; Ho, S.-T.; Chi, Y.; Moser, J.-E.; De Angelis, F.; Grätzel, M.; Nazeeruddin, M. K. Engineering of Thiocyanate-Free Ru(II) Sensitizers for High Efficiency Dye-Sensitized Solar Cells. *Chem. Sci.* **2013**, *4*, 2423.

(61) Lu, Z.; Karakoti, A.; Velarde, L.; Wang, W.; Yang, P.; Thevuthasan, S.; Wang, H. Dissociative Binding of Carboxylic Acid Ligand on Nanoceria Surface in Aqueous Solution: A Joint In Situ Spectroscopic Characterization and First-Principles Study. *J. Phys. Chem. C* **2013**, *117*, 24329–24338.

(62) Vlasova, N. N.; Golovkova, L. P.; Stukalina, N. G. Adsorption of Organic Acids on a Cerium Dioxide Surface. *Colloid J.* **2015**, *77*, 418–424.

(63) Huxter, V. M. Optical and Material Properties of Colloidal Semiconductor Nanocrystals, University of Toronto, 2009.

(64) Kormann, C.; Bahnemann, D. W.; Hoffmann, M. R. Preparation and Characterization of Quantum-Size Titanium Dioxide. *J. Phys. Chem.* **1988**, *92*, 5196–5201.

(65) Arul, N. S.; Mangalaraj, D.; Chen, P. C.; Ponpandian, N.; Viswanathan, C. Strong Quantum Confinement Effect in Nanocrystalline Cerium Oxide. *Mater. Lett.* **2011**, *65*, 2635–2638.

(66) Kuchibhatla, S. V. N. T.; Karakoti, A. S.; Baer, D. R.; Samudrala, S.; Engelhard, M. H.; Amonette, J. E.; Thevuthasan, S.; Seal, S. Influence of Aging and Environment on Nanoparticle Chemistry: Implication to Confinement Effects in Nanoceria. *J. Phys. Chem. C* **2012**, *116*, 14108–14114.

(67) Reyes-Coronado, D.; Rodríguez-Gattorno, G.; Espinosa-Pesqueira, M. E.; Cab, C.; de Coss, R.; Oskam, G. Phase-Pure TiO_2 Nanoparticles: Anatase, Brookite and Rutile. *Nanotechnology* **2008**, *19*, 145605.

(68) Grahn, H. T. *Introduction to Semiconductor Physics*; World Scientific, 1999.

(69) Tsunekawa, S.; Wang, J.-T.; Kawazoe, Y.; Kasuya, A. Blueshifts in the Ultraviolet Absorption Spectra of Cerium Oxide Nanocrystallites. *J. Appl. Phys.* **2003**, *94*, 3654.

(70) Hernández-Alonso, M. D.; Belén Hungría, A.; Martínez-Arias, A.; Coronado, J. M.; Carlos Conesa, J.; Soria, J.; Fernández-García, M. Confinement Effects in Quasi-Stoichiometric CeO_2 Nanoparticles. *Phys Chem Chem Phys* **2004**, *6*, 3524–3529.

(71) Polezhaeva, O. S.; Yaroshinskaya, N. V.; Ivanov, V. K. Synthesis of Nanosized Ceria with Controlled Particle Sizes and Bandgap Widths. *Russ. J. Inorg. Chem.* **2007**, *52*, 1184–1188.

(72) Phoka, S.; Laokul, P.; Swatsitang, E.; Promarak, V.; Seraphin, S.; Maensiri, S. Synthesis, Structural and Optical Properties of CeO_2 Nanoparticles Synthesized by a Simple Polyvinyl Pyrrolidone (PVP) Solution Route. *Mater. Chem. Phys.* **2009**, *115*, 423–428.

(73) Goharshadi, E. K.; Samiee, S.; Nancarrow, P. Fabrication of Cerium Oxide Nanoparticles: Characterization and Optical Properties. *J. Colloid Interface Sci.* **2011**, *356*, 473–480.

(74) Liu, I.-T.; Hon, M.-H.; Teoh, L. G. Structure and Optical Properties of CeO_2 Nanoparticles Synthesized by Precipitation. *J. Electron. Mater.* **2013**, *42*, 2536–2541.

(75) Ko, H.-H.; Yang, G.; Cheng, H.-Z.; Wang, M.-C.; Zhao, X. Growth and Optical Properties of Cerium Dioxide Nanocrystallites Prepared by Coprecipitation Routes. *Ceram. Int.* **2014**, *40*, 4055–4064.

(76) Tsunekawa, S.; Sahara, R.; Kawazoe, Y.; Kasuya, A. Origin of the Blue Shift in Ultraviolet Absorption Spectra of Nanocrystalline CeO_{2-x} Particles. *Mater. Trans. JIM* **2000**, *41*.

(77) Brus, L. Electronic Wave Functions in Semiconductor Clusters: Experiment and Theory. *J. Phys. Chem.* **1986**, *90*, 2555–2560.

(78) Zhang, F. Ceria Nanoparticles: Size, Size Distribution, and Shape. *J. Appl. Phys.* **2004**, *95*, 4319.

(79) Deshpande, S.; Patil, S.; Kuchibhatla, S. V.; Seal, S. Size Dependency Variation in Lattice Parameter and Valency States in Nanocrystalline Cerium Oxide. *Appl. Phys. Lett.* **2005**, *87*, 133113.

(80) Wu, L.; Wiesmann, H. J.; Moodenbaugh, A. R.; Klie, R. F.; Zhu, Y.; Welch, D. O.; Suenaga, M. Oxidation State and Lattice Expansion of CeO_{2-X} Nanoparticles as a Function of Particle Size. *Phys. Rev. B* **2004**, *69*.

(81) Tsunekawa, S.; Sahara, R.; Kawazoe, Y.; Ishikawa, K. Lattice Relaxation of Monosize CeO_{2-X} Nanocrystalline Particles. *Appl. Surf. Sci.* **1999**, *152*, 53–56.

(82) Tsunekawa, S.; Sivamohan, R.; Ito, S.; Kasuya, A.; Fukuda, T. Structural Study on Monosize CeO_{2-X} Nano-Particles. *Nanostructured Mater.* **1999**, *11*, 141–147.

(83) Babitha, K. K.; Sreedevi, A.; Priyanka, K. P.; Sabu, B.; Varghese, T. Structural Characterization and Optical Studies of CeO_2 Nanoparticles Synthesized by Chemical Precipitation. *Indian J. Pure Appl. Phys. IJPAP* **2015**, *53*, 596–603.

(84) Maensiri, S.; Masingboon, C.; Laokul, P.; Jareonboon, W.; Promarak, V.; Anderson, P. L.; Seraphin, S. Egg White Synthesis and Photoluminescence of Platelike Clusters of CeO_2 Nanoparticles. *Cryst. Growth Des.* **2007**, *7*, 950–955.

(85) Takeda, Y.; Mafuné, F. Formation of Wide Bandgap Cerium Oxide Nanoparticles by Laser Ablation in Aqueous Solution. *Chem. Phys. Lett.* **2014**, *599*, 110–115.

(86) Liu, B.; Liu, B.; Li, Q.; Li, Z.; Liu, R.; Zou, X.; Wu, W.; Cui, W.; Liu, Z.; Li, D.; *et al.* Solvothermal Synthesis of Monodisperse Self-Assembly CeO_2 Nanospheres and Their Enhanced Blue-Shifting in Ultraviolet Absorption. *J. Alloys Compd.* **2010**, *503*, 519–524.

(87) Lorite, I.; Romero, J. J.; Fernandez, J. F. Influence of the Nanoparticles Agglomeration State in the Quantum-Confinement Effects: Experimental Evidences. *AIP Adv.* **2015**, *5*, 37105.

(88) Paun, C.; Safonova, O. V.; Szlachetko, J.; Abdala, P. M.; Nachtegaal, M.; Sa, J.; Kleymenov, E.; Cervellino, A.; Krumeich, F.; van Bokhoven, J. A. Polyhedral

CeO_2 Nanoparticles: Size-Dependent Geometrical and Electronic Structure. *J. Phys. Chem. C* **2012**, *116*, 7312–7317.

(89) Inerbaev, T. M.; Karakoti, A. S.; Kuchibhatla, S. V. N. T.; Kumar, A.; Masunov, A. E.; Seal, S. Aqueous Medium Induced Optical Transitions in Cerium Oxide Nanoparticles. *Phys Chem Chem Phys* **2015**, *17*, 6217–6221.

(90) Bouchaud, B.; Balmain, J.; Bonnet, G.; Pedraza, F. pH-Distribution of Cerium Species in Aqueous Systems. *J. Rare Earths* **2012**, *30*, 559–562.

(91) Trovarelli, A. Catalytic Properties of Ceria and CeO_2 -Containing Materials. *Catal. Rev.* **1996**, *38*, 439–520.

(92) Wang, J.; Zhang, B.; Shen, M.; Wang, J.; Wang, W.; Ma, J.; Liu, S.; Jia, L. Effects of Fe-Doping of Ceria-Based Materials on Their Microstructural and Dynamic Oxygen Storage and Release Properties. *J. Sol-Gel Sci. Technol.* **2011**, *58*, 259–268.

(93) Bahnemann, D.; Henglein, A.; Spanhel, L. Detection of the Intermediates of Colloidal TiO_2-Catalysed Photoreactions. *Faraday Discuss. Chem. Soc.* **1984**, *78*, 151–163.

(94) Zawadzki, P. Absorption Spectra of Trapped Holes in Anatase TiO_2. *J. Phys. Chem. C* **2013**, *117*, 8647–8651.

(95) Schirmer, O.F.O^- Bound Small Polarons in Oxide Materials. *J. Phys. Condens. Matter* **2006**, *18*, R667–R704.

(96) Bahnemann, D.; Henglein, A.; Lilie, J.; Spanhel, L. Flash Photolysis Observation of the Absorption Spectra of Trapped Positive Holes and Electrons in Colloidal TiO_2. *J. Phys. Chem.* **1984**, *88*, 709–711.

(97) Genreith-Schriever, A. R.; Hebbeker, P.; Hinterberg, J.; Zacherle, T.; De Souza, R. A. Understanding Oxygen-Vacancy Migration in the Fluorite Oxide CeO_2: An Ab Initio Study of Impurity-Anion Migration. *J. Phys. Chem. C* **2015**, *119*, 28269–28275.

(98) Sayle, D. C.; Maicaneanu, S. A.; Watson, G. W. Atomistic Models for CeO_2 (111), (110), and (100) Nanoparticles, Supported on Yttrium-Stabilized Zirconia. *J. Am. Chem. Soc.* **2002**, *124*, 11429–11439.

(99) Tamaki, Y.; Furube, A.; Katoh, R.; Murai, M.; Hara, K.; Arakawa, H.; Tachiya, M. Trapping Dynamics of Electrons and Holes in a Nanocrystalline TiO_2 Film Revealed by Femtosecond Visible/near-Infrared Transient Absorption Spectroscopy. *Comptes Rendus Chim.* **2006**, *9*, 268–274.

(100) Rothenberger, G.; Moser, J.; Graetzel, M.; Serpone, N.; Sharma, D. K. Charge Carrier Trapping and Recombination Dynamics in Small Semiconductor Particles. *J. Am. Chem. Soc.* **1985**, *107*, 8054–8059.

(101) Qi, L.; Sehgal, A.; Castaing, J.-C.; Chapel, J.-P.; Fresnais, J.; Berret, J.-F.; Cousin, F. Redispersible Hybrid Nanopowders: Cerium Oxide Nanoparticle Complexes with Phosphonated-PEG Oligomers. *ACS Nano* **2008**, *2*, 879–888.

(102) Burnham, K. P. Multimodel Inference: Understanding AIC and BIC in Model Selection. *Sociol. Methods Res.* **2004**, *33*, 261–304.

(103) Schneider, J.; Matsuoka, M.; Takeuchi, M.; Zhang, J.; Horiuchi, Y.; Anpo, M.; Bahnemann, D. W. Understanding TiO_2 Photocatalysis: Mechanisms and Materials. *Chem. Rev.* **2014**, *114*, 9919–9986.

(104) Janotti, A.; Franchini, C.; Varley, J. B.; Kresse, G.; Van de Walle, C. G. Dual Behavior of Excess Electrons in Rutile TiO_2. *Phys. Status Solidi RRL – Rapid Res. Lett.* **2013**, *7*, 199–203.

(105) Savory, D. M.; McQuillan, A. J. IR Spectroscopic Behavior of Polaronic Trapped Electrons in TiO_2 under Aqueous Photocatalytic Conditions. *J. Phys. Chem. C* **2014**, *118*, 13680–13692.

(106) Liyanage, A. D.; Perera, S. D.; Tan, K.; Chabal, Y.; Balkus, K. J. Synthesis, Characterization, and Photocatalytic Activity of Y-Doped CeO_2 Nanorods. *ACS Catal.* **2014**, *4*, 577–584.

(107) Miyauchi, M.; Nakajima, A.; Watanabe, T.; Hashimoto, K. Photocatalysis and Photoinduced Hydrophilicity of Various Metal Oxide Thin Films. *Chem. Mater.* **2002**, *14*, 2812–2816.

(108) Serpone, N. Relative Photonic Efficiencies and Quantum Yields in Heterogeneous Photocatalysis. *J. Photochem. Photobiol. -Chem.* **1997**, *104*, 1–12.

(109) Ishibashi, K.; Fujishima, A.; Watanabe, T.; Hashimoto, K. Quantum Yields of Active Oxidative Species Formed on TiO_2 Photocatalyst. *J. Photochem. Photobiol. -Chem.* **2000**, *134*, 139–142.

(110) Bahnemann, D. W.; Hilgendorff, M.; Memming, R. Charge Carrier Dynamics at TiO_2 Particles: Reactivity of Free and Trapped Holes. *J. Phys. Chem. B* **1997**, *101*, 4265–4275.

(111) Sun, L. Z.; Bolton, J. R. Determination of the Quantum Yield for the Photochemical Generation of Hydroxyl Radicals in TiO_2 Suspensions. *J. Phys. Chem.* **1996**, *100*, 4127–4134.

(112) Anpo, M.; Shima, T.; Kodama, S.; Kubokawa, Y. Photocatalytic Hydrogenation of CH_3CCH with H_2O on Small-Particle TiO_2 - Size Quantization Effects and Reaction Intermediates. *J. Phys. Chem.* **1987**, *91*, 4305–4310.

(113) Panhans, M.; Blumenthal, R. A Thermodynamic and Electrical-Conductivity Study of Nonstoichiometric Cerium Dioxide. *Solid State Ion.* **1993**, *60*, 279–298.

(114) Baker, E.; Iqbal, M.; Knox, B. Conductivity Measurements on Ceria at High Oxygen Pressures. *J. Mater. Sci.* **1977**, *12*, 305–310.

(115) Holverson, E. L.; Kevane, C. J. Electrical Conduction by Oxygen Ions in Cerium Oxide. *J. Chem. Phys.* **1966**, *44*, 3692–3696.

(116) Shockley, W.; Read, W. Statistics of the Recombinations of Holes and Electrons. *Phys. Rev.* **1952**, *87*, 835–842.

(117) Yin, L.; Wang, Y.; Pang, G.; Koltypin, Y.; Gedanken, A. Sonochemical Synthesis of Cerium Oxide Nanoparticles—Effect of Additives and Quantum Size Effect. *J. Colloid Interface Sci.* **2002**, *246*, 78–84.

(118) Zhang, Y.-W.; Si, R.; Liao, C.-S.; Yan, C.-H.; Xiao, C.-X.; Kou, Y. Facile Alcohothermal Synthesis, Size-Dependent Ultraviolet Absorption, and Enhanced

CO Conversion Activity of Ceria Nanocrystals. *J. Phys. Chem. B* **2003**, *107*, 10159–10167.

(119) Sujana, M. G.; Chattopadyay, K. K.; Anand, S. Characterization and Optical Properties of Nano-Ceria Synthesized by Surfactant-Mediated Precipitation Technique in Mixed Solvent System. *Appl. Surf. Sci.* **2008**, *254*, 7405–7409.

(120) Kumar, A.; Babu, S.; Karakoti, A. S.; Schulte, A.; Seal, S. Luminescence Properties of Europium-Doped Cerium Oxide Nanoparticles: Role of Vacancy and Oxidation States. *Langmuir* **2009**, *25*, 10998–11007.

(121) Shehata, N.; Meehan, K.; Hudait, M.; Jain, N. Control of Oxygen Vacancies and Ce^{+3} Concentrations in Doped Ceria Nanoparticles via the Selection of Lanthanide Element. *J. Nanoparticle Res.* **2012**, *14*.

(122) Samiee, S.; Goharshadi, E. K.; Nancarrow, P. Optical Properties of Ceria Nanoparticles. *Proc. 4th Int. Conf. Nanostructures ICNS4* **2012**, 1222–1224.

(123) Manoharan, D.; Vishista, K. Optical Properties of Nano-Crystalline Cerium Dioxide Synthesized by Single Step Aqueous Citrate-Nitrate Gel Combustion Method. *Asian J. Chem.* **2013**, *25*.

CHAPTER 6

CONCLUSION

Excited electronic processes were analyzed for several ruthenium(II) polypyridyl complexes with bipyridine or phenanthroline ligands, a 1,2,3-triazole bridged supramolecular assembly of polypyridyl ruthenium(II) and cobalt(II) complexes, and Cerium Oxide nanoparticles after excitation with UV or visible light. These molecular components show potential for use as water-splitting photocatalysts, and understanding the excited-state phenomena in each system can aid in the development of more effective and efficient photocatalysis in these and other systems.

In Chapter 3, four polypyridyl complexes of the form $[Ru(bpy)_{3-n}(phen)_n]^{2+}$ (bpy = 2,2'-bipyridine, phen = 1,10-phenanthroline, n = 0, 1, 2 or 3) were analyzed using femtosecond transient absorption spectroscopy. Each complex displays an initial interligand electron-transfer (ILET) process that occurs with a rate faster than 10^{12} s^{-1}, observed as an ultrafast depolarization in time resolved anisotropy measurements. This rapid ILET results in the excited ^{3}MLCT state to be distributed statistically across all ligands at 1 ps, confirmed as equivalent contributions from each excited ligand in the magic-angle excited-state absorption (ESA) spectra. Over the next several picoseconds vibrational cooling dissipates excess energy in the complex and ILET rate slows down, becoming an activated process. As thermal barriers in the system begin to be rate limiting, rates of ILET between bpy and phen ligands start to differ, resulting in a Boltzmann distribution of ^{3}MLCT states where localization on bpy ligands is slightly more probable than localization on phen. This final distribution, established at times

>100 ps, is observable as contributions of each ligand in the ESA spectra, as well as by changes in the emission lifetime of the complexes. Using the Eyring-Polanyi equation and previous estimates of activation barriers of bpy and phen ligands, the rate of ILET in the thermally equilibrated ^{3}MLCT state are estimated to be on the time scale of tens of picoseconds.

The large changes in ILET rate observed for ruthenium complexes over the first 100 ps can help reconcile many of the disagreements in previous studies on the rates of transfer between ligands. It may also aid in the description of electron transfer process between metal-polypyridyl complexes and other electron acceptors, as these systems have been observed to undergo multiphasic electron transfer. Ultimately, an increased understanding of ILET processes on a single metal complex could be used to direct a photoexcited electron to a desired ligand, improving the efficiency of electron transfer in these photosensitized systems, which are typically connected by only one ligand.

One such photosensitized system, discussed in Chapter 4, is the supramolecular donor-bridge-acceptor complex, $[Ru\text{-}Co]^{8+}$. This multimetal assembly demonstrated an electron transfer process from an excited ruthenium polypyridyl complex to a central cobalt tris-phenanthroline complex via a 1,2,3-triazole bridge. The electron transfer process was deduced from emission of the ruthenium center, which displayed a biexponential decay with lifetimes of 140 ns and 890 ns, with relative amplitudes of 40% and 60% respectively. The small amplitude of the short lived component indicates that the electron transfer process is a minor pathway compared to the phosphorescence of the ^{3}MLCT state of ruthenium, which can be explained as a result of either a significant back electron-transfer process or a preferential localization on non-bridging bpy ligands. In

either case, the low electron transfer efficiency observed would result in a lower overall efficiency of photocatalysis.

The electron transfer process observed for $[Ru\text{-}Co]^{8+}$ is unexpectedly slow compared to other systems linking ruthenium and cobalt polypyridyl complexes, especially when considering the 1,2,3-triazole bridge allows for fast electron tunneling via π-conjugated bonds. Modeling the emission decay of $[Ru\text{-}Co]^{8+}$ indicates that the electron transfer rate occurs on timescales of hundreds of nanoseconds, which is orders of magnitude too slow to be described as an effect of ILET between ligands on the ruthenium center, which are described in Chapter 3 to occur with timescales of tens of picoseconds. It is proposed that the cause of this slow electron transfer rate is the attachment position of the bridge at the 5-position of the phenanthroline ligand. A previous study by Glazer et al. demonstrated that extending conjugation at the 5-position had almost no effect on the ^{3}MLCT transition energy or lifetime when compared to modifications to phenanthroline at the 3- or 4-positions, indicating that the beneficial effects of conjugation are particularly limited at the 5-position. This has been confirmed with computational studies, which show that the ^{3}MLCT state has no electronic density on the 5- or 6- positions of the phenanthroline ligand. Modifying the $[Ru\text{-}Co]^{8+}$ complex such that the triazole bridge is attached at the 4-position may drastically increase the electron transfer rates observed.

The photophysics and photochemical changes of citrate coated cerium oxide nanoparticles were analyzed in Chapter 5 using ultrafast transient absorption as well as long term irradiation with a UV-photoreactor. The charge transfer bands for both excited

electrons and holes are significantly blue shifted compared to TiO_2 or ZnO_2, indicating both charge carriers exist as small polarons that more deeply trapped than in other metal oxides. Time resolved decay kinetics for trapped holes displayed second order recombination kinetics with a lifetime of ~100 ps, even with excitation intensities below 1 photon per nanoparticle. This behavior is strikingly different from recombination in TiO_2 nanoparticles, which display first order kinetics under low excitation intensities. The second order nature of recombination is thought to be the result of the highly trapped nature of the electrons and holes in CeO_2, which behave as free particles rather than an excitonic pair.

The rate of electron-hole recombination in CeO_2 was found to depend on the pH of the solution, where decreasing the pH corresponded with longer recombination times, indicating that trap sites are likely at the surface. At pH below 10, the nanoparticles were also observed to undergo long-lasting reduction of Ce^{4+} to Ce^{3+}, presumably accompanied by releasing O_2 gas from the lattice structure. In acidic conditions, the Ce^{3+} ions may exit the nanoparticle as aqueous ions; however in neutral and basic pH the reduction is reversible on a timescale of minutes, showing a recovery of the nanoparticle absorption band.

Together, these photophysical investigations offer insight into the mechanisms of electron transfer that affect the overall efficiency of various water-splitting photocatalytic components. Understanding such fundamental processes can aid in the development of new and better photosensitized systems using a mechanistic, theory-driven approach.

BIBLIOGRAPHY

(1) Madureira, N. L. *Key Concepts in Energy*; Springer International Publishing: Cham, 2014.

(2) Perez, M.; Perez, R. *Int. Energy Agency SHC Programme Sol. Update* **2015**, *62*, 4–6.

(3) Statistical Review of World Energy | Energy economics | BP Global http://www.bp.com/en/global/corporate/energy-economics/statistical-review-of-world-energy.html (accessed Aug 1, 2016).

(4) Artero, V.; Fontecave, M. *Chem Soc Rev* **2013**, *42* (6), 2338–2356.

(5) Stoll, T.; Castillo, C. E.; Kayanuma, M.; Sandroni, M.; Daniel, C.; Odobel, F.; Fortage, J.; Collomb, M.-N. *Coord. Chem. Rev.* **2015**, *304–305*, 20–37.

(6) Kärkäs, M. D.; Johnston, E. V.; Verho, O.; Åkermark, B. *Acc. Chem. Res.* **2014**, *47* (1), 100–111.

(7) Concepcion, J. J.; Jurss, J. W.; Brennaman, M. K.; Hoertz, P. G.; Patrocinio, A. O. T.; Murakami Iha, N. Y.; Templeton, J. L.; Meyer, T. J. *Acc. Chem. Res.* **2009**, *42* (12), 1954–1965.

(8) Artero, V.; Chavarot-Kerlidou, M.; Fontecave, M. *Angew. Chem. Int. Ed.* **2011**, *50* (32), 7238–7266.

(9) Osterloh, F. E. *Chem. Mater.* **2008**, *20* (1), 35–54.

(10) Kudo, A.; Miseki, Y. *Chem Soc Rev* **2009**, *38* (1), 253–278.

(11) Kalisman, P.; Nakibli, Y.; Amirav, L. *Nano Lett.* **2016**, *16* (3), 1776–1781.

(12) Bamwenda, G. R.; Arakawa, H. *J. Mol. Catal. Chem.* **2000**, *161* (1), 105–113.

(13) Bamwenda, G. R.; Uesigi, T.; Abe, Y.; Sayama, K.; Arakawa, H. *Appl. Catal. Gen.* **2001**, *205* (1), 117–128.

(14) Brown, G. M.; Brunschwig, B. S.; Creutz, C.; Endicott, J. F.; Sutin, N. *J. Am. Chem. Soc.* **1979**, *101* (5), 1298–1300.

(15) Krishnan, C. V.; Creutz, C.; Mahajan, D.; Schwarz, H. A.; Sutin, N. *Isr. J. Chem.* **1982**, *22* (2), 98–106.

(16) Creutz, C.; Sutin, N. *Coord. Chem. Rev.* **1985**, *64* (MAY), 321–341.

(17) Bigi, J. P.; Hanna, T. E.; Harman, W. H.; Chang, A.; Chang, C. J. *Chem Commun* **2010**, *46* (6), 958–960.

(18) Cropek, D. M.; Metz, A.; Müller, A. M.; Gray, H. B.; Horne, T.; Horton, D. C.; Poluektov, O.; Tiede, D. M.; Weber, R. T.; Jarrett, W. L.; Phillips, J. D.; Holder, A. A. *Dalton Trans.* **2012**, *41* (42), 13060.

(19) Staehle, R.; Losse, S.; Filipovic, M. R.; Ivanović-Burmazović, I.; Vos, J. G.; Rau, S. *ChemPlusChem* **2014**, *79* (11), 1614–1621.

(20) Willkomm, J.; Muresan, N. M.; Reisner, E. *Chem Sci* **2015**, *6* (5), 2727–2736.

(21) Deponti, E.; Luisa, A.; Natali, M.; Iengo, E.; Scandola, F. *Dalton Trans* **2014**, *43* (43), 16345–16353.

(22) Asbury, J. B.; Wang, Y.-Q.; Hao, E.; Ghosh, H. N.; Lian, T. *Res. Chem. Intermed.* **2001**, *27* (4), 393–406.

(23) Kallioinen, J.; Benkö, G.; Sundström, V.; Korppi-Tommola, J. E. I.; Yartsev, A. P. *J. Phys. Chem. B* **2002**, *106* (17), 4396–4404.

(24) Benkö, G.; Kallioinen, J.; Myllyperkiö, P.; Trif, F.; Korppi-Tommola, J. E. I.; Yartsev, A. P.; Sundström, V. *J. Phys. Chem. B* **2004**, *108* (9), 2862–2867.

(25) Johansson, O.; Borgström, M.; Lomoth, R.; Palmblad, M.; Bergquist, J.; Hammarström, L.; Sun, L.; Åkermark, B. *Inorg. Chem.* **2003**, *42* (9), 2908–2918.

(26) Meylemans, H. A.; Lei, C.-F.; Damrauer, N. H. *Inorg. Chem.* **2008**, *47* (10), 4060–4076.

(27) Wenger, O. S. *Acc. Chem. Res.* **2011**, *44* (1), 25–35.

(28) Baron, A.; Herrero, C.; Quaranta, A.; Charlot, M.-F.; Leibl, W.; Vauzeilles, B.; Aukauloo, A. *Chem. Commun.* **2011**, *47* (39), 11011.

(29) Arachchige, S. M.; Shaw, R.; White, T. A.; Shenoy, V.; Tsui, H.-M.; Brewer, K. J. *ChemSusChem* **2011**, *4* (4), 514–518.

(30) White, T.; Knoll, J.; Arachchige, S.; Brewer, K. *Materials* **2011**, *5* (12), 27–46.

(31) McNamara, W. R.; Han, Z.; Yin, C.-J.; Brennessel, W. W.; Holland, P. L.; Eisenberg, R. *Proc. Natl. Acad. Sci.* **2012**, *109* (39), 15594–15599.

(32) Herrero, C.; Batchelor, L.; Baron, A.; El Ghachtouli, S.; Sheth, S.; Guillot, R.; Vauzeilles, B.; Sircoglou, M.; Mallah, T.; Leibl, W.; Aukauloo, A. *Eur. J. Inorg. Chem.* **2013**, No. 4, 494–499.

(33) Herrero, C.; Quaranta, A.; El Ghachtouli, S.; Vauzeilles, B.; Leibl, W.; Aukauloo, A. *Phys. Chem. Chem. Phys.* **2014**, *16* (24), 12067.

(34) López, A. M.; Natali, M.; Pizzolato, E.; Chiorboli, C.; Bonchio, M.; Sartorel, A.; Scandola, F. *Phys. Chem. Chem. Phys.* **2014**, *16* (24), 12000–12007.

(35) Stoll, T.; Gennari, M.; Fortage, J.; Castillo, C. E.; Rebarz, M.; Sliwa, M.; Poizat, O.; Odobel, F.; Deronzier, A.; Collomb, M.-N. *Angew. Chem. Int. Ed.* **2014**, *53* (6), 1654–1658.

(36) Herrero, C.; Quaranta, A.; Sircoglou, M.; Sénéchal-David, K.; Baron, A.; Marín, I. M.; Buron, C.; Baltaze, J.-P.; Leibl, W.; Aukauloo, A.; Banse, F. *Chem Sci* **2015**, *6* (4), 2323–2327.

(37) Wallin, S.; Davidsson, J.; Modin, J.; Hammarström, L. *J. Phys. Chem. A* **2005**, *109* (21), 4697–4704.

(38) Malone, R. A.; Kelley, D. F. *J. Chem. Phys.* **1991**, *95* (12), 8970–8976.

(39) Yeh, A. T.-W. *Ultrafast excited state dynamics of tris-(2, 2'-bipyridine) Ruthenium (II)*; Ernest Orlando Lawrence Berkeley National Lab., CA (US), 2000.

(40) Horvath, R.; Lombard, J.; Leprêtre, J.-C.; Collomb, M.-N.; Deronzier, A.; Chauvin, J.; Gordon, K. C. *Dalton Trans.* **2013**, *42* (47), 16527.

(41) Lombard, J.; Boulaouche, R.; Amilan Jose, D.; Chauvin, J.; Collomb, M.-N.; Deronzier, A. *Inorganica Chim. Acta* **2010**, *363* (1), 234–242.

(42) Kuhar, K.; Fredin, L. A.; Persson, P. *J. Phys. Chem. B* **2015**, *119* (24), 7378–7392.

(43) Holbrook, R. J.; Weinberg, D. J.; Peterson, M. D.; Weiss, E. A.; Meade, T. J. *J. Am. Chem. Soc.* **2015**, *137* (9), 3379–3385.

(44) Feskov, S. V.; Kichigina, A. O.; Ivanov, A. I. *J. Phys. Chem. A* **2011**, *115* (9), 1462–1471.

(45) Torieda, H.; Yoshimura, A.; Nozaki, K.; Sakai, S.; Ohno, T. *J. Phys. Chem. A* **2002**, *106* (46), 11034–11044.

(46) Downward, A. M.; Moore, E. G.; Hartshorn, R. M. *Chem. Commun.* **2011**, *47* (27), 7692.

(47) Shao, Y.; Lu, X.; Li, K.; Zhao, Z.; Shi, X.; Jin, D.; Zhu, H.; Yang, G.; Guo, W. *Mater. Chem. Phys.* **2015**, *162*, 6–10.

(48) Yoshimura, A.; Nozaki, K.; Ikeda, N.; Ohno, T. *J. Am. Chem. Soc.* **1993**, *115* (16), 7521–7522.

(49) Song, X.; Lei, Y.; Vanwallendal, S.; Perkovic, M.; Jackman, D.; Endicott, J.; Rillema, D. *J. Phys. Chem.* **1993**, *97* (13), 3225–3236.

(50) Fihri, A.; Artero, V.; Razavet, M.; Baffert, C.; Leibl, W.; Fontecave, M. *Angew. Chem. Int. Ed.* **2008**, *47* (3), 564–567.

(51) Canton, S. E.; Kjær, K. S.; Vankó, G.; van Driel, T. B.; Adachi, S.; Bordage, A.; Bressler, C.; Chabera, P.; Christensen, M.; Dohn, A. O.; Galler, A.; Gawelda, W.; Gosztola, D.; Haldrup, K.; Harlang, T.; Liu, Y.; Møller, K. B.; Németh, Z.; Nozawa, S.; Pápai, M.; Sato, T.; Sato, T.; Suarez-Alcantara, K.; Togashi, T.; Tono, K.; Uhlig, J.; Vithanage, D. A.; Wärnmark, K.; Yabashi, M.; Zhang, J.; Sundström, V.; Nielsen, M. M. *Nat. Commun.* **2015**, *6*, 6359.

(52) Kirch, M.; Lehn, J.-M.; Sauvage, J.-P. *Helv. Chim. Acta* **1979**, *62* (4), 1345–1384.

(53) Krist, K.; Gafney, H. *J. Phys. Chem.* **1982**, *86* (6), 951–958.

(54) Huang, S.-M. Y.; Gafney, H. D. *J. Phys. Chem.* **1977**, *81* (26), 2602–2604.

(55) Creutz, C.; Sutin, N. *Inorg. Chem.* **1976**, *15* (2), 496–499.

(56) Yoshimura, A.; Uddin, M. J.; Amasaki, N.; Ohno, T. *J. Phys. Chem. A* **2001**, *105* (48), 10846–10853.

(57) Berkoff, R.; Krist, K.; Gafney, H. D. *Inorg. Chem.* **1980**, *19* (1), 1–7.

(58) Lin, C.-T.; Sutin, N. *J. Phys. Chem.* **1976**, *80* (2), 97–105.

(59) Schulze, B.; Schubert, U. S. *Chem. Soc. Rev.* **2014**, *43* (8), 2522.

(60) Natali, M.; Ravaglia, M.; Scandola, F.; Boixel, J.; Pellegrin, Y.; Blart, E.; Odobel, F. *J. Phys. Chem. C* **2013**, 130912075807001.

(61) Natali, M.; Orlandi, M.; Chiorboli, C.; Iengo, E.; Bertolasi, V.; Scandola, F. *Photochem. Photobiol. Sci.* **2013**, *12* (10), 1749.

(62) Cardiel, A. C.; Benson, M. C.; Bishop, L. M.; Louis, K.; Yeager, J.; Tan, Y.; Hamers, R. J. *Abstr. Pap. Am. Chem. Soc.* **2012**, *243*.

(63) Schneider, J.; Matsuoka, M.; Takeuchi, M.; Zhang, J.; Horiuchi, Y.; Anpo, M.; Bahnemann, D. W. *Chem. Rev.* **2014**, *114* (19), 9919–9986.

(64) Bahnemann, D.; Henglein, A.; Lilie, J.; Spanhel, L. *J. Phys. Chem.* **1984**, *88* (4), 709–711.

(65) Zawadzki, P. *J. Phys. Chem. C* **2013**, *117* (17), 8647–8651.

(66) ASTM International: West Conshohocken, PA, 2012.

(67) Laimgruber, S.; Schachenmayr, H.; Schmidt, B.; Zinth, W.; Gilch, P. *Appl. Phys. B* **2006**, *85* (4), 557–564.

(68) Juris, A.; Balzani, V.; Barigelletti, F.; Campagna, S.; Belser, P. l; Von Zelewsky, A. *Coord. Chem. Rev.* **1988**, *84*, 85–277.

(69) Wang, S. *Photochem. Photobiol.* **1962**, *1* (2), 135–145.

(70) Kuhn, H. J.; Braslavsky, S. E.; Schmidt, R. *Pure Appl. Chem.* **2004**, *76* (12), 2105–2146.

(71) Numao, N.; Hamada, T.; Yonemitsu, O. *Tetrahedron Lett.* **1977**, No. 19, 1661–1664.

(72) Gardecki, J. A.; Maroncelli, M. *Appl. Spectrosc.* **1998**, *52* (9), 1179–1189.

(73) Damrauer, N. H.; Cerullo, G.; Yeh, A.; Boussie, T. R.; Shank, C. V.; McCusker, J. K. *Science* **1997**, *275* (5296), 54–57.

(74) McCusker, J. K. *Acc. Chem. Res.* **2003**, *36* (12), 876–887.

(75) Ardo, S.; Meyer, G. J. *Chem Soc Rev* **2009**, *38* (1), 115–164.

(76) Heimer, T. A.; DArcangelis, S. T.; Farzad, F.; Stipkala, J. M.; Meyer, G. J. *Inorg. Chem.* **1996**, *35* (18), 5319–5324.

(77) Cushing, J. P.; Butoi, C.; Kelley, D. F. *J. Phys. Chem. A* **1997**, *101* (39), 7222–7230.

(78) Shaw, G. B.; Brown, C. L.; Papanikolas, J. M. *J. Phys. Chem. A* **2002**, *106* (8), 1483–1495.

(79) Hewitt, J. T.; Vallett, P. J.; Damrauer, N. H. *J. Phys. Chem. A* **2012**, *116* (47), 11536–11547.

(80) Ghosh, R.; Palit, D. K. *Phys Chem Chem Phys* **2014**, *16* (1), 219–226.

(81) Benniston, A.; Harriman, A. *Coord. Chem. Rev.* **2008**, *252* (23–24), 2528–2539.

(82) Kumar, C.; Barton, J.; Gould, I.; Turro, N.; Vanhouten, J. *Inorg. Chem.* **1988**, *27* (4), 648–651.

(83) Chang, Y. J.; Xu, X.; Yabe, T.; Yu, S. C.; Anderson, D. R.; Orman, L. K.; Hopkins, J. B. *J. Phys. Chem.* **1990**, *94* (2), 729–736.

(84) Baggott, J.; Gregory, G.; Pilling, M.; Anderson, S.; Seddon, K.; Turp, J. *J. Chem. Soc.-Faraday Trans. Ii* **1983**, *79*, 195–210.

(85) Crosby, G.; Elfring, W. *J. Phys. Chem.* **1976**, *80* (20), 2206–2211.

(86) Cannizzo, A.; van Mourik, F.; Gawelda, W.; Zgrablic, G.; Bressler, C.; Chergui, M. *Angew. Chem. Int. Ed.* **2006**, *45* (19), 3174–3176.

(87) Tarnovsky, A. N.; Gawelda, W.; Johnson, M.; Bressler, C.; Chergui, M. *J. Phys. Chem. B* **2006**, *110* (51), 26497–26505.

(88) Chang, C.-W.; Chou, C. K.; Chang, I.-J.; Lee, Y.-P.; Diau, E. W.-G. *J. Phys. Chem. C* **2007**, *111* (35), 13288–13296.

(89) Dattelbaum, D. M.; Kober, E. M.; Papanikolas, J. M.; Meyer, T. J. *Chem. Phys.* **2006**, *326* (1), 71–78.

(90) Sullivan, B. P.; Salmon, D. J.; Meyer, T. J. *Inorg. Chem.* **1978**, *17* (12), 3334–3341.

(91) Evans, I. P.; Spencer, A.; Wilkinson, G. *J. Chem. Soc. Dalton Trans.* **1973**, No. 2, 204–209.

(92) Szafran, Z.; Pike, R. M.; Singh, M. M. *Microscale Inorganic Chemistry: A Comprehensive Laboratory Experience*, 1 edition.; Wiley: New York, 1991.

(93) Henseler, A.; Vauthey, E. *Chem. Phys. Lett.* **1994**, *228*, 66–72.

(94) Kalyanasundaram, K. *Coord. Chem. Rev.* **1982**, *46*, 159–244.

(95) Yoshimura, A.; Hoffman, M.; Sun, H. *J. Photochem. Photobiol. -Chem.* **1993**, *70* (1), 29–33.

(96) Staniewicz, R. J.; Sympson, R. F.; Hendricker, D. G. *Inorg. Chem.* **1977**, *16* (9), 2166–2171.

(97) Hughes, H. P.; Martin, D.; Bell, S.; McGarvey, J. J.; Vos, J. G. *Inorg. Chem.* **1993**, *32* (20), 4402–4408.

(98) Glazer, E. C.; Magde, D.; Tor, Y. *J. Am. Chem. Soc.* **2007**, *129* (27), 8544–8551.

(99) Sakuda, E.; Ando, Y.; Ito, A.; Kitamura, N. *Inorg. Chem.* **2011**, *50* (5), 1603–1613.

(100) Müller, P.; Brettel, K. *Photochem. Photobiol. Sci.* **2012**, *11* (4), 632.

(101) Henry, W.; Coates, C. G.; Brady, C.; Ronayne, K. L.; Matousek, P.; Towrie, M.; Botchway, S. W.; Parker, A. W.; Vos, J. G.; Browne, W. R.; McGarvey, J. J. *J. Phys. Chem. A* **2008**, *112* (20), 4537–4544.

(102) Ohno, T.; Yoshimura, A.; Prasad, D.; Hoffman, M. *J. Phys. Chem.* **1991**, *95* (12), 4723–4728.

(103) Oh, D. H.; Boxer, S. G. *J. Am. Chem. Soc.* **1989**, *111* (3), 1130–1131.

(104) Karki, L.; Hupp, J. T. *Inorg. Chem.* **1997**, *36* (15), 3318–3321.

(105) Caspar, J. V.; Meyer, T. J. *Inorg. Chem.* **1983**, *22* (17), 2444–2453.

(106) Blakley, R.; Myrick, M.; Pittman, R.; Dearmond, M. *J. Phys. Chem.* **1990**, *94* (12), 4804–4809.

(107) Sun, H.; Hoffman, M. Z. *J. Phys. Chem.* **1993**, *97* (19), 5014–5018.

(108) Motten, A.; Hanck, K.; Dearmond, M. *Chem. Phys. Lett.* **1981**, *79* (3), 541–546.

(109) Heath, G.; Yellowlees, L.; Braterman, P. *Chem. Phys. Lett.* **1982**, *92* (6), 646–648.

(110) Bensasson, R.; Salet, C.; Balzani, V. *J. Am. Chem. Soc.* **1976**, *98* (12), 3722–3724.

(111) Mahon, C.; Reynolds, W. L. *Inorg. Chem.* **1967**, *6* (10), 1927–1928.

(112) Damrauer, N. H.; McCusker, J. K. *J. Phys. Chem. A* **1999**, *103* (42), 8440–8446.

(113) Henrich, J. D.; Zhang, H.; Dutta, P. K.; Kohler, B. *J. Phys. Chem. B* **2010**, *114* (45), 14679–14688.

(114) Kovalenko, S. A.; Schanz, R.; Hennig, H.; Ernsting, N. P. *J. Chem. Phys.* **2001**, *115* (7), 3256.

(115) Middleton, C. T.; Cohen, B.; Kohler, B. *J. Phys. Chem. A* **2007**, *111* (42), 10460–10467.

(116) Bossert, J.; Daniel, C. *Coord. Chem. Rev.* **2008**, *252* (23–24), 2493–2503.

(117) Shaw, G. B.; Styers-Barnett, D. J.; Gannon, E. Z.; Granger, J. C.; Papanikolas, J. M. *J. Phys. Chem. A* **2004**, *108* (23), 4998–5006.

(118) Miller, S. A.; Moran, A. M. *J. Phys. Chem. A* **2010**, *114* (5), 2117–2126.

(119) Cooley, L.; Bergquist, P.; Kelley, D. *J. Am. Chem. Soc.* **1990**, *112* (7), 2612–2617.

(120) Schoonover, J. R.; Dattelbaum, D. M.; Malko, A.; Klimov, V. I.; Meyer, T. J.; Styers-Barnett, D. J.; Gannon, E. Z.; Granger, J. C.; Aldridge, W. S.; Papanikolas, J. M. *J. Phys. Chem. A* **2005**, *109* (11), 2472–2475.

(121) Önfelt, B.; Lincoln, P.; Nordén, B.; Baskin, J. S.; Zewail, A. H. *Proc. Natl. Acad. Sci.* **2000**, *97* (11), 5708–5713.

(122) Benkö, G.; Kallioinen, J.; Korppi-Tommola, J. E. I.; Yartsev, A. P.; Sundström, V. *J. Am. Chem. Soc.* **2002**, *124* (3), 489–493.

(123) Prier, C. K.; Rankic, D. A.; MacMillan, D. W. C. *Chem. Rev.* **2013**, *113* (7), 5322–5363.

(124) Lemmetyinen, H.; Tkachenko, N. V.; Efimov, A.; Niemi, M. *Phys Chem Chem Phys* **2011**, *13* (2), 397–412.

(125) Fujitsuka, M.; Kim, S. S.; Lu, C.; Tojo, S.; Majima, T. *J. Phys. Chem. B* **2015**, *119* (24), 7275–7282.

(126) Gilbert, M.; Albinsson, B. *Chem. Soc. Rev.* **2015**, *44* (4), 845–862.

(127) Wenger, O. S. *Coord. Chem. Rev.* **2009**, *253* (9–10), 1439–1457.

(128) Kuchi, V.; Oliver, A. M.; Paddon-Row, M. N.; Howe, R. F. *Chem. Commun.* **1999**, No. 12, 1149–1150.

(129) Bixon, M.; Jortner, J.; Verhoeven, J. *J. Am. Chem. Soc.* **1994**, *116* (16), 7349–7355.

(130) Wiberg, J.; Guo, L.; Pettersson, K.; Nilsson, D.; Ljungdahl, T.; Martensson, J.; Albinsson, B. *J. Am. Chem. Soc.* **2007**, *129* (1), 155–163.

(131) Glover, S. D.; Goeltz, J. C.; Lear, B. J.; Kubiak, C. P. *Coord. Chem. Rev.* **2010**, *254* (3–4), 331–345.

(132) Herrero, C.; Quaranta, A.; Leibl, W.; Rutherford, A. W.; Aukauloo, A. *Energy Environ. Sci.* **2011**, *4* (7), 2353.

(133) Arrigo, A.; Santoro, A.; Indelli, M. T.; Natali, M.; Scandola, F.; Campagna, S. *Phys Chem Chem Phys* **2014**, *16* (3), 818–826.

(134) Wielopolski, M. In *Testing Molecular Wires*; Springer Berlin Heidelberg: Berlin, Heidelberg, 2010; pp 27–54.

(135) Weiss, E. A.; Wasielewski, M. R.; Ratner, M. A. In *Molecular Wires and Electronics*; Springer Berlin Heidelberg: Berlin, Heidelberg, 2005; Vol. 257, pp 103–133.

(136) Salomon, A.; Cahen, D.; Lindsay, S.; Tomfohr, J.; Engelkes, V. B.; Frisbie, C. D. *Adv. Mater.* **2003**, *15* (22), 1881–1890.

(137) Joachim, C.; Magoga, M. *Chem. Phys.* **2002**, *281* (2–3), 347–352.

(138) Hu, Y.; Zhu, Y.; Gao, H.; Guo, H. *Phys. Rev. Lett.* **2005**, *95* (15).

(139) Choi, S. H.; Risko, C.; Delgado, M. C. R.; Kim, B.; Brédas, J.-L.; Frisbie, C. D. *J. Am. Chem. Soc.* **2010**, *132* (12), 4358–4368.

(140) Schubert, C.; Margraf, J. T.; Clark, T.; Guldi, D. M. *Chem Soc Rev* **2015**, *44* (4), 988–998.

(141) Chiorboli, C.; Indelli, M. T.; Scandola, F. In *Molecular Wires and Electronics*; Springer Berlin Heidelberg: Berlin, Heidelberg, 2005; Vol. 257, pp 63–102.

(142) Zabarska, N.; Stumper, A.; Rau, S. *Dalton Trans.* **2016**, *45* (6), 2338–2351.

(143) Ladomenou, K.; Nikolaou, V.; Charalambidis, G.; Coutsolelos, A. G. *Coord. Chem. Rev.* **2016**, *306*, 1–42.

(144) de Miguel, G.; Wielopolski, M.; Schuster, D. I.; Fazio, M. A.; Lee, O. P.; Haley, C. K.; Ortiz, A. L.; Echegoyen, L.; Clark, T.; Guldi, D. M. *J. Am. Chem. Soc.* **2011**, *133* (33), 13036–13054.

(145) Ganapathi, E.; Madhu, S.; Ravikanth, M. *Tetrahedron* **2014**, *70* (3), 664–671.

(146) Farràs, P.; Benniston, A. C. *Tetrahedron Lett.* **2014**, *55* (51), 7011–7014.

(147) Guo, S.; Ma, L.; Zhao, J.; Küçüköz, B.; Karatay, A.; Hayvali, M.; Yaglioglu, H. G.; Elmali, A. *Chem. Sci.* **2013**, *5* (2), 489–500.

(148) Benson, M. C.; Ruther, R. E.; Gerken, J. B.; Rigsby, M. L.; Bishop, L. M.; Tan, Y.; Stahl, S. S.; Hamers, R. J. *Acs Appl. Mater. Interfaces* **2011**, *3* (8), 3110–3119.

(149) Baron, A.; Herrero, C.; Quaranta, A.; Charlot, M.-F.; Leibl, W.; Vauzeilles, B.; Aukauloo, A. *Inorg. Chem.* **2012**, *51* (11), 5985–5987.

(150) Sun, Y.; Chen, Z.; Puodziukynaite, E.; Jenkins, D. M.; Reynolds, J. R.; Schanze, K. S. *Macromolecules* **2012**, *45* (6), 2632–2642.

(151) Sheth, S.; Baron, A.; Herrero, C.; Vauzeilles, B.; Aukauloo, A.; Leibl, W. *Photochem. Photobiol. Sci.* **2013**, *12* (6), 1074.

(152) Fang, Z.; Ito, A.; Luo, H.; Ashford, D. L.; Concepcion, J. J.; Alibabaei, L.; Meye, T. J. *Dalton Trans.* **2015**, *44* (18), 8640–8648.

(153) Sayed, S. Y.; Bayat, A.; Kondratenko, M.; Leroux, Y.; Hapiot, P.; McCreery, R. L. *J. Am. Chem. Soc.* **2013**, *135* (35), 12972–12975.

(154) Kondratenko, M.; Stoyanov, S. R.; Gusarov, S.; Kovalenko, A.; McCreery, R. L. *J. Phys. Chem. C* **2015**, *119* (21), 11286–11295.

(155) Devaraj, N. K.; Decreau, R. A.; Ebina, W.; Collman, J. P.; Chidsey, C. E. D. *J. Phys. Chem. B* **2006**, *110* (32), 15955–15962.

(156) Mukherjee, A.; Kokhan, O.; Huang, J.; Niklas, J.; Chen, L. X.; Tiede, D. M.; Mulfort, K. L. *Phys. Chem. Chem. Phys.* **2013**, *15* (48), 21070.

(157) Li, C.; Wang, M.; Pan, J.; Zhang, P.; Zhang, R.; Sun, L. *J. Organomet. Chem.* **2009**, *694* (17), 2814–2819.

(158) Palmer, R.; Piper, T. *Inorg. Chem.* **1966**, *5* (5), 864-.

(159) Kremer, S.; Henke, W.; Reinen, D. *Inorg. Chem.* **1982**, *21* (8), 3013–3022.

(160) Yamasaki, K.; Hara, T.; Yasuda, M. *Proc. Jpn. Acad.* **1953**, *29* (7), 337–341.

(161) Fabian, R. H.; Klassen, D. M.; Sonntag, R. W. *Inorg. Chem.* **1980**, *19* (7), 1977–1982.

(162) Ruminski, R.; Petersen, J. *Inorganica Chim. Acta-Artic. Lett.* **1984**, *88* (1), 63–66.

(163) Juris, A.; Barigelletti, F.; Balzani, V.; Belser, P.; Von Zelewsky, A. *Inorg. Chem.* **1985**, *24* (2), 202–206.

(164) Schofield, K.; Grimmett, M. R.; Keene, B. R. T. *Heteroaromatic Nitrogen Compounds: The Azoles*; CUP Archive, 1976.

(165) Gajardo, F.; Loeb, B. *J. Chil. Chem. Soc.* **2011**, *56* (2), 697–701.

(166) Steinfeld, J. I.; Francisco, J. S.; Hase, W. L. *Chemical Kinetics and Dynamics*, 2 edition.; Pearson: Upper Saddle River, N.J, 1998.

(167) Smallwood, I. M. *Handbook of organic solvent properties*; Arnold ; Halsted Press: London : New York, 1996.

(168) Einstein, A. *Ann. Phys.* **1906**, *19* (2), 289–306.

(169) Masuda, Y.; Yamatera, H. *J. Phys. Chem.* **1984**, *88* (16), 3425–3431.

(170) Harrowfield, J.; Sobolev, A. *Aust. J. Chem.* **1994**, *47* (4), 763–767.

(171) Váhovská, L.; Potoèòák, I. *Mater. Struct. Chem. Biol. Phys. Technol.* **2012**, *19* (2), 102–104.

(172) Krishnan, C. V.; Brunschwig, B. S.; Creutz, C.; Sutin, N. *J. Am. Chem. Soc.* **1985**, *107* (7), 2005–2015.

(173) Szalda, D. J.; Creutz, C.; Mahajan, D.; Sutin, N. *Inorg. Chem.* **1983**, *22* (17), 2372–2379.

(174) Nozaki, K.; Yoshimura, A.; Ohno, T. *J. Chem. Sci.* **1993**, *105* (6), 495–503.

(175) Palmer, M. H.; Hoffmann, S. V.; Jones, N. C.; Head, A. R.; Lichtenberger, D. L. *J. Chem. Phys.* **2011**, *134* (8), 84309.

(176) Vuik, C. P. J.; Kane-Maguire, N. A. P.; Langford, C. H. *Can. J. Chem.* **1975**, *53* (20), 3121–3127.

(177) Rau, S.; Walther, D.; Vos, J. G. *Dalton Trans.* **2007**, No. 9, 915.

(178) Schulz, M.; Karnahl, M.; Schwalbe, M.; Vos, J. G. *Coord. Chem. Rev.* **2012**, *256* (15–16), 1682–1705.

(179) Zhang, C.; Du, M.-H.; Cheng, H.-P.; Zhang, X.-G.; Roitberg, A. E.; Krause, J. L. *Phys. Rev. Lett.* **2004**, *92* (15).

(180) Wang, Y.; Cheng, H.-P. *Phys. Rev. B* **2012**, *86* (3).

(181) Guédon, C. M.; Valkenier, H.; Markussen, T.; Thygesen, K. S.; Hummelen, J. C.; van der Molen, S. J. *Nat. Nanotechnol.* **2012**, *7* (5), 305–309.

(182) Solomon, G. C.; Andrews, D. Q.; Hansen, T.; Goldsmith, R. H.; Wasielewski, M. R.; Van Duyne, R. P.; Ratner, M. A. *J. Chem. Phys.* **2008**, *129* (5), 54701.

(183) Phelan, N. F.; Orchin, M. *J Chem Educ* **1968**, *45* (10), 633.

(184) Maiti, S. K. *Solid State Commun.* **2008**, *145* (3), 126–131.

(185) Walczak, K. *Open Chem.* **2004**, *2* (3).

(186) Ma, X.; Yan, L.; Wang, X.; Guo, Q.; Xia, A. *Phys. Chem. Chem. Phys.* **2011**, *13* (38), 17273.

(187) Walter, D.; Neuhauser, D.; Baer, R. *Chem. Phys.* **2004**, *299* (1), 139–145.

(188) Arroyo, C. R.; Frisenda, R.; Moth-Poulsen, K.; Seldenthuis, J. S.; Bjørnholm, T.; van der Zant, H. S. *Nanoscale Res. Lett.* **2013**, *8* (1), 1.

(189) Zheng, K. C.; Wang, J. P.; Liu, X. W.; Shen, Y.; Yun, F. C. *J. Mol. Struct. THEOCHEM* **2002**, *577* (2), 95–105.

(190) Montini, T.; Melchionna, M.; Monai, M.; Fornasiero, P. *Chem. Rev.* **2016**, *116* (10), 5987–6041.

(191) Abanades, S.; Flamant, G. *Sol. Energy* **2006**, *80* (12), 1611–1623.

(192) Hernández-Alonso, M. D.; Fresno, F.; Suárez, S.; Coronado, J. M. *Energy Environ. Sci.* **2009**, *2* (12), 1231.

(193) Pouretedal, H. R.; Kadkhodaie, A. *Chin. J. Catal.* **2010**, *31* (11–12), 1328–1334.

(194) Ji, P.; Zhang, J.; Chen, F.; Anpo, M. *Appl. Catal. B Environ.* **2009**, *85* (3–4), 148–154.

(195) Zhai, Y.; Zhang, S.; Pang, H. *Mater. Lett.* **2007**, *61* (8–9), 1863–1866.

(196) Ji, P.; Zhang, J.; Chen, F.; Anpo, M. *J. Phys. Chem. C* **2008**, *112* (46), 17809–17813.

(197) Ganduglia-Pirovano, M. V.; Hofmann, A.; Sauer, J. *Surf. Sci. Rep.* **2007**, *62* (6), 219–270.

(198) Barreca, D.; Bruno, G.; Gasparotto, A.; Losurdo, M.; Tondello, E. *Mater. Sci. Eng. C* **2003**, *23* (6–8), 1013–1016.

(199) Marabelli, F.; Wachter, P. *Phys. Rev. B* **1987**, *36* (2), 1238–1243.

(200) Sun, C.; Li, H.; Chen, L. *Energy Environ. Sci.* **2012**, *5* (9), 8475.

(201) Zacherle, T.; Schriever, A.; De Souza, R. A.; Martin, M. *Phys. Rev. B* **2013**, *87* (13).

(202) Kumar, A.; Das, S.; Munusamy, P.; Self, W.; Baer, D. R.; Sayle, D. C.; Seal, S. *Env. Sci Nano* **2014**, *1* (6), 516–532.

(203) Fujimori, A. *Phys. Rev. Lett.* **1984**, *53* (26), 2518–2518.

(204) Wuilloud, E.; Delley, B.; Schneider, W.-D.; Baer, Y. *J. Magn. Magn. Mater.* **1985**, *47*, 197–199.

(205) Skorodumova, N. V.; Ahuja, R.; Simak, S. I.; Abrikosov, I. A.; Johansson, B.; Lundqvist, B. I. *Phys. Rev. B* **2001**, *64* (11).

(206) Arul, N. S.; Mangalaraj, D.; Ramachandran, R.; Grace, A. N.; Han, J. I. *J Mater Chem A* **2015**, *3* (29), 15248–15258.

(207) Tuller, H. L.; Nowick, A. S. *J. Phys. Chem. Solids* **1977**, *38* (8), 859–867.

(208) Tuller, H. L.; Nowick, A. S. *J. Electrochem. Soc.* **1979**, *126* (2), 209–217.

(209) Plata, J. J.; Márquez, A. M.; Sanz, J. F. *J. Phys. Chem. C* **2013**, *117* (48), 25497–25503.

(210) Paier, J.; Penschke, C.; Sauer, J. *Chem. Rev.* **2013**, *113* (6), 3949–3985.

(211) Bensalem, A.; Muller, J. C.; Bozon-Verduraz, F. *J. Chem. Soc. Faraday Trans.* **1992**, *88* (1), 153–154.

(212) Tsunekawa, S.; Fukuda, T.; Kasuya, A. *J. Appl. Phys.* **2000**, *87* (3), 1318–1321.

(213) Renuka, N. K. *J. Alloys Compd.* **2012**, *513*, 230–235.

(214) Ni, P.; Wei, X.; Guo, J.; Ye, X.; Yang, S. *RSC Adv* **2015**, *5* (118), 97512–97519.

(215) Filtschew, A.; Hofmann, K.; Hess, C. *J. Phys. Chem. C* **2016**, *120* (12), 6694–6703.

(216) Nabavi, M.; Spalla, O.; Cabane, B. *J. Colloid Interface Sci.* **1993**, *160* (2), 459–471.

(217) Karakoti, A. S.; Munusamy, P.; Hostetler, K.; Kodali, V.; Kuchibhatla, S.; Orr, G.; Pounds, J. G.; Teeguarden, J. G.; Thrall, B. D.; Baer, D. R. *Surf. Interface Anal.* **2012**, *44* (8), 882–889.

(218) Hernández-Alonso, M. D.; Hungría, A. B.; Martínez-Arias, A.; Fernández-García, M.; Coronado, J. M.; Conesa, J. C.; Soria, J. *Appl. Catal. B Environ.* **2004**, *50* (3), 167–175.

(219) Chaisorn, J.; Wetchakun, K.; Phanichphant, S.; Wetchakun, N. *Mater. Lett.* **2015**, *160*, 75–80.

(220) Arul, N. S.; Mangalaraj, D.; Kim, T. W. *Appl. Surf. Sci.* **2015**, *349*, 459–464.

(221) Primo, A.; Marino, T.; Corma, A.; Molinari, R.; García, H. *J. Am. Chem. Soc.* **2011**, *133* (18), 6930–6933.

(222) Chiang, Y. M.; Lavik, E. B.; Blom, D. A. *Nanostructured Mater.* **1997**, *9* (1–8), 633–642.

(223) Skorodumova, N. V.; Simak, S. I.; Lundqvist, B. I.; Abrikosov, I. A.; Johansson, B. *Phys. Rev. Lett.* **2002**, *89* (16).

(224) Box, G. E. P.; Hunter, J. S.; Hunter, W. G. *Statistics for Experimenters: Design, Innovation, and Discovery, 2nd Edition*, 2nd edition.; Wiley-Interscience: Hoboken, N.J, 2005.

(225) Chen, H.-I.; Chang, H.-Y. *Ceram. Int.* **2005**, *31* (6), 795–802.

(226) Chen, H.-I.; Chang, H.-Y. *Solid State Commun.* **2005**, *133* (9), 593–598.

(227) Ivanov, V. K.; Polezhaeva, O. S.; Shaporev, A. S.; Baranchikov, A. E.; Shcherbakov, A. B.; Usatenko, A. V. *Russ. J. Inorg. Chem.* **2010**, *55* (3), 328–332.

(228) Feldman, I. *Anal. Chem.* **1956**, *28* (12), 1859–1866.

(229) Faure, B.; Salazar-Alvarez, G.; Ahniyaz, A.; Villaluenga, I.; Berriozabal, G.; De Miguel, Y. R.; Bergström, L. *Sci. Technol. Adv. Mater.* **2013**, *14* (2), 23001.

(230) Bravo, M.; Olivieri, A. C.; Oelckers, B. *J. Chil. Chem. Soc.* **2009**, *54* (1), 93–98.

(231) Turner, S.; Lazar, S.; Freitag, B.; Egoavil, R.; Verbeeck, J.; Put, S.; Strauven, Y.; Van Tendeloo, G. *Nanoscale* **2011**, *3* (8), 3385.

(232) Reed, K.; Cormack, A.; Kulkarni, A.; Mayton, M.; Sayle, D.; Klaessig, F.; Stadler, B. *Env. Sci Nano* **2014**, *1* (5), 390–405.

(233) Morales, D. A. *J. Chemom.* **2002**, *16* (5), 247–260.

(234) Calatayud, M.; Maldonado, L.; Minot, C. *J. Phys. Chem. C* **2008**, *112* (41), 16087–16095.

(235) Perrin, D. D. *Dissociation constants of inorganic acids and bases in aqueous solution,*; Butterworths: London, 1969.

(236) Kosmulski, M. *Chemical Properties of Material Surfaces*; CRC Press, 2001.

(237) Zholobak, N. M.; Ivanov, V. K.; Shcherbakov, A. B.; Shaporev, A. S.; Polezhaeva, O. S.; Baranchikov, A. Y.; Spivak, N. Y.; Tretyakov, Y. D. *J. Photochem. Photobiol. B* **2011**, *102* (1), 32–38.

(238) Trujillo-Reyes, J.; Vilchis-Nestor, A. R.; Majumdar, S.; Peralta-Videa, J. R.; Gardea-Torresdey, J. L. *J. Hazard. Mater.* **2013**, *263*, 677–684.

(239) Stoianov, O. O.; Ivanov, V. K.; Shcherbakov, A. B.; Stoyanova, I. V.; Chivireva, N. A.; Antonovich, V. P. *Russ. J. Inorg. Chem.* **2014**, *59* (2), 15–23.

(240) Wang, J.; Mei, Y.; Tanner, P. A. *J. Lumin.* **2014**, *146*, 440–444.

(241) Kuyper, A. C. *J. Am. Chem. Soc.* **1933**, *55* (4), 1722–1727.

(242) Sauvola, J.; Pietikäinen, M. *Pattern Recognit.* **2000**, *33* (2), 225–236.

(243) Dunphy Guzman, K. A.; Finnegan, M. P.; Banfield, J. F. *Environ. Sci. Technol.* **2006**, *40* (24), 7688–7693.

(244) Kalyanasundaram, K.; Grätzel, M. *Coord. Chem. Rev.* **1998**, *177* (1), 347–414.

(245) She, C.; Guo, J.; Irle, S.; Morokuma, K.; Mohler, D. L.; Zabri, H.; Odobel, F.; Youm, K.-T.; Liu, F.; Hupp, J. T.; Lian, T. *J. Phys. Chem. A* **2007**, *111* (29), 6832–6842.

(246) Wang, S.-W.; Wu, K.-L.; Ghadiri, E.; Lobello, M. G.; Ho, S.-T.; Chi, Y.; Moser, J.-E.; De Angelis, F.; Grätzel, M.; Nazeeruddin, M. K. *Chem. Sci.* **2013**, *4* (6), 2423.

(247) Lu, Z.; Karakoti, A.; Velarde, L.; Wang, W.; Yang, P.; Thevuthasan, S.; Wang, H. *J. Phys. Chem. C* **2013**, *117* (46), 24329–24338.

(248) Vlasova, N. N.; Golovkova, L. P.; Stukalina, N. G. *Colloid J.* **2015**, *77* (4), 418–424.

(249) Huxter, V. M. Optical and Material Properties of Colloidal Semiconductor Nanocrystals, University of Toronto, 2009.

(250) Kormann, C.; Bahnemann, D. W.; Hoffmann, M. R. *J. Phys. Chem.* **1988**, *92* (18), 5196–5201.

(251) Arul, N. S.; Mangalaraj, D.; Chen, P. C.; Ponpandian, N.; Viswanathan, C. *Mater. Lett.* **2011**, *65* (17–18), 2635–2638.

(252) Kuchibhatla, S. V. N. T.; Karakoti, A. S.; Baer, D. R.; Samudrala, S.; Engelhard, M. H.; Amonette, J. E.; Thevuthasan, S.; Seal, S. *J. Phys. Chem. C* **2012**, *116* (26), 14108–14114.

(253) Reyes-Coronado, D.; Rodríguez-Gattorno, G.; Espinosa-Pesqueira, M. E.; Cab, C.; de Coss, R.; Oskam, G. *Nanotechnology* **2008**, *19* (14), 145605.

(254) Grahn, H. T. *Introduction to Semiconductor Physics*; World Scientific, 1999.

(255) Tsunekawa, S.; Wang, J.-T.; Kawazoe, Y.; Kasuya, A. *J. Appl. Phys.* **2003**, *94* (5), 3654.

(256) Hernández-Alonso, M. D.; Belén Hungría, A.; Martínez-Arias, A.; Coronado, J. M.; Carlos Conesa, J.; Soria, J.; Fernández-García, M. *Phys Chem Chem Phys* **2004**, *6* (13), 3524–3529.

(257) Polezhaeva, O. S.; Yaroshinskaya, N. V.; Ivanov, V. K. *Russ. J. Inorg. Chem.* **2007**, *52* (8), 1184–1188.

(258) Phoka, S.; Laokul, P.; Swatsitang, E.; Promarak, V.; Seraphin, S.; Maensiri, S. *Mater. Chem. Phys.* **2009**, *115* (1), 423–428.

(259) Goharshadi, E. K.; Samiee, S.; Nancarrow, P. *J. Colloid Interface Sci.* **2011**, *356* (2), 473–480.

(260) Liu, I.-T.; Hon, M.-H.; Teoh, L. G. *J. Electron. Mater.* **2013**, *42* (8), 2536–2541.

(261) Ko, H.-H.; Yang, G.; Cheng, H.-Z.; Wang, M.-C.; Zhao, X. *Ceram. Int.* **2014**, *40* (3), 4055–4064.

(262) Tsunekawa, S.; Sahara, R.; Kawazoe, Y.; Kasuya, A. *Mater. Trans. JIM* **2000**, *41*.

(263) Brus, L. *J. Phys. Chem.* **1986**, *90* (12), 2555–2560.

(264) Zhang, F. *J. Appl. Phys.* **2004**, *95* (8), 4319.

(265) Deshpande, S.; Patil, S.; Kuchibhatla, S. V.; Seal, S. *Appl. Phys. Lett.* **2005**, *87* (13), 133113.

(266) Wu, L.; Wiesmann, H. J.; Moodenbaugh, A. R.; Klie, R. F.; Zhu, Y.; Welch, D. O.; Suenaga, M. *Phys. Rev. B* **2004**, *69* (12).

(267) Tsunekawa, S.; Sahara, R.; Kawazoe, Y.; Ishikawa, K. *Appl. Surf. Sci.* **1999**, *152* (1), 53–56.

(268) Tsunekawa, S.; Sivamohan, R.; Ito, S.; Kasuya, A.; Fukuda, T. *Nanostructured Mater.* **1999**, *11* (1), 141–147.

(269) Babitha, K. K.; Sreedevi, A.; Priyanka, K. P.; Sabu, B.; Varghese, T. *Indian J. Pure Appl. Phys. IJPAP* **2015**, *53* (9), 596–603.

(270) Maensiri, S.; Masingboon, C.; Laokul, P.; Jareonboon, W.; Promarak, V.; Anderson, P. L.; Seraphin, S. *Cryst. Growth Des.* **2007**, *7* (5), 950–955.

(271) Takeda, Y.; Mafuné, F. *Chem. Phys. Lett.* **2014**, *599*, 110–115.

(272) Liu, B.; Liu, B.; Li, Q.; Li, Z.; Liu, R.; Zou, X.; Wu, W.; Cui, W.; Liu, Z.; Li, D.; Zou, B.; Cui, T.; Zou, G. *J. Alloys Compd.* **2010**, *503* (2), 519–524.

(273) Lorite, I.; Romero, J. J.; Fernandez, J. F. *AIP Adv.* **2015**, *5* (3), 37105.

(274) Paun, C.; Safonova, O. V.; Szlachetko, J.; Abdala, P. M.; Nachtegaal, M.; Sa, J.; Kleymenov, E.; Cervellino, A.; Krumeich, F.; van Bokhoven, J. A. *J. Phys. Chem. C* **2012**, *116* (13), 7312–7317.

(275) Inerbaev, T. M.; Karakoti, A. S.; Kuchibhatla, S. V. N. T.; Kumar, A.; Masunov, A. E.; Seal, S. *Phys Chem Chem Phys* **2015**, *17* (9), 6217–6221.

(276) Bouchaud, B.; Balmain, J.; Bonnet, G.; Pedraza, F. *J. Rare Earths* **2012**, *30* (6), 559–562.

(277) Trovarelli, A. *Catal. Rev.* **1996**, *38* (4), 439–520.

(278) Wang, J.; Zhang, B.; Shen, M.; Wang, J.; Wang, W.; Ma, J.; Liu, S.; Jia, L. *J. Sol-Gel Sci. Technol.* **2011**, *58* (1), 259–268.

(279) Bahnemann, D.; Henglein, A.; Spanhel, L. *Faraday Discuss. Chem. Soc.* **1984**, *78* (0), 151–163.

(280) Schirmer, O. F. *J. Phys. Condens. Matter* **2006**, *18* (43), R667–R704.

(281) Genreith-Schriever, A. R.; Hebbeker, P.; Hinterberg, J.; Zacherle, T.; De Souza, R. A. *J. Phys. Chem. C* **2015**, *119* (51), 28269–28275.

(282) Sayle, D. C.; Maicaneanu, S. A.; Watson, G. W. *J. Am. Chem. Soc.* **2002**, *124* (38), 11429–11439.

(283) Tamaki, Y.; Furube, A.; Katoh, R.; Murai, M.; Hara, K.; Arakawa, H.; Tachiya, M. *Comptes Rendus Chim.* **2006**, *9* (2), 268–274.

(284) Rothenberger, G.; Moser, J.; Graetzel, M.; Serpone, N.; Sharma, D. K. *J. Am. Chem. Soc.* **1985**, *107* (26), 8054–8059.

(285) Qi, L.; Sehgal, A.; Castaing, J.-C.; Chapel, J.-P.; Fresnais, J.; Berret, J.-F.; Cousin, F. *ACS Nano* **2008**, *2* (5), 879–888.

(286) Burnham, K. P. *Sociol. Methods Res.* **2004**, *33* (2), 261–304.

(287) Janotti, A.; Franchini, C.; Varley, J. B.; Kresse, G.; Van de Walle, C. G. *Phys. Status Solidi RRL – Rapid Res. Lett.* **2013**, *7* (3), 199–203.

(288) Savory, D. M.; McQuillan, A. J. *J. Phys. Chem. C* **2014**, *118* (25), 13680–13692.

(289) Liyanage, A. D.; Perera, S. D.; Tan, K.; Chabal, Y.; Balkus, K. J. *ACS Catal.* **2014**, *4* (2), 577–584.

(290) Miyauchi, M.; Nakajima, A.; Watanabe, T.; Hashimoto, K. *Chem. Mater.* **2002**, *14* (6), 2812–2816.

(291) Serpone, N. *J. Photochem. Photobiol. -Chem.* **1997**, *104* (1–3), 1–12.

(292) Ishibashi, K.; Fujishima, A.; Watanabe, T.; Hashimoto, K. *J. Photochem. Photobiol. -Chem.* **2000**, *134* (1–2), 139–142.

(293) Bahnemann, D. W.; Hilgendorff, M.; Memming, R. *J. Phys. Chem. B* **1997**, *101* (21), 4265–4275.

(294) Sun, L. Z.; Bolton, J. R. *J. Phys. Chem.* **1996**, *100* (10), 4127–4134.

(295) Anpo, M.; Shima, T.; Kodama, S.; Kubokawa, Y. *J. Phys. Chem.* **1987**, *91* (16), 4305–4310.

(296) Panhans, M.; Blumenthal, R. *Solid State Ion.* **1993**, *60* (4), 279–298.

(297) Baker, E.; Iqbal, M.; Knox, B. *J. Mater. Sci.* **1977**, *12* (2), 305–310.

(298) Holverson, E. L.; Kevane, C. J. *J. Chem. Phys.* **1966**, *44* (10), 3692–3696.

(299) Shockley, W.; Read, W. *Phys. Rev.* **1952**, *87* (5), 835–842.

(300) Yin, L.; Wang, Y.; Pang, G.; Koltypin, Y.; Gedanken, A. *J. Colloid Interface Sci.* **2002**, *246* (1), 78–84.

(301) Zhang, Y.-W.; Si, R.; Liao, C.-S.; Yan, C.-H.; Xiao, C.-X.; Kou, Y. *J. Phys. Chem. B* **2003**, *107* (37), 10159–10167.

(302) Sujana, M. G.; Chattopadyay, K. K.; Anand, S. *Appl. Surf. Sci.* **2008**, *254* (22), 7405–7409.

(303) Kumar, A.; Babu, S.; Karakoti, A. S.; Schulte, A.; Seal, S. *Langmuir* **2009**, *25* (18), 10998–11007.

(304) Shehata, N.; Meehan, K.; Hudait, M.; Jain, N. *J. Nanoparticle Res.* **2012**, *14* (10).

(305) Samiee, S.; Goharshadi, E. K.; Nancarrow, P. *Proc. 4th Int. Conf. Nanostructures ICNS4* **2012**, 1222–1224.

(306) Manoharan, D.; Vishista, K. *Asian J. Chem.* **2013**, *25* (16).